Ultrasound-assisted Modulation of the Endothelial Cell Membrane for Cellular Immunotherapy

Elahe Memari

A Thesis
In the Department
of
Physics

Presented in Partial Fulfillment of the Requirements
For the Degree of
Doctor of Philosophy (Physics) at
Concordia University
Montreal, Quebec, Canada

March 2025

CONCORDIA UNIVERSITY
SCHOOLOF GRADUATE STUDIES

This is to certify that the thesis

By: Elahe Memari
Entitled: Ultrasound-assisted modulation of the endothelial cell membrane for cellular immunotherapy

and submitted in partial fulfillment of the requirements for the degree of

DOCTOR OF PHILOSOPHY (Physics)

complies with the regulations of the University and meets the accepted standards with respect to originality and quality.

Signed by the final examining committee:

_____ Chair
Dr. Andreas Bergdahl

_____ External Examiner
Dr. Meaghan O'Reilly

_____ Examiner
Dr. Claudine Gauthier

_____ Examiner
Dr. Peter Darlington

_____ Examiner
Dr. Steve Shih

_____ Thesis Supervisor
Dr. Brandon Helfield

Approved by _____
Dr. Saurabh Maiti, Graduate Program Director

March, 2025 _____
Dr. Pascale Sicotte, Dean
Faculty of Arts and Science

ABSTRACT

Ultrasound-assisted modulation of the endothelial cell Membrane for cellular immunotherapy

Elahe Memari, Ph.D.

Concordia University, 2025

The potential of immunotherapy for brain cancer remains limited due to the presence of a restrictive blood-brain barrier and suppressive tumor microenvironment. Therefore, developing strategies to improve the efficacy of molecular and cellular immunotherapy is in urgent need. In this thesis, I explore the potential of therapeutic ultrasound under fluid flow conditions to enhance endothelial cell permeabilization and immunobiology for improving immunotherapy. Here, fluidic systems were employed to cultivate and treat two human endothelial cell types, either umbilical vein (HUVEC) or brain endothelial cells (HBEC-5i), under flow conditions. The findings demonstrated a direct correlation between microbubble flow velocity and ultrasound-assisted cell permeabilization. The velocity of microbubble perfusion also substantially influenced the dynamics of Ca^{2+} influx in endothelial cells. Additionally, shear-flow preconditioning influenced endothelial cells' cytokine profile, significantly enhancing their susceptibility to ultrasound. Furthermore, distinct microbubble flow patterns dramatically influenced the efficiency of cell permeabilization. Building on these findings, I explored the effects of microbubble-induced shear stress on endothelial cell immunobiology. Ultrasound-stimulated microbubbles led to a time-dependent upregulation of cell adhesion molecules involved in immune cell homing. Additionally, ultrasound treatment under identical conditions significantly increased the secretion of 20 cytokines and chemokines 4 hours post-sonication, improving CAR NK-92 cells homing and trafficking. Overall, this thesis highlights the potential of ultrasound-activated microbubbles to overcome the challenges of tumor microenvironments, thereby enhancing the efficacy of cellular immunotherapy.

Acknowledgements

Before anything else, I would like to thank my supervisor, Dr. Brandon Helfield. I feel incredibly fortunate to have had the opportunity to learn from you. Your constant support and belief in me have meant more than I can put into words. Beyond the knowledge you have shared, you have set an example of the kind of scientist and person I want to be. Your integrity, dedication and compassion have not only shaped my research journey but have also shown me what it means to lead with kindness. Thank you for challenging me to think critically, celebrating even the smallest successes, and guiding me toward a research path I am genuinely excited about.

Thank you to Dr. Ryan Alkins for giving me the opportunity to get hands-on experience in the MRI-guided focused ultrasound lab at Queens University, where I benefited from his expertise in ultrasound-mediated brain cancer treatment. I also sincerely appreciate Dr. Christopher Nicol for hosting me in his lab and Dure Khan for her support and friendship during my time there.

I would like to sincerely thank my supervisory committee, Dr. Claudine Gauthier and Dr. Peter Darlington, for their invaluable feedback and encouragement throughout my graduate studies. And a special thank you to Dr. Meaghan O'Reilly for kindly taking on the role of external examiner and giving me the opportunity to benefit from her extensive expertise in therapeutic ultrasound.

Many thanks to the Helfield lab for being such incredible friends and colleagues. Your support, humour, and all the fun moments, both in the lab and at conferences, made this journey unforgettable. From experiments to travels, I am so grateful for the memories we have made. Shoutout to Zoe Katz, Davindra Singh, Stephanie He, Emma Beisswanger, Kyle Hazel, Zakary Guertin, Megan Mcmanus, Ana Baez, Alexander Kaloyannis, Ellen Fong, and Setareh Eftekhari.

Thank you to my family and friends, for their unconditional love and support throughout this journey. Your encouragement has been my anchor through the highs and lows, and I am endlessly grateful for the strength you have given me. I am so thankful for having you by my side through every challenge and victory. And finally, a special thank you to my mother. No words will ever be enough to express how deeply grateful I am for your love and sacrifices. You have always encouraged me to dream bigger, aim higher and never settle for less than what I am capable of.

To my father, Iraj, whose presence I have carried in my heart every step of the way.

This work is in your honour, with the hope of making you proud.

List of Contributions

This thesis consists of an introduction (chapter 1), four published articles (chapters 2, 3, 4, 5), results for an upcoming article (chapter 6), and conclusion and future directions (chapter 7).

Chapter 1: Introduction was written by me and reviewed by Dr. Brandon Helfield.

Chapter 2: Memari, Elahe, et al. "Focused ultrasound-assisted delivery of immunomodulating agents in brain cancer." Journal of Controlled Release (2024). I am responsible for conceptualization, data curation and analysis, investigation, methodology and writing the original draft. Dure Khan contributed to review & editing. Dr. Ryan Alkins contributed to conceptualization and review & editing. Dr. Brandon Helfield contributed to conceptualization, project design, supervision, investigation, methodology and review & editing.

Chapter 3: Memari, Elahe, et al. Fluid flow influences ultrasound-assisted endothelial membrane permeabilization and calcium flux. Journal of Controlled Release (2023). I am responsible for conceptualization, data curation and analysis, investigation, methodology and writing the original draft. Fiona Hui contributed to investigation. Hossein Yusefi contributed to methodology. Dr. Brandon Helfield contributed to conceptualization, project design, supervision, investigation, methodology and review & editing.

Chapter 4: Memari, Elahe, et al. Shear stress preconditioning and microbubble flow pattern modulate ultrasound-assisted plasma membrane permeabilization. Materials Today Bio, (2024). I am responsible for conceptualization, data curation and analysis, investigation, methodology and writing the original draft. Dr. Brandon Helfield contributed to conceptualization, project design, supervision, investigation, methodology and review & editing.

Chapter 5: Memari, Elahe, et al. Shear stress and microbubble-mediated modulation of endothelial cell immunobiology. Small Science, (2024). I am responsible for conceptualization, data curation and analysis, investigation, methodology and writing the original draft. Davindra Singh contributed to investigation. Dr. Ryan Alkins contributed to conceptualization and review & editing. Dr. Brandon Helfield contributed to conceptualization, project design, supervision, investigation, methodology and review & editing.

Chapter 6: Investigating the effects of US on CAR NK-92 cell recruitment and infiltration in vitro. I am responsible for conceptualization, data curation and analysis, investigation, methodology and writing. Dr. Brandon Helfield contributed to conceptualization, project design, supervision, investigation, methodology and revision.

Chapter 7: Conclusion and future directions were written by me and reviewed by Dr. Brandon Helfield.

Contents

Lists of Figures

List of Tables

Abbreviations

5-ALA……5-Aminolevulinic acid

ABC……...ATP-binding cassette

AD…….....Alzheimer's Disease

ACT……...Adoptive cell transfer

ADCC……..….Antibody-dependent cellular cytotoxicity

ALS ……..Amyotrophic lateral sclerosis

ALL ……..Acute lymphoblastic leukemia

APC …….....Antigen presenting cells

ATP…….....Adenosine triphosphate

B-ALL……..…..B cell acute lymphoblastic leukemia

BEC……....Brain endothelial cells

BBB ……...Blood-brain barrier

BBBD……..BBB disruption

BBBO……..Blood-brain-barrier opening

BDNF..…….Brain-derived neurotrophic factor

BMDM……....Bone-marrow derived macrophages

BTB…….....Blood-tumor barrier

CAR…….Chimeric antigen receptor

CAM……Cell adhesion molecule

CTL……..Cytotoxic T cells

CVD….……Cardiovascular disease

DPPA……1,2-dipalmitoyl-sn-glycero-3-phosphate

DPPC……....1,2-dipalmitoyl-sn-glycero-3-phosphocholine

DPPE ……..…..1,2-dipalmitoyl-sn-glycero-3-phosphoethanolamine

ECM……...Extracellular matrix

EGM-2……....Endothelial cell growth medium

EGF…….Epidermal growth factor

ER……Enrichment ratio

ET……Essential tremor

FBS……..Fetal bovine serum

FGF-2……..Fibroblast growth factor-2

FUS…….Focused ultrasound

GBM……...Glioblastoma multiforme

GO…….....Gene ontology

GVHD……Graft versus host disease

HIFU……...High intensity focused ultrasound

HER2……..Human epidermal growth factor receptor 2

HBEC-5i…….Human cerebral microvascular endothelial cells

HUVEC…….....Human umbilical vein cells

IQR…….Interquartile range

IFN-γ……...Interferon-γ

IL-13Rα2…….....IL-13 receptor α2

LAG-3…….Lymphocyte activation gene-3

LIPU……....Low-intensity pulsed ultrasound

LDL…….…....Low-density lipids

LIFUS……..Low intensity focused ultrasound

MACE…….Major adverse cardiovascular event

M-HIFU…….….Mechanical high intensity ultrasound

MI……..…..Mechanical index

MMPs…….Matrix metalloproteinases

MHC……...Histocompatibility complex

NK cells……Natural killer cells

NF-κB……...Nuclear factor κB

ORA…….Over-representation analysis

PECAM-1…..……Platelet endothelial cell adhesion molecule-1

PI…….……Propidium iodide

PRI…….....…Pulse repetition interval

PBS……..……...Phosphate-buffered saline

PBS-BSA……..…...Bovine serum albumin

ROS……...…..Reactive oxygen species

RNS……...…..Reactive nitrogen species

RT……...….Radiotherapy

SMC……....Smooth muscle cells

SDT…….....Sonodynamic therapy

SRS……..…...Stereotactic radiosurgery

TAMs……..Tumor-associated macrophages

TCR……T-cell receptor

TIGIT…….……T cell immunoreceptor with Ig and ITIM domains

TIFP…….…...Tumor interstitial fluid pressure

TIM-3…….……T cell immunoglobulin and mucin domain-containing protein 3

TME……Tumor microenvironment

TDPD……..Tremor-dominant PD

TILs……....Tumor-infiltrating lymphocytes

TRAIL……Tumor necrosis factor-related apoptosis-induced ligand

TANs……Tumor-associated neutrophils

Tregs……....Regulatory T cells

VEGF……...Vascular endothelial growth factor

VEGFR2……..Vascular endothelial growth factor receptor 2

VE-cadherin……..Vascular endothelial cadherin

USMD……Ultrasound-stimulated microbubbles destruction

1. Introduction and Background Motivation

1.1. Brain Cancer

Primary and metastatic brain tumors remain one of the leading causes of death worldwide due to the complexity of these neurological malignancies. The central nervous system (CNS) is a common site for metastasis from lung cancer, with the highest rate of 20-56%, followed by breast cancer, with a range of 20-30%, based on the cancer subtype. CNS metastasis occurs when circulating malignant cells enter from the primary tumor sites into the neurovascular system, followed by tumor development throughout the neuroaxis[1]. However, intracranial metastasis is the most prevalent type, dominantly forming within the brain parenchyma. Despite the higher incidence rate of metastatic versus primary brain tumors, glioblastoma multiforme (GBM), which is a grade IV astrocytoma, is known as the most lethal brain cancer. Additionally, GBM has the highest incidence rate among adults, with a poor survival rate of less than 15 months when patients undergo standard-of-care therapy. A significant contributing factor in the poor prognosis of GBM is the inter- and intra-tumoral heterogenicity in the genetic aberrations, as well as the cellular and molecular composition of their tumor microenvironment (TME), which contribute to treatment resistance. Beyond the tumor heterogenicity, the distinct physiology of brain tumor vasculature poses significant challenges to treatment outcomes. Brain tumor vasculature is characterized as an irregular network of tortuous vessels with high permeability and the presence of dead-end vessels. Despite the dissimilarities of the primary and metastatic brain tumors, their prognosis faces comparable challenges, including the presence of the blood brain barrier (BBB) and TME. As an enclosed and tightly regulated organ, the brain protects itself from systemic immunity by confining the trafficking of adaptive immune cells using the BBB. Therefore, as compared to peripheral cancers, TME of CNS tumors, whether primary or metastatic, experience limited infiltration of effector immune cells, especially T cells, which contribute to development of a highly immunosuppressive environment around the tumor. Given the restricted immune profile of brain tumors, they are considered as a cold tumor, which is linked to the poor response to current immunotherapies. Therefore, to unlock the potential of immunotherapy strategies, we must first explore the underlying challenges, more specifically the BBB and TME[2].

1.2. Blood Brain Barrier

The blood-brain barrier (BBB) is a tightly regulated microenvironment that shields the brain and spinal cord by forming a restrictive barrier between bloodstream and CNS parenchyma. It comprises a single layer of endothelial cells, supported by pericytes and astrocytic perivascular processes. One of the distinctive characteristics of the BBB is the expression of specialized tight junction proteins between endothelial cells, creating a highly restricted barrier which prevents the paracellular diffusion of the majority of molecules and therapeutic agents. Additionally, the BBB actively prevents the transcellular entry of most molecules and blood-derived compounds through the high expression of active efflux pumps, especially ATP-biding cassette (ABC) transporters, including P-glycoproteins, and the multi-drug resistance-associated protein 1 and 2 on brain endothelial cells [3]. Despite the highly restrictive nature of the BBB, it permits the passage of ions and essential nutrients for normal brain function, including amino acids, peptides, vitamins, glucose and folic acid. Additionally, it allows the entry of small molecules under 400 Da with high lipid solubility, typically characterized as molecules with less than eight hydrogen bonds [4]. However, not all small hydrophilic molecules can cross the BBB, and 98% of the small molecules are unable to penetrate this highly limited barrier. This presents a significant challenge for developing therapeutic agents to treat brain malignancies, as all large macromolecules, including recombinant proteins and monoclonal antibodies, along with most small therapeutic agents are unable to cross this barrier[5]. Unlike the healthy brain, the integrity of the BBB is compromised in many brain conditions such as brain cancer, Alzheimer's disease, amyotrophic lateral sclerosis and multiple sclerosis. The vascular structure in brain tumor is remarkably heterogeneous, with a highly permeable endothelium in the tumor core, while the vessels at the tumor periphery remain largely intact. One factor that contributes to the BBB disruption is an elevated level of vascular endothelial growth factor (VEGF) which can increase the permeability of the BBB by the disruption of tight junctions between endothelial cells[6]. Furthermore, the tumor-secreted factors and pro-inflammatory cytokines in the GBM environment result in the loss of a fraction of tight junction proteins, including claudin-3 and the downregulation of claudin-1 and claudin-5, which lead to BBB disruption[7].

1.3. Tumor Microenvironment

The brain TME is a unique niche comprised of cancerous cells, diverse immune cells, mesenchymal stem cells, fibroblasts, and a network of cerebral vessels. Additionally, TME is

enriched with varied cytokines, chemokines and growth factors, depending on the cancer type. Notably, TME composition determines the cancer progression and its response to immunotherapies. More specifically, cellular components of TME are critical targets for developing novel immunotherapy strategies for brain cancer treatment [8]. Among these components, tumor-infiltrating T lymphocytes play a dual role, either promoting tumor growth or facilitating tumor clearance. While cytotoxic T cells (CTL) can strongly eradicate tumor cells, the majority of CTLs within the TME are either exhausted or functionally impaired[9]. Furthermore, most CD4+ T cells in TME are regulatory T cells, further contributing to the suppressive features of TME. Besides T lymphocytes, brain TME is enriched with tumor-associated macrophages (TAM), a key component of the tumor's immune landscape. TAMs are the dominant population of immune cells in GBM TME, making up approximately 30% of the tumor mass. These cells are classified into two groups of bone-marrow derived macrophages (BMDM) and microglia originating from the yolk sac. It has been shown that BMDMs constitute a more significant proportion of TAMs in GBM TME. Other critical immune cells in the TME are NK cells, which are capable of targeting and eradicating cancerous cells by detecting the danger signal. However, GBM cells can evade NK cell-mediated cytotoxicity by expressing HLA-G, which interacts with inhibitory receptors on NK cells, resulting in their functional suppression. Given the critical role of TME in cancer behaviour and response to treatment, understanding its variations between primary and metastatic brain tumors is essential. Interestingly, meaningful differences exist in both TME composition and tumor vascularization, not only between primary and metastatic brain tumors, but also among brain metastasis originating from different cancers. For instance, the TME of secondary brain tumors from lung cancer is dominantly infiltrated with T cells, whereas breast cancer brain metastasis is mainly populated with myeloid cells. Furthermore, while the TME of primary brain tumors is rich in NK cells, metastatic brain tumors largely lack NK cells[10].

Aside from the immune cell population within TME, glioma stem cells (GSC) are a fundamental component of the GBM environment. The proportion of GSCs within the TME directly correlates with the tumor grade and angiogenesis. GSCs promote tumor progression through the recruitment of monocytes and triggering their polarization to pro-tumor macrophages. Moreover, GSCs adversely affect T cell population within the TME by inhibiting the effector T cells and activating regulatory T cells. Another critical cell type within the TME is astrocyte, which plays a crucial role in brain homeostasis and maintaining the integrity of the BBB in the healthy brain. However, in

the presence of tumor, astrocytes contribute to tumor progression by secreting pro-tumor cytokines and growth factors.

1.4. Research Statement

Given the highly infiltrative nature of brain tumors into the surrounding brain parenchyma, the first line of treatment is maximal surgical resection of tumor mass without damaging the healthy brain tissues. Following surgery, repeated sessions of radiotherapy will be performed to remove the remaining tumor mass, which depends on the cancer type, location and stage. Repeated radiotherapy can cause radio-necrosis of the brain's healthy tissues. Therefore, the potential toxicity of whole-brain radiation therapy has highlighted the necessity of more targeted approaches, such as stereotactic radiosurgery (SRS). Despite the effectiveness of this strategy for the early stages of brain metastasis, it fails in the case of widespread brain metastasis[1]. Additionally, as a supplement to surgery and radiotherapy, chemotherapy is administered to eradicate the remaining tumor mass further and prevent tumor recurrence. However, chemotherapy for brain cancers is faced with significant challenges, the first of which is the inability of most therapeutic agents to pass across the BBB and reach the tumor site. Additionally, the systemic administration of therapeutic agents can lead to off-target effects and systemic toxicity. Another factor that decreases the efficiency of chemotherapeutic agents is intra-tumoral molecular heterogenicity, which is partly due to the evolving genetic profile of the tumor cells[11]. Therefore, the failure of traditional treatments to improve the patients' long-term survival has led to the emergence of novel therapies such as immunotherapies. Over the past few decades, immunotherapy strategies, including immune checkpoint blockade and the adoptive transfer of engineered chimeric antigen receptor (CAR) T or NK cells, have shown considerable potential for cancer therapy, especially hematological malignancies such as B cell acute lymphoblastic leukemia (B-ALL) and multiple myeloma. While CAR-T cells have been approved for treating several blood-borne cancers, CAR-NK cells are emerging as a better alternative for cancer therapy due to their intrinsic ability to kill abnormal cells and substantially lower side effects. Despite the potential of CAR-T and CAR-NK cells, their application for brain cancer treatment remains poor due to their inability to cross the BBB and the presence of a highly suppressive TME around the brain tumors. Therefore, there is an urgent need to develop novel strategies to promote an anti-tumor immune response and improve the trafficking of effector immune cells into the tumor site.

In this regard, focused ultrasound emerges as a promising solution to address the treatment challenges of brain malignancies that are posed by conventional therapies.

Focused ultrasound presents its therapeutic applications through varied mechanisms of action, one of which is inducing mechanical effects when combined with intravenously injected microbubbles. Ultrasound-stimulated microbubbles have been extensively investigated for their application in the transient opening of the BBB, allowing the penetration of therapeutic agents such as drugs with a molecular weight of >400 Da and monoclonal antibodies. In addition to drug delivery applications, ultrasound-stimulated microbubbles have gained increasing interest due to their potential to elicit a strong immune response and modulate TME. One proposed mechanism is through the transient yet large magnitude shear stress that is applied to the vascular endothelium by the oscillating microbubbles in an ultrasound field. In general, shear forces such as shear stress induced by blood flow are suggested to influence the surface expression of critical cell adhesion molecules (CAMs) and anti-tumor cytokines and chemokines. Therefore, the shear-induced molecular changes play a crucial role in the recruitment and trafficking of effector immune cells into the tumor site, thus modulating the TME. Another critical factor is the abnormal morphology of the tumor vasculature, which results in disturbed blood flow and consequently impacts the microbubble perfusion pattern within the tumor tissue.

To address these challenges, this thesis investigates the influence of ultrasound in combination with continuously flowing microbubbles under fluid flow in local enhancement of immune cell trafficking to improve the efficacy of cellular immunotherapy in the context of brain cancers. The following sections of this chapter will provide background context on NK-mediated cellular immunotherapy – including immune cell trafficking and shear stress considerations – followed by an introduction to focused ultrasound and its main applications.

1.5. NK and CAR-NK Cells

Natural killer cells (NK cells) are characterized as large granular lymphocytes, which are a part of the innate immune system. NK cells target a wide range of tumor cells and some virus-infected cells. Due to their lymphocyte-like characteristics, NK cells serve as a bridge between innate and adaptive immune systems[12]. They account for 5-15 % of peripheral leukocytes, with the majority belonging to $CD56^{dim}$ $CD16^{high}$ subset with high cytotoxicity and less than 15 % belonging to $CD56^{bright}$ $CD16^{low}$ subset, known as immature NK cells[13]. A distinguishing feature of NK cells

is their ability to lyse the target tumor cells without prior exposure or specific immunization, which makes them an ideal target for cellular immunotherapy. NK cell's function relies on a balance between the activating and inhibitory receptors on their surface. Activating receptors such as NKG2D and NKP30 can interact with stress-induced ligands on the target cells. In contrast, inhibitory receptors like KIR and NKG2A suppress NK cells by binding to MHC class I on normal cells. Under normal conditions, the suppression of NK cells via their inhibitory receptors is essential to prevent damage to healthy tissues. However, the reduction or loss of MHC class I molecules on infected or malignantly transformed cells, known as 'missing self' prevents the inhibitory signals, thus allowing the NK cells to promote an inflammatory response[12]. In contrast, activating receptors can engage with cell-surface proteins on the target cells that have been stimulated via metabolic stress known as 'stress-induced self,' which shifts the balance toward the activation of NK cells when at least two activating receptors on NK cells are triggered. From a functional perspective, NK cells are unique in having several mechanisms to eliminate the target cells , one of which is relatively similar to the cytotoxic function of CD8-positive T cells. NK cells contain cytotoxic granules loaded with perforin and granzyme B within their cytoplasm, which are released upon exposure to infected or malignantly transformed cells. Perforins lead to the pore formation in the target cell membrane, which allows the penetration of granzymes, which then induces cell apoptosis. Another primary cytotoxic mechanism is the expression of tumor necrosis factor-related apoptosis-induced ligand (TRAIL), which is expressed on the NK cells and interacts with death receptors on the surface of many cells. The death receptors that interact with TRAIL ligands on NK cells are DR4 and DR5, which are a part of the TNFR superfamily. Upon the interaction, DR4 and DR5 stimulate the caspase 8-induced apoptosis of the target cells. The third cytotoxic mechanism of NK cells is called antibody-dependent cellular cytotoxicity (ADCC). In this process, the interaction of NK cell's surface FC receptors with antibody-coated target cells leads to the release of cytotoxic granules, followed by target cell lysis. In addition to the direct cytolytic function of NK cells, they can indirectly regulate the immune response through the secretion of cytokines. The main cytokine secreted by NK cells is interferon-γ (IFN-γ), which can activate innate immunity through the activation of macrophages, as well as adaptive immunity through activating dendritic cells and stimulating the differentiation of CD4 T cells toward a pro-inflammatory state. As mentioned before, the activation of NK cells depends on a dynamic interplay between clusters of germline-encoded activating and inhibitory receptors. When NK cells

encounter the stress-induced target cells, the activating receptors will engage with these ligands and trigger the secretion of IFN-γ, followed by the release of cytotoxic granules, which can lead to target cell eradication[14].

Chimeric antigen receptor-transduced NK cells (CAR-NK cells) are highly targeted NK cells that are genetically modified to express a unique chimeric antigen receptor designed to interact with specific tumor antigens. One distinctive feature of CAR-NK cells is their ability to function independently of HLA recognition, which enables them to target the tumor cells in HLA-diverse patient populations. Besides, CAR structures can target a range of molecules beyond proteins, including carbohydrates and glycolipids[15]. CAR constructs consist of three moieties, including a single-chain antibody variable fragment as an extracellular domain which interacts with a specific tumor antigen, a transmembrane linker, and a signalling intracellular domain. CAR constructs are categorized into five generations based on the intracellular domain composition. First-generation CARs consist solely of the CD 3ζ signalling domain, which results in limited survival and activation of CAR-modified cells. Conversely, the second and third-generation CARs consist of CD 3ζ, in addition to one (e.g., CD28, CD137 or CD-134) or two (e.g., CD28 and CD137) costimulatory signals, respectively, which enhances the persistence and activity of CAR cells. While the second- and third-generation CAR constructs have exhibited better cytotoxicity than the first-generation, their limited total efficacy led to the emergence of fourth-generation CARs. The fourth-generation CAR structures are designed to incorporate a transgenic payload in the effector immune cellsgenome to enable the cell to secret a specific cytokine, such as IL-12, IL-15 and IL-18, to enhance the activation and cytotoxicity of the engineered cells[16].

1.6. Immune Cell Trafficking

Immune cells, such as T cells and NK cells, continuously monitor the body for infected or abnormal cells in a process known as immune surveillance However, in normal conditions, the vascular endothelium is inactivated, with lower expression levels of CAMs, which are essential intermediaries of immune cell trafficking. Additionally, the absence of chemotactic stimuli in the normal conditions leads to transient rolling of immune cells along the vessel walls without forming a firm adhesion and extravasation into the underlying tissues. In contrast, inflammation or tumor presence triggers the secretion of varied pro-inflammatory cytokines and chemokines, which regulate the activation of rolling and adhesion process through multiple mechanisms. One

immediate effect of the pro-inflammatory cytokines is the upregulation of immunoglobulin-like superfamily CAMs such as ICAM-1 and VCAM-1, which are critical for the firm adhesion of immune cells and their extravasation to the inflamed tissues. Pro-inflammatory cytokines also result in the conformational changes in integrins, including LFA-1 (CD11a: CD18) and CR3 (CD11b: CD18) on the effector immune cells, shifting them to a high-affinity conformation, which further enhances the possibility of the interaction between immune cells and endothelium. Generally, the process of rolling and adhesion of immune cells consists of several steps. Initially, immune cells roll along the endothelial monolayer by binding their fucosylated oligosaccharide ligands to the low-affinity selectins [14]. he immune cells' interaction with selectins is fragile and breaks rapidly due to the blood shear forces, which allows the immune cells to decelerate within the blood circulation. As they roll, immune cells are exposed to the systemic and locally secreted inflammatory chemokines from endothelial cells. These chemokines bind to immune cell receptors and trigger the heterodimeric integrins to unfold, which shifts their conformation to a high-affinity state. Next, immune cells interact with a subset of CAMs such as ICAM-1 and VCAM-1, forming firm adhesion and arrest. These firm interactions activate signalling pathways within the immune cells, which triggers morphology change and enables immune cells to squeeze between the endothelial cells and extravasate into the underlying tissues.

1.7. Shear Stress

Endothelial cells, lining the lumen of vessels, have long been shown to be regulated by chemical stimuli such as hormones, cytokines and neurotransmitters, which contribute to the maintenance of normal function of blood vessels. Beyond the chemical mediators, blood flow applies continuous mechanical forces on endothelial cells in the form of cyclic stretch and shear stress. Among these, cyclic stretch is generated by the intravascular pressure and is primarily sensed by the smooth muscle cells (SMC). In contrast, shear stress is a flow-induced frictional drag force applied tangentially on endothelium and is mainly sensed by the endothelial cells. Both SMCs and endothelial cells use mechanosensory molecules on their surface to sense the hemodynamic forces and convert them into various cellular responses including modulation of gene expression and cell function, a process referred to as mechanotransduction. Some known sensory molecules on endothelial cells include ion channels, junctional proteins, receptor tyrosine kinases, membrane lipid bilayers and specific CAMs such as platelet endothelial cell adhesion molecule-1 (PECAM-1). In particular, ion channels are key sensory molecules that respond to shear stress by rapidly and

strongly inducing the ionic flow. Among them, calcium channels are especially critical as they respond to shear stress by rapid intracellular calcium influx. The elevated cytosolic calcium in endothelial cells maintains homeostasis by inducing vasodilation via activating the release of nitric oxide and relaxation of smooth muscle cells. Additionally, the intracellular Ca^{2+} influx stimulates the hyperpolarization of endothelium by opening calcium-activated potassium channels, followed by hyperpolarization of smooth muscle cells through the gap junctions. Notably, shear-induced adenosine triphosphate (ATP) release is involved in initiating intracellular Ca^{2+} influx. Studies have shown that intracellular Ca^{2+} influx is activated through either ATP-sensitive cation channels like P2X4 at low extracellular ATP concentrations or G-protein-coupled receptors like P2Y2 at high ATP concentrations[17]. In some pathological conditions such as atherosclerosis and solid tumors, hemodynamic forces are altered due to the blood flow disturbance, followed by mechanotransduction impairment. Defective mechanosensing can lead to disruption of vascular integrity and remodelling. Additionally, it can influence vascular endothelial cells at a molecular level by altering the production of reactive oxygen species, growth-promoting and growth-inhibiting factors, pro-inflammatory cytokines, and modifying the expression of CAMs. Notably, some critical CAMs involved in immune cell rolling and adhesion are strongly shear sensitive. Accordingly, defective mechanotransduction in the tumor vasculature is an underlying cause of impaired immune cell trafficking due to the reduced expression of CAMs on tumor vasculature. Moreover, integrins on resting immune cells are in a low-affinity conformation for binding to CAMs on endothelial cells, with the headpiece of integrin facing down. However, under mechanical stretch, the integrin on immune cells unfolds and converts into a high affinity state for its ligand, thus promoting adhesion to endothelial cells. Therefore, defective mechanotransduction in tumor vasculature can negatively influence immune cell recruitment and trafficking through reduced expression of CAMs on endothelial cells and decreased affinity of integrins on immune cells.

Blood flow patterns vary across different anatomical sites throughout the circulatory system, which can lead to varied molecular and cellular responses. The blood flow profile in the straight arterial regions is laminar with a constant shear stress. It has been shown that laminar flow with high shear stress results in an anti-inflammatory response, whereas low laminar shear stress triggers a pro-inflammatory response. The shear-mediated inflammation activates as the mechanical signal is sensed by PECAM-1 on endothelial cells, which creates a signalling complex with vascular

endothelial cadherin (VE-cadherin) and vascular endothelial growth factor receptor 2 (VEGFR2). The engagement of the PECAM-1/VE-cadherin/VEGFR2 complex results in the activation of integrins and transient activation of nuclear factor κB (NF- κB) pathway. On the other hand, at the vessel branch points and bifurcations, the blood flow is disturbed with varying shear stress. The disturbed blood flow profile at the arterial branch points induces a pro-inflammatory response, which is involved in the initiation and development of atherosclerosis. Additionally, the disturbed blood flow exists at the tumor vasculature, due to the disorganized morphology of the vessels, adding to the complexity of tumor.

1.8. Focused Ultrasound

Ultrasound refers to high-frequency sound waves above 20 kHz and has been extensively exploited in medical imaging since the 1970s. The mechanism of ultrasound imaging relies on how ultrasound waves interact with various body tissues. As ultrasound waves travel through the body, they partially transmit deep in the tissue based on the tissue's acoustic properties and partially reflect back to the transducer as echoes[18]. The strength of return ultrasound signals depends on acoustic impedance, a property of the tissue which depend on the tissue density and resistance to sound propagation. The resolution of ultrasound imaging is also influenced by the characteristics of the transducer, including size, frequency, and bandwidth. Frequency is a critical factor in imaging resolution, as the ultrasound waves with higher frequency have more series of compression and rarefaction over a given distance, which leads to higher image resolution. However, when the ultrasound beam propagates through the body, the ultrasound energy declines due to attenuation, resulting in a decrease in the center frequency of ultrasound. Since attenuation elevates with tissue depth and ultrasound frequency, thus for imaging of deeper tissues, lower center frequencies around 2-5 MHz are commonly employed[19]. Beyond imaging, the therapeutic applications of ultrasound have been widely investigated. Ultrasound applies its biological effects through either thermal or mechanical mechanisms. The first efforts to exploit the thermal effects of ultrasound for therapeutic applications go back to 1962, when high-intensity ultrasound was utilized to induce thermo-ablation via a cranial window[6]. More recently, there has been growing interest in leveraging low-intensity focused ultrasound for therapeutic applications. The following section will provide a more detailed description of these therapeutic methods.

1.9. Ultrasound Contrast Agents

Ultrasound contrast agents, known as microbubbles, are polydisperse spheres with a size of 1-5 μm, composed of a low water-solubility gas core, which is encapsulated in a thin shell of lipid, polymer or protein. Microbubble's stability primarily depends on its gas core solubility, shell composition, and bubble size. The first generation of microbubbles, including Albunex and Quantison, were comprised of serum albumin shells encapsulating an air-filled core. However, these agents had significant challenges, including short longevity of the air-filled core due to rapid air diffusion in the surrounding liquid and poor scattering properties of rigid albumin shell. To address these challenges, the second generation of microbubbles, including Definity, SonoVue and Sonazoid, were developed. These microbubbles comprise flexible lipid shells, encapsulating high molecular weight gases, such as perfluorocarbon or sulfur hexafluoride, which significantly enhance their stability in the bloodstream[20]. Microbubbles were initially used as diagnostic contrast agents to improve the resolution of ultrasound imaging. They have long been exploited for diagnosing and assessing cardiovascular diseases such as atherosclerosis and stroke, in addition to blood flow evaluation, especially in the microvasculature, where the blood flow is extremely slow[21], [22]. Beyond the microbubble's applications for diagnostics, these agents exhibit promising therapeutic potential due to their innate ability to focus acoustic energy. The strong scattering properties of microbubbles, which are derived by high differential impedance between the microbubble gas core and the surrounding medium, are the key to their imaging applications. Under acoustic exposure, the successive compression and expansion of microbubbles with each pressure cycle magnifies their scattered signal, making them distinctive from the surrounding tissue[20]. Ultrasound propagation within a liquid containing microbubbles induces periodic liquid pressure changes, leading to pressure fluctuation within the microbubble's gas core. Given that pressure within microbubbles is directly correlated with bubble size, gas molar ratio and absolute temperature, any pressure fluctuations lead to changes in at least one of these factors. Due to the high compressibility of the gas core, microbubbles respond to pressure changes with volumetric oscillations under alternating positive and negative pressures of ultrasound waves. Their oscillatory behaviour depends on their size, ultrasound amplitude and frequency, as well as medium properties such as viscosity and interfacial tension. Under low-pressure amplitudes, microbubbles compress and expand symmetrically with the sound waves, which leads to a nearly sinusoidal bubble oscillation. When the acoustic pressure increases, the expansion magnitude

elevates with the rhythm of the transmitted sound wave, whereas the compression remains limited due to the restricted compressibility of the gas core. Consequently, under relatively higher ultrasound pressures, microbubble oscillation becomes increasingly asymmetric, which can lead to a faster bubble collapse. Microbubble oscillation behaviour under varying acoustic pressures can be categorized as stable cavitation and inertial cavitation. Stable cavitation occurs under low ultrasound pressures, with sustained volumetric oscillation of microbubbles over time. The stable changes in the bubble radius can push and pull endothelial cell membranes, inducing microstreaming by transferring momentum to the surrounding fluid. Microstreaming can apply shear stress on the vascular wall and influence signalling pathways. Stable cavitation has been widely explored for the transient and controlled opening of the BBB and localized therapeutic displacement to facilitate drug delivery to the targeted locations. Conversely, above a certain acoustic pressure, microbubbles undergo inertial cavitation, characterized by the highly non-linear and unstable oscillation of microbubbles, with bubbles experiencing significant expansion over time but limited compression. Therefore, intense oscillation of microbubbles triggers the bubble collapse, which can induce shock waves, high-speed jets of fluid and large-magnitude shear forces[23]. Inertial cavitation has been shown to increase cell membrane permeability and improve therapeutic agent distribution and uptake. However, it carries a higher risk of damaging healthy tissues through irreversible destruction of vascular walls, hemorrhage, oxidative stress and inflammation.

Microbubbles cavitation can be monitored acoustically, as the vibrating microbubbles generate acoustic signals depending on the ultrasound pressure, which can be exploited for tracking microbubbles behaviour during ultrasound treatment[24]. Under stable cavitation, microbubbles can emit higher harmonics, sub-harmonics, and ultra-harmonics of the transmitted frequency, with the latter two being characterized as the hallmarks of stable cavitation. However, inertial cavitation generates broadband noises, which span a wide range of ultrasound frequencies. Passive cavitation detection monitors microbubble behaviour in real time and controls the treatment outcomes. It is important to note that the safety of pre-clinical and clinical studies is regulated by a parameter called mechanical index (MI), which relies on the peak negative pressure and center frequency of the ultrasound wave. Given that the MI level is associated with microbubble behaviour and stability, a range of 0.05 to 0.2 is FDA-approved for imaging applications in the presence of

microbubbles. At the same time, any MI higher than 0.2 could lead to microbubble destruction [25].

Beyond the cavitation dynamics, ultrasound radiation force can also influence microbubble behaviour and treatment efficacy. Radiation force is the acoustic force applied on the microbubbles, leading to their displacement in the direction of sound propagation. This phenomenon could induce varying bioeffects as the primary radiation force could potentially direct microbubbles toward the vascular wall. Furthermore, secondary radiation force can lead to microbubble aggregation, which is influenced by multiple factors, including microbubble concentration, vessel diameter, and acoustic parameters. Notably, ultrasound radiation force has been shown to increase microbubble retention within the vasculature and improve localized drug delivery[26]. Overall, the distinctive characteristics of microbubbles make them a promising tool for therapeutic applications, which will be discussed in more detail in the following sections.

1.10. Low Intensity Focused Ultrasound

In 1994, low-intensity focused ultrasound received U.S. FDA approval for its healing effects on fresh bone fractions[27]. Since then, low-intensity ultrasound has been increasingly utilized with or without microbubbles to exert various therapeutic effects owing to its mechanical effects. The common acoustic parameters for this treatment approach include 0.5-3 MHz frequency with short pulses, 5-50% duty cycle, acoustic intensities of 0.02–1 W/cm^2, and MI below 1.9[19]. The therapeutic effects of low-intensity focused ultrasound predominantly rely on cavitation, microstreaming and mechanical stimulation[27]. One of its major advantages is the ability of low-intensity sound waves to pass through the intact skull and penetrate deep into the brain up to 10 cm beneath the cortex, which will be discussed in more detail in the following sections Thus, this strategy has demonstrated great potential in targeting deep-seated brain tumors with millimetre spatial precision, without significant energy loss and heating the skull. One of the most recent applications of low-intensity ultrasound is sonodynamic therapy (SDT), a targeted and non-invasive approach, which combines therapeutic ultrasound with systemically administered sonosensitizers. In this approach, a systemically administered sonosensitizer such as 5-aminolevulinic acid (5-ALA), a biocompatible and safe agent, selectively accumulates within the tumor tissue. The tumor is then exposed to ultrasound with short pulses, which leads to temperature and pressure elevation due to microbubble cavitation. This procedure induces the production of

reactive oxygen species (ROS) from the tumor cells, which triggers a dual therapeutic effect by localized eradication of tumor mass via direct cytotoxicity and promoting an anti-tumor immune response by stimulating the release of pro-inflammatory cytokines. Additionally, low-intensity focused ultrasound has gained attention in neuromodulation, where precise deposition of ultrasound energy in the targeted brain regions can stimulate neural activity and motor function [28]. Notably, for neuromodulation purposes, typically pulse-average intensities of <190 W/cm^2 are used[29]. Focused ultrasound, beyond its applications as a standalone treatment, can be paired with microbubbles for the BBB opening, which can facilitate drug delivery to the targeted locations. In the following, some of the therapeutic applications of low-intensity focused ultrasound will be discussed in more detail.

1.11. Ultrasound-mediated BBB Opening

As mentioned before, the highly restrictive nature of the BBB poses a significant challenge for brain chemotherapy. To overcome this, various studies have explored BBB opening using different strategies including therapeutic ultrasound. However, ultrasound application for brain diseases has long been challenging primarily due to the strong scattering properties of the human skull. The high intensity of the bone results in a strong reflection and attenuation (>90%) of ultrasound energy. Additionally, the marrow-filled pores of the trabecular bone layer of the skull strongly scatter the ultrasound beam, further necessitating craniectomy to enable the ultrasound beam to propagate into the brain parenchyma. Attempts to develop strategies for employing transcranial ultrasound through the intact skull date back to 1977, when the Fry brothers revealed that ultrasound with frequencies below 1 MHz could cross the skull. Nevertheless, their efforts to establish transcranial ultrasound failed due to the distortion of the sound waves by the human skull and focal point shifting. To address this issue, Hynynen et al in 1998 explored the use of a spherically curved transducer array, with a corrected phase algorithm to minimize the ultrasound beam distortion[30]. The phased array transducer consists of multiple elements, each of which is accurately controlled based on the individual's skull properties to emit ultrasound waves with correct frequencies, tailored to the varying thickness of the skull in different regions. To determine skull's properties, a computed tomography scan of the head will be performed and will be used to fine-tune the driving element frequencies based on the regional skull thickness. For the safe and precise delivery of ultrasound energy, the treatment outcome is closely monitored by employing real-time MR thermometry to monitor the temperature, along with passive cavitation detection to

track microbubble cavitation behaviour and prevent tissue damage[19], [31]. This innovation facilitated the application of ultrasound for brain disorders.

In the initial attempts, both thermal and mechanical effects of ultrasound were exploited for the BBB opening. However, the thermally induced tissue damage shifted the focus toward the cavitation-based mechanisms as a safer strategy. While the mechanical effects of ultrasound provided a more controllable and targeted approach for the BBB opening, it requires high ultrasound energy to generate small bubbles within the tissue to serve as cavitation nuclei. Deposition of high-energy ultrasound within the brain not only damages the brain tissue and causes hemorrhage but also results in the skull heating. To address these issues, a study done by Hynynen and his colleagues in 2001 suggested that the use of intravenously injected microbubbles can significantly reduce the amount of required energy for the BBB opening, as these microbubbles serve as cavitation nuclei. Their findings illustrated the possibility of safe and reversible opening of the BBB using low-frequency ultrasound, which is marked as a turning point in the field of therapeutic ultrasound for brain malignancies. Subsequent studies expanded this approach to deliver a variety of small and large therapeutic molecules to the brain of rodents and non-human primates. Notably, the safety of the BBB opening is directly related to ultrasound parameters such as acoustic pressure, pulse duration, number of pulses and duty cycle. The underlying mechanism of ultrasound-stimulated microbubbles in the BBB opening relies on mechanical forces induced by oscillating microbubbles on the cerebrovascular endothelium[32]. Therefore, microbubble-induced shear forces result in the local disruption of tight junctions between endothelial cells, facilitating paracellular drug transport. Furthermore, ultrasound-induced microstreaming under stable cavitation of microbubbles can transiently enhance the permeability of endothelial cells, without permanent damage to the cerebral vessels. In addition to cavitation-assisted cellular permeability, ultrasound may also enable Caveolae-mediated endocytosis, both of which facilitate transcellular transport of chemotherapeutics across the BBB[31]. To ensure the safe opening of BBB, real-time monitoring systems have been developed to distinguish stable from inertial cavitation by detecting acoustic emissions. When broadband emissions are detected, as it is indicative of inertial cavitation, the system acts as a feedback loop to adjust the acoustic pressure or stop sonication to prevent tissue damage.

1.12. Ultrasound-mediated Drug and Gene Delivery

Conventional chemotherapies for solid tumors often require the administration of a high dose of therapeutic agents; nevertheless, they commonly fail to deliver the chemotherapeutics specifically to the targeted cells, resulting in systemic cytotoxicity. Additionally, the need for repeated chemotherapy in high doses ultimately develops multiple drug resistance. Beyond the adverse effects of systemic chemotherapy, its success is largely influenced by TME pathophysiology. Among these, the abnormal and leaky tumor vasculature, in addition to defective lymphatic drainage leads to high interstitial fluid pressure within the TME, thereby preventing the sufficient uptake of therapeutic agents by the tumor cells[33]. Therefore, these challenges have led to the emergence of various strategies over the years for efficient drug and gene delivery. Among different approaches, therapeutic ultrasound has gained popularity to safely deliver pharmacological agents to the targeted locations or replacing missing or defective genes in abnormal cells. Notably, the underlying mechanism of ultrasound-mediated drug/gene delivery relies on the acoustic intensity. Studies have shown that ultrasound pressure of less than 100 kPa can derive the stable cavitation of administered microbubbles and facilitate drug delivery through endocytosis. In contrast, ultrasound intensities of higher than 100 kPa transiently generate small pores in the plasma membrane, leading to reversible cell permeabilization, a phenomenon known as sonoporation. This process is facilitated by ultrasound-mediated cavitation effects either through the formation of bubbles within the sonicated tissue or activating externally administered microbubbles, the latter providing a safer and more efficient drug delivery approach as it reduces the required ultrasound energy. Importantly, the intravenous nature of microbubbles allows them to closely interact with vascular endothelial cells and facilitate drug extravasation from the bloodstream[23]. In addition to the cavitation effects, oscillating microbubbles in an acoustic field generate small currents of fluid around them, which further aid the entry of the therapeutic agents into the targeted cells. Microbubbles can serve as vehicles for therapeutic agents, either by encapsulating the drugs, when small quantities are sufficient for therapeutic effect, or by being injected simultaneously with the drugs. This facilitates their entry into the cells or their passive transport across the BBB. Although injected microbubbles circulate throughout the vascular network, they will only be activated at the targeted tissue, where the focused ultrasound is applied, which prevents any systemic side effects.

1.13. Ultrasound-mediated Immunotherapy

Recently, immunotherapy strategies such as immune checkpoint inhibitors and monoclonal antibodies have emerged as efficient strategies for the treatment of hematological malignancies. However, their applications for solid tumors, in particular brain cancers, have remained unsuccessful due to the presence of the BBB and TME. In this context, focused ultrasound has emerged as a powerful approach to address the present obstacles for brain cancer immunotherapy. The immune-boosting potential of ultrasound can be exploited by leveraging either its thermal or mechanical effects. As discussed before, sonicating tumor tissue with high-intensity ultrasound can induce hyperthermia, which potentially stimulates the anti-tumor immune response. One immediate effect of hyperthermia is the release of tumor antigens which can activate dendritic cells, followed by recruitment and activation of helper T cells. Furthermore, hyperthermia has been found to balance the CD4/CD8 T cells ratio in the TME, further promoting an anti-tumor environment. At higher ultrasound intensities, the temperature within the sonicated tissue exceeds 60°C, resulting in thermoablation. It has been shown that thermoablation promotes the anti-tumor immunity through a distinct mechanism as compared to hyperthermia[34]. Thermoablation mediates the tumor disruption, leading to a significant release of cellular debris, in addition to damage-associated molecular patterns. Given the release of large amounts of debris during tumor necrosis, thermoablation potentially activates both local and systemic immune responses. Additionally, thermoablation was found to activate the dendritic cells more significantly and result in stronger immunogenicity versus hyperthermia. Despite these differences, both hyperthermia and thermoablation induce the secretion of IL-2, TNF-α and INF-δ, all of which contribute to an anti-tumor immune response.

Another mechanism by which ultrasound stimulates immunogenicity is through its mechanical effects for regulating TME. Ultrasound-induced mechanical effects provide a precise and safe strategy for eliciting an anti-tumor immune response without leading to coagulative thermal damage. Various mechanical effects of ultrasound can be used to promote cancer immunity, with ultrasound-stimulated microbubbles emerging as a promising strategy to boost immunogenicity through cavitation effects. As previously mentioned, stable cavitation of microbubbles under low ultrasound pressures can transiently open the BBB, which can facilitate the delivery of immunotherapeutic agents to the brain parenchyma. Ultrasound-stimulated microbubble destruction (USMD) is another promising strategy, that involves perfusing tumor vasculature with

microbubbles, followed by delivering high-intensity ultrasound. Under this treatment regimen, the violent oscillation of microbubbles results in the destruction of tumor vessels, considered a form of physical anti-vascular therapy. The destruction of tumor vessels produces a significant mass of cellular debris which stimulates the maturation of antigen-presenting cells (APC) and promotes immune response. Additionally, USMD has been shown to upregulate TNF-α, which can promote the release of proinflammatory cytokine and chemokines, and consequently enhance cytotoxic T cell infiltration into the tumor site[34].

1.14. Overall Structure of Proposed Thesis

Given that focused US and microbubble treatment can both locally disrupt the BBB and have the potential to alter the TME, our overall hypothesis is that US and microbubbles can be used to locally enhance immune cell recruitment to tumor sites to improve the efficacy of cellular immunotherapy.

1. To assess the effect of fluid flow dynamics on US-assisted endothelial permeability.

2. To investigate how endothelial preconditioning under varied flow patterns influences microbubble-mediated endothelial cell permeabilization.

3. To examine whether US-stimulated microbubbles modulate CAM expression and endothelial cell cytokine profile

4. To assess the effects of US on CAR-NK cell recruitment and trafficking in vitro.

2. Focused ultrasound assisted delivery of immunomodulating agents in brain cancer: a review

Manuscript published as: Memari et al., *Journal of Controlled Release* (2024) discusses the applications of therapeutic ultrasound in both molecular and cellular immunotherapy as a potential strategy for the treatment of primary and metastatic brain malignancies. It also presents a summary of pre-clinical and clinical studies, with a focus on glioblastoma and breast cancer brain metastasis.

Abstract:

Focused ultrasound (FUS) combined with intravascularly circulating microbubbles can transiently increase the permeability of the blood-brain barrier (BBB) to enable targeted therapeutic delivery to the brain, the clinical testing of which is currently underway in both adult and pediatric patients. Aside from traditional cancer drugs, this technique is being extended to promote the delivery of immunomodulating therapeutics to the brain, including antibodies, immune cells, and cytokines. In this manner, FUS approaches are being explored as a tool to improve and amplify the effectiveness of immunotherapy for both primary and metastatic brain cancer, a particularly challenging solid tumor to treat. Here, we present an overview of the latest groundbreaking research in FUS-assisted delivery of immunomodulating agents to the brain in pre-clinical models of brain cancer and place it within the context of the current immunotherapy approaches. We follow this up with a discussion on new developments and emerging strategies for this rapidly evolving approach.

2.1. Introduction

As per the Canadian Cancer Society, 3200 Canadians were diagnosed with central nervous system (CNS) malignancies, with an estimated 27 new primary brain tumors diagnosed every day in 2022[35]. While 85% of patients with a non-malignant brain tumor diagnosis survive 5 or more years, the median survival of patients with malignant primary or secondary brain tumor is limited to 12-14 months, despite aggressive treatments[36]. Primary and metastatic CNS tumors are quite

distinct entities, but share some common treatment challenges (*e.g.* location in the brain). While primary CNS tumors can originate from a variety of cell types including astrocytes, meningothelial cells, ependymal cells, oligodendrocytes or neuroectoderm[37], the most common primary malignant brain tumor is glioblastoma[1], accounting for 80% in adults[39]. Glioblastoma originates from astrocytes and mostly occurs in the cerebral hemispheres, but it can be found anywhere in the CNS including the cerebellum, brain stem and spinal cord. Although it is highly infiltrative in normal brain tissue, it rarely metastasizes outside the CNS[39]. It is one of the most aggressive and difficult-to-treat brain cancers, with a 5-year survival rate of 5%[40]. In contrast, metastatic tumors within the brain arise from a different primary site and account for one-fourth to one-half of all intracranial tumors[41], affecting 8-10% of all cancer patients[42]. Common primary tumor sites with frequent brain metastases include lung, breast, skin, kidney, and gastrointestinal tract[41]. Lung cancer, which is the leading cause of death in both males and females in North America[43], is the predominant source of brain metastasis (accounting for ~40-50%[42]), with a median survival between 9-15 months[44]. Breast cancer, the second most common malignancy in women globally with almost half of all patients developing metastasis[45], is the second main cause of brain metastases[41] - especially breast cancer with human epidermal growth factor receptor 2 (HER2) amplifications. A recent study has shown that 25% of patients with advanced breast cancer are likely to develop brain metastasis, mostly in the cerebellum, with a median overall survival of 4 to 25 months after this occurs[46].

While the specific treatment protocol for the particular type of cancer within the brain will depend on a variety of factors *(e.g.* pathology, location, size, patient preference, etc.), a commonality is that they all require a multidisciplinary approach. In high-grade gliomas, such as glioblastoma, maximal safe resection is the goal but complete microscopic resection of the tumor is probably never achieved due to the infiltrative and diffuse nature of the tumor. Indeed, even with gross total resection, the vast majority of glioblastomas recur locally, usually within a couple of centimeters from the resection margins[47]. For more than four decades, postoperative radiotherapy has also been part of the standard treatment strategy for these patients[48]. The seminal work by Stupp et al.[36] provided evidence that combining radiotherapy (RT) with concurrent temozolomide (TMZ) chemotherapy after resection significantly increased 2-year survival rates compared to surgery and

[1] Defined here prior to the 2021 update to the WHO classification of tumors[38]

RT (26.5% versus 10.4%). As a result of this work, the current standard of care for high-grade gliomas consists of maximal safe surgical resection, 60 Gy in 30 fractions of radiotherapy plus concomitant daily temozolomide, followed by six cycles of adjuvant TMZ, resulting in a mean survival for these patients of 14.6 months[49]. In contrast, brain metastases, such as those from breast cancer, non-small cell lung cancer, and melanoma, are treated with a number of situation-specific approaches including surgery, stereotactic radiosurgery, whole-brain radiation, and in some cases, chemotherapy; or most often, a combination of these therapies.

Given the rather bleak best-case scenarios, alternative therapies for patients with primary or secondary brain cancers are currently being actively investigated. One such exciting approach is immunotherapy, *i.e.* activating or supplementing the immune system for therapeutic benefit against cancer. Immunotherapy strategies such as the use of monoclonal antibodies, both against neoantigens and as immune checkpoint inhibitors, and adoptive transfer of engineered chimeric antigen receptor (CAR) T or NK cells (*i.e.* a type of cellular immunotherapy) are rapidly expanding approaches with considerable potential to transform cancer therapy. Several checkpoint inhibitors have now been adapted into mainstream use in a number of solid malignancies including breast[50], lung[51], and melanoma[52]. However, the extension of many of these immunotherapy strategies to intracranial tumors has been challenging and the results much less favourable, due in part to the relative impediment of the blood-brain-barrier (BBB) – which restricts systemic agents from reaching the brain parenchyma – and the hostile tumor microenvironment (TME) – which generates an anti-immune, pro-tumor physiological milieu.

Focused ultrasound (FUS) offers a promising solution to this, as it is a non-invasive, radiation-free therapeutic technique that directs acoustic energy deep within the body. In combination with microbubbles, which are typically employed as contrast imaging agents[53], FUS can be made to induce local immunomodulating bioeffects within target tissues; including the modulation of Ca^{2+} signalling[54], influencing pro-inflammatory signalling[55], [56], and eliciting transcriptional changes[57]. However, a more established technique is that of microbubble-mediated MR-guided FUS as a tool to reversibly permeate the BBB, allowing for targeted accumulation of otherwise ineffective therapeutic agents in the brain[58], [59], [60], [61]. Recently, there has been exciting pre-clinical work demonstrating this approach towards the delivery of immunomodulating agents; defined here as cells or proteins that are directly involved in immunotherapies and/or target an

immune pathway. Here, we first provide the salient context for current cancer immunotherapy approaches and challenges, specific to glioblastoma, followed by a brief description of FUS and its mechanisms of action. Next, we review the literature demonstrating FUS-assisted local delivery of immunomodulating agents using pre-clinical models of brain cancer; either glioblastoma or metastatic (*e.g.* breast or lung). Finally, we discuss future perspectives on this active and rapidly evolving field.

2.2. Immunotherapy

Immunotherapy consists of treatments that are designed to specifically revive, initiate or supplement antitumor immune responses. While not a new concept, it has re-emerged at the forefront of cancer therapy due to ongoing advancements in fundamental immunology. Perhaps one of the earliest techniques, monoclonal antibodies (mAbs) have long been employed to selectively bind to malignant cells, primarily directed against tumor-specific surface molecules. Since the FDA approval of rituximab in 1997, which targets CD20 in non-Hodgkin's lymphoma, over 30 anti-cancer mAbs have been approved for cancer treatment[62], typically targeting hematological cancers. Monoclonal antibodies can be deployed in cancer therapy to elicit very targeted responses through several mechanisms including blocking vital cell signalling pathways, but also by directly triggering many immune responses, including complement activation, opsonization, and antibody-dependent cellular toxicity (NK cell activation). More recently, based off pioneering work by Leach et al.[63], a new class of mAb therapy has emerged that relies on an entirely different immunological mechanism. Immune checkpoint therapy, which targets regulatory pathways in T cells to enhance cytotoxic T populations or inhibit tumor-mediated T cell killing, was first FDA approved in 2011 (ipilimumab, which targets CTLA-4)[64].

Another exciting form of immunotherapy is adoptive cell transfer (ACT), which is a rapidly growing area of clinical investigation. This involves harvesting a patient's (or donor's) immune cells (often T cells), growing or modifying them in culture, and reinfusing them back into the patient. The first type of ACT therapy is to isolate tumor-infiltrating lymphocytes (TILs) from the peripheral blood, lymph nodes and solid tumors. The concept here is to allow the expansion of TILs away from the suppressive tumor microenvironment. First performed with adjuvant IL-2 in melanoma patients over four decades ago[65], there are currently several ongoing clinical trials using TILs towards other solid cancer types, including head and neck cancer (NCT03991741),

non-small cell lung cancer (NCT03645928), ovarian cancer (NCT03610490), cervical carcinoma (NCT03108495) and sarcoma (NCT04052334).

As a natural extension of TILs, T-cell receptor (TCR)-engineered T cells (and NK cells) is another approach to ACT, in which gene transfer technology is applied to *ex-vivo* lymphocytes to generate cells with transgenic TCRs or CARs that target molecules expressed on malignant cells– a strategy that has become commercialized. While both these approaches consist of genetic modification of T cells, CAR T cells overcome some of the earlier limitations of engineered TCR T cells, such as the need for major histocompatibility complex (MHC) expression and co-stimulation – the details of which are excellently outlined in a recent review article by June and colleagues[66]. CAR cell therapy has found tremendous success in B cell malignancies, particularly those targeted to CD19. Indeed, CD19 is a cell surface marker on B cells that is highly expressed in B cell malignancies, required for normal B cell development and is not expressed outside of the B cell lineage. Since the first CARs were approved by the FDA in 2017, there are now six approved CAR T cell therapies, the majority of which target CD19[67], and have shown excellent results in patients with follicular lymphoma[68], diffuse large B cell lymphoma[69], mantle-cell lympohoma[70], indolent non-Hodgkin lymphoma[71] and multiple myeloma[72]. Aside from these, there are numerous ongoing clinical trials that are continuing in the field of hematologic malignancies, and more recently, into the arena of solid tumors[73].

2.2.1. The Challenges of Immunotherapy for Glioblastoma

Despite the accumulating successes of immunotherapies in treating extra-cranial cancers, treatment of brain cancers with this approach still remains challenging. Immune checkpoint inhibitors, for example, have shown successful outcomes in a variety of solid tumor contexts[74], [75]. The seven currently FDA-approved agents, either as a monotherapy or in combination, have over 50 indications[76], spanning metastatic melanoma[74], [77], non–small cell lung cancer[78], [79], extensive stage small cell lung cancer[80], [81], bladder cancer[82], renal cell carcinoma[83], hepatocellular carcinoma[84], mesothelioma[85], and colorectal cancer[86]. Despite this tremendous progress, checkpoint inhibition has not yet resulted in improved clinical outcomes in cohorts of glioblastoma patients[87]. Although numerous studies have shown pre-clinical success in glioblastoma rodent models[88], [89], recent controlled phase III trials assessing nivolumab (anti-PD-1) have failed to demonstrate a survival advantage in glioblastoma patients. In the

CheckMate 143 trial[90], the first large randomized clinical trial investigating the inhibition of the PD pathway in glioblastoma, nivolumab failed to prolong overall survival in patients with recurrent glioblastoma as compared to bevacizumab control patients. Subsequently, the Checkmate 498 trial[91] focused on patients with newly diagnosed glioblastoma with an unmethylated MGMT promoter. This was in part motivated by the fact that TMZ treatment is less effective in unmethylated MGMT glioblastoma patients; silencing of the MGMT gene by promoter methylation decreases MGMT expression which compromises DNA repair and confers chemosensitivity to drugs like TMZ[92]. The primary endpoint of improved overall survival using a combination of nivolumab and RT was not met; indeed, the median overall survival in this group was 13.4 months compared to 14.9 months with TMZ and RT. In the CheckMate 548[93] trial, newly diagnosed glioblastoma patients receiving nivolumab + RT + TMZ compared with RT + TMZ demonstrated comparable median overall survival rates of 28.9 months versus 32.1 months, respectively. Despite these negative large-scale trials, there have been numerous case reports suggesting specific patient subgroups may have prolonged survival under immune checkpoint inhibitor therapy[94], [95], [96], [97], and this is an active and enthusiastic area of ongoing research[87].

In addition to checkpoint inhibitor therapies, there are several ongoing clinical trials using CAR T cell and CAR NK cell therapy for the treatment of glioblastoma, targeted towards one of three antigens: EGFRvIII, human epidermal growth factor receptor 2 (HER2) and IL-13 receptor α2 (IL-13Rα2)[98], [99], [100], [101]. While demonstrating exciting preliminary results, including feasibility and safety, significant hurdles remain that are specific to glioblastoma, including heterogenous expression of target antigens in tumor cells and a compensatory immunosuppressive response[102]. In fact, the efficacy of immunotherapy in general for the treatment of malignant tumors situated in the brain is limited due to two major challenges, including the requirement to cross the BBB and the requirement to overcome the immunosuppressive nature of the TME. These two major hurdles will be briefly discussed in the next sub-sections – but for a more comprehensive review on the cell biology and immunology of either of these subjects, the reader is referred to recent review articles on these matters[103], [104].

2.2.1.1. Blood-Brain Barrier

The BBB is a complex structure that regulates molecular transport into the brain. It is composed of a monolayer of endothelial cells lining the cerebrovascular walls, supported by vascular pericytes and astrocytes[105]. Endothelial cells lining the BBB are tightly connected to one another through transmembrane protein complexes called tight junctions, consisting of junctional adhesion molecule-1, claudin and occludin, as well as adherens junctions and gap junctions. The BBB restricts the paracellular transports of macromolecules mainly through junctional complexes, with the exception of lipophilic molecules which move across the BBB paracellularly by dissolving in the endothelial cell plasma membranes. Furthermore, small water-soluble molecules can diffuse into the brain transcellularly by diffusing through tight junctions, whereas endothelial cells restrict the trans-cytoplasmic transport of other molecules by means of low pinocytotic activity and the expression of efflux transporters including p-glycoproteins and multi-drug resistance related proteins[106]. However, most macromolecules and vital substances require transcytosis, carrier-dependent, or receptor-mediated transport mechanisms to be able to pass through BBB. Essential nutrients such as glucose and amino acids bind the transport proteins, leading to the conformational changes that facilitate the transportation through the membrane, with or without ATP, based on the concentration gradient [107]. Conversely, the selective uptake of macromolecules such as growth factors, enzymes, and plasma proteins occurs through receptor-mediated transcytosis. Additionally, positively charged substances such as cationic proteins and cell-penetrating peptides interact with the negatively charged plasma membranes, which facilitates their passage across the BBB through the adsorptive-mediated transcytosis[108]. Distinctive biological features of BBB prevent the passage of most therapeutic agents, except drugs that meet specific criteria including a molecular weight of less than 400 Da, and low hydrogen binding which results in high lipid solubility [107], [108]. In progressing glioma, BBB integrity is heterogeneously disrupted, forming what is known as the blood-tumor barrier (BTB)[109]. The intricate structure of the BTB is mediated by various factors, among which the overexpression of vascular endothelial growth factor (VEGF) plays a crucial role[110]. The increased level of VEGF results in the breakdown of intercellular junctions between brain endothelial cells (BEC)[111]. Additionally, the glioma microenvironment introduces proinflammatory cytokines which mediate the downregulation of tight junction proteins in cerebral capillaries, ultimately disrupting the integrity of cerebrovascular endothelium[112]. Another significant element is increased

mitochondrial oxidative stress resulting from mitochondrial dysfunction in the BEC. The excessive production of reactive nitrogen (RNS) and oxygen species (ROS) within the glioma TME disturbs the vascular tone by impacting the level and localization of tight junction proteins[113], [114]. Oxidative stress also indirectly activates matrix metalloproteinases (MMPs) which increase endothelium permeability through the degradation of basement membrane proteins and disturbance of tight junction assembly[113]. Despite the higher permeability of BTB, the passage of therapeutic agents across this barrier is challenging due to various factors, one of which is the heterogeneous disruption of glioma BTB[109]. Notably, the necrotic core of glioma experiences poor blood flow and inconsistent oxygen supply, leading to hypoxia. This, in turn, induces the release of VEGF, resulting in enhanced permeability of the central tumor vasculature[115]. In contrast, the peripheral regions of glioma tumor, which experience less hypoxia, largely maintain the integrity of cerebral microvasculature[116]. Adding to the complexity, glioma cells originating from the tumor periphery invade the cerebral parenchyma, where a tightly regulated BBB exists. Furthermore, the peripheral tumor microvasculature exhibits an upregulation of efflux transporters, predominantly p-glycoproteins, further restricting the delivery of chemotherapeutics to the cancer cells, and contributing to GBM chemoresistance[117].

2.2.1.2. Tumor Microenvironment

Aggressive tumors, including GBM, modify their microenvironment to favor the development of tumorigenic properties, including cell migration and invasion. Within GBM, the intricate TME is composed of cellular (*e.g.* glioblastoma stem-like cells, endothelial cells, microglia, tumor infiltrating lymphocytes and macrophages) and non-cellular (*e.g.* extracellular matrix, hypoxia (< 10 mmHg), acidity (pH 6.5-6.8)) features. GBM stem-like cells, which demonstrate self-renewal and differentiation[118], [119], are thought to drive pharmacological, surgical and radiological resistance[120], [121]. Tumor-associated macrophages (*e.g.* resident microglia, infiltrating macrophages), which make up a large portion of the glioma microenvironment[122] – become polarized towards a pro-tumorigenic phenotype (*e.g.* via glioma-releasing colony-stimulating-factor CSF1) and can thus release growth factors (*e.g.* epidermal growth factor) to promote tumor progression[123]. Indeed, these macrophages can also produce anti-inflammatory cytokines (IL-4, IL-10, TGF-β), tumor-promoting factors (*e.g*. PDGF), activate immune checkpoints (*e.g*. expressing PD-L1), and promote angiogenesis (VEGF, IL-8)[124]. The TME is also characterized in part by cytokine dysfunction, where tumor cells can secrete immunosuppressive cytokines (*e.g.*

TGF-β, IL-10) to drive a Th2 response and recruit regulatory T cells (T_{regs}) that further amplify the suppressive response[125], [126]. Further, GBMs are poorly infiltrated by T and NK cells, and thus only constitute a small fraction of within tumor immune cells[127]. Even when present within the GBM TME, CD8+ and CD4+ T cells are typically dysfunctional as a result of anergy and/or exhaustion[128]. Regulatory T cells present within GBM suppress the function of antigen-presenting cells (APCs), and inhibit the proliferation and effector function capabilities of T cells. Moreover, GBM are highly vascularized tumors and thus endothelial cells are an active component of GBM development. In addition to cells within the hypoxic environment (typically at the peripheral of the necrotic core) secreting pro-angiogenic markers (*e.g*. VEGF), studies have shown transdifferentiation of glioblastoma stem-like cells into endothelial cells[129], in addition to vascular mimicry[130] (*i.e.* glioblastoma cells that stimulate an endothelial phenotype), both of which promote angiogenesis and invasiveness.

In addition to these, another escape mechanism of GBM tumor cells is the formation of a physical barrier via the modulation of the extracellular matrix (ECM) (*e.g.* collagen, laminin). Infiltrative tumor cells are capable of degrading and remodeling this extracellular space via MMP release[131]. GBM tissue highly expresses MMP-2 and MMP-9, the concentration of which has been linked to poor GBM patient prognosis[132], and GBM cells have been shown to modify other components of the ECM as well[133], [134]. This ECM however does present a physical barrier for T cell infiltration and, along with the modulation of the endothelial expression of important adhesion molecules and integrins, immune cell recruitment within the GBM TME is severely hindered[135].

2.3. Focused Ultrasound for Brain Therapy

Traditionally a diagnostic tool, medical ultrasound can be modified to elicit a high-intensity beam within a small focal volume, while ensuring minimal energy deposition elsewhere – *i.e.* focused ultrasound. Transcranial FUS therapy is made possible by the implementation of phased or geometrically FUS arrays and the use of MRI guidance. With high-intensity focused ultrasound, ultrasound absorption within the focal volume results in a local temperature elevation[136] which can be monitored using MR thermometry[137]. Extreme temperature elevation can cause tissue necrosis, the principle behind thermoablation approaches, and is currently FDA-approved for thalamotomy for essential tremor (ET) and tremor-dominant PD (TDPD)[138]. Indeed, FUS has

been shown to be able to selectively target different regions in the brain with submillimetre accuracy – both surface and more deeply located regions[59]. Aside from these clinical applications, ongoing clinical trials are examining the effectiveness of US-assisted thermoablation in patients with obsessive-compulsive disorder[139], major depression[140], and chronic pain[141]. Further, pre-clinical work has only begun to examine how the thermal effects of local transcranial ultrasound deposition can be used as a tool to locally modulate the immune environment, which highlights ultrasound-assisted release of damage-associated molecular patterns and alteration of local gene expression patterns[142].

Aside from thermoablation, the other main application of transcranial therapeutic ultrasound, and the subject of this review article, is in conjunction with clinically approved ultrasound contrast agent microbubbles for the localized and reversable opening of the BBB[58], [59], [105], [143] – see Figure 1. Microbubble agents are gas-filled bubbles that are encapsulated with a thin biocompatible shell, ranging in size from about 1-5 μm in diameter. As they are highly compressible, they vibrate within the oscillating pressure of an ultrasound field, expanding and contracting around their equilibrium radius, and re-radiate ultrasound energy to provide a significant imaging signal boost to the vasculature to which they are confined[144]. Microbubble vibrational physics can be broadly categorized into two regimes[145]. Under low to moderate acoustic pressure, microbubble vibration exhibits a relatively low amplitude of deformation, resulting in the generation of consistent harmonic content – termed stable cavitation (*e.g.* [146]). Under more forceful driving conditions, bubbles can grow in size rapidly and subsequently collapse due to the inertia of the surrounding fluid – termed inertial cavitation (*e.g.* [147]). Ultrasound contrast imaging utilizes both of these characteristics depending on the application, and microbubbles are currently clinically used with indications in cardiovascular applications and radiology[53]. Under specific ultrasound settings, these bubble oscillations can elicit bioeffects on the neighbouring microvascular walls that may result in endothelial perturbation[148], enhanced intracellular and vascular permeability[54], [149], [150], and the disassembly of tight junctions[151]. Numerous investigations have contributed towards a mechanistic understanding of these bioeffects of both mechanical and biochemical origin. Both stable and inertial cavitation have been shown to exert large-magnitude shear stress on neighbouring tissue, inducing direct membrane permeabilization[150], [152], [153], [154]. Indeed, the formation of high-speed liquid jets within the inertial cavitation regime[147], [155], [156] – a result of bubble involution – has

been shown to disrupt membrane integrity and make play a role in microbubble-induced bioeffects. Others have shown microbubble-induced biochemical effects, including the generation of reactive oxygen species[157], induction of intracellular calcium signalling[54], [158], [159], [160], and local ATP release[161], [162]. While ultrasound-mediated BBB opening has been demonstrated without co-injection of microbubbles, the related bioeffects were unpredictable and varied[105]. Indeed, one of the advantages of using these exogenously administered microbubbles is that they act as amplifiers and concentrate acoustic energy to the neighbouring vasculature, minimizing the level of input acoustic energy that would otherwise be necessary and spatially localizing the reversible opening. This exciting approach has been shown pre-clinically to feasibly deliver a wide array of therapeutic payloads to the brain, see Table 1. With over two decades of promising pre-clinical studies, clinical trials employing transcranial ultrasound-assisted BBB opening are currently underway, examining the safety of this technique in the context of glioblastoma[163], Alzheimer's disease[164], and amyotrophic lateral sclerosis (ALS)[165].

Since the first demonstration of MR-guided FUS as a tool for the reversible opening of the BBB[60], there have been numerous investigations into the degree and extent of BBB opening, including the effects of several factors including frequency, pressure amplitude[166], duration, pulse length[167], and microbubble characteristics[168]. While MRI is the established method for evaluating BBB opening post-treatment, there are several advances in monitoring microbubble cavitation signals to provide real-time feedback[169]. Further, recent advances in engineering have brought forth new and emerging transducer systems designed to generate FUS in conjunction with contrast agent microbubbles for BBB opening, an overview of which has recently been presented[170]. Here, we focus on reviewing the investigations into the FUS assisted delivery of immunomodulating agents, either mAbs, immune cells, or immune-related cytokines for the purpose of advancing brain cancer immunotherapy, a summary of which is presented in Table 2.

2.4. Focused ultrasound-assisted delivery of immunomodulating agents to glioblastoma and metastatic brain tumors

2.4.1. Antibodies

While immunotherapeutic agents including monoclonal antibodies have a great potential for a wide variety of malignancies, insufficient therapeutic delivery across BBB/BTB remains a challenging obstacle. Therefore, frequent dosing is required, which has a high risk of

immunogenicity and other side effects. Kinoshita et al.[171], [172] were the first to demonstrate that FUS in combination with clinical microbubble contrast agent can be used to locally deliver antibodies to the brain in a murine model. In a more recent study conducted on the glioma mouse model, the combination of low-intensity pulsed ultrasound (LIPU)-mediated BBB disruption (BBBD) with anti-PD-1 checkpoint inhibitor on the antibody delivery to the tumor was investigated[173]. The results revealed an increase in the delivery of anti-PD-1 antibodies and an improvement in the recruitment of peripheral APCs due to the release of tumor antigens[173]. In addition, Arvanitis et al.[174] examined the FUS-mediated delivery of T-DM1, an antibody–drug conjugate, into the brain microenvironment of an orthotopic xenograft model of HER2-positive BCBM. The study demonstrated that FUS treatment, immediately following T-DM1 administration, improves the delivery of this agent to the tumor cells by increasing interstitial convective transport and vascular barrier disruption. They showed that FUS-mediated BBB/BTB disruption promotes hydraulic conductivity, followed by fast fluid flow into the interstitial space, which leads to an enhanced T-DM1 delivery to the tumor site[174]. The relationship between tumor interstitial fluid pressure (TIFP), hydraulic conductivity and blood vessel permeability is well established. As such, the increased vascular permeability caused by FUS is likely the reason for an increase in the interstitial hydraulic conductivity of therapeutic agents in the brain[175]. Separate investigations conducted on a rat model of HER2-positive MDA-MB-361 examined the synergistic effect of trastuzumab and pertuzumab, two HER-2 targeting antibodies, with FUS-mediated BBBD on antibody delivery into the brain[176]. They observed that the group receiving antibody-only treatment for six weeks showed no inhibition of tumor growth. However, out of ten treated animals, four that received a combination of six weekly antibody and FUS-mediated BBBD treatments exhibited a substantial reduction in the tumor growth. The positive outcomes observed in the group of responders were mainly due to FUS-induced BBB opening. This was evidenced by the lack of impact on tumor growth in the antibody-only treatment group. However, the synergistic effect of the treatment was limited to six weeks, after which the responders' tumor growth rate returned to that of the non-treated groups. Regardless, the temporary slowing down of the tumor growth led to an increase in the median survival of animals treated with a combination of FUS and antibody as compared to the non-treated animals. These studies highlight the ability of FUS, when used in combination with intravenously injected microbubbles, in the safe and local delivery of a variety of high molecular weight antibodies to brain tumors by the transient opening of BBB/BTB.

2.4.2. Cells

Despite the potential of T cells for immunotherapy, their anti-tumor immunity is limited due to the specific characteristics of the TME such as hypoxia, rigid stroma and high interstitial fluid pressure. Tumor-associated fibroblasts promote tumor progression by creating a dense network of extracellular fibres around the tumor, preventing immune cells infiltration into the TME. The hypoxic TME stimulates the production of immunosuppressive molecules that restricts the anti-tumor function of immune cells including T cells, and has been correlated with downstream induction of immunosuppressive regulatory T cells; T_{reg}[177], [178]. Indeed, through production of immunosuppressive cytokines (*e.g.* TGF-β, IL-10) thymic-differentiated and induced T_{regs}, tumor-associated macrophages, and cancer cells can contribute to T cell exhaustion or dysfunction – including causing impaired production of anti-tumor effector cytokines like IL-2, IFN-δ, or TNF-α. In a seminal study by Alkins et al.[179], it was demonstrated for the first time that systemic injection of HER2-targeted NK-92 cells, which do not normally traffic in the CNS, followed by BBB disruption using MRI-guided FUS led to a marked increase in the ratio of HER2-specific NK cell: MDA-MB-231-HER2 cells in brain tumor-bearing rodents as compared to passive administration of immune cells (see Figure 2). Likewise, this study confirmed the accumulation of a sufficient density of NK cells in the tumor mass delivered with FUS, with preserved cytolytic function, required for effective tumor cell lysis. Their follow-up paper demonstrated a 50% long-term survival with MRI-guided FUS delivery of CAR NK-92 cells compared to NK cells administered without FUS. Sabbagh et al.[173] investigated the synergistic effect of LIPU-induced BBB disruption with the administration of genetically modified immune cells, either ffLuc-labeled EGFRvIII-CAR T cells or CXCL10-secreting antigen-presenting cells (APC), to EGFRvIII-U87 and GL261-bearing glioma mouse models, respectively. This study found that LIPU monotherapy had not influenced the expression profile of immune-related genes in the glioma microenvironment of GL261 mice, neither had it prolonged their survival. This finding shows that while FUS-mediated BBBD has the potential to trigger the release of tumor antigens and activate the peripheral APCs, FUS bioeffects alone is not strong enough to elicit an anti-tumor immune response. Alternatively, the trafficking of systemically administered ffLuc-labeled EGFRvIII-CAR T cells without FUS sonication to the glioma microenvironment was investigated using bioluminescence imaging. Interestingly, most of the administered CAR-T cells ended up in the lung and liver, with a distribution of only a few cells in the brain. However, combining LIPU with

CAR-T cells demonstrated a slight increase in the CAR-T cell trafficking into the brain 4 to 8 hours post-sonication. Subsequently, there was considerable CAR T-cell infiltration in the brain tumor at 24- and 72-hours post-treatment, potentially due to an increase in antigen availability or the recognition of tumor antigens. CAR-T cell delivery through LIPU also increased the median survival by more than 129% as compared to systemic administration of CAR-T cells. In addition, LIPU-induced BBBD facilitated the localized accumulation of CXCL10-secreting APCs in the TME. This increase in the number of APCs within the glioma microenvironment, which secreted chemokines that attracted T cells, transiently enhanced T cell infiltration at the tumor site. Consequently, this resulted in a significant improvement in the overall survival of GL261 glioma-bearing mice[173].

2.4.3. Immunomodulating molecules

Despite the potential of immune-triggering molecules, including interferons and interleukins, in the activation of local immune response, their systemic administration can cause severe cytotoxicity and autoimmune responses[180]. In addition, delivery of peripherally administered cytokines to the tumor tissue is more challenging in brain cancers due to the presence of BBB/BTB, which can be circumvented by intratumoral injection; however, the relative invasiveness of this approach restricts its applicability. In this regard, ultrasound-mediated BBB opening presents a potential solution to optimize the local delivery of immunotherapeutic molecules into brain tumors[181]. Furthermore, FUS-induced BBB opening can activate an anti-tumor immune response and increase the recruitment of immune effector cells to the tumor site[180]. Chen et al.[181] reported that systemic administration of IL-12, which has anti-angiogenic and anti-glioma properties, increased the total population of tumor-infiltrating lymphocytes, however did not impact tumor progression and animal survival. However, the combination of IL-12 administration and FUS-induced BBB opening led to a significant reduction in the tumor volume as compared to the non-treated group, followed by an improvement in the animal survival rate[181].

2.4.4. Clinical Trials

The supporting pre-clinical evidence outlined above has begun to translate into clinical trials, specifically for the use of co-injected mAbs, and is summarized in Table 3. The clinical trial in France (NCT04021420) employs the SonoCloud-9^{TM} (Carthera, Paris, France), which is implanted within the skull at the time of surgery and consists of a nine-element ultrasound array that is

powered via a transcutaneous power supply. In this trial, BBB disruption in combination with nivolumab injection (240mg over 30 minutes) is being examined in patients with brain metastases from melanoma. The other ongoing trials use transcranial FUS devices, and one such trial (NCT04446416 which incorporates the NaviFUS system from NaviFUS, Corp. Taipei, Taiwan) is being used in conjunction with bevacizumab in patients with recurrent glioblastoma. The remaining clinical trials employ the Exablate system (Insightec, Haifa, Israel), which consists of 1024 individually driven elements with independent phase and amplitude control, encased within a 30-cm diameter hemispherical dome. These trials are examining the opening of the BBB with this device in conjunction with mAb immunotherapy for patients with recurrent glioblastoma (NCT05879120), and brain metastases (NCT03714243, NCT05317858). For a more detailed review of the clinical FUS devices used for targeted BBB opening, the reader is referred to a recent review article on this subject matter[170].

2.5. Future Outlook and Conclusions

For over two decades, transcranial FUS in conjunction with intravascular microbubble contrast agents has been shown an effective tool for targeted and reversible BBB opening and localized deposition of otherwise impermeable macromolecules; clinical trials of which are ongoing in both adult and pediatric patients. Continual improvements in cancer immunology, FUS systems and image-guidance strategies, as well as acoustically-sensitive agents are driving this technology towards GBM immunotherapy applications.

2.5.1. Consensus on Ultrasound and Microbubble Parameters

Broadly speaking, the sonication parameters employed for delivery of immunomodulating agents via BBB opening (Table 2) are consistent with its other applications (Table 1). The FUS conditions examined here range in frequency (0.22-1.64 MHz), peak negative pressure (< 1 MPa), burst length (mostly 10 ms; 6.67-100 ms reported), pulse repetition frequency (1-5 Hz), duration (40 s to 5 min.), microbubble composition (19 studies reported clinical, commercial agents; 2 reported in-house agents) and microbubble administration route (bolus injections). While these parameters have been shown effective, optimal conditions will depend on a range of factors. While most of the studies examined here utilize clinical agents, microbubble composition and size distribution can vary significantly between commercial agents[182], [183], as well as activation strategies of a given agent[184], [185]. This is a key factor as the vibrational dynamics of microbubbles under an

acoustic field are strongly influenced by bubble size and composition[20], [144], all other acoustic parameters equal. Agents which possess a broader size distribution can be expected to elicit a wider range of bioeffects, as bubble vibration physics plays a role in the magnitude of stress applied to neighboring vasculature. To this end, there have been pre-clinical studies that have explored the effect of bubble size on FUS-mediated BBB opening, generally concluding that larger microbubbles elicit BBB opening at lower acoustic pressures[186], [187], [188], from which the suggestion of microbubble gas volume as a unifying factor between agents as been put forth[189]. Moreover, as the frequency employed in BBB disruption for GBM is typically over a relatively narrow and low range due to the intervening skull[190], there is some leeway in applied frequency as a result of the FUS instrument employed, generally ranging from 0.22-1 MHz for clinical GBM trials[170]. Given the strong influence of frequency and transmit pressure on bubble response, the mechanical index (MI), defined as the peak negative pressure in MPa divided by the square root of the frequency in MHz[191], has been suggested as another unifying factor for BBB opening[192], in this case collapsing the frequency and transmit pressure dimensions. In addition, the optimal acoustic parameters will also depend on the molecular size of the desired immunotherapeutic. Indeed, several studies have demonstrated that the size of BBB opening – as measured with fluorescently labeled dextran - increases with increasing acoustic pressure; or equivalently that the concentration of macromolecule delivery to the brain parenchyma is higher for smaller sized agents at a given pressure[193], [194], [195]. However, this rather simple trend is not necessarily observed with immunologically active agents *(e.g.* antibody isotypes[196], [197]), which highlights the interplay between the physics and biology of BBB opening-mediated delivery of immune agents. Indeed, the downstream biological response of and the resulting immunomodulation of BBB opening[55], [56], [198], [199], [200], [201] in the context of GBM will be an important avenue to thoroughly investigate in order to holistically assess consensus FUS parameters.

2.5.2. Acoustic Monitoring of BBB opening

MRI is currently the modality used to monitor or assess the outcome of FUS procedures – gadolinium-based T1-weighted sequences to confirm BBB permeability and both T2- and T2*-weighted sequences to assess US-induced edema or hemorrhage, respectively. There is however increasing interest in using the scattering properties of the microbubbles themselves as an indicator of treatment outcome. This is primarily due to the real-time nature of their emissions, as well as

the fact that it would obviate the need for repeated gadolinium injections for longitudinal studies, which may come with increased risk to patients[202]. Microbubble-based monitoring relies on the premise that the bubble spectral characteristics are indicative of the underlying bubble vibrational physics, and thus remote detection of these oscillations can be exploited as a tool for therapy guidance. In one such approach, bubble emissions are recorded passively during US treatment, and numerous recent studies have reported correlations with bubble echo characteristics and the extent of BBB opening/closing timescales and the presence of unwanted damage[203], [204], [205]. Based on these initial studies, cavitation control algorithms have been developed and employed as a real-time feedback tool to mitigate unwanted damage and ensure reliable and repeated therapeutic delivery to the brain, typically involving the monitoring of wideband and subharmonic bubble emissions[168], [206], [207], [208], [209]. Indeed, harmonic microbubble emissions have been shown to correlate with controlled BBB opening, as quantified by gadolinium-enhanced MRI signal[206], [210] and chemotherapeutic delivery[208]. In the context of the delivery of immunomodulating agents, very recent and robust work conducted by Lee and colleagues[211] employs a cavitation-based feedback mechanism reliant on the third harmonic emissions from clinical Definity^{TM} microbubbles (*i.e.* a component of its stable cavitation). In their study, they show a direct correlation between the amount of anti-PDL1 antibody delivered to the brain in a rodent GBM model and the third harmonic bubble emission dose. Additionally, the cavitation-control/feedback technique was well correlated with cellular immunomodulation within the TME, including high correlation with ICAM-1 and activated microglia (via IBA-1 staining). As an extension to this, the use of multi-element passive US arrays enables both temporal and spatial information regarding transcranial bubble activity[212], [213], which allows conformation of the intended localization of the therapy and detection of any off-target bubble activity[214] and is a rapidly evolving technology[169].

2.5.3. Targeting the GBM vascular compartment

Table 2 demonstrates that the majority of FUS-mediated delivery of immunological agents target the immune checkpoint inhibitor axis. In addition to the immune cell components of the GBM TME, endothelial cells play an active role in GBM progression vis-a-vis its role in angiogenesis and vessel co-option. Indeed, there have been several clinical trials taking aim at angiogenesis in GBM patients via the administration of anti-angiogenic agents, most of which target the VEGF pathway[215], [216], [217]. While promising, anti-angiogenic therapy in GBM patients thus far

has failed to show a survival benefit in randomized clinical trials[218]. To this end, alternative mechanisms of vessel recruitment within GBM have been examined, including pre-clinical investigations into the key molecular actors involved in communication between glioma and endothelial cells. Angiopoietin-1 and -2 have been shown to regulate the crosstalk between these two cell types[219], and endothelial release of bradykinin has been reported as a key chemoattractant for glioma cells[220]. These studies and others that examine endothelial expression profiles and secretomes (*e.g.* IL8[221]) as well as alternative pro-angiogenic pathways driven by hypoxia (*e.g.* HGF, FGF)[222] within a GBM context suggest the expansion of immunological payload delivery with FUS and microbubbles. As an aside, microbubble-based approaches to both detect[223] and modulate angiogenesis[224] have a rich history, including applications in oncology and cardiovascular disease. As microbubbles are intravascular agents, targeted approaches towards the modulation of endothelial cell biology have also begun to be explored[225], independently of GBM. In the same vein, while FUS-mediated delivery of immunological agents has thus far very promising results (Table 2), extending the therapeutic paradigm to targeting other angles of GBM including tumor-derived endothelial cells will further contribute to the success of this new technique.

2.5.4. Focused ultrasound assisted immunotherapy: Alzheimer's Disease (AD)

It is important to note here that FUS-assisted delivery of immunomodulating agents to the brain is not limited to cancer applications. The prevalence of Alzheimer's disease (AD), which is the most common form of dementia, is projected to double every 20 years, affecting nearly 130 million people by 2050. AD is characterized by extracellular Aβ deposits and intraneuronal Tau protein aggregates, and most currently approved therapeutics do not target the underlying pathology. With the recent regulatory approval of aducanumab in 2021, which targets the Aβ pathways, immunotherapy development targeting both Aβ and Tau for AD is on the rise[226]. However, despite promising pre-clinical work, it has been met with limited success in large patient cohort studies[227] – and one of the main challenges is mAb penetration through the BBB.

To this end, there have been exciting pre-clinical developments in using FUS-assisted opening of the BBB to treat AD. In fact, simply opening the BBB without any extrinsic therapy has been shown to ameliorate AD pathology and improve cognitive function in mice models[228], [229]. Further, in conjunction with mAb immunotherapies, this approach has shown the clearance of

pathological proteins in the brain[230], [231], [232]. Based on this ongoing preclinical evidence, there are numerous clinical trials assessing the safety of this approach in AD patients (*e.g.* NCT04118764, NCT03739905, NCT03671889, NCT02986932). For a more detailed overview of this field, the reader is referred to recent reviews on the subject[233].

2.5.5. US-controllable immunotherapy using genetically engineered bacteria

While mostly demonstrated pre-clinically in extracranial tumors, bacterial-based targeted cancer therapy is garnering renewed interest. Upon systemic administration, various types of non-pathogenic bacteria have been shown to infiltrate and selectively replicate within solid tumors with an accumulation over 10000-fold greater than within healthy tissue[234], in part due to the fact that the tumor microenvironment creates a favorable niche for these selected bacteria to grow. Given this intrinsic tumor targeting mechanism and due to the relative ease with which bacterial genetics can be manipulated, several types of bacteria can be engineered to function as effective cellular therapies for solid tumors – including those encoded to locally deliver small molecules, pro-drug-converting enzymes, immunomodulators, and siRNA[235]. Incorporation of specific promoter sequences upstream of therapeutic genes of interest has enabled the control of transcription via external stimulus. With temperature sensitive transcriptional regulators, FUS can be used to selectively activate bacterial gene expression[236], as it is well known that under specific acoustic regimes, US can be used to cause local heating. Unlike the studies that have been reviewed above, this strategy does not incorporate contrast agent microbubbles and in fact relies on thermal, as opposed to mechanical, mechanisms of action. Recent work by Abedi and colleagues[237] demonstrated genetic modification of *E. coli Nissle 1917* in such a manner to incorporate FUS activatable secretion of CTLA-4 and PD-L1 nanobodies (*i.e.* via a temperature sensitive repressor). After systemic injection of these genetically-engineered bacteria, it was demonstrated that the FUS activation results in signficant tumor suppression in a B cell lymphoma murine cancer model. Further, using similar approaches, Chen and colleagues[238] engineered an US responsive bacteria that can induce the expression of IFN-γ, and confirmed controllable increases in levels of anti-tumor activity within a breast cancer murine model.

2.5.6. Concluding Remarks

Focused ultrasound brain therapy offers a disruptive alternative or complement to surgery and targeted drug therapies, with increasing clinical indications every year. Leveraging the initial

successes of cancer immunotherapy, robust pre-clinical work has explored the delivery of immunomodulating agents to the brain using microbubble-mediated BBB disruption; which has begun to translate into clinical trials worldwide (Table 3). Indeed, in addition to the emerging and exciting localized immune modulating effects of FUS and microbubbles alone, this technique can serve as a powerful adjunct when paired with other immunomodulating agents that cannot readily accumulate in the brain – including mAbs, immune cells and cytokines. At the current pace, FUS will greatly contribute to the success of cancer immunotherapy towards otherwise difficult-to-treat brain cancers like glioblastoma.

Table 2.1:Examples of agents that have been delivered to the brain parenchyma via focused ultrasound blood-brain-barrier disruption.

Agent Category	Examples	Size Range
Chemotherapeutics	Doxorubicin[239]	< 1kDa
Liposomal chemotherapeutics	Liposomal Doxorubicin[240]	75-125 nm
Nanoparticle conjugated chemotherapeutics	Cisplatin-conjugated gold nanoparticles[241]	5-300 nm
Antibodies	Herceptin[172], Amyloid-β antibodies[228]	~50-150 kDa
Antibody drug conjugates	Ado-trastuzumab- emtansine (KADCYLA)[174]	~50-150 kDa
Naked plasmids	Firefly luciferase gene (reporter gene)[242]	~kDa range
Viral vectors	AAV9 encoding GFP[243]	~20-100 nm
Cells	Neuronal stem cells[244], Natural killer (NK) cells[179]	~5-20 μm

Table 2.2: Summary of the investigations using focused ultrasound to deliver immunomodulating agents to the brain.

Authors	Model/ Tumor Type	Therapeutic agent / Administration	Ultrasound	Summary

Antibody				
Kinoshita et al. 2006[171]	Healthy mice	Anti-Dopamine D4 receptor / IV	0.69 MHz, 10ms bursts, 1 Hz PRF, 40s duration, 0.6-1.1 MPa. Optison™ (10 or 50 µl bolus).	BBBD (confirmed with contrast MRI and trypan blue post-mortem) led to increased levels of antibody, confirmed using IHC 3 hrs post sonication. Sonication under 0.8 MPa yielded no or minimal histological damage.
Kinoshita et al. 2006b[245]	Healthy mice	Herceptin (Trastuzumab) / IV	0.69 MHz, 10ms bursts, 1 Hz PRF, 40s duration, either 0.6 or 0.8 MPa. Optison™ (50 µl bolus).	MRIgFUS for BBBD at 0.6 and 0.8 MPa led to an increase in Herceptin level in the targeted regions by 1,504 and 3,257 ng/g of tissue, respectively. At higher acoustic pressure, minimal histological changes were observed including red blood cell extravasation and apoptotic cells, which were not considered serious.
Park et al. 2012[246]	Nude rats / HER2/neu-positive human breast cancer model (BT474)	Trastuzumab / IV	0.69 MHz, 10ms bursts, 1 Hz PRF, 60s duration, 0.69 MPa. Definity™ (10 µl/kg bolus).	The experiment involved administering six weekly sessions of MRIgFUS in conjunction with trastuzumab. Seven weeks post-treatment, animals treated with MRIgFUS demonstrated a significant reduction in tumor growth compared to those treated with either FUS or trastuzumab alone, as well as the control group. Moreover, the combination therapy extended the survival rate of the animals by a minimum of 32% when compared to the control.
Kobus et al. 2016[176]	xenograft HER2-amplified brain metastasis nude rats / 1) MDA-MB-361-H2B-GFP model 2) BT-474-H2B-GFP model	Trastuzumab and Pertuzumab / IV	0.69 MHz, 10ms burst, 1 Hz PRF, 60s duration, 0.46-0.62 MPa. Optison™ (100 µl/kg bolus).	The study involved three treatment groups: 1) control, 2) six weekly administrations of antibodies, and 3) six weekly sessions of antibodies combined with FUS-BBBD. In the FUS + antibody group, four out of ten animals experienced a reduction in tumor growth that lasted up to six weeks post-treatment. However, after six weeks, the tumor growth rate returned to the same level as the other groups. Despite this, the temporary

				reduction in tumor growth increased the median survival of responders as compared to the control group.
Liu et al. 2016[247]	Nude mice U87 human glioma	Bevacizumab (Avastin) / IV	0.4 MHz, 10 ms bursts, PRF-1 Hz, 60s duration, 0.4-0.8 MPa. SonoVue™ (details not provided)	Applying acoustic pressures of 0.4 and 0.8 MPa led to a significant increase of 5.73-fold and 56.77-fold, respectively, in bevacizumab penetration into the CNS. Furthermore, combination of 0.4 MPa sonication with bevacizumab resulted in 45% reduction in tumor progression and prolonged the survival by 2.35-fold as compared to the control.
Arvanitis et al. 2018[174]	Healthy and BCBM mouse models / xenograft HER2-amplified brain metastasis model	An antibody–drug conjugate (T-DM1) / IV	1.025 MHz, 10ms bursts, every 1 sec for 2 min, 0.48 MPa. Definity™ (20 µl/kg bolus).	FUS significantly improved the penetration of T-DM1 in the solid tumor by increasing interstitial convective transport and vascular barrier disruption. However, 5 days post-sonication, the treatment effect gradually decreased due to BBB resealing.
Brighi et al. 2020[248]	Patient-derived xenograft orthotopic mouse model of high-grade glioma	Radiolabelled EphA2-4B3 antibody / IV	1.1 MHz, 10ms burst, every 2.5s for 2 min., 0.85 MPa. Definity™ (2% dilution infusion of 200 µl over 60s)	A correlation was found between the extent of FUS-mediated BBB opening (measured via MRI) and antibody uptake (PET imaging), while leaving untreated areas unaffected with minimal damage (histology).
Ye et al. 2021[249]	Healthy and intracranial glioma mice / GL261-eGFP mouse glioma model	Fluorescently labelled-anti-PD-L1/ IN	1.5 MHz, 0.43 MPa, 6.7ms pulses, 5 Hz PRF, 60s duration. Lipid bubbles (30 µl at $8x10^8$ bubbles/ml bolus)	At 14 days post-implantation, anti-PD-L1 was administered either via intranasal (IN) or FUS-mediated IN delivery (FUSIN). In both non-tumor and glioma mouse models, FUSIN resulted in a 4.03-fold and 3.74-fold increase in the delivery efficiency of anti-PD-L1 to the brainstem, respectively, as compared to IN. While IN delivery only allowed distribution of anti-PD-L1 in the perivascular space, FUSIN delivered antibodies also deep in the brain parenchyma. Additionally, in the FUSIN

				group, bound PD-L1 to tumor cells was observed.
Sheybani et al. 2021[250]	C57BL/6 mice GL261 mouse glioma striatum	Radiolabelled CD47 antibody / IV	1.14 MHz, 0.5% duty cycle, 2 min. treatment, 0.4 MPa. Albumin bubbles (10^5 bubbles/g bolus)	This study demonstrates that the timing of antibody injection with respect to FUS BBB opening is critical, resulting in significant uptake when administered 15 min. post treatment, and none when issued immediately prior to FUS delivery (assayed using PET imaging).
Sabbagh et al. 2021[173]	C57BL/6 mice, NSG mice / GL261 Gliomas, EGFR VIII-U87 Gliomas	Anti-PD-1 / IV	1 MHz, 25000 cycle pulses, 1 Hz PRF, 120 s duration, 0.3 MPa. Lumason™ (200 µl bolus)	Compared to untreated controls, anti-PD-1 concentration was increased in the brain following US. They examined the timing of treatment with respect to tumor progression. In both early and late cases, median survival was longer in the US+anti-PD-1 group compared to antibody alone. Further, anti-PD-1 treatment with or without US both resulted in mice that were more resistant to tumor re-challenge.
Meng et al. 2021[251]	Human patients with confirmed HER2+ brain cancer metastasis (NCT03714243)	In-BzDTPA-NLS-trastuzumab / IV	ExAblate Neuro system (220 kHz), 0.74% duty cycle, 8-19 W, 50 s duration. 106-178 minutes total treatment time per patient. Definity™ (<20 µl/kg).	The study found that MR-guided FUS-mediated BBB opening enhanced the localized penetration of radiolabeled trastuzumab in patients with Her2-positive breast cancer brain metastasis without any serious adverse events. This treatment improved both early and delayed drug uptake by the tumor compared to the unsonicated tumor. Additionally, the treatment reduced tumor size by an average of 19 ± 12%.
Lee et al. 2022[211]	C57BL/6 mice/GL261 GBM	Anti-PD1 / IV	1.64 MHz, 10 ms pulses, 1 Hz PRF, 120 s duration, variable acoustic pressure.	They designed a closed-loop controlled, MB-FUS system which can promote MB acoustic emission (AE)-dependent ICAM-1 expression, and anti-PD-1 delivery in mice. This system enhanced the

			Definity™ (100 µl/kg bolus)	colocalization of anti-PD-1 and macrophages /microglia in the TME by up to 5.5-fold compared to the control. Moreover, at 12h post-sonication, there was a substantial increase in the population of PD1+ CD8 T cells within the TME, whereas no difference was observed in the similarly sonicated contralateral hemisphere. Further, the combination therapy led to a subtle but significant improvement in the animal survival.
Ahmed et al. 2023[252]	GL261 GBM mouse model	Anti-PD-L1 / IV	CarThera transducer, 1 MHz, 0.3 MPa, 25000 cycle burst at 1 Hz PRF, 120 s duration. Sonovue™ (10ml/kg)	The combination of anti-PD-L1 with BBB opening, in comparison to anti-PD-L1 alone, not only increased the activation of microglia but also significantly extended the overall survival of GBM-bearing mice. PCR analysis demonstrated that US-BBBO led to the release of circulating tumor DNA within 30 minutes following sonication. Additionally, BBB opening notably elevated the brain-to-plasma ratio of Nivolumab, a size-matched IgG1 isoform, at the 3, 24, and 48-hour marks after sonication.
Fadera et al. 2023[253]	Healthy pigs	Anti-PD-L1 / IV	15-element annular-ring FUS transducer, 0.65 MHz, 3 MPa, 1Hz PRF, 10ms pulse length, 3min sonication. Definity™ (10 ul/kg)	MRI verified BBB opening without any notable edema or hemorrhage. Additionally, fluorescent imaging demonstrated a 2.1-fold enhancement in the anti-PD-L1 delivery to the targeted regions. Histological evaluation confirmed the absence of significant tissue damage associated to FUS.
Porret et al. 2023[254]	Athymic nude mice/ U251 cells	Cetuximab / IV	1.5 MHz, 69% duty cycle, 127s duration, 430 kPa, SonoVue™ (100 µl bolus)	Delivery of 89Zr-labelled cetuximab (89Zr-CTX) to EGFR+ tumor cells improved when combined with FUS treatment. Longitudinal PET-imaging revealed that FUS didn't

				increased the accumulation of CTX in the tumor as compared to the control. FUS led to a maximal activation of glial cells 48h post-sonication, however the effect was too transient to improve the survival as compared to CTX alone.
Cells				
Burgess et al. 2011[244]	Healthy rats	Iron-labeled, green fluorescent protein (GFP)-expressing neural stem cells / intracarotid	0.558 MHz, 10ms bursts, 1 Hz PRF, 120s duration, 0.24 MPa. Definity™ (0.2 mg/kg bolus)	IHC showed successful MRIgFUS-mediated delivery of 32 ± 8.7 stem cells per cm^2 of brain region, as well as their differentiation to the neuronal lineage. Additionally, expression of nestin and polysialic acid indicated the survival of these cells post-implantation. No severe tissue damage was observed.
Alkins et al. 2013[179]	Nude Rats / Human HER2 positive MDA-MB-231 model	HER2-specific NK-92 zeta cells / IV	0.551 MHz, 10 ms pulses, 1 Hz PRF, 120 s duration, 0.32–0.35 MPa. Definity™ (0.2 mg/kg infusion over 1 min).	BBBD using MRIgFUS in combination with HER2-targeted NK cells resulted in a significant rise in the ratio of HER2-specific NK cell to MDA-MB-231-HER2 cells within the tumor volume. Additionally, the preserved cytolytic function of NK-92 cells was indicated by IHC.
Alkins et al. 2016[255]	Athymic Nude Rats / xenograft HER2-amplified brain metastasis	HER2-targeted NK-92 cells / IV	0.551 MHz, 10 ms pulses, 2 Hz PRF, 120 s duration, acoustic pressure controller. Definity™ (0.2 mg/kg infusion over 1 min).	Treatments including either FUS, targeted NK-92 cells, or FUS+NK-92 cells were delivered either twice per week for 4 weeks or 5 treatments in the first week, followed by decreased number of treatments. High frequency of FUS+NK-92 cells delivery at the first week, when the tumor burden is small, showed a significant decrease in tumor progression, followed by survival prolongation in some treated animals.
Lee et al. 2020[256]	Healthy Rats	Mesenchymal Stem Cells / IV	0.515 MHz, 10 ms burst, 1 Hz PRF, 5 min duration, 0.25 MPa.	FUS treatment along with an MSC co-injection resulted in approximately a 2-fold increase in MSC in the brain versus untreated controls. Mechanistic

			Definity™ (details not provided).	studies point to increased expression of CAMs.
Sabbagh et al. 2021[173]	C57BL/6 mice, NSG mice / GL261 Gliomas, EGFR VIII-U87 Gliomas	ffLuc-labeled EGFRvIII-CAR T cells, CXCL10-secreting APCs / IV	1 MHz, 25000 cycle pulses, 1 Hz PRF, 120 s duration, 0.3 MPa. Lumason™ (200 µl bolus)	This study showed a significant increase in CAR T-cell trafficking to the tumor site at 24- and 72-hours post-sonication, resulting an improvement in the median survival. Furthermore, the presence of LIPU+CXCL10-secreting APCs contributed to an increased recruitment of T cells to the tumor site.
Immunomodulating Agents				
Chen et al[181].	Rats / C6 glioma	Interleukin-12 (IL-12) / IP	0.5 MHz, 100 ms pulses. PRF = 1 Hz, 90 s duration, 0.36 - 0.7 MPa. SonoVue™ (0.1mg/kg bolus)	Animals were categorized in 4 groups including 1) control 2) 3 FUS sessions 3) 5 days IL-12 administration 4) 5 days IL-12 in combination to 3 FUS sessions. Systemic administration of IL-12 increased the total population of tumor-infiltrating lymphocytes, while did not impact on tumor progression and animal survival. Nevertheless, the combination of IL-12 administration and FUS-induced BBB opening significant reduced tumor volume as compared to non-treated group, followed by an improvement in the animal survival rate.

IV: intravenous, PRF: pulse repetition frequency, IHC: immunohistochemistry, MRgFUS: MR-guided ultrasound, HER2: human epidermal growth factor, BCBM: breast cancer brain metastasis, anti-PD-LI: anti-programmed cell death ligand, IN: intranasal, APC: antigen presenting cells, MSC: Mesenchymal Stem Cells, IP: intraperitoneal

Table 2.3: Summary of the ongoing clinical trials using focused ultrasound to deliver immunomodulating agents to the brain.

Location	Patients	Therapeutic Agent	ID	Device	Start / Estimated Completion Date

Sunnybrook Research Institute (Toronto, Canada)	Metastatic Her2-positive breast cancer with brain metastases	Trastuzumab (Herceptin)	NCT03714243	ExAblate 4000 Model 2	2019-09-18/2022-03-01
St Louis Hospital (Paris, France)	Metastatic Melanoma	Nivolumab (OPDIVO™)	NCT04021420	SonoCloud	2019-10-24/2023-07-05
Multi-center trial (USA and Canada)	Metastatic Non-small cell lung cancer	Pembrolizumab (Keytruda™)	NCT05317858	Exablate Model 4000 Type 2	2022-08-12/ 2024-12-01
MD Anderson Cancer Center (Houston, USA)	Recurrent GBM	Pembrolizumab (Keytruda™)	NCT05879120	Exablate Model 4000 Type 2	2023-07-30/ 2026-07-19
Linkou Chang Gung Memorial Hospital (Taoyuan City, Taiwan)	Recurrent GBM	Bevacizumab	NCT04446416	NaviFUS	2020-07-21/ 2023-08-04

Figures

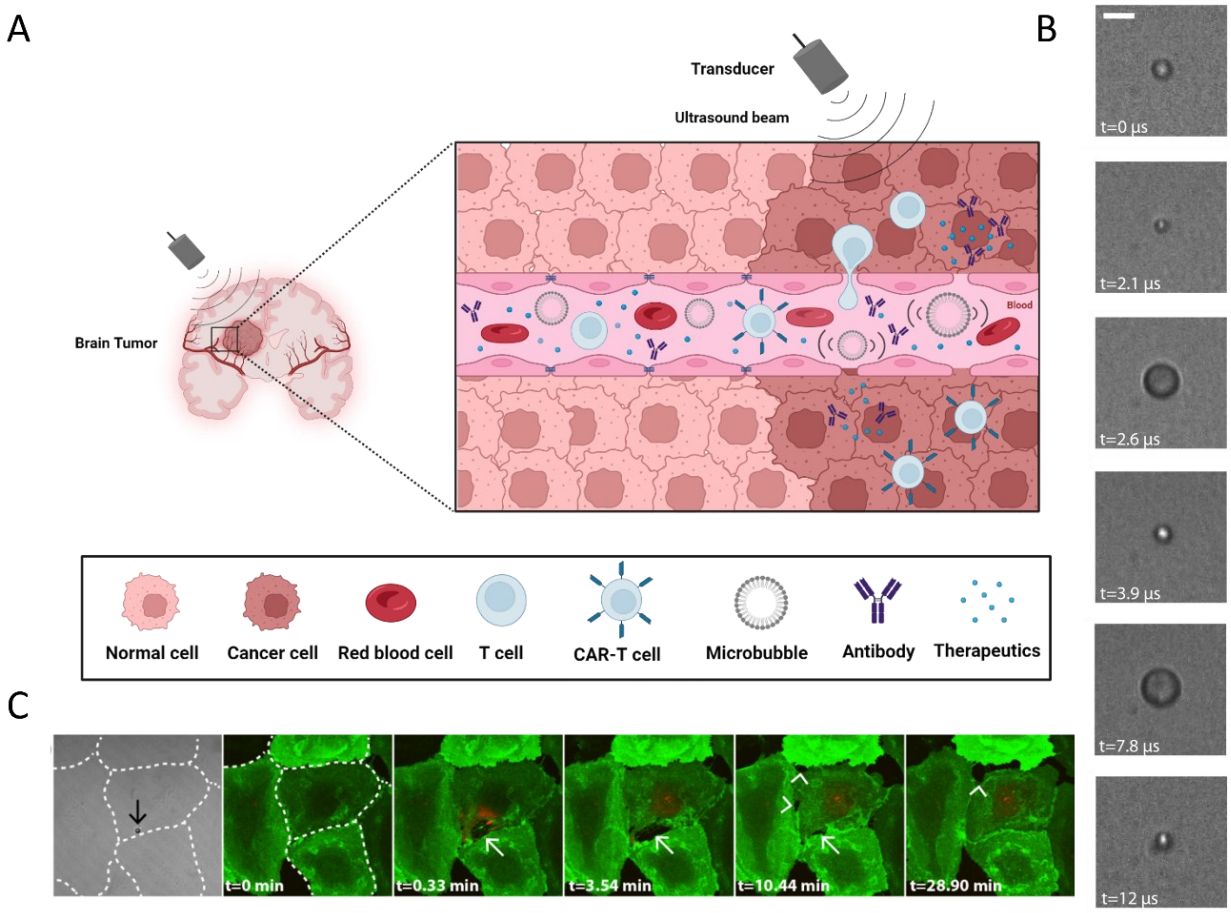

Figure 2.1: Concept of focused ultrasound assisted delivery of immunomodulating agents. A. Schematic view of focused ultrasound and intravascular microbubble interactions selectively targeted towards the region of brain disease. Microbubble vibration can locally increase vascular permeability to allow passage of otherwise impermeable immunomodulating agents (e.g. antibodies, cells, or cytokines). See text for details. B. Ultrafast microscopy observations of a vibrating microbubble contrast agent. Microbubbles expand and contract within an ultrasound field, and generate local shear stress on neighboring cells and tissues. Scale bar is 5 micrometers. C) Real-time confocal microscopy sequence highlighting both the temporary endothelial membrane (green) permeability (white arrow; red; surrogate macromolecule) and intercellular permeability (white arrowheads denote opening and closing of cell-cell contacts). Figures adapted from Helfield et al. PNAS 2016 with permission from the authors.

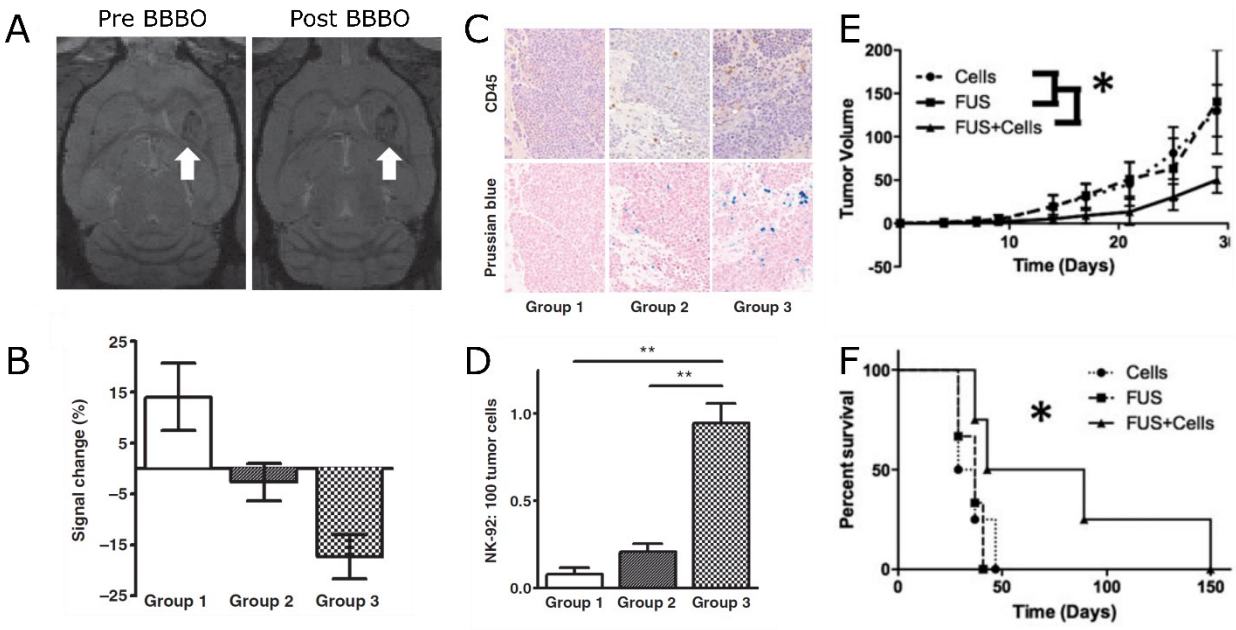

Figure 2.1: **Demonstration of MRI-guided focused US-mediated delivery of CAR NK-92 cells to the brain in rodent metastatic brain tumor models.** In panels A-D, SPIO labeled CAR NK-92 cells expressing HER2 were injected either alone (Group 1), after FUS-mediated blood-brain-barrier opening (BBBO; Group 2), or immediately before BBBO (Group 3). Panel A shows an axial T2*-weighted MR image with the tumor identified in the left frontal striatum (white arrow) both pre and post-BBBO, quantified for each of the groups in panel B (average ± SEM). A negative change suggests the accumulation of iron-labeled effector cells. There is a statistically significant change between groups 3 and 1. Panels C and D confirm the accumulated presence of CAR NK-92 cells via histology, whereby CD45 and Prussian blue are used to co-localize the iron-loaded NK-92 cells. Panels E and F highlight treatment efficacy of this approach. Animals were treated 5 times in the first week, followed by twice in the second week and one treatment the third week. Tumor volume is significantly smaller at day 30 for the US+cells treatment group (E) compared to controls, and overall survival significantly improved for this group as well (F). Figures adapted from Alkins et al. 2013 and Alkins et al. 2016 with permission from the author and publishing groups.

3. Fluid flow influences ultrasound-assisted endothelial membrane permeabilization and calcium flux

Manuscript published as: Memari et al., *Journal of Controlled Release* (2023) develops a custom-designed acoustically coupled microscopy system to explore the effects of flow dynamics on ultrasound-mediated endothelial cell permeabilization and calcium influx in real-time. This study further investigates the influence of multiple short pulses versus a single long pulse ultrasound on ultrasound-assisted cell perforation.

3.1 Introduction

Ultrasound contrast agent consists of a suspension of encapsulated gas-filled microbubbles, typically polydisperse and ranging in size from 1-8 μm in diameter and coated with a compliant biocompatible shell (*e.g.* phospholipid monolayer) [144]. Microbubbles, including commercially available Definity^{TM}, are clinically available and employed in cardiovascular imaging (left ventricular opacification) and recently approved for pediatric imaging [257]. As they remain intravascular due to their size, microbubbles act as red blood cell tracers and significantly enhance the ultrasound signal from within the vascular network [258]. Indeed, as microbubbles vibrate within a focused ultrasound beam, there have been many investigations into their dynamics and scattering behaviour, typically a function of intrinsic factors (*e.g.* bubble size [185], [259], shell constituents [260]) and extrinsic factors (*e.g.* presence of nearby boundaries [261], [262]).

Aside from their diagnostic applications, there has been tremendous progress on using these agents to elicit localized bio-effects; ranging from modulating vascular and cellular permeability [152], [263], blood flow [162], local thermal absorption [264], clot lysis [265], cellular signaling [266], [267] and neuromodulation [268]. Microbubbles can be made to vibrate with spatial (ultrasound beam focusing, attachment of targeting ligands on the bubble surface [269]) and temporal (ultrasound pulsing scheme) precision and in this sense, present a tremendous opportunity for site-specific modulation of bio-activity. The expansion and contraction of the microbubble within an acoustic field gives rise to local fluid streaming around the bubble [270], [271], resulting in shear and circumferential stresses on the vascular wall [272], [273]. Of particular interest is the localized enhanced cellular and vascular permeabilization for the purposes of targeted drug and/or gene delivery. Ultrasound-mediated drug/gene delivery as a platform has seen recent success in many applications. Under MRI guidance, focused ultrasound microbubble-mediated blood brain barrier

opening [61], [274] has been shown to promote the delivery of many formats of molecular therapeutics (*e.g.* chemotherapeutics [275], adeno-associated virus capsids [276], stem cells [244], NK cells [179], antibodies [171], and cytokines [181]) to targeted regions of the brain that would otherwise be incapable of transiting the cerebrovasculature. The pre-clinical success in this area has led to numerous clinical trials worldwide for enhanced BBB permeability in a variety of pathological contexts (*e.g.* glioblastoma, Alzheimer's disease). Additionally, while still mostly in the pre-clinical stages, microbubble-mediated therapy has also been shown to enhance drug/gene deposition in non-brain models of cancer (*e.g.* breast [277], pancreatic [278], carcinomas [279]). Aside from these neurological [280] and oncology-based [281] applications, another major area of investigation is for cardiovascular disease therapy [282], where microbubble-mediated gene therapy has shown promise in a variety of disease states, including cardiomyopathy [283], myocardial infarction [284], ischemia [224], and coronary microembolization [265]. Most recently, there has been a surge of interest in using this technique to modulate the local immune environment for the purposes of immunotherapy [285], [286].

Central to the effectiveness of all of these approaches is the oscillation and translational dynamics of microbubbles – particularly those behaviours that lead to the threshold level of stress required to elicit sono-permeabilization [152]. While many investigations have examined salient ultrasound and microbubble factors and how they relate to therapeutic efficiency [150], [154], [287], [288], [289], [290], including transmit frequency, peak-negative pressure, sonication time, and microbubble dose, relatively little is known about how the local fluid flow conditions alter microbubble-mediated bio-effects. For a fixed bubble dose (*i.e.* inter-bubble spacing), ultrasound focal volume, and treatment time, the number of microbubbles that interact with a given set of endothelial cells increases with faster laminar flow. Further, the relative position between a given microbubble and a neighboring cell, and the contact-time of their interaction, is a known factor in the propensity to elicit transient membrane permeability [291]. Given all else equal, the spatial-temporal flow dynamics will greatly affect the proximity of a microbubble to its nearest cell.

Indeed, as the applications of microbubble-mediated drug/gene delivery expand, so too do the local fluid flow conditions under which the microbubbles are situated. In cancer therapy applications, tumor blood vessels are known to be highly irregular in their architecture as compared to those in healthy tissues: geometrically, tumor vessels are heterogeneous in their spatial distribution, dilated

and tortuous; and functionally, the abnormal tumor vasculature is characterized by a large number of fenestrae and irregular basement membranes. This elevated geometric and viscous vascular resistance leads to comprised blood flow velocities [292], which can change as a function of tumor type and state of progression [293] and are less dependent on tumor vessel diameter than within healthy tissue. With respect to cardiovascular applications, the severity and extent of ischemia (one of the more investigated cardiovascular applications of microbubble-mediated therapy [282]) will dictate the resulting downstream flow velocity (*e.g.* [294]), with regions within the centre of the infarcted area exhibiting lower flow than in the peripheral zones [295].

Here, we examine the effects of vascular flow on microbubble-mediated endothelial cell bioeffects using a custom designed acoustically-coupled microscopy system. First, we examine how microbubble velocity effects the propensity of ultrasound-assisted enhanced permeability. Second, we investigate how modification of the ultrasound pulse sequence allows for more effective endothelial cell treatment. Next, we explore how flow rate alters intracellular Ca^{2+} delivery – a ubiquitous secondary messenger - and its transmission to neighboring, untreated cells. Indeed, Ca^{2+} plays a pivotal role in living cells, with perhaps its most direct role here being its requirement for plasma membrane repair [296]. However, both intracellular Ca^{2+} transients and intercellular Ca^{2+} communication are also well known regulators of many cellular processes, including gene expression and transcriptional regulation [297], endothelial tight junctional contact regulation [298], cell migration and shape [299], and cytokine release [300]. Further, it provides important information on the spatial influence and temporal rate of ultrasound-microbubble treatment on cellular processes. Finally, we discuss the implications of our findings towards modulation of microbubble-assisted drug/gene therapy applications.

3.2. Materials and Methods

3.2.1. General Cell Culture

Due to the intravascular nature of microbubbles, we employed two human endothelial cells models; human umbilical vein cells (HUVEC, C2519A; Lonza, Walkersville, MD, USA) and human cerebral microvascular endothelial cells (HBEC-5i, CRL-3245TM; ATCC, Manassas, VA, USA). All culture-ware used to culture HBEC-5i cells were first pre-coated with 1 ml gelatin (0.1%; ATCC) per 10 cm^2 in a shaker incubator at 37°C for 60 minutes prior to use. Both cell types were grown in T-75 flasks within an incubator maintained at 5% CO_2 at 37°C until 90%

confluency. HUVECs were cultured in endothelial cell growth medium (EGM-2; CC3162, Lonza) until reaching passage numbers between 3 and 9. HBEC-5i cells, an immortal cell line (SV40 large T antigen transformation), were cultured in DMEM:F12 (Wisent, Canada) cell culture medium, supplemented with 10% fetal bovine serum (FBS, Wisent) and 40 µg/ml endothelial growth supplement (ECGS, ATCC). These cells were used for experiments up to passage 20 from thaw. For either HUVECs or HBEC-5i cells, cells were seeded in collagen-iv-coated 0.8 mm flow chamber slides (Ibidi, Gräfelfing, Germany) with a 2.5 cm^2 growth area at an initial seeding density of 120,000 cells/cm^2 two days prior to the experiments. Cell culture medium was replaced every one or two days for cells cultured either in static or under flow conditions, respectively (see below).

3.2.2. Cell Culture Under Fluid Flow Conditions

To assess the effect of fluid flow conditions on ultrasound-mediated endothelial bioeffects, a subgroup of each type of endothelial line was seeded within the 0.8 mm flow chamber, as above, and placed in the incubator for 2 hours to allow cell adherence to the growth surface of µ-slides. After the culture media was replaced with fresh media, the slide was connected to the fluidic system within the incubator. This system was mounted with a compatible perfusion set consisting of air filters with 0.2 µm pore size, 10 ml syringe reservoirs, 50 cm silicone tubing with an inner diameter of 1.6 mm, an elbow luer connectors (yellow/green perfusion set, Ibidi, Gräfelfing, Germany). Each reservoir was filled up with 6 ml of pre-warmed cell culture medium (*i.e.* either EGM-2 for HUVEC or completed DMEM: F12 for HBEC-5i) and the fluid unit was connected to the ibidi pump system. The flow system was run with a gradient flow cycle, starting from a low flow rate and increasing gradually up to a flow rate of 37 ml/min corresponding to a shear stress of 9 dyn/cm^2. This procedure allows cells to get used to the presence of fluid flow, without being detached from the growth surface of the slides. Shear stress is automatically calculated by flow software based on flow rate, cell culture medium viscosity, perfusion tubing diameter and flow chamber height.

3.2.3. Microbubble Preparation

We synthesized an in-house phospholipid encapsulated agent using constituents that closely mirror clinical available agent Definity™ (Lantheus Medical Imaging, North Billerica, MA, USA), see Figure 1. These bubbles were fabricated using a lipid mixture including 1,2-dipalmitoyl-sn-glycero-3-phosphoethanolamine-N- [methoxy (polyethylene glycol)-5000] (DPPE-PEG5K, 16:0

PEG5000 PE), 1,2-dipalmitoyl-sn-glycero-3-phosphate (DPPA, 16:0 PA), 1,2-dipalmitoyl-sn-glycero-3-phosphocholine (DPPC, 16:0 PC) (Avanti Polar Lipids, Alabaster, AL). To prepare the lipid solution, lipid components (0.82 DPPC: 0.1 DPPA: 0.08 DPPE-PEG5K) were dissolved in pre-heated propylene glycol, followed by adding an appropriate amount of pre-heated glycerol. The resulting mixture was placed in the water bath until most of the lipids were dissolved. In the next step, phosphate-buffered saline (PBS) was added and kept in the heated water bath for 20 minutes. The final lipid solution with 1 mg/ml total lipid concentration was sonicated in a water bath sonicator at 52°C until the solution was clear. Aliquots of lipid solution (1.5 ml) were added to glass vials and the headspace replaced with octafluoropropane gas. The microbubbles were activated at room temperature [184] with the Vialmix^{TM} (Lantheus) for the standard 45s period and allowed to cool back to room temperature prior to the experiments. Microbubble concentration and size distribution were measured using a Coulter Counter (Multisizer 4e; Beckman Coulter). Briefly, fresh room temperature agent was hand-mixed and an aliquot was extracted after a 2 minute decantation using a 19 G needle placed just above the rubber stopper (and another 19G for venting purposes). Microbubbles were diluted 1000x in ISOTON II (Beckman Coulter) and sampled using the 30 μm aperture, which enables an effective measurable size range of 0.6-18 μm. Microbubble concentration and size distribution were measured every 15 minutes for up to an hour, and repeated in triplicate (see Fig 1), resulting in a native concentration of (5.46 ± 0.49) x 10^9 microbubbles/ml and a bimodal volume peak distribution at (1.1± 0.2) μm and (4.9± 0.3) μm. Note that the bimodal nature of the volume-weighted peak distribution is characteristic of clinical Definity^{TM} agent [185], and that volume-weighted size distributions are typically used in this context as it has been shown to correlate with microbubble acoustic activity [259], [301].

3.2.4. Fluorescent Markers

Propidium iodide (PI; 450 μM, P1304MP; Molecular Probes) was used as a real-time marker for endothelial cell permeability. As a non-fluorescent, cell-impermeant compound, PI exhibits a significant increase in fluorescence upon binding to RNA/DNA complexes (535/617 nm) – and thus reports measurable signal within cells with increased membrane permeability, while excluded from those cells that do not. Fluo-4AM (10 μM; F14201, Molecular Probes) is a cell permeant compound that, upon entering a cell, is cleaved by intracellular esterases and remains within the cell, exhibiting a 100x increase in fluorescence (495/516 nm) upon binding to calcium (Ca^{2+}). Given cytosolic baseline levels of Ca^{2+} (~100 nM), increases in intracellular Ca^{2+} were measured

as a fractional increase in Fluo-4AM signal intensity, normalized to its level prior to ultrasound delivery. Finally, Hoechst dye (Thermo Fisher) was used to stain cell nuclei at a 1:500 v/v dilution for 10 minutes at 37°C, following by three washing steps.

3.2.5. Ultrasound Delivery and Experimental Protocol

The exposure platform in this study was an acoustically coupled inverted microscope (Ti2-A, Nikon, Melville, New York, USA) which served to co-visualize the acoustic focus with the microscope field of view. A custom-made support and coupling cone were designed to secure a single-element ultrasound transducer with 1 MHz center frequency (unfocused, diameter $2a$ = 12.7 mm; A303S-SU, Olympus, Waltham, MA, USA) at an angle of 45° to the normal in an attempt to minimize reflections. The tip of the coupling cone was set at a 2 mm distance from the chamber's surface, with the transducer surface to sample monolayer surface distance at 27 mm. This was chosen based off of the Rayleigh distance of this un-focused transducer ($z = {a^2}/{\lambda} \approx {40.3}/{1.5} =$ 26.9 mm). Given this geometry, the projected acoustic beam-width BW at the surface of microbubble-cell interaction is on the order of $1.4\,{z\lambda}/{2a}\cos(\theta) \approx$ 3.5 mm [302]. The transducer was driven by a signal generator (Tektronix, AFG31052 series, Chicago, USA), and amplified by a 150 W power amplifier (Amplifier research, Model: 150A 100B, Mississauga, USA).

Flow chambers were connected to the fluidic system, filled up with pre-warmed cell culture medium, and placed upon the inverted microscope. For all experiments, chambers were co-perfused with a solution of phospholipid encapsulated microbubbles (diluted either 1:500 v/v or 1:1000) and PI as a membrane permeability tracer. From one to four locations of each chamber were insonicated using a 1 MHz, 20 cycle pulse with a pulse repetition interval (PRI) of 1 ms. All experiments were conducted within 8 minutes of microbubble dilution to minimize the effects of both microbubble dissolution and appreciable bubble size distribution stratification due to buoyancy. As the gravitational forces (g) are balanced by diameter and speed-dependent viscous drag forces, we can employ Stoke's equation for a sphere of radius r moving through a fluid to estimate the timescale over which bubble floatation occurs [185]. The time t for a bubble to rise a distance d is given by:

$$t \cong \frac{9d\mu_l}{2\rho g r^2}, \tag{1}$$

where μ_l is the fluid viscosity and ρ is the fluid density. For bubbles within the size range employed here (Fig. 1), this results in a timescale from 30 s (8 μm diameter bubble) to over 1500 s (1 μm diameter bubble).

The peak-negative pressure of the beam was measured at the region of interest in a separate water tank using a hydrophone (Onda Corp., Sunnyvale, CA, USA, HGL-200) to be 305 kPa in free-space. Acoustic measurements were also performed in the presence of the ibidi chambers used here, resulting in a minor transmission loss of 5% (see Fig. 2). We acknowledge that, despite the minimal transmission loss, the acoustic beam at the interface of the endothelial cell-cultureware surface can be complex. The impact of our findings remains unaffected by this, as we are making comparative measurements between systems under the same acoustic stimulus. Generally, fluorescence microscopy videos were recorded for 90 s at a frame rate of 1 fps, starting 5-10 s prior to ultrasound exposure in order to capture the salient effects before, during, and after ultrasound delivery - including any prior fluorescent artefacts or dead cells prior to sonication. All data analysis was performed using in-house software in MATLAB (The Mathworks Inc., Natick, MA, USA).

3.2.6. The Effect of Fluid Flow on Ultrasound-mediated Cell Membrane Permeabilization

We examined the effect of fluid flow conditions on membrane permeabilization *a)* during cell culture and *b)* during ultrasound treatment. Both cell lines, either HUVEC or HBEC-5i, were cultured in 0.8 mm flow chambers either under static conditions or under unidirectional flow (9 dynes/cm^2) for 2 days. Chambers were then co-perfused with microbubbles and PI at a flow rate of either 5 or 30 ml/min, and interrogated for a treatment duration of 2 s. With these flow rates, a given microbubble is present within the acoustic focal volume for approximately 0.18 s (5 ml/min) or 0.03 s (30 ml/min). The selection of these flow rates warrants some discussion. Given that blood velocity varies in terms of anatomical location (*e.g.* big vs small vessels) and pathological state (healthy vs diseased tissue), we chose a range to encompass small to large vessel flow; although the correlation between blood velocity and vessel size is not clear in tumor vasculature[292], [293]. The cross-sectional area of our flow chamber is (5x0.8) mm = 4mm^2. For the flow rate used in our manuscript, this corresponds to a velocity of 2 – 12 cm/s. This range encompasses the velocities typically found within larger healthy arterioles to arteries, and is appropriate for the given cross-

sectional area of the fluid chamber. Multi-color recordings (Hoechst and PI) were employed to obtain co-registered images per time point. These co-aligned Hoechst images were used as an image processing mask to delineate cells, and PI signal intensity was quantified using in-house MATLAB software. The total number of cells D was determined via Hoechst staining (D = 6376 ± 682 per field of view over all datasets), and the presence of PI by the end of the recording was used to delineate between endothelial cells with (PI+) or without (PI-) enhanced cell membrane permeability.

3.2.7. The Effect of Multiple Short Pulses on Cell Membrane Permeabilization

To compare the effect of a single pulse versus multiple short pulse ultrasound, a subset of cells was pre-seeded under unidirectional flow for two days. These two types of pulse sequences, either a single pulse or repeated short pulses, were designed with a fixed number of total ultrasound bursts M. These were programmed on the signal generator via MATLAB. For these experiments, flow chambers were co-perfused with microbubbles and PI with a flow rate of 30 ml/min. We investigated treatment paradigms with M = 100, 200, and 300 bursts (Fig. 2); the single pulses were characterized by similar transmit parameters as the first set of experiments (N = 20, PRI = 1ms), but with a duration of either 100, 200 or 300 ms. The multi-pulse sequence was identical but split into 25 ms intervals separated by 1 second (Δt = 1s); namely 25 ms intervals repeated either 4 (M = 100), 8 (M = 200), or 12 (M = 300) times. Data analysis was performed similarly to section 2.6., whereby we compare the relatively efficiency of permeabilization between the two pulsing schemes.

3.2.8. The Role of Flow Rate on Ultrasound-mediated Ca^{2+} transients

A subset of either HUVEC or HBEC-5i cells were pre-seeded under unidirectional flow for two days and incubated with Fluo-4AM for 30 minutes at 37°C. Following wash steps, baseline images were acquired to assess native intracellular Ca^{2+} levels. Chambers were then co-perfused with microbubbles (1:500 dilution) and PI at a flow rate of either 5 or 30 ml/min, and interrogated for a treatment duration of 2 s. Video microscopy was performed for 90 seconds with increased frame-rate (2 fps) in order to assess the spatial and temporal breadth of Ca^{2+} dynamics. Calcium positive cells (Ca^{2+} positive) were defined as those that exhibited an increase in intracellular fluorescence (in arbitrary units a.u.) greater than a given threshold, determined from sham experiments (see below). Among the Ca^{2+} positive cells, cell population sets can be split between directly treated

cells (those that are Ca^{2+} positive and PI positive) and those that are not directly permeated by ultrasound (Ca^{2+} positive and PI negative). All data analysis was performed using in-house software in MATLAB.

3.2.9. Statistical Tests

Statistical analysis was performed using MATLAB. Two-tailed, un-paired two-sample Student's t-tests were applied to ascertain statistical significance in enhanced membrane permeability (the percent of PI+ cells) for any given set of conditions. Pearson's correlation coefficient was employed to test linear dependence between the extent of Ca^{2+} positive and PI positive cells. The Wilcoxon rank sum test was applied to assess equality of population medians for maximum intracellular Ca^{2+} signal as a function of flow rate. A resulting *p*-value of less than 0.05 was assumed to be statistically significant.

3.3. Results and Discussion

Figure 3 depicts a representative epi-fluorescence micrograph of the effect of shear conditions during cell culturing. It is well established that *in-vivo* endothelial cells, which are exposed to blood flow, exhibit phenotypic, biomechanical and genetic differences as compared to those cultured statically; including extended F-actin fibers and altered cytoplasmic and plasma membrane mechanical properties (*e.g.* [299], [303]). Indeed, culturing endothelial cells, either HBEC-5i or HUVEC, under 9 dyn/cm^2 shear flow for seven days (Fig. 3a) greatly altered the cellular morphology as compared to conventional static cell cultivation (Fig. 3b). Endothelial cells in the static state displayed heterogeneous morphology with random orientation, whereas cultured cells under fluid flow, with similar culture conditions, were more homogeneous and elongated in the flow direction. Although the presence of shear flow for seven days led to a substantial morphologic transition in endothelial cells, exposing both HUVEC and HBEC-5i to shear flow even as few as two days impacted cellular shape (data not shown). In addition, statically cultured cells in chamber slides developed disrupted boundaries between adjacent cells, while seeded cells under unidirectional flow with the same confluency formed more physiologically relevant cell-to-cell contacts, with minimal extracellular gaps. This result indicates that, under the specific conditions employed here, cultivation of endothelial cells under a steady fluid flow significantly alters endothelial physiology and mimics a more physiologically relevant environment.

With this said, our first goal was to assess whether the efficiency of ultrasound-mediated enhanced endothelial cell permeability, which occurs under fluid flow, is modulated by the fluid flow rate itself. First, we conducted an exhaustive set of control experiments (shams) for every experimental condition, *i.e.* under flow with microbubbles but with no ultrasound treatment (Fig 4). This was to tease out the extent to which ultrasound and microbubble treatment is responsible for changes in endothelial permeability and Ca^{2+} influx versus that of the fluid shear flow itself – which is known to modulate intracellular Ca^{2+} levels. As can be seen from the figure, control experiments conducted on over 60000 cells per endothelial cell line reveal negligible PI uptake, on the order of 0.2% of cells over all conditions (no statistical difference between any of the groups). It should be noted here that this data also inherently captures any systematic error associated with the offline processing algorithm. Similar experiments investigating the effect of fluid flow on Ca^{2+} flux, estimated from over 30000 cells per endothelial cell line, reveals small fluctuations. For the Ca^{2+} sham controls, data is presented as the distribution of maximum intracellular Ca^{2+} levels throughout the video recording, whereby the top and bottom of the boxes denote the 25th and 75th percentiles, respectively, with the whiskers extending to 1.5 times the interquartile range (IQR). The notches in the boxes can be interpreted as a comparison interval around the median values (median $\pm\ 1.57\ IQR\ /\ \sqrt{n}$) where n is the number of cells within that group. While there is no statistical difference between the Ca^{2+} sham experiments at the two flow rates for HUVECs, there is an increase in maximum intracellular Ca^{2+} signal at 30 ml/min versus 5 ml/min for HBEC-5i cells (1.3 vs. 0.4 a.u.; $p<0.001$). However, all experimental data employing ultrasound and microbubbles to be presented in the subsequent figures were found to be highly significantly different to its respective sham experimental group ($p<0.001$). Having firmly established a baseline from which we may interpret ultrasound-mediated changes in permeability and Ca^{2+} flux, the results depicted in Figure 5 demonstrate a significant increase in PI positive cells under a situation in which microbubbles are flowing at a faster rate. Figure 5a and 5b highlight a representative example of the time-lapse microscopy data acquired before, during, and after ultrasound exposure. As can be seen by the fluorescence still-frames (first frame is Hoechst-stained for nucleus detection), the uptake of otherwise impermeable PI indicates endothelial cell membrane perforation, which continues long after the ultrasound exposure is over (2 seconds, in this example). Previous studies have examined similar-looking PI uptake curves to extract salient parameters of membrane perforation (*e.g.* [287]). However, as the PI tracer employed here is only

visible at our current optical magnification as it reaches the nucleus, its uptake rate and plateau level are confounded by the diffusion distance between its point of entry (*i.e.* the membrane perforation) and the nucleic cavity. As such, these curves were employed as a surrogate for the presence or absence of a directly perforated cell in a binary sense. Note that within the cytoplasm at the site of PI entry (*i.e.* not confounded by the nucleus and thus where the diffusion equations hold), the intracellular PI level is strongly correlated with microbubble-induced shear stress [152].

With endothelial monolayers cultured under shear, the extent of permeabilization from microbubbles diluted 1:500 v/v under a flow rate of 30 ml/min increased drastically, resulting in an 8.2 fold (HUVEC) and 2.7-fold (HBEC-5i) increase compared to treatment under a flow rate of 5 ml/min ($p<0.001$; $p<0.003$ for HUVEC and HBEC-5i respectively) – shown in Fig. 5c. To gain some physical insight, it is helpful to examine the bubble travel distances within a single PRI (1 ms). At the slower flow rate (2 cm/s), this corresponds to approximately the length scale of a single endothelial cell (20 μm), whereas this increases to several cell widths at the faster flow rate (120 μm). If we assume that a given bubble is not disrupted as it passes through the ultrasound beam, the bubbles traveling at the faster flow rate have the potential to interact with many more cells than it would at the slower flow rate during a given fixed duration ultrasound treatment. This is a potential explanation for the increased cell membrane permeability at the faster flow rate, regardless of endothelial cell type.

Additionally, for comparison, our results show a similar pattern for endothelial monolayers cultured statically (Fig. 5d), resulting in increased cell perforation with increasing flow rate (9.7-fold, $p<0.001$; 2.2-fold, $p<0.001$ for HUVEC and HBEC-5i respectively). This confirms that the effect of microbubble flow rate on cell membrane permeability was independent of the cell seeding state. It is interesting to note here that comparison between Figs. 5c and 5d reveals a slight increase in the number of permeabilized cells for those monolayers that were cultured statically versus those cultured under shear at both treatment flow rates. While not the purpose of this study, this is consistent with previous work investigating the effect of culture condition on static ultrasound-mediated endothelial permeability [304]. Given these results, we chose to continue the rest of our investigations employing endothelial cells that were cultured under flow (*i.e.* as in Fig. 5c) to preserve *in-vivo* relevance.

Having established a stark effect of microbubble flow rate on ultrasound-mediated endothelial permeability, we hypothesized that modulating the pulsing scheme to allow for replenishment of microbubbles between bursts would have an impact on permeability (given a fixed microbubble dose, fluid velocity, and acoustic stimulus). In addition, we explored two different microbubble doses to examine the concentration-dependence of this effect. At a fixed fluid flow rate of 30 ml/min, the effect of multiple short pulses with 1 s inter-pulse delays was compared to single long pulse ultrasound (see Fig. 2b for pulsing scheme schematic) with microbubble dilutions of 1:500 (Fig. 6) or 1:1000 (Fig. 7). An inter-pulse delay of 1 s was chosen in order to supply sufficient time for a completely fresh replenishment of microbubbles. Indeed, this results in a microbubble displacement of 20 mm (5 ml/min) and 120 mm (30 ml/min), well beyond the acoustic beam width (see Methods section). For a given number of ultrasound bursts, either $M = 100$ (Fig. 6a), $M = 200$ (Fig. 6b), or $M = 300$ (Fig. 6c), repeated short pulses at 1:500 dilution relative to the single long pulses considerably elevated ultrasound-induced cell membrane permeability for both endothelial cell types (1.5-fold ($p<0.01$), 1.7-fold ($p<0.007$), 1.5-fold ($p<0.004$) increase for HUVEC; 1.5-fold ($p<0.01$), 1.8-fold ($p<0.004$), 2.3-fold ($p<0.001$) increase for HBEC-5i). While expectedly resulting in fewer permeated cells, the same numerical trends were observed for the cells which were treated with a more dilute concentration (1:1000 dilution) of microbubbles (1.3-fold ($p=0.1$), 1.9-fold ($p=0.8$), 2.0-fold ($p<0.02$) increase for HUVEC; 1.3-fold ($p=0.1$), 1.3-fold ($p<0.03$), 1.6-fold ($p=0.06$) increase for HBEC-5i). As it is illustrated in Figs. 6d and 7d, the ratio of repeated short pulses versus single long pulse ultrasound exhibits an increasing trend with the total number of bursts. Note here that in this figure, a value of 1 indicates no difference between the two pulsing schemes. This effect is likely due to the accumulation of inter-pulse delays from the pulses with larger burst number, which leads to the replenishment of more fresh microbubbles in the treatment region and allows for the native treatment of new, otherwise untreated endothelial cells. Given knowledge of our acoustic beam width, we can estimate the minimum required inter-pulse delay to achieve this; *i.e.* to ensure that a given set of microbubbles is given sufficient time to exit the ultrasound beam width, resulting in a minimum Δt of 29.2 ms (30ml/min) and 175 ms (5ml/min) for the two flow rates. The inter-pulse delay time of 1 second selected here therefore corresponds to the time required to traverse ~34 (30 ml/min) and ~6 (5ml/min) beam widths, significantly out of the acoustic beam.

In order to postulate that the above effects of pulsing scheme are not of thermal origin, we can estimate the 'worst-case' temperature increase ΔT_{max}. Firstly, we assume that the culture media approximates water, namely that the speed of sound c, the density ρ, the heat capacity per unit volume C_v and the ultrasound absorption coefficient α_0 are given by c=1500 m/s, ρ=1000 kg/m^3, C_v=4.18 J/cm^3°C and α_0=0.002 dB/cm/MHz. Secondly, we assume the worst-case scenario; that is to say to ignore heat transfer from perfusion (*i.e.* that the media is moving with a given velocity) and assume a continuous (not pulsed) ultrasound wave (duty cycle=100%) of the maximum duration used in this study, Δt=0.3 s. Given this, we can estimate the rate of heat generation per unit volume $\dot{Q}$ given the temporal averaged intensity I_{TA} as [136], [305]:

$$\dot{Q} = 2\alpha I_{TA};\ I_{TA} = \frac{p^2}{2\rho c}. \tag{2}$$

where p is the pressure amplitude at the source of heat generation, *i.e.* the focal spot of the transducer. If we consider that no heat is lost due to conduction, convection, or any other format, the maximum temperature increase ΔT_{max} is approximated by [306]:

$$\Delta T_{max} = \frac{\dot{Q}\Delta t}{C_v}. \tag{3}$$

With our selection of ultrasound parameters, this results in a maximum 'worst-case' temperature increase of ΔT_{max} =1.02x10^{-4} °C; a negligible increase. In practice, we would assume the maximum temperature increase to be even smaller since we employed pulsed ultrasound (duty cycle=2%) in a fluid flow environment.

A summary of the effect of fluid-flow on ultrasound-mediated intracellular Ca^{2+} transients is depicted in Fig. 8. As Ca^{2+} is known to be modulated by shear stress, control groups were subjected to microbubble perfusion with either 5 or 30 ml/min flow rate and without any ultrasound delivery (see Fig. 4). In the top panel (Fig. 8a), a representative microscopy time-lapse of ultrasound-induced Ca^{2+} influx in HBEC-5i is shown for both treated under 30 ml/min (top) and 5 ml/min (bottom). In this panel, the last frame for both flow rates is merged with the resulting propidium iodide map – denoting the cells that were directly treated by the end of 90 second recording time. From this visual representation, there is a clear and significant difference in terms of both intracellular Ca^{2+} levels and the extent of Ca^{2+} signalling between the two flow rates examined. As

has been previously observed in experiments conducted in static conditions, Ca^{2+} influx occurs not only in the directly perforated cell but intracellular Ca^{2+} concentration is also modulated in adjacent, neighboring and/or non-directly treated cells [158], [160], [267]. This can be due to direct microbubble cavitation below a given threshold [152] so as not to permeate the membrane but trigger shear-sensitive Ca^{2+} channels [54], or due to cell-to-cell Ca^{2+} propagation. Calcium propagation has long been observed as a result of localized membrane wounds [307], and has in part as its mechanistic source intercellular communication via gap junctions [54]. This phenomenon can be qualitatively examined in the first panel (Fig. 8a) by noting endothelial cells with both Ca^{2+} and PI positive signals (*i.e.* directly permeated) and those that stain positive for Ca^{2+} but without PI signal (*i.e.* indirectly modulated). Indeed, the timing of Ca^{2+} influx and the resulting dynamics over time are sampled in Fig. 8b, whereby the traces from the six cells denoted in Fig. 8a are shown. In this panel, ultrasound delivery commenced at approximately 10 seconds into the recording for both of the experiments (cells 1-3, 30 ml/min; cells 4-6, 5 ml/min). From this panel, it is clearly observed that the intracellular Ca^{2+} signal drastically increases at the time (or slightly after) ultrasound is delivered, and that the signal is much stronger in those cells that were treated at the faster flow rate than those at the slower flow rate. While the influx dynamics are likely due to the localized microbubble-induced shear stress and resulting perforation size/duration, Ca^{2+} is actively pumped out of cells (*e.g.* ion channels, through gap-junctions). Quantification of all datasets revealed a strong correlation between the number of Ca^{2+} and PI positive cells, as shown in Fig. 8c with the flow rate dimension and endothelial cell type collapsed (r=0.79, p<0.001, although each cell line is independently correlated too; r_{HUVEC}= 0.90, p_{HUVEC} <0.001; r_{HBEC} = 0.74, p_{HBEC} <0.005). Further, the maximum intracellular Ca^{2+} intensity (*i.e.* the peaks of the curves shown in Fig. 8b) is much greater within the cohort treated at 30 ml/min, as shown in Fig. 8d, for either type of endothelial cell (p<0.001 for both HUVEC and HBEC-5i). As previously discussed in the context of sham experiments (Fig. 4), the notches in the boxes can be interpreted as a comparison interval around the median values (median $\pm$ $1.57\,IQR/\sqrt{n}$) where n is the number of cells within that group. When treated under the larger flow rate, maximum intracellular Ca^{2+} levels increased by a factor of 1.3-fold and 2.1-fold for HUVEC and HBEC-5i cells respectively. Note that while there was no significant difference in this metric at 5 ml/min between endothelial cell types (p=0.1), the HBEC-5i cohort of cells exhibited much higher peak Ca^{2+} levels as compared to the HUVEC cohort at 30 ml/min (1.7x increase, p<0.001). In addition

to Ca^{2+} dynamics, it is of particular interest to examine the proportional of cells that exhibited Ca^{2+} influx but were not directly perforated. Indeed, this 'remote' effect – namely modulation of cellular signaling without direct contact with a vibrating microbubble – is of particular interest for non-vascular applications of ultrasound-mediated therapeutics. To this end, Fig. 8e quantifies the percentage of all Ca^{2+} positive cells that exhibited Ca^{2+} influx without PI influx (the intersection of the Ca^{2+} positive set with the PI negative set normalized to the total number of Ca^{2+} cells; $Ca^{2+} + \cap PI -$). Ultrasound-mediated endothelial permeabilization under the slower flow rate resulted in more of these cells than under the faster flow rate (p<0.001 for both HUVEC and HBEC-5i). Indeed, this is not accounted for by the increased total number of Ca^{2+} positive cells at 30 compared to 5 ml/min (3.58 ± 0.32-fold increase over all cells) since the extent of direct membrane perforation increases linearly with it (Fig. 8c). As individual cell shape and morphology is known to be modulated post-US treatment (*e.g.* [308]), one hypothesis for this observation is that slight changes in cell morphology due to the perforation recovery at the faster flow rate (typically much larger Ca^{2+} peaks compared to the slower flow) appreciably uncouples the cell-cell contact required for gap-junctional communication between neighboring cells – one of the major mechanisms for Ca^{2+} efflux [54]. This would imply that more effective remote cellular modulation due to ultrasound (*i.e.* indirect cellular 'bystander' effect) is accomplished under slower flow conditions. With this in mind, the design of pulsing schemes in which the range of target tissue blood flow is a consideration is warranted.

In addition to pulsing schemes, microbubble size distribution relative to the transmit frequency (*i.e.* resonant sizes) will likely play a role in the absolute magnitude of endothelial bioeffects. The resonant microbubble behaviour under an acoustic pressure similar to those used for microbubble-mediated therapy is complex; exhibiting nonlinear resonance phenomena and strong harmonic vibrations [144], [273], [309], [310], [311]. In conjunction with both size-dependent effects (*e.g.* bubble flotation) and varying flow rates, the initial bubble distribution is another aspect that in principle can augment therapeutic efficacity.

It is also interesting to note that, while the trends observed in this work are consistent among the two types of endothelial cells examined (confirming that this phenomenon is not unique to a given cell line), the absolute magnitude of the effect is not the same – it is amplified within HUVECs. It is well understood that cellular mechanobiology in part dictates the response of an endothelial cell

to the complex set of dynamic mechanical stresses (*e.g.* flow-derived stresses, local curvature) [312], [313], [314]. It is thus not surprising that membrane permeabilization due to localized shear will depend on the constituents and biophysical properties of the plasma membrane itself – in this case from vein (HUVEC) versus cerebral microvasculature (HBEC-5i) origin. Further, the present study examines the specific effect of laminar flow rate. Indeed, endothelial cells are continuously subjected to various mechanical forces. However, the primary hemodynamic force is flow-induced shear stress, with varied flow patterns such as laminar, disturbed, or pulsatile in different regions of the arterial tree. Studies (*e.g.* [315]) have shown that shear flow affects a wide variety of endothelial cellular functions (*i.e.* gene expression, proliferation, apoptosis, migration, permeability), including the modulation of atherosclerotic genes (*e.g.* increases due to disturbed flow at the branch points of the arteries). Our control studies (Fig. 4) indicate no significant detectable cellular permeability without ultrasound-induced microbubble vibration. There is evidence however that laminar flow reduces endothelial cell proliferation and results in improved barrier function (*i.e.* decreased endothelial permeability) in comparison with more chaotic flow patterns. While not examined here, we would speculate that the more intrinsically permeable endothelial cell membranes found under disturbed flow would more easily perforate under ultrasound and microbubbles while under all other conditions equal. It is an important consideration since, as previously mentioned, the local vascular flow patterns can differ substantially between healthy and pathological tissue. This warrants further investigation and is the subject of future studies.

3.4. Conclusions

An acoustically coupled microscopy system was developed to investigate ultrasound-assisted endothelial cell permeabilization under varying fluid flow conditions. The results revealed the substantial impact of microbubble flow velocity over the adjacent endothelial cells on the efficacy of microbubble-mediated cell perforation. The flow rate of 30 ml/min was found to drastically increase endothelial cell membrane permeability in both human umbilical vein (HUVEC) and microvascular brain (HBEC-5i) endothelial cells as compared to the flow rate of 5 ml/min. In addition, a faster flow rate significantly elevated the intracellular Ca^{2+} levels in both endothelial cell types, followed by a more extensive propagation of Ca^{2+} influx in the indirectly treated neighbouring cells. However, the population of Ca^{2+} positive cells without direct membrane permeation represented a larger fraction of Ca^{2+} positive cells at the slower flow rate. Furthermore,

our results have shown that modulating the pulsing scheme to incorporate an inter-pulse delay of $\Delta t = 1$ s between multiple short pulses greatly extended cell membrane permeability due to the replenishment of fresh microbubbles to the acoustic focus. These findings provide an understanding of the effects of vascular flow conditions on microbubble-assisted cell permeabilization and aid developing an efficient, application-dependent therapeutic delivery system.

Figures

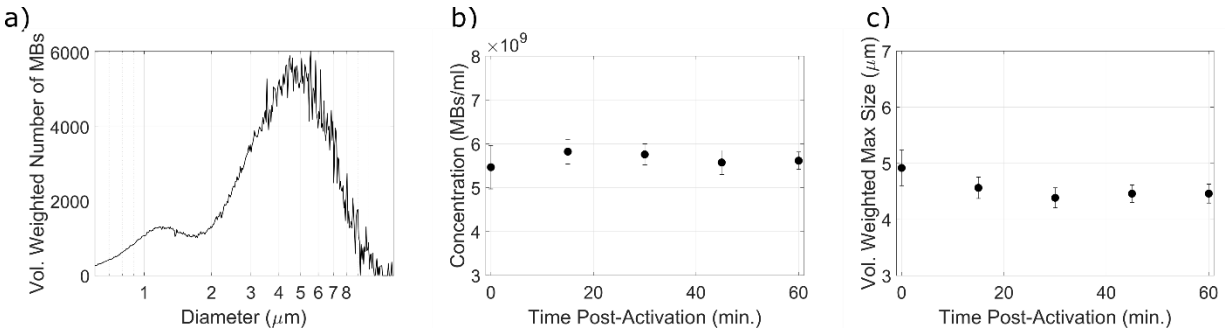

Figure 3.1: The in-house phospholipid encapsulated agent is stable for a least up to an hour. a) The volume-weighted distribution highlights a double peak: at (1.1± 0.2) µm and (4.9± 0.3) µm. Note that this double peak characteristic is similar to clinically employed Definity™ agent. Panels b) and c) highlight a stable microbubble concentration and volume-weighted peak size over the course of 60 minutes. All experiments were conducted within one hour of vial activation, and individual experiments were complete within 8 minutes of agent dilution within the pre-warmed media cocktail.

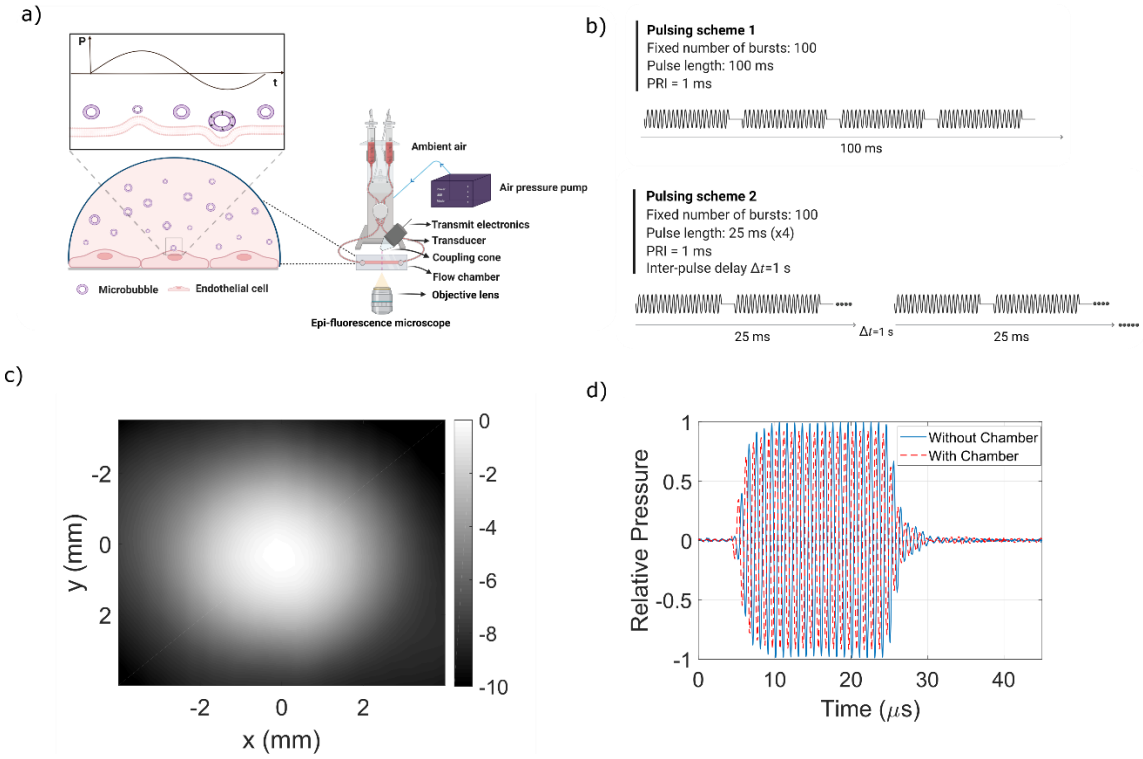

Figure 3.2: Schematic representation of experimental setup and pulse design. a) Flow chambers were placed upon an acoustically coupled inverted microscope and co-perfused with a solution of phospholipid agent and propidium iodide (PI). Inlet highlights a schematic representation of ultrasound-triggered bubble dynamics to show bubble expansion during the negative pressure cycle and bubble compression during the positive pressure cycle. Not drawn to scale. b) For a fixed number of ultrasound bursts (100 or 200), the treatment paradigms consist of either a single pulse (N=20, PRI=1ms, duration 100, 200 or 300 ms) or a sequence with a 1s delay (N=20, PRI=1ms, duration 25 ms; repeated either 4, 8 or 12 times at Δt = 1s). These were investigated with a view towards enhancing endothelial cell permeabilization. c) Beam profile (normalized to peak – in dB) of the single-element transducer (1 MHz) used in this study obtained via hydrophone measurements. See text for details. d) The transmission loss at the focus of the beam through the culture chamber employed in this study. The solid (blue) curve denotes the beam unimpeded, and the red (dashed) curve depicts transmit pressure with the chamber in the beam path. Transmission loss is estimated at 5%.

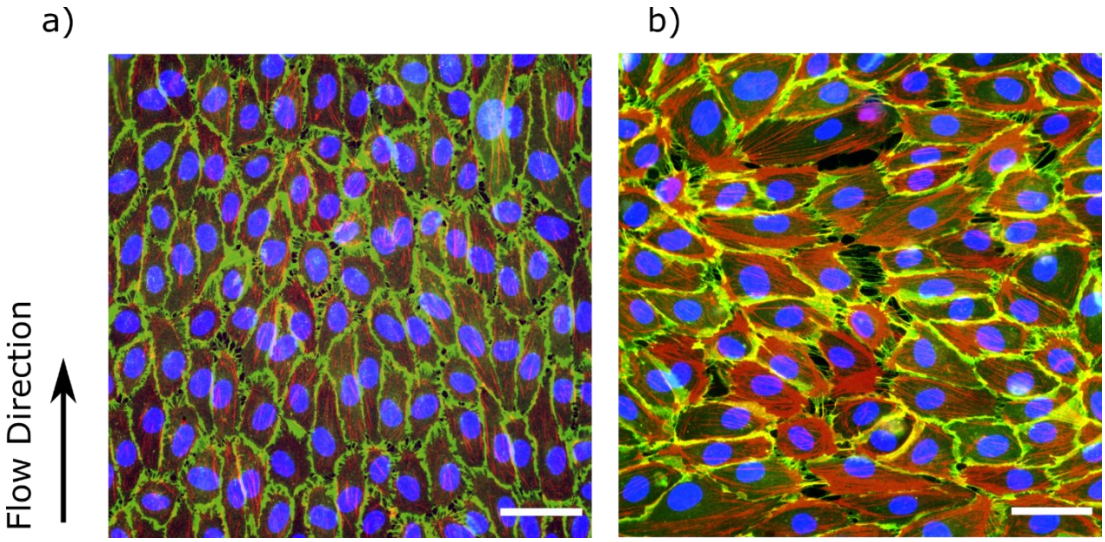

Figure 3.3: The presence of shear flow affects the physiology of vascular endothelial cells. a) An endothelial monolayer (HUVEC) was cultured either a) subjected to laminar flow (9 dyn/cm²) for seven days or b) statically under the same confluency and duration. Actin filaments were stained in red (phalloidin), PECAM-1 in green, and DAPI in blue. Our results show that shear flow leads to the cellular orientation of endothelial cells in the direction of flow over time, as well as developing a more physiologically relevant cell-to-cell contact regime, whereas statically cultured cells displayed large extracellular gaps, disorganized directionality and weak (lower in magnitude) cell-cell contacts. These effects are similar for HBEC-5i (data not shown). The scale bar is 50 µm.

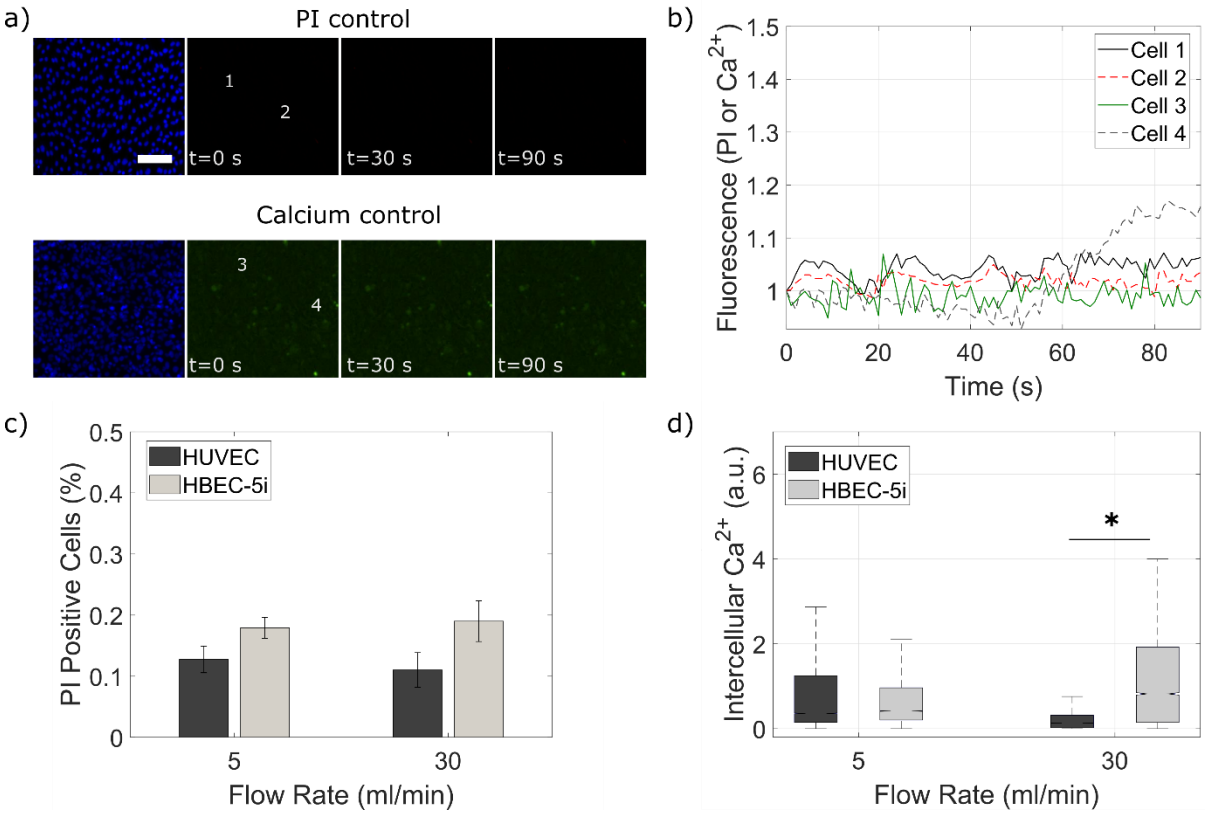

Figure 3.4: Control (sham) experiments reveal fluid flow alone does not alter endothelial permeability and modulates Ca^{2+} in HBEC-5i endothelial cells only. a) Representative examples of the raw time-lapse microscopy data from a HUVEC dataset under a flow rate of 30 ml/min. Hoechst stain (blue) highlights cell monolayer nuclei, and (top) propidium iodide uptake (PI; in red) is used as a surrogate for plasma membrane permeability while (bottom) Ca^{2+} influx (green) is monitored by Fluo4-AM. Scale bar is 50 µm. b) The PI and Ca^{2+} uptake curves for the four cells denoted in panel a) gives a sense of the baseline level of these metrics. Aggregate data for c) permeability (n>60000 cells per endothelial type) and d) calcium influx (n>30000 cells per endothelial type). Note that the permeability data is presented as mean ± standard deviation, while the Ca^{2+} data is represented as medians and interquartile ranges. See text for details. While there are slight differences between endothelial lines and flow rates, the global quantification reveals no more than 0.2% of cells are permeabilized under flow itself (note that this inherently includes systematic errors associated with the offline image processing). While there is no effect of fluid flow on intracellular Ca^{2+} signal distribution for HUVEC cells, there is for HBEC-5i (p<0.001). Note that all of the experiments conducted with ultrasound (Fig. 5-8) are highly significantly different with respect to its respective control dataset shown in this figure.

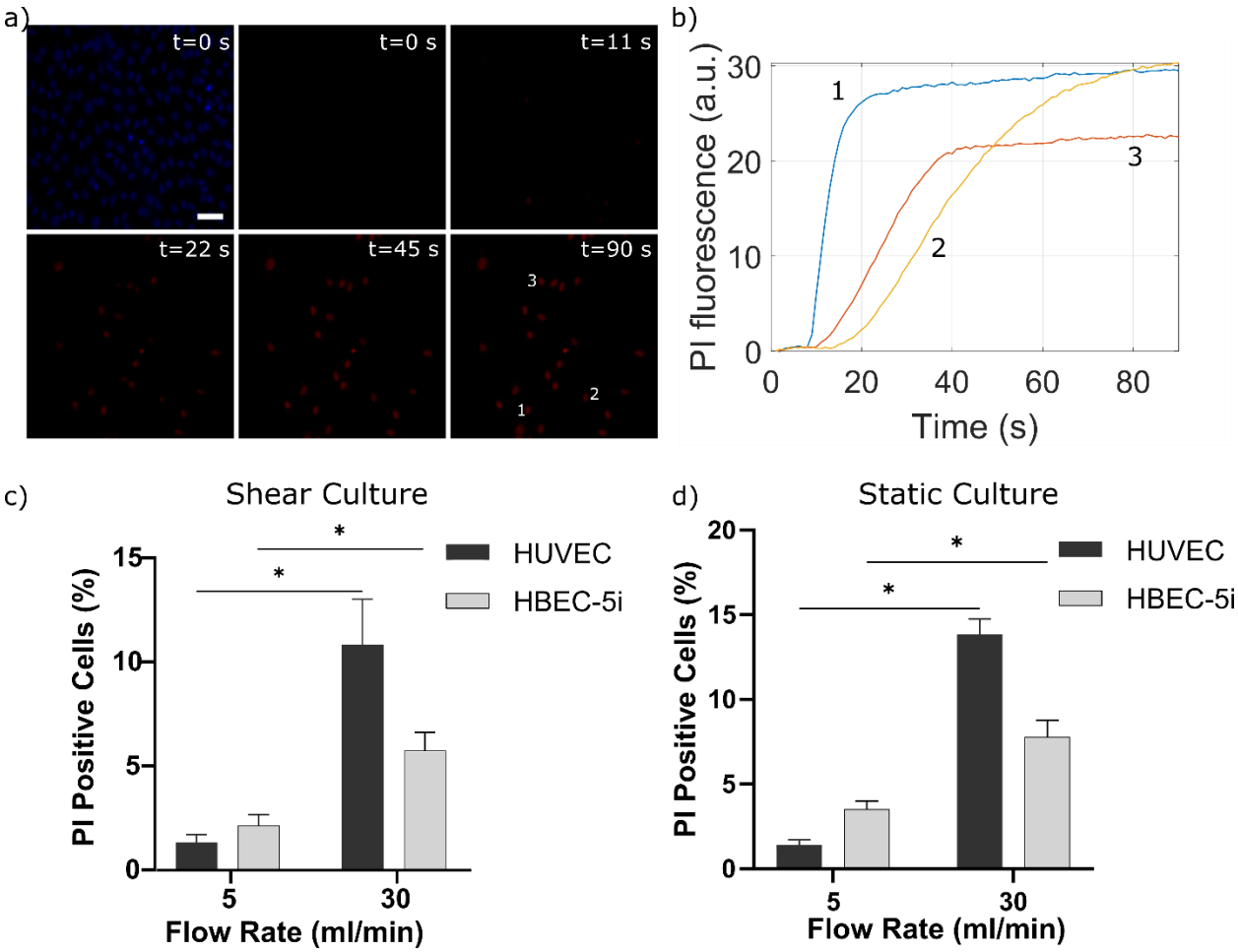

Figure 3.5: Faster microbubble flow increases ultrasound-mediated endothelial cell permeabilization. a) Representative example of the raw time-lapse microscopy data during real-time ultrasound-mediated endothelial cell permeabilization. Hoechst stain (blue) highlights cell monolayer nuclei, and propidium iodide uptake (PI; in red) is used as a surrogate for plasma membrane permeability. Ultrasound is delivered at approximately the 10 second mark for a duration of 2 seconds. Scale bar is 50 µm. b) The PI uptake curves for the three cells denoted in panel a). Note that the shape of these curves, including the plateau level and initial slope, is related to the perforation characteristics and the distance between the perforation and the nucleus (see text for details). In aggregate, either HUVEC (black bars) or HBEC-5i (grey bars) were pre-seeded in flow chambers for two days c) under unidirectional flow or d) under static conditions. Under an identical acoustic stimulus, microbubbles flowing at 30 ml/min led to a substantial increase in cell membrane perforation (8.2-fold, $p<0.001$; 2.7-fold, $p<0.003$ for HUVEC and HBEC-5i respectively) as compared to microbubbles flowing at 5 ml/min. This effect was independent of cell seeding state, showing very similar results for cells cultured statically (9.7-fold, $p<0.001$; 2.2-fold, $p<0.001$ for HUVEC and HBEC-5i respectively). Asterisks denote statistical significance.

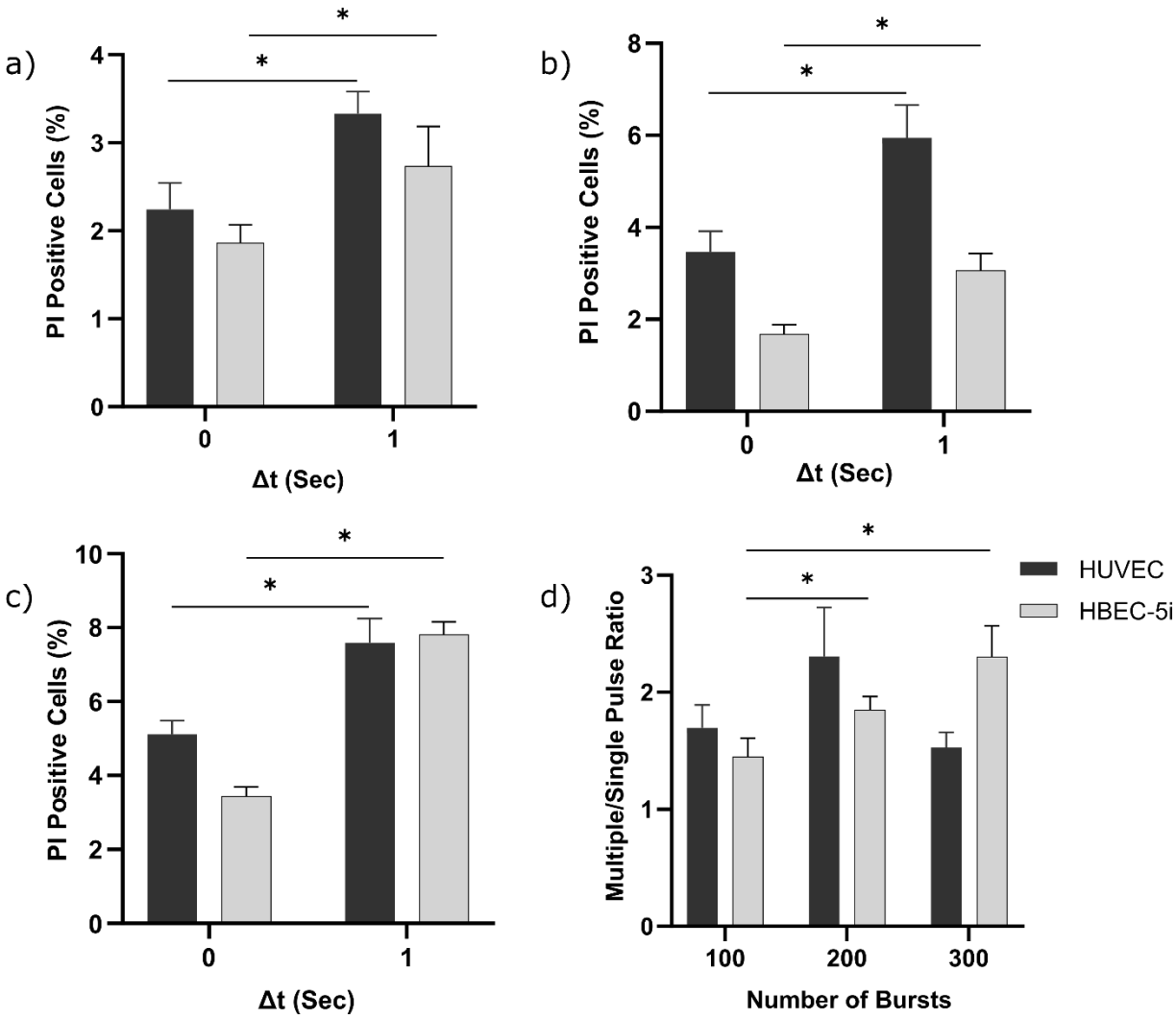

Figure 3.6: Multiple short pulses rather than a single long pulse ultrasound significantly increase endothelial cell permeabilization. The comparison of the percentage of directly perforated cells (PI positive cells) between short and long pulse ultrasound with a) M=100 bursts, b) M=200 bursts and c) M=300 bursts for HUVEC (black) and HBEC-5i (gray) endothelial cells. A time delay Δt=0 is equivalent to pulsing scheme 1 in Fig. 2. This represents a one long pulse with a PRI of 1 ms (and thus a duration of 100, 200 or 300 ms respectively). A time delay Δt=1s (pulsing scheme 2 in Fig. 2) is characterized by 25 bursts (PRI = 1ms) spaced by Δt=1s and repeated for 100, 200 or 300 pulses, respectively. Microbubbles were diluted 1:500 in cell culture media. Multiple repeated short pulses, either 25ms repeated 4, 8, or 12 times (panels a), b) and c) respectively) enhanced perforation percentage in both HUVEC and HBEC-5i. All comparisons were statistically significant for either type of endothelial cell. d) The ratio of multiple short pulses to single long pulse ultrasound increased as the total number of bursts was raised. A value of 1

here indicates no difference, and a value above 1 indicates a more efficient sequence at generating PI positive cells.

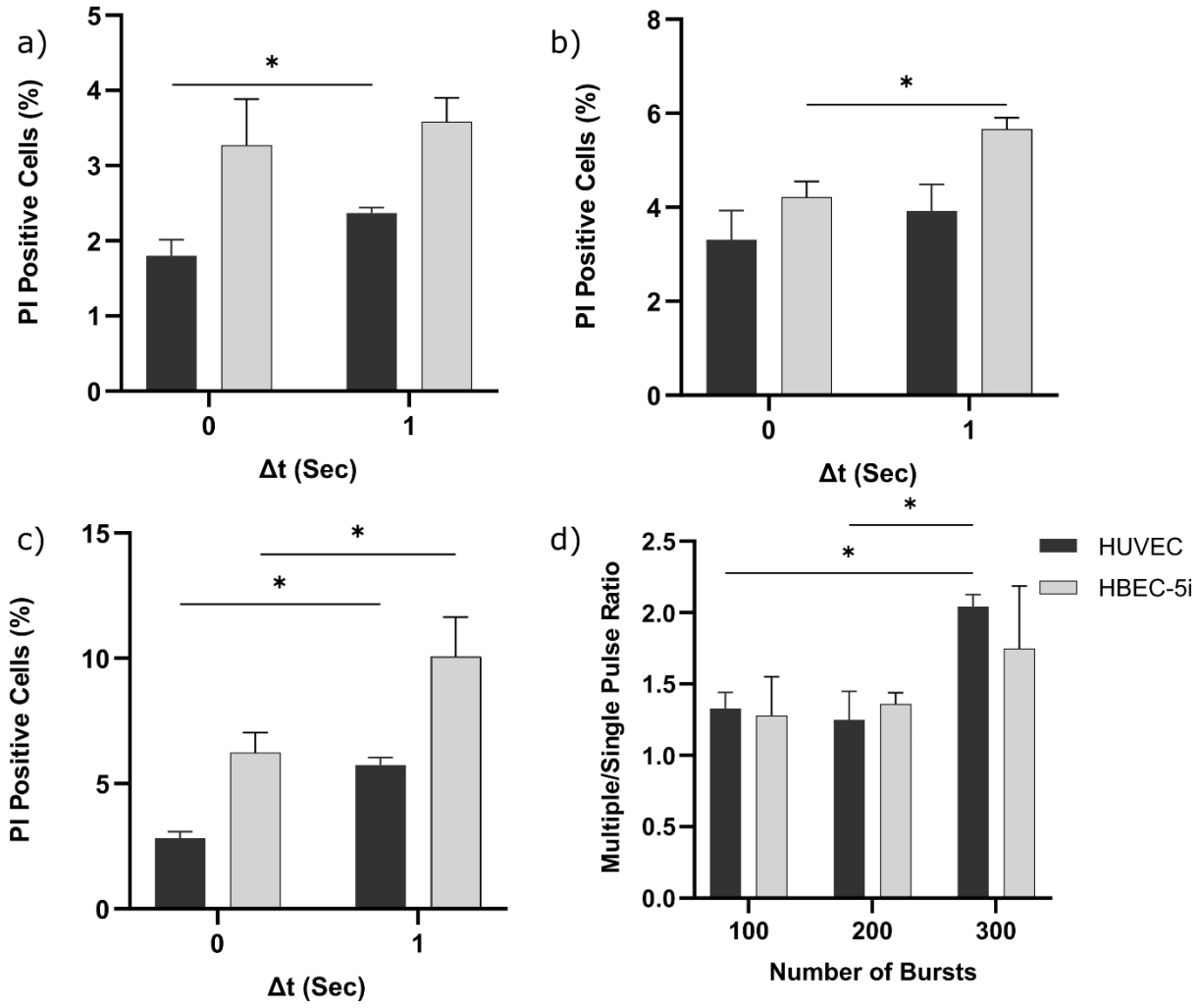

Figure 3.7: Multiple short pulses rather than a single long pulse ultrasound significantly increases endothelial cell permeabilization. The comparison of the percentage of directly perforated cells (PI positive cells) between short and long pulse ultrasound with a) *M*=100 bursts, b) *M*=200 bursts and c) *M*=300 bursts for HUVEC (black) and HBEC-5i (gray) endothelial cells, along with d) the ratio between multiple short pulses to single long pulse. This is the same experiment as that conducted in Fig. 6, however with microbubbles diluted at 1:1000 in cell culture media. Note that, as expected, the same trends persistent albeit with less absolute membrane permeabilized cells.

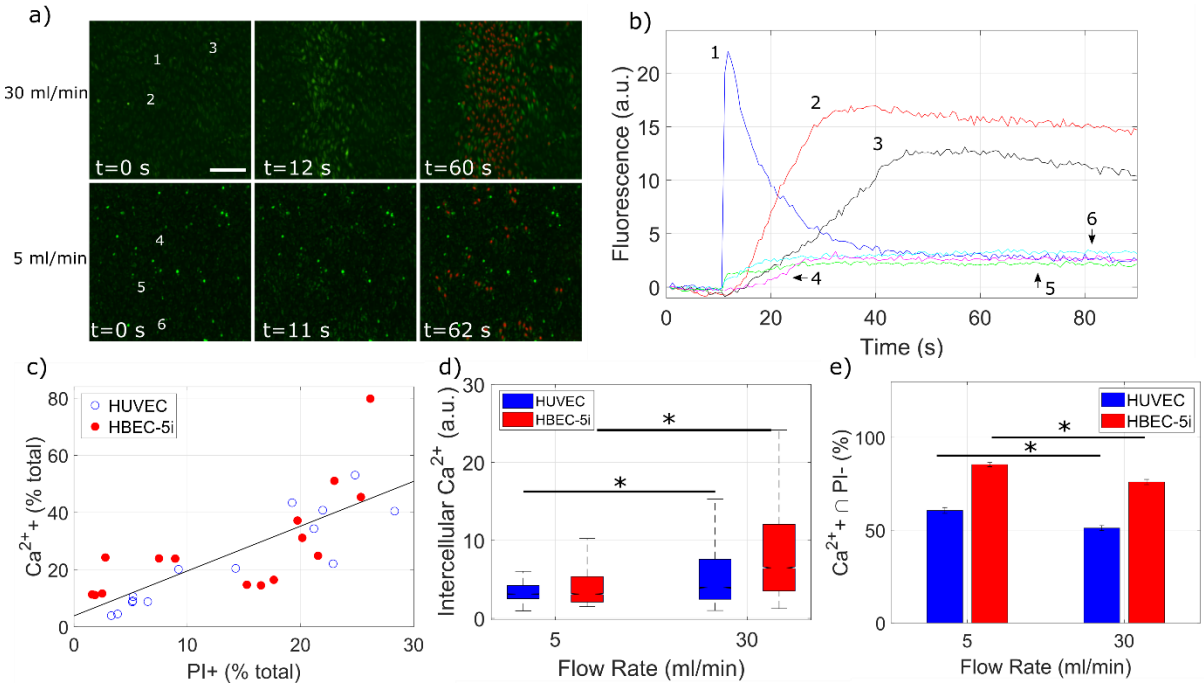

Figure 3.8: Fluid flow rate affects ultrasound induced intracellular Ca^{2+} transients in endothelial cells. Ultrasound-stimulated microbubbles triggers transient influx of Ca^{2+} from the extracellular environment in both HBEC-5i and HUVEC, subjected to either flow rates of 5 or 30 ml/min. a) Representative Ca^{2+} fluorescence images (HBEC-5i) during treatment under (top) 30 ml/min and (bottom) 5 ml/min. Green signal is proportional to Ca^{2+} concentration, and the last frame overlays the PI signal taken at the end of the recording (90 s post treatment). Note that the absolute number of Ca^{2+} positive cells is clearly larger from treatment under the faster flow rate. Scale bar is 1 mm. b) The intracellular Ca^{2+} trace over time for the six cells depicted in the panel a). c) As expected, the extent of Ca^{2+} positive cells is directly proportional to the extent of direct membrane permeabilization (PI+ cells) for both endothelial cell lines examined (r=0.78; p<0.0001). d) The maximum intracellular Ca^{2+} intensity was significantly higher for those treated under 30 ml/min flow than for 5 ml/min (p<0.0001, Mann-Whitney test for both cell lines) e) For both HUVEC and HBEC-5i endothelial cells, the percentage of Ca^{2+} cells that did not exhibit direct membrane perforation (Ca^{2+}+ ∩ PI-) was higher than those Ca^{2+} positive cells that did (p=0.0006; p=0.0003). This suggests that the 'remote' effect of microbubble-mediated endothelial treatment (affecting the local cellular environment of those cells not in direct contact with a microbubble) is increased at slower flow rates.

4. Shear stress preconditioning and microbubble flow pattern modulate ultrasound-assisted plasma membrane permeabilization

Expanding on chapter 3 findings, manuscript published as: Memari et al. Materials Today Bio (2024) uses the same ultrasound setup described in previous chapter to further evaluate cell permeabilization under varied flow profiles. Given that the flow patterns vary across different anatomical sites, this study explores the influence of various microbubbles flow patterns either laminar, pulsatile or oscillatory flow on ultrasound-mediated endothelial cell permeabilization. Additionally, it investigates the effects of shear flow preconditioning on endothelial cell perforation.

4.1. Introduction

Atherosclerosis stands as a chronic inflammatory disease, characterized by thickening of large vessels due to the accumulation of low-density lipids (LDL), trans-endothelial migration of immune cells into the arterial walls, and the development of fatty plaques[316]. As the plaque progresses, it can begin to erode or rupture, resulting in severe clinical consequences including myocardial infarction, peripheral artery disease, and ischemic stroke. Indeed, this condition serves as a fundamental basis for the majority of cardiovascular disease (CVD) and ranks among the leading causes of death worldwide[317]. Although the multifactorial nature of the disease (*e.g.* hypercholesterolaemia) is systemic, atherosclerotic plaques preferentially develop in regions with disturbed blood flow patterns[313]. The current standard of treatment for atherosclerosis includes systemic administration of cholesterol-lowering agents such as statins (HMG-CoA reductase inhibitors) and anti-platelet drugs, alongside surgical interventions for severe cases of the disease[318]. However, given the limited efficacy of current treatments and the inability to prevent the reoccurrence of the disease, there is an urgent need for finding novel strategies to target the underlying causes of atherosclerosis. To this end, there has been an influx of investigations into the use of pharmacological agents that target inflammation directly, and these have shown excellent pre-clinical results (*e.g.*[319]). Leveraging this success, recent clinical data has highlighted the direct benefit of targeting the inflammatory pathway on patient outcomes[320], [321]. Perhaps the most successful of which is the CANTOS (Canakinumab Anti-Inflammatory Thrombosis Outcome Study) trial[322], in which the systemic delivery of the neutralizing IL-1β antibody canakinumab (50-150 mg) was shown to reduce the risk of a first major adverse

cardiovascular event (MACE) by 15% in patients with prior myocardial infarction, along with a dose-dependent reduction in IL6 (19-38%) and C-reactive protein levels (26-41%). Despite these exciting results, canakinumab was not approved by the FDA for this indication due to an increased level of fatal infections, suggesting the need for robust spatial targeting of the therapeutic antibody.

In designing an efficient drug delivery system for atherosclerosis, it is crucial to appreciate how complex blood flow patterns at the atherosclerotic prone regions influence endothelial permeability and susceptibility to treatment. Indeed, endothelial cells detect shear flow patterns via mechanosensors, including membrane receptor kinases, integrins, ion channels, intercellular junctions, and cytoskeleton components[323]. The regulation of endothelial gene expression via such mechanosensors in response to local shear stress is considered a major deterministic factor in atherosclerosis susceptibility[313]. Endothelial cells subjected to sustained laminar or unidirectional pulsatile flow correlate with transcription profiles considered protective against atherosclerosis (*e.g.* downregulation of pro-inflammatory genes). However, at the vascular regions with complex geometry such as vessel branch points, bifurcation and curved areas that result in uneven or disturbed flow, endothelial cells are exposed to low shear stress with high temporal gradients including oscillatory shear[324]. These more complex flow profiles are correlated with pro-inflammatory and atherogenic phenotypes, resulting in an increased endothelial cell turn over rate, endothelial permeability, and vascular bed impairment[325]. It is therefore of interest to consider the influence of shear stress preconditioning on endothelial cell permeability and integrity. In recent decades, various drug delivery methods have been explored for targeted deposition of therapeutic molecules within the context of CVD, including atherosclerosis. Of particular interest is the emergence of ultrasound-assisted therapy, as echocardiography already plays a key role in the diagnosis and management of patients with CVD. Contrast ultrasound, which employs ultrasound contrast agent microbubbles, is approved for use for left ventricle opacification in both adult and pediatric patients and used in many off-label clinical cardiac applications (*e.g* myocardial perfusion, neovascularization imaging)[53]. Intravenously injected microbubbles are small (1-8 μm) gas-core microspheres, stabilized by a thin flexible shell composed typically of phospholipids, that remain intravascular due to their size. Exposure to diagnostic ultrasound results in their nonlinear vibration which enables the detection and separation of their echo from that of the surrounding tissue[326]. Beside diagnostic applications, microbubbles have shown tremendous therapeutic potential[327], the most clinically advanced

application of which is the reversible opening of the blood-brain-barrier for targeted drug delivery[328], [329]. Indeed, depending largely on microbubble physics and the surrounding tissue properties, oscillating ultrasound-stimulated microbubbles – which result in local, rapid fluid motion within the vicinity of the bubble itself - can exert targeted bioeffects via the application of shear and circumferential stress to neighboring vessels and tissues, ranging from reversible cell permeabilization[150], [152], modulation of intracellular Ca^{2+} flux[330], [331], enhanced blood flow perfusion[161], [332], and modulation of inflammatory responses[56]. Given this context, here we aim to investigate the influence of flow pattern and magnitude on ultrasound-assisted endothelial cell permeabilization, including laminar, non-reversing pulsatile, and reversing oscillatory conditions. First, we examine the effect on shear preconditioning on the susceptibility of endothelial cells towards ultrasound-enhanced permeability, with a particular focus on the influence of shear-mediated cytokine and chemokine expression. Next, we investigate how microbubble fluid flow patterns during ultrasound treatment alters its efficiency, motivated by the intrinsic differences in flow profiles at different anatomical sites, including those in atherosclerotic prone regions.

4.2. Materials and Methods

4.2.1. General Cell Culture

Human umbilical vein endothelial cells (HUVEC, C2519A; Lonza, Walkersville, MD, USA) were cultured in endothelial cell growth medium (EGM-2; CC3162, Lonza), and maintained at 37℃ with 5 % CO2 and 95 % air atmosphere. Independent of culture condition, endothelial cells were cultivated in collagen-iv coated µ-Slide I Luer type with a single channel (Ibidi, Gr¨afelfing, Germany) at a density of 120,000 cells/cm^2. The slides used in this study have a growth surface area of 2.5 $cm^{2,}$ with channel heights ranging from 0.4 to 0.8 mm. Based on the experiment, endothelial cells were cultured either statically or under flow conditions for two days.

4.2.2. Flow Apparatus

For fluid flow-based experiments, the ibidi fluidic system, consisting of fluidic units, pump system and flow control software, was employed. For all experiments, the fluidic units were mounted with a yellow-green perfusion set (10 ml syringe reservoirs, filters, 1.6 mm silicon tubing), and connected to a pump system to generate the fluid flow – ranging from laminar, non-reversing pulsatile, and reversing oscillatory flow patterns (Fig. 1). The ibidi flow software was used to

regulate the flow parameters and create the fluid flow profiles. The shear-flow was calculated using the flow control software, given by $\tau = \alpha\eta \cdot \Phi$, where τ is shear stress (dyne/cm²), η is dynamical viscosity (dyne·s/cm²), Φ is the flow rate of the perfused medium (ml/min), and α is a constant that is dependent on the chamber geometry.

Prior to cell cultivation under flow, a unidirectional flow was generated using the ibidi pump system for at least 30 minutes to remove any air bubbles in the perfused medium. To cultivate cells under flow, independent of the flow pattern, an augmented gradient of fluid flow was applied for two hours to allow the cells to adapt to the flow condition and prevent cell detachment from the slide's growth surface. While laminar flow needed only one fluidic unit, pulsatile flow requires two fluidic systems: primary and secondary units (see Fig. 1a). The primary unit was mounted with a perfusion set and was used to generate a laminar flow with a long switching time to provide a lasting circulation of fluid in the fluidic system. Additionally, the secondary unit without any perfusion set was used to generate pulsations by interrupting the laminar flow with a frequency of either 0.5 or 1 Hz. The flow control software creates pulsations by periodically changing the flow rate during the short switching time of the secondary unit but with a constant flow direction (non-reversing pulsatile flow). The third flow pattern investigated in this study was oscillatory flow, created using two fluidic systems with separate perfusion sets but interconnected air pressure tubing (reversing oscillatory flow). Similar to the pulsatile flow, the primary unit generated a laminar flow, whereas the secondary unit applied oscillations by reversing the flow direction alternatively with a frequency of either 0.5 or 1 Hz (1s or 0.5s switching time, respectively).

4.2.3. Experimental Protocol

The ultrasound delivery platform has been reported previously[149]. Briefly, a customized acoustically coupled inverted microscope (Ti2-A, Nikon, Melville, New York, USA) was developed by fixing a compatible support and coupling cone for the ultrasound transducer (single-element 1 MHz, unfocused, diameter 2a = 12.7 mm; A303S-SU, Olympus, Waltham, MA, USA) on the microscopy platform. The transducer was fixed at a 45° to the normal and 27 mm distance from the cell monolayer surface. With this setup, the acoustic beamwidth at the microbubble-cell interface is approximately 3.5 mm. The transducer was driven by a signal generator (Tektronix, AFG31052 series, Chicago, USA) and amplified by a 150 W power amplifier (Amplifier research, Model: 150A 100B, Mississauga, USA).

4.2.4. Fluorescence Markers

For real-time fluorescence imaging, cell nuclei were stained using Hoechst dye (Thermo Fisher) at a dilution of 1:500 v/v and maintained at 37℃ for 10 minutes, followed by washing with PBS (3x). To visualize cell permeabilization induced by ultrasound-stimulated microbubbles, propidium iodide (PI; 450 µM, P1304MP; Molecular Probes) was used as a real-time marker. This is a standard stain to differentiate permeabilized from non-permeabilized live cells since it is impermeable to cells with intact plasma membranes. Upon penetration into the cells, it binds to DNA, becoming fluorescent by shifting the fluorescence excitation/emission from 493/636 to 535/617 nm. Here, we employ it as a surrogate drug and real-time marker for ultrasound-assisted enhanced endothelial permeabilization, as has been done previously[333]. As it does not fluoresce within the bulk solution, real-time recording during treatment of time-dependent cellular permeability is possible due to the fact that the fluorescence intensity enhances only as it becomes intracellular.

4.2.5. Immunohistochemistry

To assess the effect of cell cultivation conditions on cell physiology, the endothelial cells were seeded in the 0.4 mm chamber slides either statically or under a pulsatile flow profile. Two days post-cultivation, cells were fixed using 2% paraformaldehyde for 30 minutes. Subsequently, cells were permeabilized using 0.1 % Triton X100 for 10 minutes, followed by blocking the non-specific interactions with milk powder plus 5 % bovine serum albumin (BSA) for 45 minutes, washed with BSA (5x). Next, cells were incubated with mouse anti-CD31 (PECAM-1) monoclonal antibody for 1 h at room temperature, followed by washing (5x) with BSA to remove the unbound primary antibodies. We are interested in PECAM-1 due to its known role as a mediator in atherosclerosis[334], [335]. Afterward, cells were incubated with Alexa Fluor 488-conjugated donkey anti-mouse IgG (A21202, Invitrogen) for one hour, and washed (5x) with BSA. Actin filaments were counterstained with Alexa fluor 647-labeled phalloidin (A22287, Invitrogen) with a dilution of 1:400 v/v for 20 minutes and the unbound phalloidin was removed using washing (5x) with PBS. Cells were stained with either primary or secondary antibodies alone as negative controls. Cell nuclei were stained with DAPI with a dilution of 1:500 v/v. All the immunostaining steps were performed at room temperature. At least five random regions from each slide were imaged using a four-channel fluorescence inverted Nikon microscope with a 40X objective lens.

4.2.6. Shear Stress Preconditioning on Ultrasound-assisted Membrane Permeabilization

To examine the effect of cell culture condition on cell susceptibility to sonication, endothelial cells were cultured in μ–Slides with a 0.8 mm channel height, either statically or under pulsatile flow for two days prior to the ultrasound treatment. For cultivation under pulsatile flow, cells were seeded statically for two hours, followed by an augmented gradient of shear flow up to 8 or 16 dyne/cm^2 with a 1 Hz pulsatile frequency. For the ultrasound treatment, cell-seeded slides were connected to a fluidic system, followed by perfusion of the chamber slides with a cocktail consisting of Definity^{TM} microbubbles (1:500 dilution) and PI in culture media under pulsatile flow. Independent of culture conditions, cells were treated under the same two pulsatile flow regimens as they were cultured with: either at 8 or 16 dyne/cm^2 at a 1 Hz pulsatile frequency. After incubating the slide under flow for at least 30s to ensure a homogeneous distribution of microbubbles, each slide was sonicated (1 MHz frequency, 20 cycles, 1 ms pulse repetition frequency, 300 kPa peak-negative pressure) for a treatment duration of 4s, while the flow of microbubbles was maintained throughout the ultrasound treatment. Simultaneously, fluorescence microscopy recordings were obtained for 90s. The fluorescence microscopy recordings were started 8s before sonication to obtain information on the extent of baseline PI signal prior to sonication. Four non-overlapping locations from each sample were acquired (total growth area per slide of 250 mm^2), and the percentage of cells that were permeated under US and microbubble therapy was quantified using in-house software in MATLAB. The selection of these acoustic conditions was based on ensuring no cell detachment while exhibiting reliable measurable signal from the microscopy system over the range of flow rates employed in this study; following our previous work[149]. Further, the acoustic field in free space as well as the loss of signal due to the presence of the chamber slide (~5% attenuation of signal) was measured using a hydrophone (Onda Corp., Sunnyvale, CA, USA, HGL-200); as previously reported[149]. Despite this, we do expect some proportion of reflected ultrasound within the chamber itself, resulting in the potential for an uneven acoustic field. Given that results and interpretations therein are relative (*i.e.* the independent variables are shear preconditioning, flow magnitudes, and flow patterns all under a fixed ultrasound condition and acoustic field), we do not foresee this as a confounding factor. All experiments were completed within 10 minutes after commencing flow with the diluted microbubble agent.

4.2.7. The Effect of Shear Stress on Endothelial Cytokine Expression Profile

To assess the effect of pulsatile flow on cytokine release from endothelial cells, cells were seeded under the same pulsatile conditions as for the previous section (8 or 16 dyne/cm^2, 1 Hz). Simultaneously, cells with the same confluency were cultured statically as control (to mimic ischemic conditions). Two days post-cultivation, 100 µl cell culture media were collected from each chamber slide, with two repeats for each condition. To examine the cytokine profile, a multiplex assay was used to analyze 96 human cytokines and growth factors (human immunology panel, Bio-Rad Laboratories, Hercules, CA). This multiplex assay functions via fluorescent detection of any array of color-coded beads conjugated to a specific capture antibody. The data was analyzed via a bead analyzer (Bio-Plex 200, Bio-Rad), which combines 2 lasers and high-throughput fluidics.

4.2.8. The Influence of Microbubble Perfusion Pattern on Ultrasound-assisted Permeabilization

To exclude the effect of cultivation conditions on the efficiency of US-mediated therapy, endothelial monolayers were cultured statically in chamber slides for two days before ultrasound delivery. First, the impact of pulsatile flow on microbubble-assisted endothelial cell perforation was assessed by connecting the slides to fluidic systems with either laminar or pulsatile flow (15-30 ml/min, 0.5-1 Hz). To further explore physiologically relevant flow conditions, a subset of the slides was connected to the secondary flow unit with an oscillatory flow profile; consisting of either a flow rate of 8 or 16 ml/min and an oscillation frequency of 0.5 or 1 Hz. In both pulsatile and oscillatory scenarios, four non-overlapping regions were sonicated with the same ultrasound conditions as given above, and real-time, simultaneous video recordings with two fluorescence channels for Hoechst and PI were recorded. The Hoechst channel was employed to determine the total number of cells within the field of view. To ascertain the overall count of permeabilized cells, in-house MATLAB software was written to quantify the extent to which cells were permeated over the 90s recording. As a fluid flow condition control, another subset of the slides was connected to the primary unit, co-perfused with microbubbles and PI under laminar flow and sonicated with the same ultrasound conditions.

4.2.9. Justification of Shear Stress Magnitudes

In-vivo shear stress magnitudes have been reported to range from 10-70 dyne/cm^2 in healthy arteries, 1-6 dyne/cm^2 in veins, and ±4 dyne/cm^2 in atherosclerosis-prone arterial regions[324], [336]. To examine the role of shear-stress preconditioning in the context of ischemic heart disease, the selection of shear magnitudes was chosen to represent flow conditions within ischemic (static; 0 dyne/cm^2), borderline (8 dyne/cm^2) and the lower range of healthy vasculature (16 dyne/cm^2). The flow velocities used to examine non-reversing pulsatile microbubble perfusion on statically cultured endothelial cells - stated here as flow rates instead of shear stress magnitudes due to the short perfusion time - do correspond to regions spanning recently re-perfused arterial vessels (~4 to ~8 dyne/cm^2). Finally, the dataset confirming the effects of reversing oscillatory shear to mimic disease-state disturbed flow are within the atherosclerosis-prone range (±2 and ±4 dyne/cm^2 respectively[325], [337].

4.2.10. Statistical Analysis

All data were analyzed using GraphPad prism and are presented as mean ± SEM. The fluorescence microscopy videos were analyzed using in-house software in MATLAB to quantify the percentage of cell perforation. The endothelial permeabilization datasets were repeated on at least five independent samples for each condition. The PECAM-1 mean fluorescence intensity was quantified using ImageJ from at least 8 random fields of view. Two-tailed, unpaired two-sample Student's t-tests were performed to determine the significance in comparison between treatment groups, using the Bonferroni multi-comparison correction when appropriate. Correlation coefficients and their associated statistics were calculated in MATLAB. For all datasets, a *p*-value of <0.05 was assumed to be statistically significant.

4.3. Results and Discussion

Our previous work confirmed that the flow rate of laminar microbubble perfusion greatly influenced endothelial permeability and calcium intracellular signaling[149]. Here, we are examining the influence of shear-stress preconditioning, non-laminar microbubble perfusion, and their associated correlations as detailed below.

4.3.1. Shear Stress Preconditioning on Ultrasound-assisted Membrane Permeabilization

Figure 2a depicts a fluorescence microscopy example of how endothelial culturing condition influences cell physiological characteristics, such as morphology and cell-to-cell contact. As illustrated in Fig. 2a, statically cultured cells exhibited a heterogeneous orientation and morphology, characterized by large extracellular gaps due to the discontinuous distribution of intercellular junctional proteins. Conversely, cultured cells under pulsatile flow demonstrated a relatively aligned orientation in the direction of flow, more homogenous morphological features, and minimal extracellular gaps between cells. More specifically, these microscopy images highlight the effect of pulsatile flow cultivation on the expression of PECAM-1 (shown in green). PECAM-1 expression was highly heterogeneous in cells cultured statically, exhibiting regions of varying intensity. Under pulsatile flow, the expression of PECAM-1 became more pronounced as the shear-flow increased from 8 to 16 dyne/cm^2 at 1 Hz pulsatile frequency, as quantified in Fig. 2b ranging from 1.8-2.5-fold increase under shear-flow than static culturing (p<0.01). Note here that the static culturing condition is denoted as 0 dyne/cm^2. Figure 2 also shows how cultivation condition affects human endothelial cell sensitivity to ultrasound-mediated cell perforation. Here, we are examining the effect of endothelial culture preconditioning (static and pulsatile flow at either 8 or 16 dyne/cm^2 with 1 Hz pulsatile frequency) on the resulting endothelial susceptibility to ultrasound and microbubble treatment given the same acoustic stimulus. We investigated two different flow treatment regimes, with microbubbles circulating over the endothelial monolayer under pulsatile flow of 8 or 16 dyne/cm^2 to match the culturing conditions. Figure 2c depicts a representative example of the time-lapse microscopy data of preconditioned endothelial monolayers (static [top] or under a pulsatile flow of 8 dyne/cm^2 [bottom]) undergoing microbubble therapy under the same treatment conditions, where the red denotes enhanced permeability as reported by intracellular PI entry. The first frame from each condition shows a Hoechst staining of the cell nucleus, which was used to quantify the number of cells in the field of view. Figure 2d&e summarize our findings. With microbubbles perfusing the endothelial monolayers under a pulsatile flow pattern of 8 dyne/cm^2, those that were preconditioned under shear-flows of 8 or 16 dyne/cm^2 exhibited an augmented enhancement of ultrasound-assisted membrane permeability by 1.44 and 2.04-fold (p<0.005) in comparison to those statically cultured, exhibiting an approximately linear trend (Fig. 2d). Further, those subjected to microbubble treatment under a pulsatile flow rate of 16

dyne/cm^2 similarly exhibited an increased sensitization to permeabilization based on shear-stress preconditioning, increasing by 1.98 ($p < 0.001$) with 8 dyne/cm^2 and 1.21-fold with 16 dyne/cm^2 compared to static culturing, respectively. It is well established that endothelial cells exposed to prolonged fluid shear stress elongates their morphology to the direction of flow, in agreement with the results presented here. PECAM-1 is an established mediator of atherosclerosis and has been shown to influence the initiation and progression of atherosclerosis both negatively and positively, depending on the vascular site[338], [339]. Further, PECAM-1 expression is correlated with increased vascular integrity[339] and changes in endothelial plasma membrane stiffness[340]. From a purely physical perspective, this change in cell morphology should increase the available cellular surface area – and thus probability for microbubble-cell interactions - for ultrasound-assisted permeabilization. In addition to this cell area-based argument, the plasma membrane biomechanics for a given endothelial cell are altered when pre-exposed to fluid shear, one major effect of which is to induce an increase in plasma membrane fluidity as compared to static controls[341], [342]. Increased membrane fluidity is correlated with increased passive cellular permeability[343], and fluid flow shear preconditioning has been demonstrated to increase the baseline levels of human endothelial cell cellular permeability due to this average increased inter-phospholipid distance[342]. While not yet thoroughly investigated, there is some evidence that ultrasound-assisted cell permeabilization is facilitated when plasma membrane fluidity is increased[344], and thus consistent with the present findings. These results indicate that, overall, subjecting cells to a pulsatile flow pattern considerably enhances the endothelial cell sensitivity to the ultrasound-stimulated microbubbles.

4.3.2. The Effect of Shear Stress on Endothelial Cytokine Expression Profile

To further investigate the relationship between shear preconditioning and susceptibility to ultrasound-mediated permeabilization, we assayed differential endothelial cell cytokine expression. Our findings indicate that cell cultivation under pulsatile flow at 8 and 16 dyne/cm^2 significantly altered the expression of 23 and 25 cytokines/growth factors, respectively, as compared to the statically cultured monolayers. Significance here is quantified as at least a 2-fold change that meets the threshold significance level of $p<0.05$. Figure 3a&b illustrate the volcano plots containing all the analytes with a concentration within the detectable range of the standard curve (8 and 16 dyne/cm^2, respectively). The analytes with out-of-range concentration, either below or above the standard curve, were excluded from the volcano plots. In these figures, each

of the secreted molecules is represented by a circle. Those that exhibited at least a statistically significant 2-fold increase ($log_2 = 1$) or decrease ($log_2 = -1$) compared to static controls are illustrated in red along with nonsignificant and/or smaller changes denoted in blue. The analytes exhibiting large magnitude differential secretions are then depicted for each flow condition in Fig. 3c&d. It is interesting here to broadly categorize the cytokine functions within two major groups: angiogenesis and inflammation. Indeed, as expected, induction of prolonged flow significantly upregulated pro-angiogenesis factors, including vascular endothelial growth factor-A (VEGF-A), epidermal growth factor (EGF), and fibroblast growth factor-2 (FGF-2) - see Fig. 3e. Among these factors, the largest magnitude change is VEGF-A, which was upregulated by 10.7-fold and 34.5-fold (3.43 and 5.11-fold in log_2 units) under preconditioning of pulsatile flow of 8 and 16 dyne/cm^2 compared to static control, respectively. VEGF-A is a well-known modulator of vascular development and angiogenesis via its interaction with its endothelial receptor (mainly VEGFR2, although it also binds to VEGFR1). VEGF-A and other pro-angiogenic factors (*e.g.* FGF-2) have been identified as key endothelial survival signals involved in the maintenance of endothelial homeostasis and vascular integrity[345], the disruption of which helps mediate atherosclerosis[346]. Indeed, autocrine VEGF signaling – as is the case here – is known to play a critical role in maintaining endothelial cell viability[347]. It is well understood that VEGF-A, along with other pro-angiogenic markers, can disrupt endothelial cell-cell contacts (*e.g.* tight junctions, adherins), change endothelial cell morphology, and increase vascular leak[348]. Further, prolonged exposure of endothelial cells to VEGF-A can induce the formation of small pores (*i.e.* fenestrations) within the plasma membrane, allowing the uptake of small molecules[349], [350]. It is therefore not particularly surprising that – under the influence of significantly increased concentrations of these pro-angiogenic cytokines, the endothelial cell membrane is more susceptible to permeabilization from mechanical perturbations (via microbubble vibrations) than otherwise, as it is already characterized by increased fluidity. Aside from these, Fig. 3 demonstrates a consistent downregulation of a broad range of pro-inflammatory cytokines, the majority of which are shared between the two shear conditions (*e.g.* G-CSF, M-CSF, MCP-1). It is important to note here that while some of these pro-inflammatory cytokines have been shown to exhibit time-dependent increases in secretion under flow for short periods of time (*e.g.* MCP-1)[351, p. 1], [352], the data presented here is consistent with prolonged application of shear (>24 hrs). Indeed, the suppression of the myriad of pro-inflammatory secretions by long-term shear conditioning

observed here is broadly consistent with many other works in which isolated cytokines were examined independently[353], [354], as well as with the general downregulation of pro-inflammatory genes under chronic shear stress observed via microarray data[353], [355], [356]. While it is acknowledged here that the interaction between the complete endothelial secretome and how it influences the susceptibility of the plasma membrane to an external energy source like ultrasound is complex, it is perhaps still instructive to dissect the correlation between shear stress preconditioning and ultrasound-assisted enhanced permeability on an individual cytokine level. Specifically, Figure 4 depicts nine noteworthy correlations that identify three global categories: angiogenesis, leukocyte chemotaxis, and lymphocyte chemotaxis, with correlation coefficients R ranging here from $0.82 \leq |R| \leq 0.99$. Note that while some display statistically significant correlations, many are highly trending towards significance. Firstly, it is interesting to note that ultrasound-assisted permeabilization is highly positively correlated with preconditioning from pro-angiogenic cytokines (VEGF-A, EGF, FGF-2) – Fig 4a-c. In addition to these relations, ultrasound-assisted endothelial permeabilization was highly negatively correlated with pro-inflammation mediators, in particular those that both modulate leukocyte (*e.g.* MCP-1, GCP-2, MCP-3) and lymphocyte (*e.g.* I-TAC, SDF-1, CXCL16) chemotaxis, among more general inflammation markers (*e.g.* IL6, not shown). Indeed, many of these mediators can act in autocrine and play a role in endothelial migration and physiology (*e.g.* CXCL16[357], MCP-1[358]). It is of interest to note that the endothelial plasma membrane itself is a known mechano-sensor, and when placed under shear stress exhibits a marked reduction in its cholesterol content[359]. This has implications when considering lipid rafts – a potent platform for signal transduction – the disruption of which can hinder cytokine signaling and attenuate the cytokine response[360], [361]. In fact, the majority of differentially secreted cytokine/chemokines were downregulated under flow (Fig. 3c&d) and thus correlate negatively with membrane fluidity and ultrasound-assisted membrane permeabilization (Fig. 4d-4i).

4.3.3. Microbubble Perfusion Flow Pattern and Endothelial Cell Permeabilization

Irrespective of preconditioning, we next explored how the fluid pattern of the perfusing microbubbles during ultrasound treatment modulated the therapeutic result. Firstly, pulsatile perfusion was compared to flow rate-matched laminar perfusion (Fig. 5). Representative microscopy images (Fig. 5a) reveal qualitatively that pulsatile flow results in an increase of

ultrasound-assisted membrane permeability, the effects of which are quantified at two flow rates of 15 and 30 ml/min in panels Fig. 5b&c. At the faster flow rate of 30 ml/min, endothelial cells subjected to ultrasound therapy under a pulsatile flow, with either 0.5 or 1 Hz pulsation frequency, demonstrated a significant enhancement in membrane permeability as compared to those treated under laminar flow by 1.62-fold ($p < 0.05$) and 2.05-fold ($p < 0.001$), respectively. We further confirmed this trend by examining the differential permeability between these two treatment flow patterns at a slower flow rate of 15 ml/min (Fig. 5c). Pulsatile flow with 1 Hz pulsing frequency similarly enhances the extent of cell permeability compared to a flow-matched laminar condition (1.69-fold, $p<0.001$), however when the interval of time was increased (0.5 Hz) at the slower flow rate, we failed to see an elevated percentage of endothelial cell perforation. We next examined the more complex scenario of microbubble perfusion under reversing oscillatory flow, shown in Figure 6, under two physiological shear-rates (±2 dyne/cm^2 and ±4 dyne/cm^2). First, we examined this effect at a relatively slow flow rate of ±8 ml/min (3.33 cm/s), in which, independent of oscillation frequency, there was no observable cell permeabilization. When increasing the flow rate to ±16 ml/min, oscillatory flow at 0.5 Hz increased the percentage of permeabilized cells by 1.76-fold ($p < 0.005$). While reversing oscillatory flow at 1 Hz at this flow rate yielded no significant change as compared to laminar flow, it still indeed induced permeation (unlike at the slower flow rate). To place the results of the effect of microbubble perfusion pattern on ultrasound-assisted membrane permeabilization into context, it is perhaps instructive here to first consider the purely physical argument of local microbubble density and proximity to the endothelial layer. In first considering the non-reversing pulsatile data (Fig. 5), the flow rate of 30 ml/min corresponds to a linear velocity of 12.5 cm/s, given the cross-sectional area of the flow chamber. At this velocity, the microbubbles travel the length of the projected acoustic focus (3.5 mm) in 2.8 ms, with a microbubble displacement of 1.25 mm during the 1 ms PRI (~3 ultrasound bursts per microbubble in principle). During the intervals in which flow is temporarily stopped, the microbubble population will tend towards size stratification via differential flotation[185]. Relatively speaking, these intervals are rather large (1000 ms and 500 ms for 0.5 and 1 Hz pulsing frequency, respectively) compared to the ultrasound PRI, and represent a significant percentage of the treatment duration – fixed to 4 s in this study. In this arrangement and within a fixed time period, the bubble size distribution within close proximity to the endothelial layer slightly shifts to smaller bubbles. Estimation of this differential flotation away from the endothelial monolayer by Stoke's equation yields a ~0.5-35

μm shift for bubbles ranging in radius from $0.5 \leq r \leq 4$ μm within 1 second of flow cessation (0.5 Hz), for example. While this translation may not represent a significant change within the acoustic focus (<< 1%), it does bring the microbubbles within closer proximity to each other. Indeed, at the bubble dilution used here, the average inter-bubble spacing is ~25 μm. With a net displacement on the order of tens of microns (*i.e.* very small inter-bubble spacings), we can expect to see significant vibrational effects due to the influence of one microbubble on another[362]. Further, the probability of microbubble-microbubble interactions via secondary radiation forces, for example the coalescence of two or more bubbles into a larger bubble, is increased at these shorter inter-bubble distances. It is also important to consider microbubble residence time within the acoustic beam (*e.g.* for the bubbles arrested within the beam for 1 s, the same/similar population will be interrogated 1000 times at this PRI). This represents a trade-off between the propensity of eliciting sufficient microbubble vibration to include membrane permeabilization[152] versus the likelihood for microbubble disruption (and therefore no more sources of localized stresses to permeate cells), both of which increase with number of transmit bursts. At some point during the acoustic pulse, it is indeed probable that microbubble disruption occurs and thus bubble replenishment by the resuming of flow will contribute positively to the number of endothelial cells undergoing ultrasound-assisted permeabilization.

The interactions between the microbubbles circulating under reversing oscillatory flow and the endothelial layer were more heterogeneous (Fig. 6). Circulation of microbubbles flowing at the slower speed (±8ml/min) corresponds to a linear travel distance of 33.3 μm within the 1 ms PRI, which is approximately the length of the two endothelial cells. In principle, at this slow of a rate, the microbubbles that are entering the acoustic beam are likely undergoing acoustically induced disruption (subjected to ~105 ultrasound bursts while within the acoustic focus). Thus, even within the first positive phase of oscillatory motion, there would be no more microbubbles able to re-enter the acoustic beam – either distally (reverse phase of fluid motion) nor proximally (forward phase) to the acoustic focal zone. At the faster flow rate of 16 ml/min (6.66 cm/s), our hypothesis here is that only partial disruption occurred and thus enables the replenishment of new microbubbles within the acoustic focus. It is important to note here that, even at the slowest microbubble flow rates employed, the imaging frame rate used here (~50 Hz) is too slow to obtain reliable information on microbubble population pattern and acoustically induced disruption. Simultaneous bright-field imaging with a fast-frame camera, with frame rates on the order of kHz, would be an

invaluable tool to shed mechanistic insight into the relationship between microbubble translational dynamics and endothelial permeabilization under flow, and is the subject of future endeavors.

4.4. Conclusion

The effects of fluid flow and the resulting shear stress on microbubble-mediated endothelial cell permeabilization was investigated in two contexts. First, sustained shear-stress preconditioning of human endothelial cells increases their susceptibility to ultrasound-assisted cell membrane permeabilization under identical acoustic stimulation up to 2-fold as compared to non-preconditioned cells. Multiplex examination of the endothelial secretome under these conditions revealed correlations between enhanced ultrasound-assisted cell membrane permeability and expression of cytokines involved in angiogenesis (*e.g.* VEGF-A, EGF, FGF-2) and inflammation – including both leukocyte (*e.g.* MCP-1) and lymphocyte (*e.g.* SDF-1) chemotaxis. Secondly, the microbubble fluid flow pattern (non-reversing pulsatile, reversing oscillatory) as it perfuses endothelial cells significantly modifies the efficiency of this treatment technique given the same acoustic stimulus, resulting in up to a 2.4-fold increase in the percentage of permeability when treated under pulsatile conditions versus a flow rate-matched laminar flow, depending on the specific flow parameters. Reversing oscillatory fluid flow, as compared to laminar flow, can result in up to a 1.7-fold increase or a complete shutdown for endothelial membrane permeability, highlighting a more heterogeneous response. The results from both of these contexts emphasizes the fact that microbubble-assisted therapeutics is strongly dependent on both the pathophysiology of the vascular compartment and the local microbubble density and distribution as it perfuses the vasculature. Among others, this work has implications for emerging anti-inflammatory drug delivery approaches for atherosclerosis, which have had recent success in clinical trials, whereby

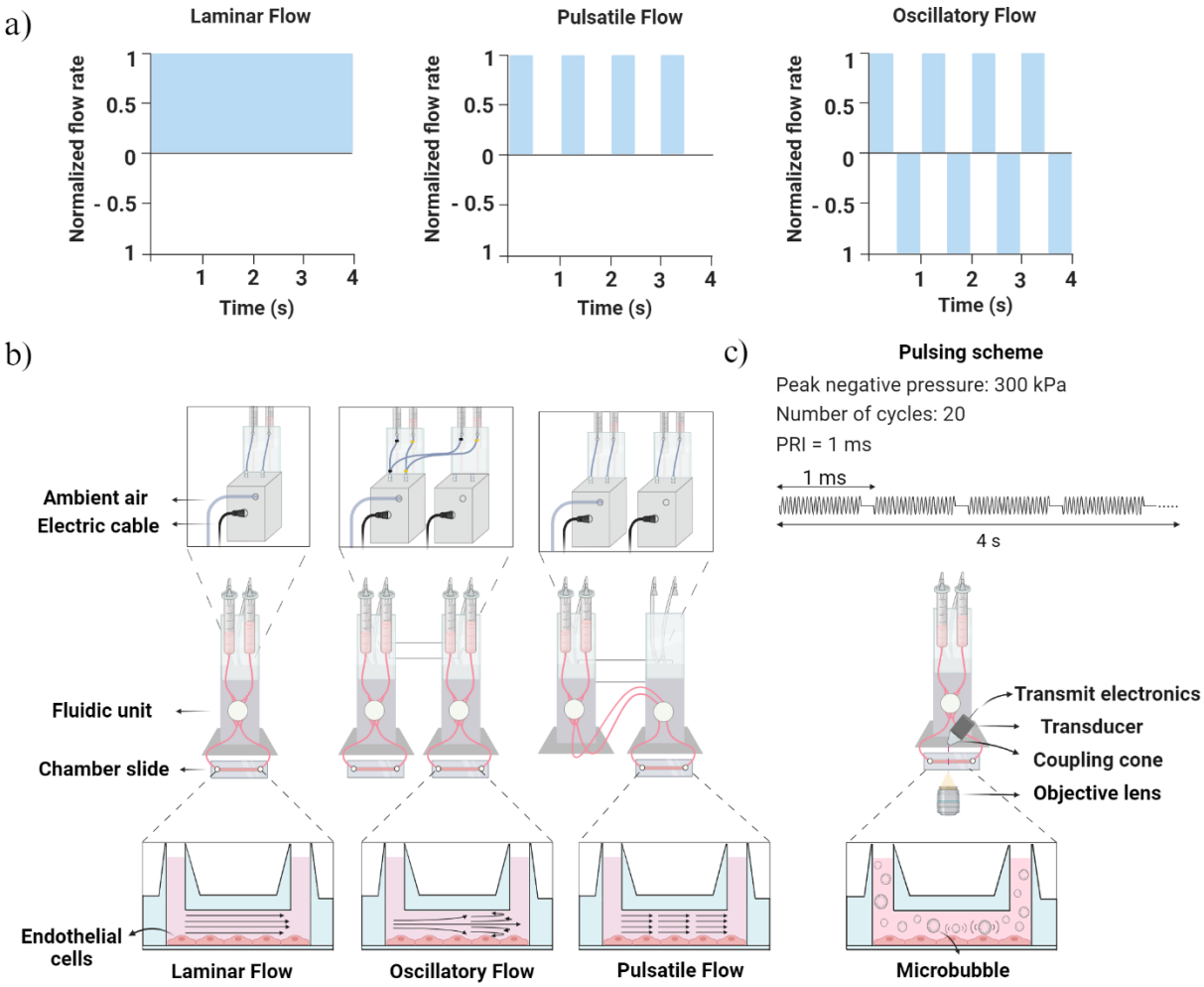

Figure 4.2: Schematic overview of the experimental apparatus and flow conditions. a) Sample timing diagrams illustrative of the flow patterns used in this study, depicting laminar flow (left), non-reversing pulsatile flow (middle), and reversing oscillatory flow (right). Pulsatile and oscillatory flow frequencies ranged from 0.5-1 Hz (1-0.5 s switching time), and the ultrasound experiments were conducted for a fixed duration of 4 s. See specific experiments for details on shear magnitude/flow velocity, and the Methods text for the justification of their values in the context of healthy and atherosclerosis-prone regions. b) Overview of the tubing arrangements for the ibidi units required to achieve such flow patterns. c) Schematic view of the ultrasound pulsing scheme used throughout this work, as well as the acoustically-coupled microscopy system employed to examine microbubble-assisted endothelial permeability under flow.

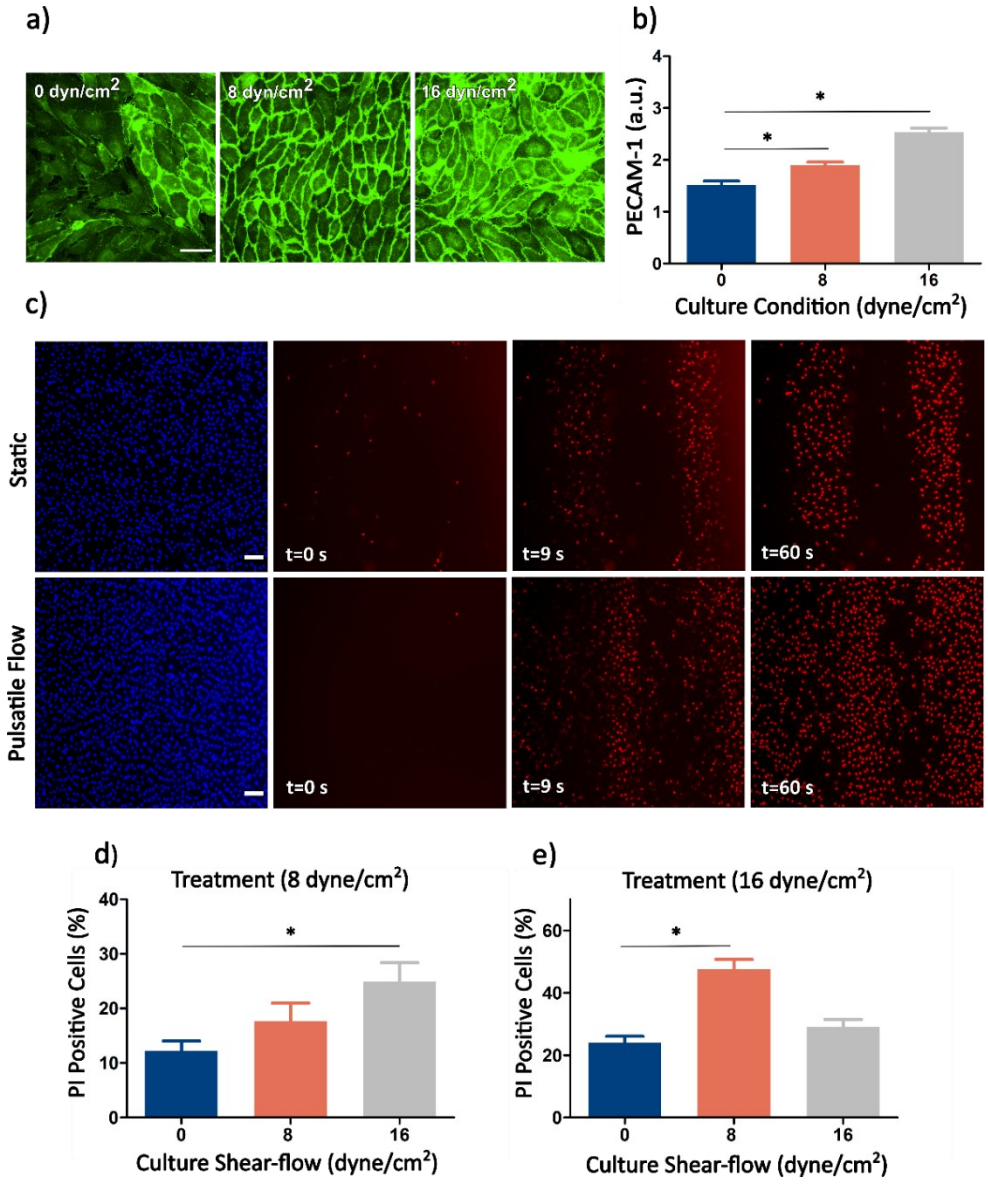

Figure 4.2. Endothelial cell cultivation under pulsatile flow sensitizes cells to ultrasound-mediated cell permeabilization. a) Human endothelial cells were cultivated in chamber slides either statically or under pulsatile flow with shear stress magnitudes of either 8 or 16 dyne/cm^2 for two days. Immunofluorescence staining was performed for PECAM-1 (green). Fluorescence microscopy images demonstrate that cell cultivation under pulsatile flow leads to a more uniform cellular morphology, organized cell-to-cell contact, and reduced extracellular gaps between endothelial cells, as compared to statically cultured cells. Scale bar is 50 μm. b) Quantification of PECAM-1 expression illustrates a direct correlation between pulsatile shear flow and PECAM-1 expression. c) A representative example of time-lapse microscopy images from endothelial cells that were cultured either statically (top panel) or under

pulsatile flow (bottom panel) during ultrasound treatment. Flow condition during ultrasound treatment remained constant within different subgroups. Nuclei were stained with Hoechst (blue) and the surrogate macromolecule (red) was used to indicate cell membrane permeabilization. d) Endothelial cells with microbubbles perfusing via a pulsatile flow of 8 dyne/cm^2 or e) 16 dyne/cm^2 exhibited an increased susceptibility to ultrasound-mediated cell permeabilization versus statically cultured cells (noted here as a culture shear-flow of 0 dyne/cm^2). The magnitude of this effect increased with variations in shear flow during cultivation and microbubbles perfusion velocity. Asterisks denote statistical significance.

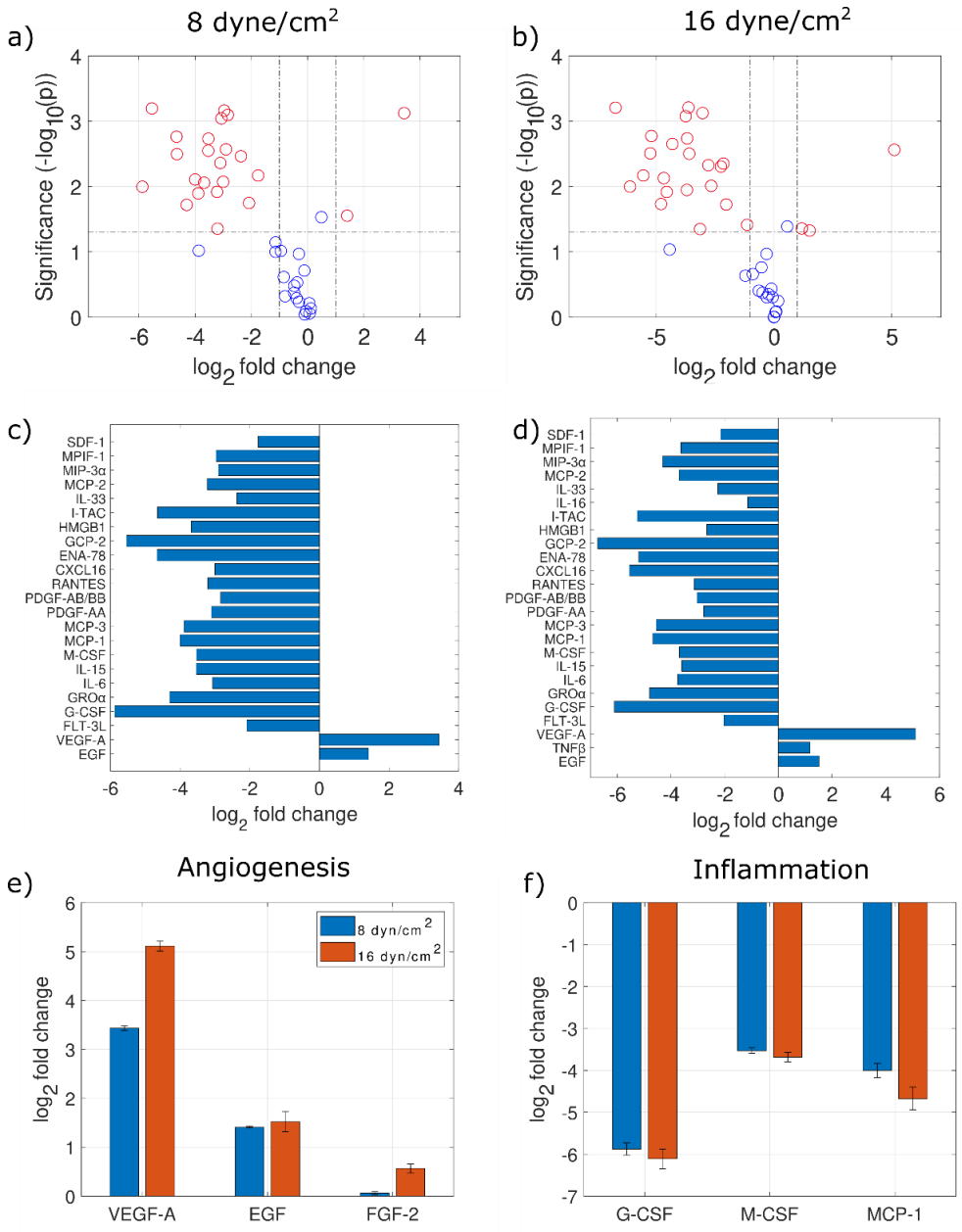

Figure 4.3. Prolonged pulsatile shear-flow modulates human endothelial cell secretome. a,b) Volcano plots illustrating modulation of cytokine expression when exposed to 8 dyne/cm^2 or 16 dyne/cm^2 in comparison to statically cultured cells. Every analyte examined is represented with a circle – the ones shown in red demonstrate at least a 2-fold change and are statistically significant (dotted lines represent 2x increase [$log_2 = 1$] or 2x decrease [$log_2 = -1$], and the vertical line represents the line above which $p<0.05$), whereas the blue dots represent analytes with a small change (less than 2-fold change) or no change, and are not statistically significant. c, d) Identification of those analytes with significant and large magnitude differential secretions upon endothelial cell cultivation (the red circles in the volcano plots). Select examples are shown for three cytokines with known involvement as e) pro-angiogenic and f) pro-inflammatory. Prolonged shear-stress preconditioning showed similar effects at both shear magnitudes: significantly downregulating many important factors of the endothelial secretome (e.g. pro-inflammatory) and upregulating those with pro-angiogenesis properties.

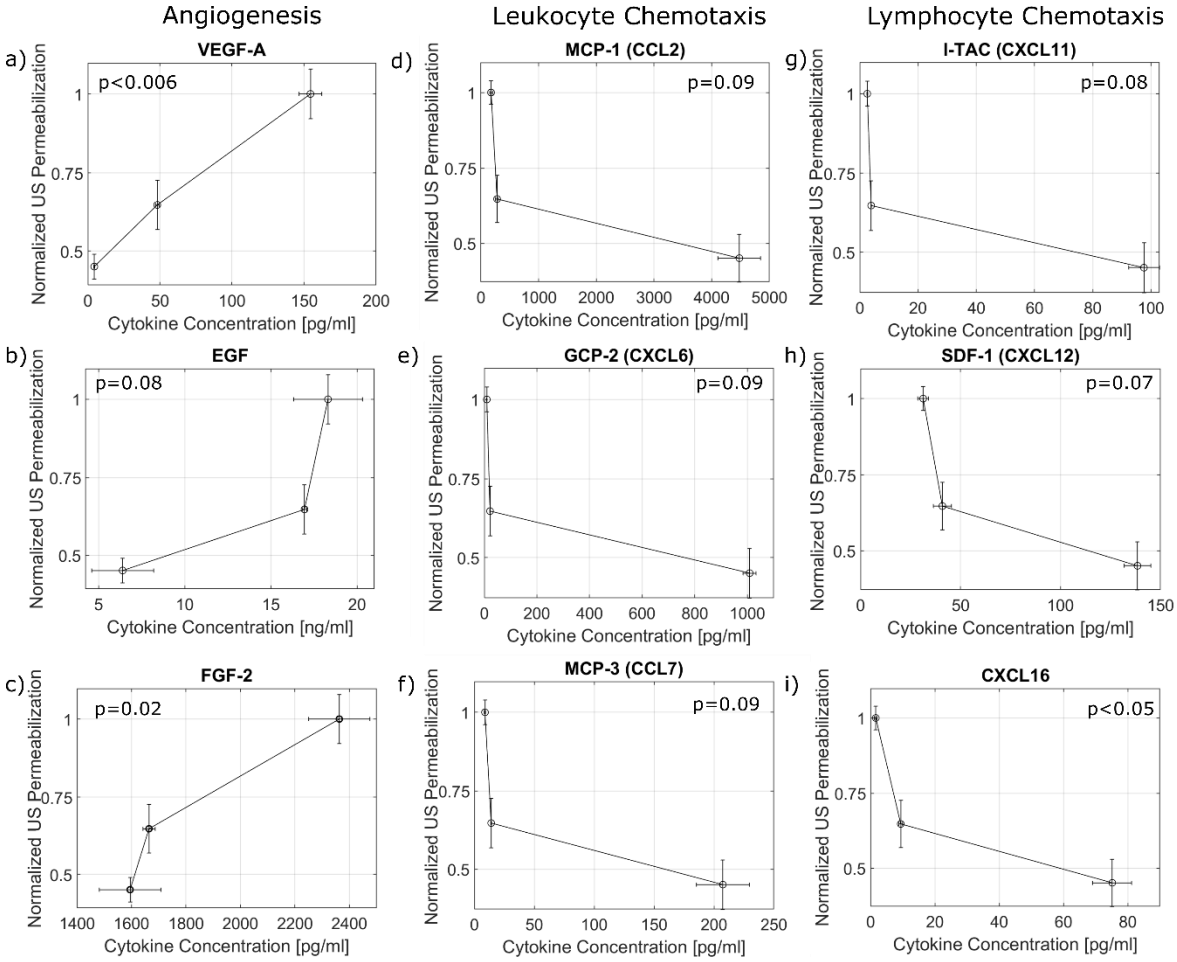

Figure 4.4. Microbubble-mediated human endothelial permeability is directly correlated with the presence of pro-angiogenesis markers and inversely correlated with pro-inflammatory ones. a-c) This first column highlights the general positive correlation of VEGF-A, EGF, and FGF-2 and ultrasound treatment – three cytokines with well established roles in angiogenesis. All other analytes show an inverse correlation, including those involved in d-f) leukocyte (MCP-1, GCP-2, MCP-3) and g-i) lymphocyte (I-TAC, SDF-1, CXCL16) chemotaxis. Pearson correlation coefficients range from $0.82 \leq |R| \leq 0.99$, and statistical significance is shown within the panel for each analyte. It is important to note here that many of these are trending towards significance, including others not shown here (e.g. IL6). The ultrasound permeabilization quantity shown is normalized to its maximum, taken from the data obtained when treated at 8 dyne/cm^2. This data is strongly suggestive that the local cytokine environment in which the endothelial cells are situated modifies its susceptibility to external perforation.

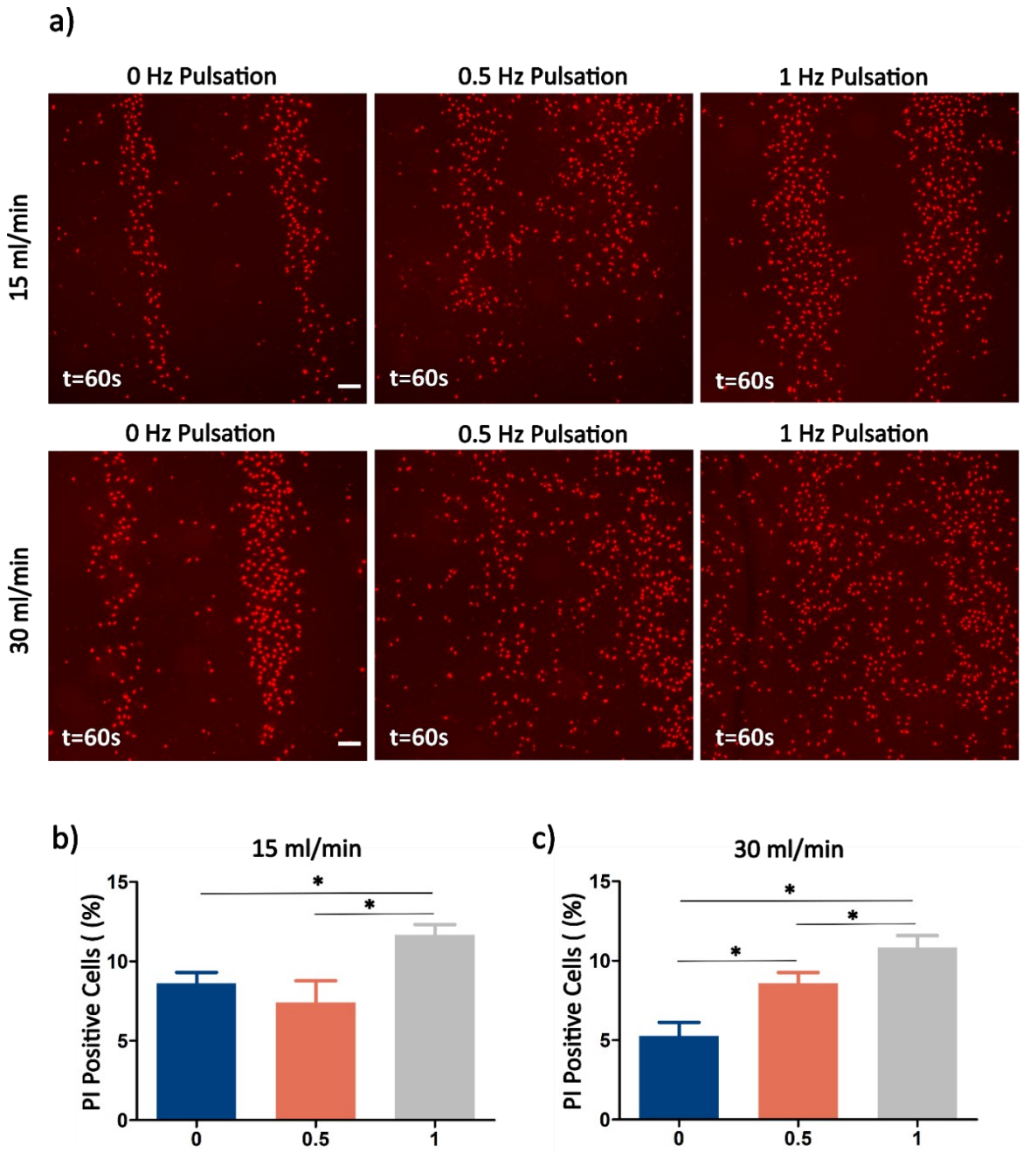

Figure 4.5. Pulsatile perfusion of microbubbles influences ultrasound-mediated endothelial cell permeabilization. a) Representative fluorescence images at the end of recording (60 s), illustrating macromolecular uptake under varying flow profiles. Data shown for microbubbles perfusing at 15ml/min (top panel; ~4 dyne/cm^2) and 30 ml/min (bottom pane, ~8 dyne/cm^2). The scale bar is 50 μm. b) The extent of microbubble-mediated cell perforation significantly increases when perfused at 15ml/min at 1 Hz pulsation frequency (1.69-fold, $p < 0.001$), while increasing the flow rate to 30/min elevated cell perforation as compared to laminar flow at 0.5 Hz and 1 Hz respectively (1.9-fold, $p < 0.05$; 2.4-fold, $p < 0.001$). These observations underscore the significant influence of microbubble flow dynamics on ultrasound-mediated cell perforation efficacy. Note that laminar flow here is indicated by a pulsing frequency of 0 Hz. Please note that no shear preconditioning was applied here (cells were cultured statically).

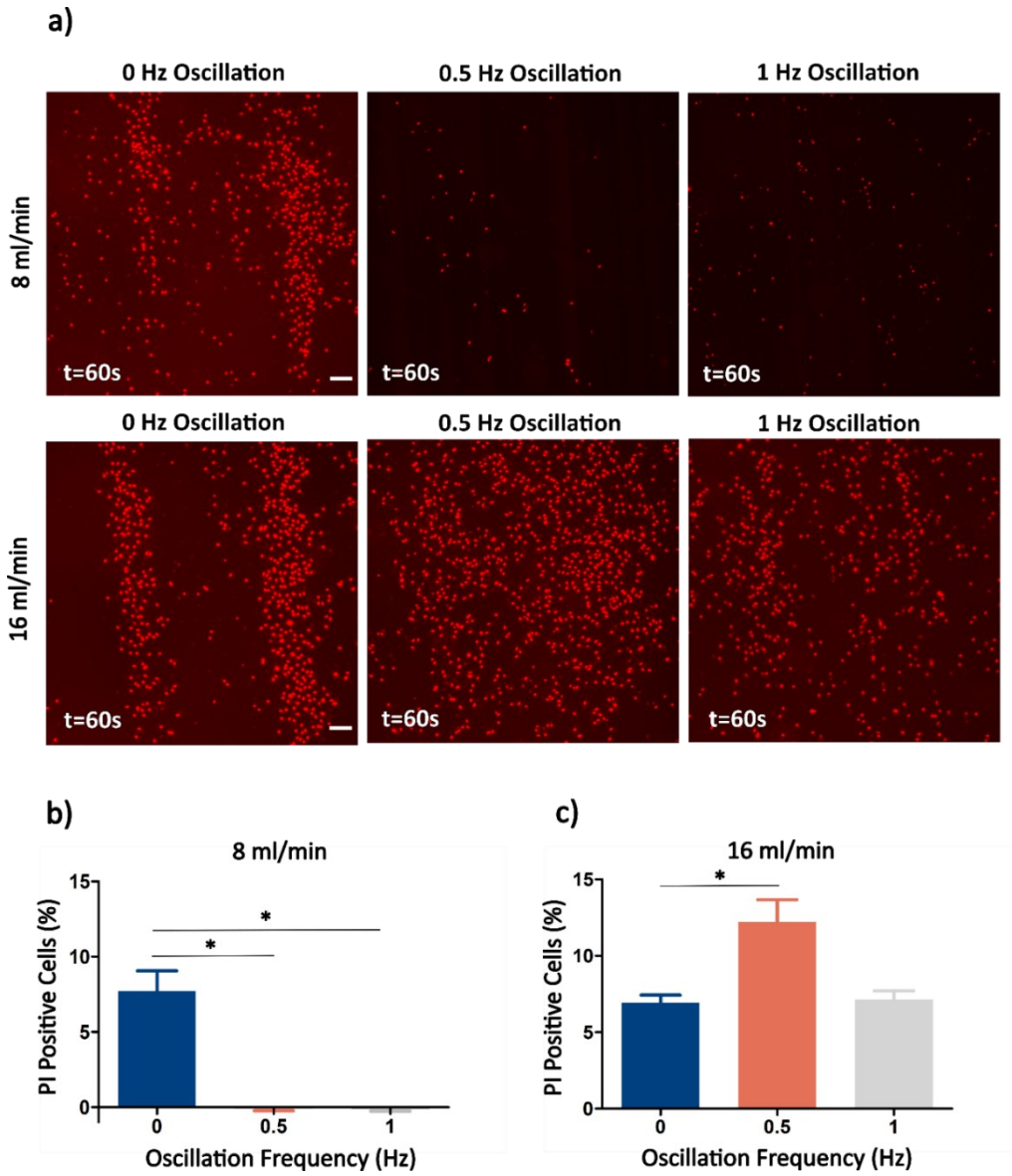

Figure 4.6. Oscillatory flow perfusion enhances ultrasound-mediated cell permeabilization when characterized with high flow velocity and low oscillation frequency. a) Representative fluorescence microscopy examples illustrating microbubble-induced cell perforation – indicated here by the presence of an otherwise impermeable macromolecular in red - under varied flow conditions with shear flows of either 8 ml/min (top; ±2 dyne/cm^2) or 16 ml/min (bottom; ±4 dyne/cm^2). Scale bar is 50 µm. Statically cultured cells were perfused with microbubbles under three flow profiles: i) laminar (blue bars), and oscillatory with oscillation frequency of 0.5 Hz (orange bars) or1 Hz (grey bars) and fluid velocity of either b) 8 or c) 16 ml/min. Our results demonstrate a significant enhancement in cell permeability when microbubbles flow at 16ml/min at 0.5 Hz frequency (1.76-fold, $p < 0.005$), whereas 1 Hz oscillation frequency fails to elevate

cell perforation. Interestingly, when perfused at the slower speed of 8 ml/min, a complete suppression of cell permeabilization was observed for either oscillation frequency condition. Note that laminar flow here is indicated by an oscillation frequency of 0 Hz. Please note that no shear preconditioning was applied here (cells were cultured statically).

5. Shear stress and microbubble-mediated modulation of endothelial cell immunobiology

Chapter 3 and 4 established the influence of fluid flow on endothelial cell permeabilization, both in cell preconditioning and during the treatment. Building on this, manuscript published as: Memari et al., *Small* (2024) explores the effects of shear stress on endothelial immunobiology, with the goal of improving immune cells recruitment and trafficking to the tumor site in future studies. This study specifically focuses on examining the time-dependent influence of shear flow and microbubble-induced shear stress on endothelial cell immunobiology. To this aim, endothelial cell cytokine profile and surface expression of CAMs involved in immune cell trafficking was investigated at different time points post-sonication.

Abstract:

Cellular immunotherapy remains hindered in the context of solid tumors due to the immunosuppressive tumor microenvironment, in which key endothelial cell signaling and adhesion molecules (CAMs) are suppressed. Microbubble-mediated focused ultrasound is being explored for targeted immunotherapy and can exert local shear-stress upon neighboring endothelial cells. However, fluid and microbubble-induced shear modulation of endothelial immunobiology is not well understood. Here, we examined the influence of both types of shear-stress on CAM expression and secretion of over 90 cytokines using acoustically-coupled microscopy. Fluid flow resulted in time-dependent modulation of CAM expression, where ICAM-1 expression peaked at 4h (1.98-fold, $p<0.001$, HUVEC) and 24h (1.56-fold, $p<0.001$, HBEC-5i). While some chemokines were significantly enhanced (up to 16.2-fold; $p<0.001$) from both endothelial cell types (e.g. IL-8, MCP-1, MCP-3), others were differentially expressed (e.g. CCL5, CXCL-16, SDF-1). Under identical ultrasound conditions, ICAM-1 expression at 4h post-sonication was increased (~1.4-fold, $p<0.01$) and resulted in large-magnitude (>2-fold) and significant ($p<0.05$) differential expression of 20 cytokines, most of which had immune-activating function and within a subset of those induced by shear-flow. Microbubble-mediated ultrasound positively regulated ICAM-1 expression and the human endothelial secretome towards an immune cell recruitment paradigm, and thus potential to reinforce cellular immunotherapy efforts for solid tumors.

5.1. Introduction

In recent years, cancer immunotherapy has had major successes in the field of oncology – techniques of which include monoclonal antibody therapy (e.g. rituximab targeted against CD20) and more recently immune checkpoint blockade (e.g. pembrolizumab targeted for PD-1). In addition to antibody-based strategies, a subset of immunotherapy in which immune cells are either expanded (adoptive cell transfers) or engineered (chimeric-antigen-receptor; CAR) ex-vivo to specifically express a given TCR with hyper affinity – cellular immunotherapy – has been recently deployed. There have been over 1000 clinical trials worldwide investigating the use of CAR T cells, most in lymphoma or leukemia using CD19-specific CARs[363], [364]. Indeed, this relatively new treatment paradigm has had extraordinary results in blood-borne cancers; for example, the results from the ELIANA trial showed an overall remission rate of 81% at 3 months[365] in patients with relapsed or refractory acute lymphoblastic leukemia (ALL) and no other treatment options, with a median event-free survival of 24 months[366]. Despite this, cellular immunotherapy approaches have had limited success when targeting solid tumors (e.g. glioblastoma, renal cell carcinoma, colorectal cancer[367]). This can be attributed to numerous physical and biological immunosuppressive factors including antigen heterogeneity, the downregulation of tumor-specific endothelial cell surface expression of adhesion molecules (for instance ICAM-1, MadCAM-1), creating immunologically inaccessible sites (physical barriers like collagen and fibrin prevent the entry of immune cells), and tumor-induced immune suppression within the microenvironment (e.g. release of factors that directly inhibit T cells or induce regulatory T cells)[368], [369]. Further, solid tumor mechanopathology factors (e.g. increased tumor stiffness)[370] can cause extensive vascular compression and heterogenous blood flow and shear stress profiles, further impeding the success of cellular immunotherapeutic approaches[371]. In this context, shear stress plays a critical role in modulating endothelial cell immunobiology within the tumor microenvironment (TME). Shear force sensed by the endothelial cell mechanosensory molecules (e.g. cytoskeleton, integrins, growth factor receptors, ion channels, and several cell adhesion molecules) influence the signaling networks involved in inflammatory responses[372]. Therefore, shear-mediated mechanisms that can modulate suppressive nature of TME hold a significant potential for improving cellular immunotherapy.

Focused ultrasound is an innovative therapeutic strategy capable of exerting various bioeffects through both thermal and mechanical mechanisms. In hyperthermia, a regime characterized by a

mild temperature rise (~up to 43°C,) an immune response can be elicited by releasing cell debris and activating antigen presenting cells[373], and can augment chemotherapy and radiotherapy approaches[59]. At higher acoustic intensities, the nonlinear effects of US can increase the temperature beyond 60°C, known as thermo-ablation. This technique, capable of causing rapid tissue necrosis, is currently approved for the treatment of essential tremor and tremor-dominant Parkinson's disease[59]. In addition to thermal effects, another mechanism is via mechanical effects which can be exploited with or without clinically used contrast agent microbubbles to apply diverse bioeffects. An emerging strategy is utilizing a combination of low intensity ultrasound with microbubbles, which can locally and reversibly modulate the permeability and gene expression of the neighboring vasculature and surrounding tissue[263], [374]. The most clinically advanced application of the latter is in the temporary opening of the blood-brain-barrier[274], which has been examined as a targeted drug delivery approach in the contexts of neurodegenerative disease (Alzheimer's[231], ALS[165], Parkinson's[375]), and neuro-oncology[241], [376] [20–22]. Indeed, the delivery of immunomodulating agents to brain tumors using this method, including monoclonal antibodies[251], has reached the clinical trial stage, with many other types of immune-altering agents currently under pre-clinical investigations[329].

Aside from the targeted delivery of a therapeutic, ultrasound treatment has been shown to modulate intracellular signaling[162], including the release and expression of pro-inflammatory factors[57], [377]. Indeed, on a single-cell level, ultrasound-stimulated microbubble response has shown to exhibit physical forces (e.g. shear) on neighboring endothelial cells[148], to cause reversible alterations in both plasma membrane permeability[152], [153] and vascular permeability[151], [378], and to initiate sustained calcium ion entry and downstream signaling[149], [330].

Given the heterogeneous TME, including the physiological hostile milieu and abnormal shear-stress patterns exerted on endothelial cells, our objective here is to ascertain the extent to which microbubble-assisted ultrasound treatment alters endothelial cell immunobiology and to make qualitative connections to flow-induced shear stress, with a view towards enhancing immune cell trafficking and recruitment. Using two human endothelial cell lines of differing origins (umbilical vein HUVEC; brain microvasculature HBEC-5i), we first examined the shear-flow induced changes in key immune-cell recruitment surface molecules ICAM-1 and MadCAM-1 and the endothelial secretome in a time-dependent manner. Next, using acoustically-coupled microscopy,

we explore the ultrasound conditions that, when used with perfusing microbubbles, modulate these same endothelial markers and observe how these secreted factors change as compared to untreated, sham controls. Finally, we conclude with implications of our results in the broad context of ultrasound-assisted immunomodulation.

5.2. Results and Discussion

5.2.1. The Influence of Shear Flow Preconditioning on Cell Adhesion Molecule Expression

As depicted in Fig 1, we first investigated how endothelial cell cultivation under shear flow affects cellular morphology. Shear flow preconditioning led to a more physiologically relevant morphology, characterized with cell elongation in the direction and well-defined cell-to-cell contact. In contrast, statically cultivated cells exhibited a heterogeneous morphology, and large extracellular gaps between cells with random orientation (Fig. 1b). Then, we examined the extent to which shear flow preconditioning influences the expression of CAMs on HUVECs, a more commonly studied human endothelial line of venous origin (Fig. 2a-c). Fig 2a depicts representative micrographs of ICAM-1 (green) and MadCAM-1 (red) expression at different time-points of ongoing shear. Quantification of these expression profiles revealed maximum expression of ICAM-1 as early as 4 hours after flow exposure (1.98±0.15-fold increase compared to no flow, $p<0.001$), a transient short-lived effect as evidenced by its decrease back to baseline levels by 8 hours (Fig. 2b). The shear-stress induced surface expression of ICAM-1 – a major regulator of leukocyte trafficking to inflammatory sites – has long been known to exhibit time dependence. Indeed, the data presented here is consistent with previous works in which an approximate 2-fold increase was observed between 4-6 h and returned to baseline by >8 h[379], [380]. The MadCAM-1 profile (Fig. 2c), however, responded quite differently to the flow shear stress, locally peaking slightly after 1h and then reaching a global minimum by 4 h (0.67±0.18, fold compared to no flow $p<0.05$). MadCAM-1 expression has been observed on the brain endothelium in chronically inflamed cerebral vasculature associated with autoimmune encephalomyelitis. It has been suggested that MadCAM-1 is involved in the homing of α4β7-integrin expressing lymphocytes[381]. While to our knowledge there is no direct information on the effect of shear flow on MadCAM-1 expression profile, we can perhaps intuit an understanding by examining VCAM-1, which shares a similar pattern to shear flow preconditioning. It has been shown that

under laminar shear stress, VCAM-1 significantly downregulates in a time-dependent manner, leading to a reduced number of lymphocytes adhering to the endothelial cells[382].

Next, we conducted the same experiments examining shear stress preconditioning and surface expression of ICAM-1 and MadCAM-1 on HBEC-5i (Fig. 2d-e). Similar to HUVECs, quantification of microscopy images revealed a time-dependent upregulation of ICAM-1 on HBEC-5i (Fig 2d), however with a peak increase in expression observed at 24 hours (1.56-fold compared to static, $p<0.001$), returning to baseline levels by 48 hours – resulting in a relatively delayed response compared to HUVECs (Fig. 2b). A similar comparative effect is shown with MadCAM-1 (Fig. 2e), in which the surface expression exhibited by HBEC-5i reached a minimum much later than HUVEC, here at 24 h (0.48 ± 0.10 compared to static, $p<0.001$). While, to the best of our knowledge, time-dependent shear flow CAM surface expression of human brain endothelial cells has never been reported, our dataset is broadly consistent with previous work by Cucullo et al.[383] in which they demonstrated a small flow-mediated increase (~1.25-fold) in both ICAM-1 and MadCAM-1 gene expression in human brain endothelial cells, albeit under an entirely different flow regime. Further, work by Rochfort and Cummins[384] demonstrated the time-dependent shear-induced (8 dyn/cm2) expression of thrombomodulin in human brain endothelial cells, peaking at 24 hours – similar in timescale to what we report here for ICAM-1.

It is not entirely surprising that the temporal nature of shear-induced CAM expression differs between the human brain microvascular cells (HBEC-5i) and umbilical vein endothelial cells (HUVECs). It has been long demonstrated that both native levels and pro-inflammatory cytokine-induced expression of ICAM-1 are amplified in HUVEC compared to human brain endothelial cells[385], a subset of data that confirms drastic differences in static CAM surface expressions across human endothelial cell types of distinct origins[383], [386], [387].

5.2.2. The Effect of Shear Flow Preconditioning on Endothelial Cell Secretome

Given the heterogeneity in flow-induced shear stress within the TME and its relation to disease progression (e.g. glioblastoma[388], [389]), we investigated the secretome of these cells under the same shear flow condition as above, to gain deeper insight into the physiological influence of shear flow preconditioning on endothelial cell immunobiology. Further, we assayed endothelial secretome as a function of time at the same time points as determined from our surface ICAM-1 expression dataset. In Fig. 3a, the fold-change in shear-induced cytokine expression compared to

static control as a function of time is displayed for both HUVEC and HBEC-5i, in which the color is indicative of the magnitude of change (blue is a decrease; red is an increase) and star symbols denote statistical significance. Here, only analytes that exhibited significant signal above the noise floor are shown. With respect to the HUVEC secretome, we observed a significant decrease in the secretion level of a subset of factors such as SDF-1, CXCL-16, CCL5, EGF, FGF-2, IL-1α, VEGF-A, TNF-β, CCL28, and ENA-78. The observed results for HUVEC align with previous studies, reporting that high laminar shear stress under short durations suppresses the signaling pathways involved in the pro-inflammatory responses[390], [391]. As displayed in Fig. 3a, there is a stark contrast when considering the HBEC-5i secretome, which revealed a significant increase in the concentration of 19 cytokines, chemokines and growth factors including GRO-α, IL-6, IL-8, MCP-1, RANTES, TNF-α, VEGF-A, SDF-1, M-CSF, PDGF-AA, sCD40L, TNF-β, CCL28, CXCL16, ENA-78, GCP-2, IL-11, LIF and SCF.

A global summary of cytokine fold-change expression at both 4 hours and 16 hours under shear is depicted in Fig. 3b-c for both endothelial cell lines. Here, this plot represents the total number of cytokines that were either upregulated or downregulated at time points shared by the two endothelial cell types. For HUVECs under shear flow (Fig. 3b), there is an approximate even distribution between those cytokine secretions that exhibited an increase (10 at 4 h; 8 at 16 h) and a decrease (11 at 4 h; 13 at 16 h) under shear. Conversely, the human microvasculature brain endothelial cells (Fig. 3c) exhibited more increased cytokine production (17 at 4 h; 19 at 16 h), with relatively few factors in reduction (6 at 4 h; 4 at 16 h) under shear preconditioning. Indeed, it is perhaps useful here to examine the differences in the absolute value of cytokine concentration (pg/mL) exhibited by these two human endothelial cell types. The absolute levels of six cytokines under shear (Fig. 3e-f) highlight that, even among the cytokines in which both endothelial cell types secrete significantly more compared to static conditions (Fig. 3a), HBEC-5i endothelial cells produce these cytokines in vastly larger amounts, ranging from 2.2 to 36-fold more than HUVEC under the same conditions. Of note, SDF-1 and TNF-B are exceptions here, with HUVEC showing 1.34 and 16.59-fold higher concentration in comparison with HBEC-5i at 4 h shear preconditioning. However, SDF-1 and TNF-B concentration increased rapidly in HBEC-5i over time, reaching 2.58 and 2.22-fold higher than HUVEC at 16 h shear flow, respectively. These observations suggest that brain microvascular endothelial cells not only have higher baseline levels

of multiple inflammatory cytokines, but also demonstrate a more pronounced response to laminar shear stress by substantially enhancing the secretion of these key cytokines.

One of the clearer results from this figure is the heterogeneity in shear-stress mediated time-dependent secretome expressed by the two endothelial cell types – further articulated in Fig. 4. Some signaling molecules were differentially expressed (e.g. CCL5, SDF-1, TNF-B were increased from HBEC-5i up to 16.2-fold but decreased from HUVEC up to 0.75-fold; $p<0.001$), with others, including TNF-α, CXCL-16 and LIF, expressed highly in HBEC-5i (up to 7.2-fold, $p<0.05$), yet not at all from HUVEC (Fig. 4d-f). A possible explanation for the observed differences in endothelial secretome changes in response to the 9 dyn/cm2 shear stress used here may be related to the magnitude of this shear stress in relation to its normal, physiological levels. Indeed, endothelial exposure to high laminar shear stress (relative to its baseline) leads to suppression of pro-inflammatory pathways through the inactivation of NADH oxidase, whereas low shear stress exposure leads to the production of ROS by activation of NADH oxidase, which subsequently leads to oxidative stress and promotes an inflammatory response[392], [393]. The shear stress used here is slightly higher than the physiological shear range for HUVEC, which might explain the downregulation of most pro-inflammatory cytokines for this cell type. For HBEC-5i, in contrast, it is actually in the lower range of the physiological shear for human brain capillaries, which may contribute to the activation of pro-inflammatory pathways.

Despite the observed differences in the effect of shear flow on the secretion level of most analytes from HBEC-5i as compared to HUVEC, multiple factors including MCP-1, PDGF, IL-6, IL-8, GRO-α, EGF and FGF-2 showed a similar trend in both cell types (Fig. 4 g-i). These factors were significantly increased (up to 8.8-fold; $p<0.001$) from both endothelial cell types under flow throughout the time range analyzed (Fig. 4c). Exposure to high laminar shear stress has been shown to activate the NF-κB pathway, which is consistent with factors including PDGF, IL-6, IL-8, and MCP-1[382]. While other studies reported that laminar shear flow increases the level of growth factors such as FGF-2 and EGF, we observed a decrease in the concentration of these factors after exposure to shear flow in both HBEC-5i and HUVEC. This conflicting observation could be attributed to a difference in the exposure time to the shear stress, the magnitude of shear stress, and the cell type[382].

As many of these cytokines have been shown to be involved in mediating inflammation and CAM expression, we sought to next correlate individual cytokine concentration with CAM expression, with a specific focus on ICAM-1 for HUVEC and HBEC-5i endothelial cells, shown here in Figure 5. It has been shown that chemokine signaling transiently expedites the rolling and adhesion of immune cells by stimulating the generation of high avidity integrins within seconds of shear flow exposure, leading to firm adhesion of leukocytes to immunoglobulin family cell adhesion molecules such as ICAM-1, VCAM-1 and MAdCAM-1 on the endothelial cells[394]. This indicates that the upregulation of chemokines and immunoglobulin family of adhesion molecules in an inflammatory condition probably takes place in close succession, both facilitating the firm adhesion of rolling immune cells to the endothelium in an inflammatory condition[54]. Regarding the direct influence of cytokines on the expression of ICAM-1 in either HUVEC or brain endothelial cells, most studies focused on TNF-α and IL-1β, as it has been reported that they are the key mediators of CAM modulation[395], [396]. O'Carroll et al [395] studied the effect of pro-inflammatory factors, specifically TNF-α and IL-1β, on the immunophenotype features of brain endothelial cells including the surface expression of ICAM-1, revealing a differential response of brain endothelial cells to IL-1β and TNF-α. The treatment of brain endothelial cells with TNF-α and IL-1β (5 ng/mL) triggered an inflammatory response, followed by a substantial increase in the secretion of 13 inflammatory factors including soluble ICAM-1, soluble VCAM-1, IL-6, IL-8, MCP-1, and CCL5. They showed that the elevated levels of CCL5 and IL-8 were associated with TNF-α-mediated inflammatory response. This is consistent with our results, observing a simultaneous increase in the secretion of TNF-α, CCL5 and IL-8 in HBEC-5i under laminar flow, with the latter two possibly secondary to the enhanced level of TNF-α. In contrast, the level of TNF-α in HUVEC remained negligible over time, potentially explaining the downregulation of CCL5 and several other inflammatory cytokines in HUVEC. While IL-8 secretion level in HUVEC increased over time up to 2.7-fold, this increase was less pronounced than HBEC-5i, which showed 5.7-fold enhancement in the IL-8 concentration under the same condition, likely attributed to the higher concentration of TNF-α in the HBEC supernatant. Additionally, this study showed that conditioning of brain endothelial cells with a range of 50 pg/mL to 50 ng/mL TNF-α and IL-1β directly upregulated the surface expression of ICAM-1 at 24 hours post treatment[395]. Another study reported that the increased local concentration of chemokines considerably reduces the rolling distance of immune cells before their arrest at the site of inflammation, which confirms the

supplementary role of chemokines and cell adhesion molecules in the adhesion of immune cells to the endothelium[397]. Two examples are IL-8 and MCP-1, shown to stimulate the firm adhesion of CXCR1/CXCR2-expressing neutrophils and CCR2-expressing monocytes to the endothelium, respectively. As illustrated in Fig. 5, the correlation of ICAM-1 expression with IL-8 and MCP-1 under shear flow in HUVEC and HBEC-5i follows a non-linear pattern, with the peak ICAM-1 expression happening at 4- and 24-hours of shear flow preconditioning, whereas the IL-8 and MCP-1 secretion continue to increase over a time course of 48 hours under flow condition. Theofilis, et al.[398] suggest that following the elevated level of inflammatory cytokines, critical cell adhesion molecules for rolling and adhesion of leukocytes, including ICAM-1, VCAM-1, E-selectin and P-selectin will be upregulated on the endothelium, which is consistent with our results.

5.2.3. Ultrasound-assisted Treatment During Microbubble Perfusion

With controlled shear-flow modulation as a basis, we next treated human endothelial monolayers under flowing microbubbles with ultrasound; first using HUVECs. Employing the flow-based data as a point of comparison, we compared ICAM-1 surface expression at 1 and 4 h post-sonication. Globally, we observed a modest increase in ICAM-1 expression ranging from 10-30% when treated with any of the ultrasound conditions employed here compared to sham controls (Fig. 6a-c); with 150 kPa for 2 min and 4 min, along with 210 kPa for 1 min obtaining statistical significance ($p<0.05$ for all three of these conditions). Furthermore, the responses due to ultrasound treatment on HBEC-5i were similar (Fig. 6d-e), reaching increases of surface ICAM-1 expression of 1.33-fold and 1.36-fold at the 150 kPa for 2 and 4-min treatments compared to untreated sham controls ($p<0.03$; $p<0.02$ respectively) at the 4-h post-sonication time-point. Indeed, our results here are consistent with studies that have explored the response of focused ultrasound and microbubbles on rodent brain vasculature. While direct comparisons are difficult due to the native acoustics and immunology differences between models, a subset of these in-vivo studies note that focused ultrasound treatment to the brain can result in a 2.1-fold increase in the number of ICAM-1 expressing cells[256], an approximate 2.5-fold increase in ICAM-1 gene expression[377], and an estimated 2.5-fold increase in ICAM-1 expression in brain tumors[211] compared to non-treated regions, and depending on the specifics of the treatment paradigm used. Following this, we next explored the subset of CAM-modulating acoustic conditions here on the expression of MadCAM-1. While there were no significant differences determined from HUVECs (data not shown), we did observe a 2.16-fold increase in surface MadCAM-1 expression in HBEC-5i under 150 kPa

treatment for 2 min as compared to sham controls at 1-hour post-sonication (Fig. 6f; $p<0.05$); with this transient increase returning to baseline by 4 hours post-sonication. Indeed, plasma membrane properties including stiffness (which may be different between these two cells of endothelial origin) may play a role in ultrasound-induced bioeffects under the same acoustic paradigm[399]. Given the more robust response of the human brain microvascular cells, we next proceeded to examine the ultrasound-modulated secretome of this cell type at both 1-hour and 4-hour time points (see Fig. 7). In this figure, the first two panels depict volcano plots in which the -log10 p-value is plotted against the magnitude of the fold-change (in 〖log〗_2 units) of the ultrasound treated group relative to the untreated sham control. Here, each cytokine/analyte is denoted by a point, with blue ones representing a strong (at least 2-fold; 〖log〗_2 of the fold change ≤-1) significant downregulation and red points representing significant upregulation (〖log〗_2 of the fold change ≥1) of a given cytokine. The identity of these analytes is shown in Fig. 7c-d, with the earlier time point characterized by the decreased expression of 4 cytokines, while only 2 analytes demonstrated increased concentrations. At the later time-point of 4 hours, there is increased secretion of 20 cytokines, many of which serve immune-activating roles (e.g. IL-8, CXCL9, IP-10, MIP-3α). Beyond highlighting the fold-change of individual secreted analyte concentrations, we performed gene over-representation analysis (ORA) of this 4-hour dataset to ascertain whether and to what extent changes in the secretome can be linked to known biological processes (Fig. 7e). Indeed, ORA analysis revealed multiple over-represented pathways involved in immune cell recruitment. Specifically, enrichment ratios were significant for several gene ontology (GO) terms including the chemotaxis and migration of leukocytes, and the modulation of IL-17, TNF, and NFκB signaling pathways. We note here that these ultrasound-induced changes are broadly consistent with whole-tissue analysis performed on focused ultrasound-treated pre-clinical models in the context of brain and brain tumors[377], [400], [401]. We acknowledge here that the role of these cytokines/chemokines is pleiotropic, highly contingent on the local environment, the presence of neighboring cells and tissue, and the magnitude and time course of its secretion. That being said, we explore the potential implications of ultrasound-induced increases in selected secreted analytes reported here in the following sections.

Among the chemokines most influenced by microbubble-mediated focused ultrasound shown here, IP-10 (CXCL10) has been shown to strongly attract T-cells and NK-cells and has generally

exhibited anti-tumor properties[402]. In fact, CXCL10 immune therapy strategies have been successfully implemented in murine models of glioblastoma, particularly from a dendritic cell vaccine viewpoint[403], [404], and very recently as an adjuvant therapy to immune checkpoint antibodies[405]. Along with CXCL9 – also shown here to increase under focused ultrasound treatment – CXCL10 secretion has shown a huge impact on the success of immune checkpoint inhibitor therapy[406]. Given the relatively large increased secretion from human brain endothelial cells shown here (5-fold for CXCL10 and 2.2-fold for CXCL9 over non-ultrasound controls), this data suggests that focused ultrasound may aid in augmenting local T-cell infiltration within the brain via the CXCL10 and CXCL9 axes.

Another analyte that was largely impacted by ultrasound treatment is VEGF-A. Indeed, angiogenesis has long been considered one of the hallmarks of tumor progression[407], and VEGF is one of the most prominent and well-studied angiogenic factors - with its expression positively correlating with tumor microvascular density and poor prognosis in many human tumors[408], [409]. Numerous anti-angiogenic agents targeted towards VEGF signaling are used clinically (e.g. bevacizumab targeting VEGF-A; ramucirumab targeting VEGFR-2) – however the success of this approach has not met its full potential[410]– notably in glioblastoma, where despite its highly vascularized nature, anti-VEGF treatment via bevacizumab corresponds with increased tumor cell infiltration (invasive potential)[411] and has not translated to any improvement in patient survival. Indeed, among other tumor and angiogenesis-related complexities[412], VEGF-A can either positively or negatively regulate endothelial activation; with prolonged exposure inhibiting endothelial-leukocyte interactions and decreasing endothelial responsiveness to proinflammatory cytokines. However, short-term exposure has been shown to increase adhesion molecular expression and leukocyte infiltration in in-vivo models[413], [414]. Here, our results indicate increased levels of VEGF-A up to ~3.8-fold sham-treated control at 4 h post-ultrasound exposure, which suggests that this may be used as a short-term strategy to transiently increase leukocyte infiltration – although this requires further investigation.

Within the TME itself, it is well understood that the hostile physiological milieu - including the balance of pro and anti-inflammatory molecules - plays a distinct role in hindering immunotherapies. To this end, particular attention has been paid to tumor-associated macrophages (TAMs), which can make up a large portion (30-50%) of a solid tumor by weight [415]. Indeed,

TNF-α plays a large role as a polarizing cytokine to induce TAMs towards the M1-like macrophage phenotype; a subset of macrophages that strongly presents antigens and secretes many pro-inflammatory chemokines and cytokines, including TNF-α itself[416]. Furthermore, TNF-α serves many other immune-activating roles, including downregulating immune-suppressing regulatory T cells within the TME[417], and attraction of neutrophils and monocytes to take part in anti-tumor responses[418] – notably when transiently present in high local concentrations[419].

Our results also highlight that ultrasound-assisted microbubble treatment increases endothelial secretion of IL-8 (CXCL8), a potent chemoattractant for neutrophils. While traditionally not considered a major player in the TME, recent evidence suggests that neutrophils can play a role in tumor initiation, development and progression. There are several studies that suggest neutrophils may exert direct cytotoxic activities or indirectly lead to tumor regression through the recruitment and induction of tumor-specific T cell responses[420], [421]. Tumor-associated neutrophils (TANs), similar to TAMs, can acquire an antitumor (N1) or immunosuppressive (N2) phenotype (e.g. in the absence/presence of TGF-β), the extent to which can influence the outcomes of emerging immunotherapies, including immune checkpoint therapy (e.g.[422]). Indeed, TANs differ from naïve bone-marrow neutrophils in that they show an enhanced chemokine secretion profile[423], thereby contributing to a feedback mechanism for recruiting more neutrophils and other immune cells to the TME; specifically, chemokines including CCL3, CXCL2, and CXCL1 (GROα)[424]; some of which are also enhanced under the current ultrasound exposure regimen (Fig. 7f).

Finally, we directly compare the modulated expression of seven cytokines that are shared between the shear-flow mediated (Fig. 4a) and ultrasound-mediated therapy – see Fig. 7f. Here, the fold-change expression of LIF, GCP-2, VEGF-A, TNFβ, M-CSF, IL-8 and GROα exhibited by HBEC-5i under shear flow (blue bars) and ultrasound and microbubble treatment (red bars) at 4 hours is displayed. We note here that this is only a subset of those induced via flow (Fig. 4a) and microbubble-mediated ultrasound (Fig. 7c-d). While both the flow-induced ICAM-1 surface expression and endothelial secretome modulation share some qualitative similarities with the ultrasound dataset, further research will involve in-depth pathway analysis to highlight the degree of mechanistic similarity. Indeed, the shear stress induced by vibrating microbubbles is expected

to be much larger in magnitude (~15 kPa, or 15 kdyn/cm2)[31] but over a much shorter timescale (~μs – ms).

5.3. Conclusion

Here, we report on the endothelial over-expression of two surface adhesion molecules (ICAM-1 and MadCAM-1) and the modulation of endothelial secretome due to flow-induced shear stress and microbubble-mediated focused ultrasound therapy. Indeed, preconditioning under flow resulted in time-dependent modulation of CAM expression, the character of which was dependent on the endothelial origin. Further, there was a heterogeneity in the time-dependent modulation of cytokines and chemokines; with some significantly enhanced (up to 16.2-fold; $p<0.001$) from both endothelial cell types under flow (e.g. IL-8, MCP-1, MCP-3), and others differentially expressed (e.g. CCL5, CXCL-16, SDF-1). Under ultrasound exposure, both endothelial cell types demonstrated increased surface levels of ICAM-1 expression at 4h post-sonication, while only HBEC-5i demonstrated enhancement of MadCAM-1 compared to untreated controls. Microbubble-mediated therapy resulted in large-magnitude (>2-fold) and significant ($p<0.05$) differential expression of 20 cytokines at 4 hours post-treatment, most of which had immune-activating function and were within a similar subset to those induced by shear-flow. Taken together, this dataset suggests that focused ultrasound-induced changes in endothelial immunobiology share some, but not all, general characteristics of flow-induced shear. Specifically, increased expression of immune-modulating factors including surface CAM and pro-inflammatory secretions.

5.4. Experimental Methods

5.4.1. General Cell Culturing

Two human endothelial cell models, either umbilical vein (HUVEC, C2519A; Lonza, Walkersville, MD, USA) or cerebral microvascular endothelial cells (HBEC-5i, CRL-3245TM; ATCC, Manassas, VA, USA), were employed in this study. The cerebral HBEC-5i were seeded in pre-coated culture dishes with 1 mL gelatin (0.1%; ATCC) per 10 cm2, and were grown in DMEM:F12 (Wisent, Canada) cell culture medium supplemented with 10% fetal bovine serum (FBS, Wisent) and 40 μg/mL of endothelial growth supplement (ECGS, ATCC). Since HBEC-5i is an immortal cell model (SV40 large T antigen transformation), they were used up to passage 20. HUVECs were cultured in endothelial cell growth medium (EGM-2; CC3162, Lonza) up to passage 9. Ibidi chamber slides (Ibidi, Gr¨afelfing, Germany) were used for cell cultivation and

treatment under flow. These slides have a 2.5 cm2 growth area, originally treated with collagen-IV. However, 45 min prior to HBEC-5i cultivation, the growth surface of the chamber slides was coated with 0.1% gelatin to provide extra support for HBEC-5i adherence. Endothelial cells, either HBEC-5i or HUVEC, were seeded in the chamber slides at a density of 120,000 cells/cm2. All seeded slides, whether cultured statically or under fluid flow conditions, were maintained within an incubator at 37℃ with 5% CO2 and 95% air atmosphere.

5.4.2. Flow Apparatus

The flow system has been described previously[149], see Figure 1a for experimental schematic. Briefly, the ibidi flow system consists of a fluidic unit, air pressure pump, and flow controller software used to cultivate and treat endothelial cells under unidirectional laminar flow. To generate a constant flow, the fluidic unit was mounted with a yellow/green perfusion set with a total working volume of 13.3 mL. The air pump provided air pressure to drive the fluid flow through the fluidic unit. Additionally, the flow controller software was used for precise regulation of flow parameters including flow rate, shear stress and flow cycle gradient. Before cell cultivation under flow, the perfusion set was primed with cell culture media and flow was applied for at least 30 min to remove any air bubbles in the fluid to prevent flow interruption. The ibidi flow software calculates flow parameters based on the characteristics of the perfusion set, chamber slide geometry and the viscosity of perfusion medium, which is assumed to be 0.0072 dyn /cm2 due to its similarity to that of water at 37°C. Flow shear stress is determined via $\tau = \eta \cdot$ factor. Φ, where τ is shear stress (dyn/cm²), η is dynamical viscosity (dyn /cm²), and Φ is the flow rate of the perfused medium (mL/min).

5.4.3. Cell Culturing Under Shear Flow

To assess the effect of shear flow preconditioning on endothelial cell physiology, cells were cultivated statically in 0.2 mm µ–Slides for two hours to allow cell adherence to the growth surface, followed by exposure to an augmented gradient of shear flow ranging from 1.5 to 7 dyn/cm2 for cell adaptation to the flow condition. Subsequently, cells were subjected to a shear flow of 9 dynes/cm^2, corresponding to a 2.8 mL/min flow rate, for a duration ranging from 0-48 hours. First, to assess the effect of time-dependent shear flow on the endothelial secretome expressed by either HUVEC or HBEC-5i, a small sample (100 µl) of cell media supernatant was collected from each chamber slide at different time points (from 1-48 hours post gradient shear flow, depending on the

endothelial cell type). Subsequently, the level of these factors was quantified using Luminex xMAP technology (see below). Additionally, HUVEC and HBEC-5i, cultivated under similar conditions, were examined for the surface expression of either ICAM-1 or MadCAM-1 using immunohistochemistry (see below). The secretome and expression of ICAM-1 and MadCAM-1 under static cultivation were used as respective controls.

5.4.4. Immunohistochemistry

Endothelial cells were fixed with 2% paraformaldehyde (3C28557, Millipore Sigma) for 30 min, followed by incubation with 0.1% Triton X-100 (Triton® X-100 Surfactant, Millipore Sigma) for cell permeabilization. In order to block the non-specific binding of mABs and prevent the high intensity background, cells were incubated with a blocking buffer consisting of regular non-fat milk powder at a concentration of 0.05 g/mL in 5 phosphate-buffer saline with 5% bovine serum albumin (PBS-BSA) for 45 minutes. Subsequently, cells were incubated with either ICAM-1 monoclonal antibody (MA5407, Invitrogen) or MadCAM-1 polyclonal antibody (PA598417, Invitrogen) for 1 hour, followed by washing five times with PBS-BSA to remove any unbound antibodies. Due to the specific geometry of chamber slides which can trap air bubbles if medium is fully removed, continuous medium exchange was used for washing with PBS-BSA. For each wash, 50 µl PBS-BSA was added through one inlet and removed from the opposite inlet. This process was repeated three times for each wash, in a total of 15 times to complete the 5 washes with a total volume of 750 µl PBS-BSA per slide. Next, the cells were incubated with secondary antibodies including either Alexa Fluor 488 (Donkey anti-mouse IgG, A21202, Invitrogen) or Alexa Fluor 555 (goat anti-rabbit IgG, A21428, Invitrogen), respectively, and washed five times with PBS-BSA. In the end, cell nuclei were counterstained with DAPI (Thermofisher) for two min. As a negative control, some slides were stained with only primary or secondary antibodies. All the staining steps were performed at room temperature. To examine the surface expression of CAMs, cells were visualized using an inverted fluorescence microscope (Nikon Ti2A, Melville, NY) equipped with an LED light source (D-LEDI, 10-50% intensity, Nikon) and DAPI (#96389, 378/447 nm; Nikon), GFP (#96392, 466/525 nm; Nikon, and DAPI (#96394, 554/609nm; Nikon) filter cubes. At least five non-overlapping locations (1.2 by 1.2 mm field of view) from each slide were imaged using a 10x objective (#MRH00101, Nikon), and images were quantified using in-house MATLAB software to calculate the signal intensity per cell.

5.4.5. Multiplex Cytokine Release Assay

For the assessment of human cytokines, chemokines and growth factors under either shear flow preconditioning or ultrasound treatment, multiplex immunoassay was used to measure the secretion concentration of 96 factors in each sample. The multiplex analysis utilizes uniquely color-coded magnetic beads, each of which is coupled with a specific capture antibody for each analyte. To be able to examine the level of 96 factors, two 48-plex kits (MilliporeSigma, Burlington, Massachusetts, USA) were used: panel A consist of sCD40L, EGF, Eotaxin, FGF-2, FLT-3 Ligand, Fractalkine, G-CSF, GM-CSF, GROα, IFN-α2, IFN-γ, IL-1α, IL-1β, IL-1RA, IL-2, IL-3, IL-4, IL-5, IL-6, IL-7, IL-8, IL-9, IL-10, IL-12(p40), IL-12(p70), IL-13, IL-15, IL-17A, IL-17E/IL-25, IL-17F, IL-18, IL-22, IL-27, IP-10, MCP-1, MCP-3, M-CSF, MDC, MIG/CXCL9, MIP-1α, MIP-1β, PDGF-AA, PDGF-AB/BB, RANTES, TGFα, TNF-α, TNF-β, and VEGF-A, and panel B consists of 6CKine, APRIL, BAFF, BCA-1, CCL28, CTACK, CXCL16, ENA-78, Eotaxin-2, Eotaxin-3, GCP-2, Granzyme A, Granzyme B, HMGB1, I-309, I-TAC, IFNβ, IFNω, IL-11, IL-16, IL-20, IL-21, IL-23, IL-24, IL-28A, IL-29, IL-31, IL-33, IL-34, IL-35, LIF, Lymphotactin, MCP-2, MCP-4, MIP-1δ, MIP-3α, MIP-3β, MPIF-1, Perforin, sCD137, SCF, SDF-1, sFAS, sFASL, TARC, TPO, TRAIL, and TSLP. First, antibody-coated microspheres are incubated with the sampled cell supernatant, followed by washing to remove the non-attached analytes. Next, the coated beads with the captured analytes are incubated with biotinylated antibodies against all the targets, followed by another wash. In the end, the beads are exposed to the reporter streptavidin-phycoerythrin to detect the bound analytes. LuminexTM 200 (Luminex, Austin, TX, USA), which is a dual laser system, was used to identify the detected analytes, as well as their concentration. In this system, the first laser excites the internal color of each bead to identify the presence of each analyte, whereas the second laser quantifies the intensity of the phycoerythrin signal, which is proportional to the concentration of each analyte. For a subset of this dataset, gene over-representation analysis was performed using web-based software (https://www.webgestalt.org/). This was to determine statistically significant (Fisher's exact test) over-representation of the modified secretome set compared to the human protein encoding genome. The enrichment ratio (ER) reported is defined here as the number of genes within our list that fall within a given functional/signaling category divided by the expected number, given the total number of genes in the database (KEGG database) for that category. Only those with false discovery rates (adjusted for multiple comparisons) less than 0.05 are shown.

5.4.6. Ultrasound-assisted Treatment During Microbubble Perfusion

A customized acoustically coupled inverted microscopy system was developed, by aligning a coupling cone for the transducer to the microscope field of view, to visualize the ultrasound bioeffects during the sonication. The coupling cone was fixed at 27 mm distance from the growth area of the chamber slides, with 45° angle from the normal to minimize ultrasound reflection. Given the geometry of the system used here, the acoustic beam width projected along the surface of the cells is approximately 3.5 mm. Acoustic characterization of the beam resulted in a transmission loss due to the chamber slide on the order of 5% [149]. To enable treatment under flow, a fluidic system was placed next to the ultrasound delivery system and mounted with a perfusion set. The reservoirs were primed with 15 mL cell culture medium, and the fluid flow was initiated using the ibidi pump system for 30 min to remove any air bubbles in the fluid. Next, a cell-seeded chamber slide was connected to the perfusion set and perfused with DefinityTM microbubbles (1:2500 dilution) for two min to allow a uniform distribution of microbubbles. DefinityTM microbubbles were activated from room temperature using the VialmixTM shaker for 45s, after which they were allowed to rest for another 15 min to equilibrate to room temperature[425]. Native, undiluted microbubble size and concentration were confirmed using a Coulter Counter Multisizer 4 (Beckman Coulter, Indianapolis, IN, USA) to be consistent with the literature (~1010 bubbles/ml; bi-modal volumetric peak in size distribution). The surface of the slide was water coupled with the coupling cone, and four non-overlapping regions from the slide were sonicated (1 MHz frequency, 20 cycles, 1 ms PRI), at a peak-negative pressure of either 150 or 210 kPa with a sonication duration ranging from 1-4 min. The acoustic beam was characterized in a separate water-tank with a hydrophone (HGL-200, Onda Corp., Sunnyvale, USA). The surface expression of either ICAM-1 or MAdCAM-1 was assessed as a factor of time post-sonication, either 1 or 4 hours. For a subset of these, the supernatant was collected for cytokine analysis. In this case, immediately after ultrasound treatment, the flow was stopped, and the chamber slide was disconnected from the fluidic unit to prevent the dilution of cell supernatant with the media in the reservoirs. To be consistent with all other experiments, the chamber slides were placed in an incubator at 37℃ with 5% CO2 for either 1 or 4 hours. Next, 100 µl of cell media supernatant was sampled from each slide, and the concentration of 96 factors, similar to the shear-flow assay, was examined using the same multiplex immunoassay.

5.4.7. Justification of Parameter Selection

It is worth discussing the justification for the shear flow, molecular biology readouts and acoustic conditions employed in this study. Firstly, the shear stress in arterial vessels and veins has been reported to range between 10 to 70 dyn/cm^2 and 1-6 dyn/cm^2, respectively[336], whereas brain microvasculature experiences shear flow ranging from 5 to 23 dyn/cm^2 [426]. Our selected shear stress of 9 dyn/cm^2 falls on the lower end of these physiological ranges, albeit slightly above the reported range for venous blood flow. In terms of our selection of endothelial surface expression markers, downregulation of ICAM-1 and MadCAM-1 (and others) have been reported in tumor-associated vessels from a range of human malignancies[368], [427]. Firstly, ICAM-1 is a notably important adhesion molecule in the context of immune cell adhesion and trafficking and has long been studied in this context[428], [429]. Further, MadCAM-1 is expressed on human brain endothelium and plays a role in NK cell transmigration[430], [431]. With respect to the ultrasound treatments, the microbubble concentration was chosen (1:2500 dilution) to fall within the clinical implementation, which typically reaches a dilution of approximately 1:2500-1:5000 after intravenous administration. The ultrasound parameters were chosen after a pilot study to minimize losses in cell viability and detachment in both endothelial cell lines, while still within the range of those reported for immunomodulation studies elsewhere, and relevant to therapeutic parameters used clinically.

5.4.8. Statistical Analysis

The data in this study have been analyzed using GraphPad prism and are reported as mean ± SD. To assess the surface expression of CAMs, a minimum of 4 independent slides were analyzed, and imaging was performed on 5-10 randomly selected regions on each slide, with at least n=3 slides per condition. The level of CAM expression was quantified using in-house software in MATLAB by measuring the fluorescence intensity of the cells. All secretome data was assessed on at least n=2 samples per condition. Statistical comparison across different treatment regimens on the CAM expression was made by two-tailed, unpaired two-sample Student's t-tests. A p-value of <0.05 was taken to be statistically significant.

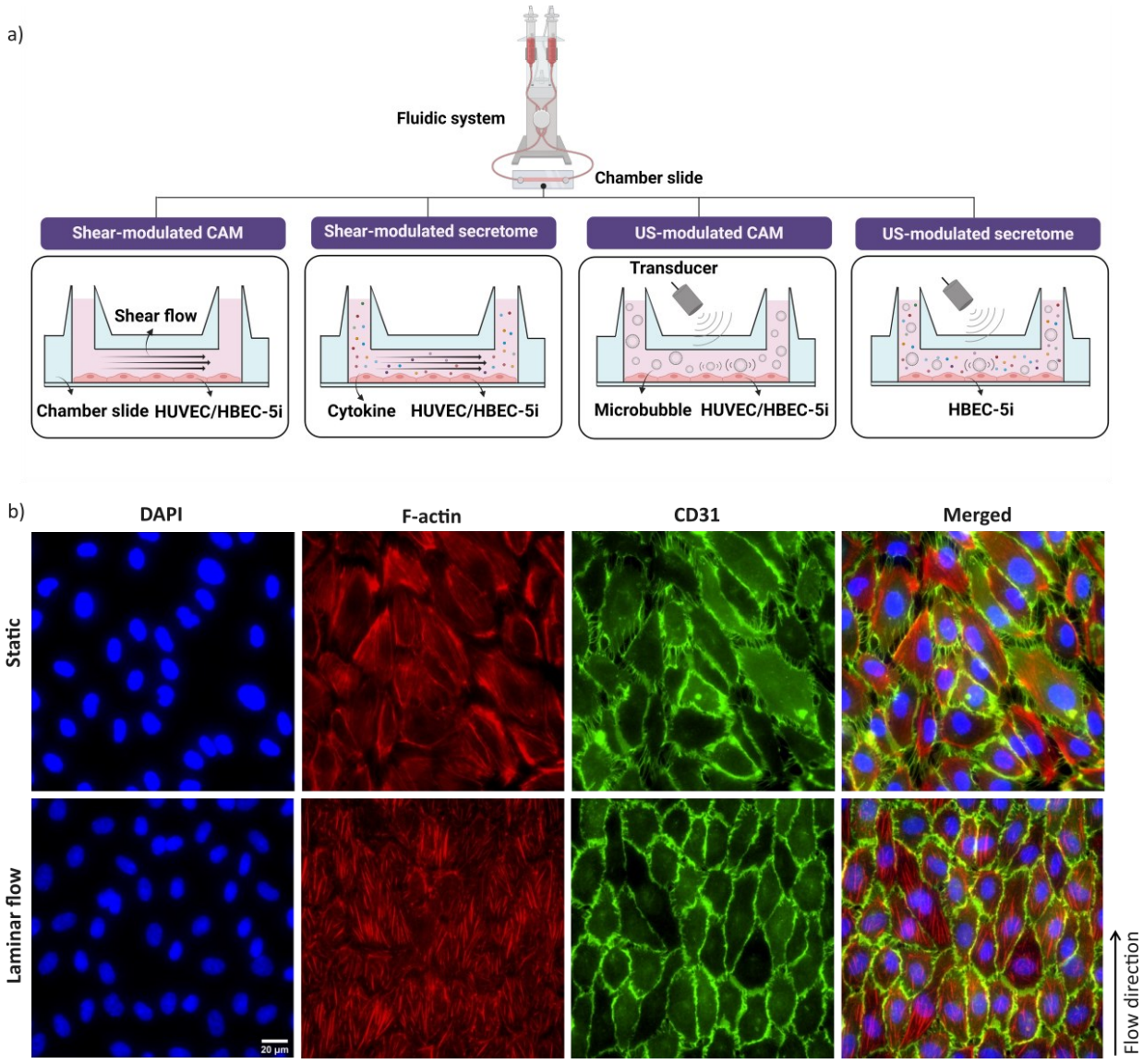

Figure 5.1: Schematic illustration of the experimental setup and the influence of shear flow on cellular morphology. a) Human endothelial cells, either HUVEC or HBEC-5i, were subjected to 9 dyn/cm^2 shear flow for 0-48 hours. The effect of laminar shear stress on the surface expression of ICAM-1 and MadCAM-1 was conducted using immunofluorescence microscopy, and endothelial secretome profiling was assessed through multiplex immunoassay. Additionally, the effect of ultrasound-stimulated microbubbles (1 MHz, 150-210 kPa, 20-cycle burst, 1 ms PRI, 1–4 min durations) was investigated on the surface expression of ICAM-1 and MadCAM-1 in HUVEC and HBEC-5i. Finally, microbubble-mediated modulation of cytokine profile was further studied in HBEC-5i. b) Fluorescence microscopy images represent the effect of laminar shear flow precondition on HUVEC morphology as compared to statically cultivated cells. Cell nuclei are stained in blue, actin filaments are stained in red and PECAM-1 (CD31) is stained in green. The fluorescent images indicate that long-term laminar flow preconditioning results in a more uniform morphology, improved cell-to-cell contact, reduced extracellular gaps and cell orientation in the direction of flow. In

contrast, statically seeded cells display highly heterogeneous morphology, random orientation and significantly larger extracellular gaps between endothelial cells.

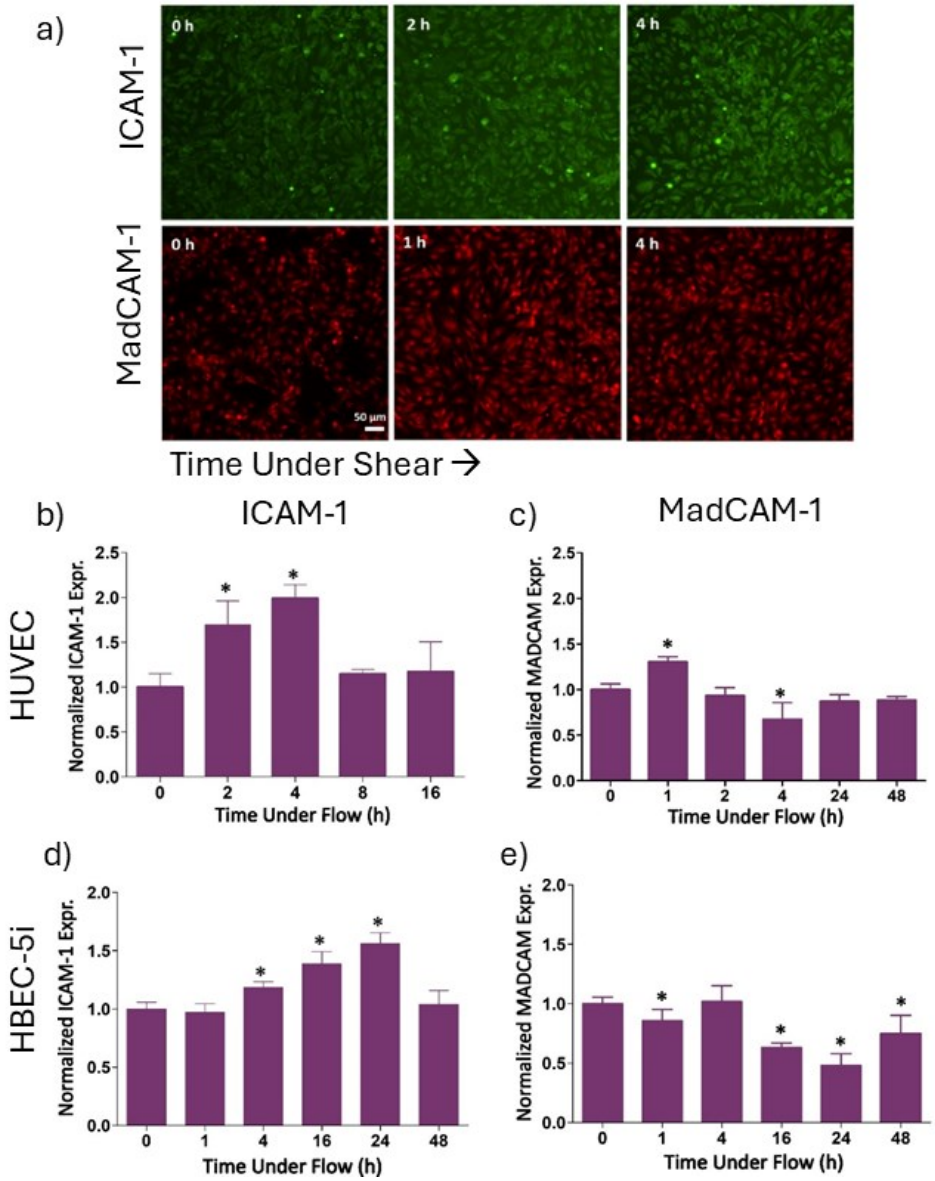

Figure 5.2: Time-dependant shear flow differentially modulates the surface expression of ICAM-1 and MadCAM-1 on human endothelial cells. A confluent endothelial monolayer was seeded in chamber slides and exposed to 9 dyn/cm^2 shear flow ranging from 0-48 hours. a) Representative fluorescence microscopy images illustrating a temporal regulation of ICAM-1 (top panel) and MadCAM-1 (bottom panel) expression under shear flow conditions for HUVEC. ICAM-1 is marked in green, stained by Alexa fluor 488-conjugated antibody, whereas MadCAM-1 is shown in red, stained by Alexa fluor 555-conjugated antibody For HUVEC, b) Quantification of ICAM-1 expression showed a significant upregulation in response to shear flow preconditioning, with a peak increase at 4 h, and it returned to the baseline level by

8 h. c) MadCAM-1 expression revealed a different temporal pattern, reaching a minimum of 8 h after exposure to shear flow. For HBEC-5i, d) Quantification of ICAM-1 surface expression revealed a time-dependent upregulation, with a peak increase at 24 h post-exposure to shear flow and it returned to the baseline by 48 h. e) In contrast, MadCAM-1 expression under shear flow preconditioning showed an opposite trend, and the expression level reached a minimum by 4 h. No statistical difference between the treatment and sham control was observed unless marked on the plot.

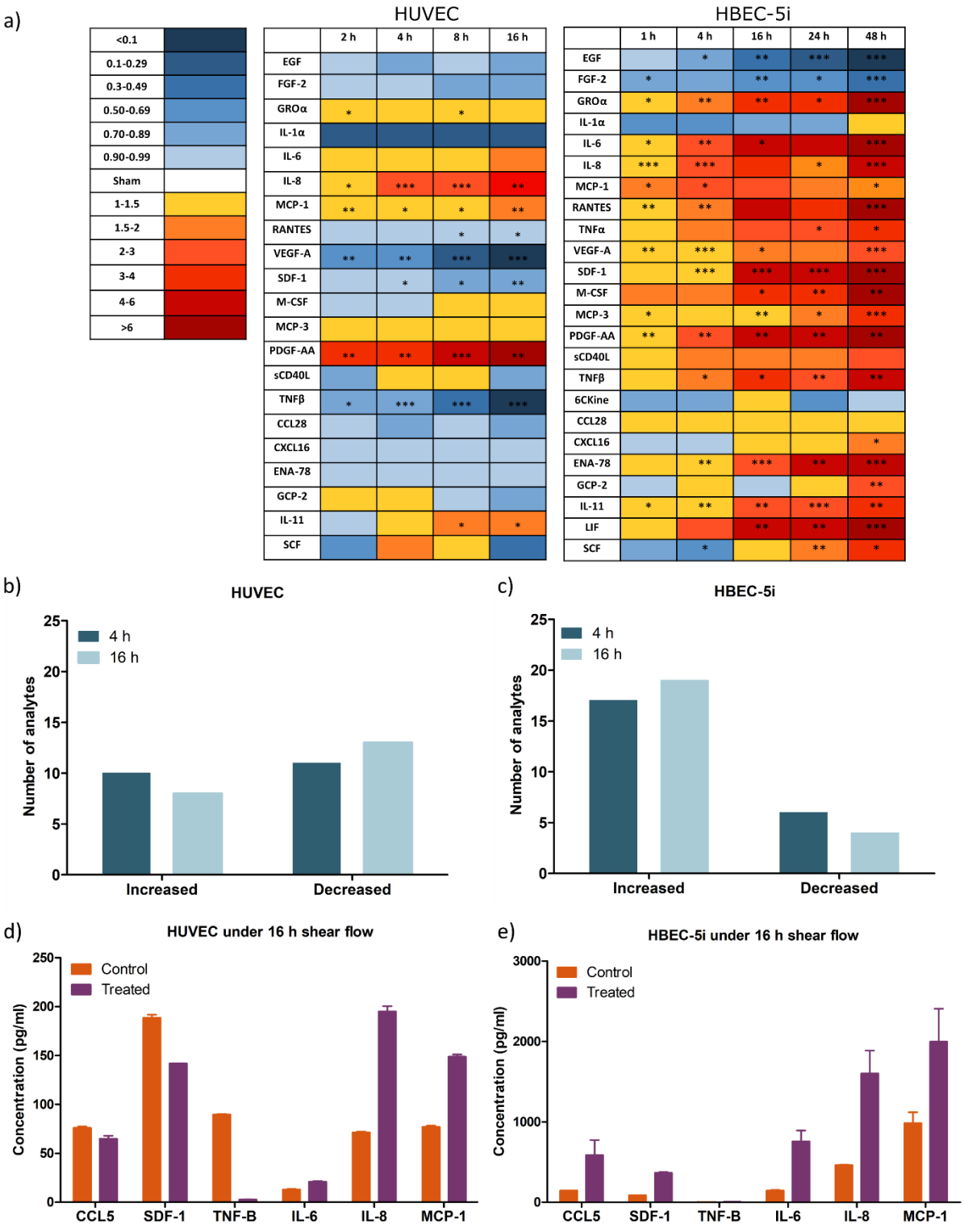

Figure 5.3. Shear flow preconditioning modulates endothelial secretome based on cell origin. a) Heat maps display the influence of shear flow preconditioning on (left) HUVEC and (right) HBEC-5i secretomes. The secretion level of different analytes was quantified using Luminex™ 200 technology and

normalized to the static control. Asterisks indicate statistical significance, with *, **, *** denoting $p<0.05$, $p<0.01$, $p<0.001$, respectively). Our results revealed that shear flow preconditioning differently influences both secretomes; shear flow increased the secretion level of most examined analytes in HBEC-5i, including a subset of immune cell trafficking markers such as CCL-5, CXCL-15 and SDF-1, whereas the secretion level of these factors decreased in HUVEC under similar flow conditions. b,c) A summary of cytokine fold-change following 4- and 16-hour shear flow preconditioning. These plots display the number of cytokines, chemokines, and growth factors that were either upregulated or downregulated in HUVEC or HBEC-5i in response to 4- and 16-hour laminar shear flow preconditioning. Finally, selected factors that were differentially secreted by d) HUVEC and e) HBEC-5i after shear preconditioning for 16 hours are illustrated here. Our findings indicate that a subset of critical factors involved in inflammation and immune cell recruitment exhibit differential responses to the same shear flow conditions depending on the cell origin. Additionally, the baseline concentration of these cytokines varies considerably between these two cell types, with HBEC-5i generally displaying a significantly higher concentration of proinflammatory mediators than HUVEC.

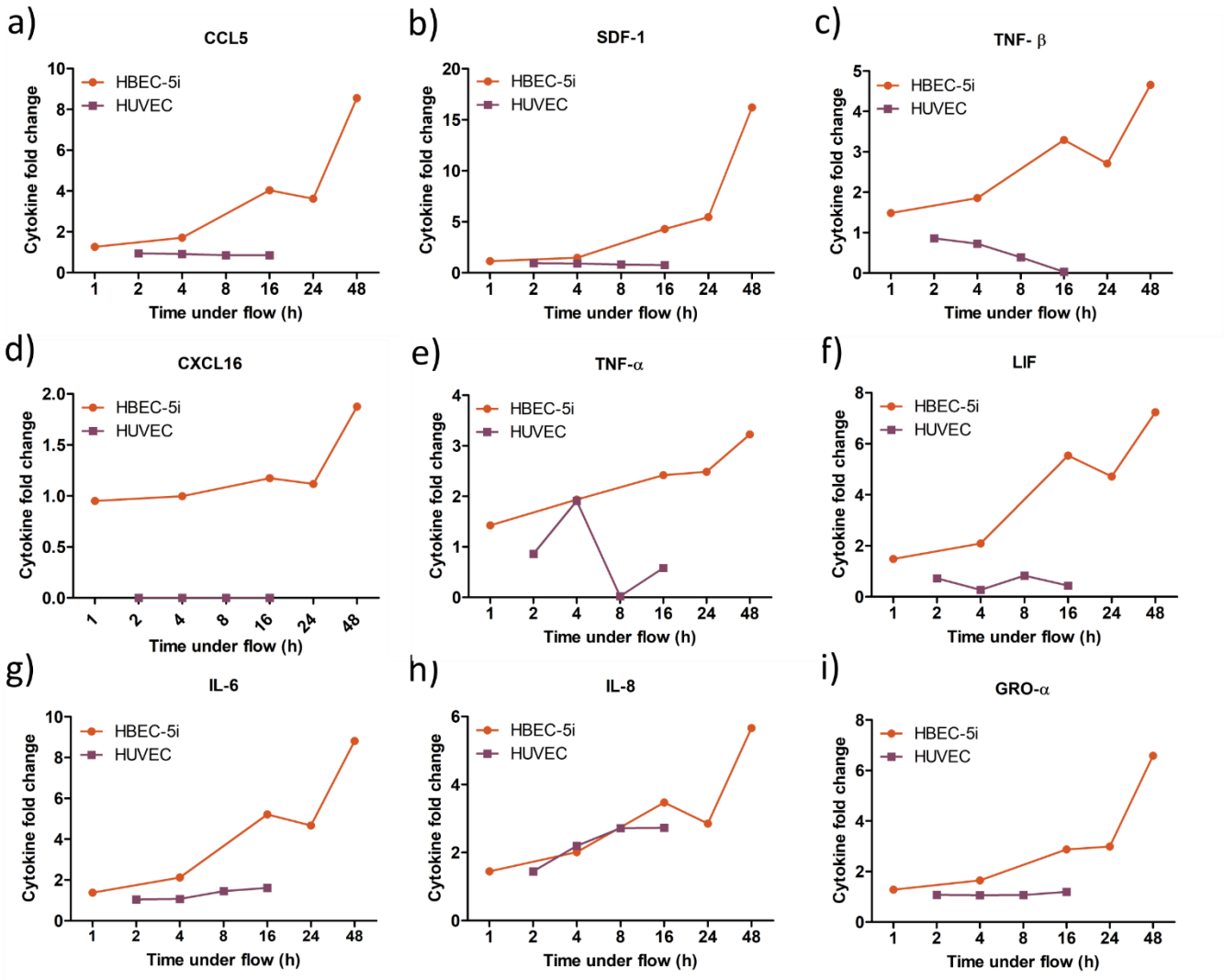

Figure 5.4: Shear-mediated modulation of selected inflammatory factors in HUVEC and HBEC-5i exhibit different temporal patterns. a-c) These plots illustrate the reverse pattern of cytokine secretion between HVEC and HBEC-5i in response to shear flow preconditioning under the same condition. Over time, each cytokine in HBEC-5i shows a significant upregulation up to 16-fold at 48 hours, whereas cytokine secretion is considerably downregulated in HUVEC. d-f) Analytes listed here are highly expressed in HBEC-5i, with an increase in their secretion level under shear flow over the course of 48 hours. However, the baseline level of these factors in HUVEC is extremely low, or completely absent in the case of CXCL16. g-h) The last row indicates a subset of chemokines with similar secretion patterns in HUVEC and HBEC-5i under shear flow conditions, showing an increase in secretion levels over time.

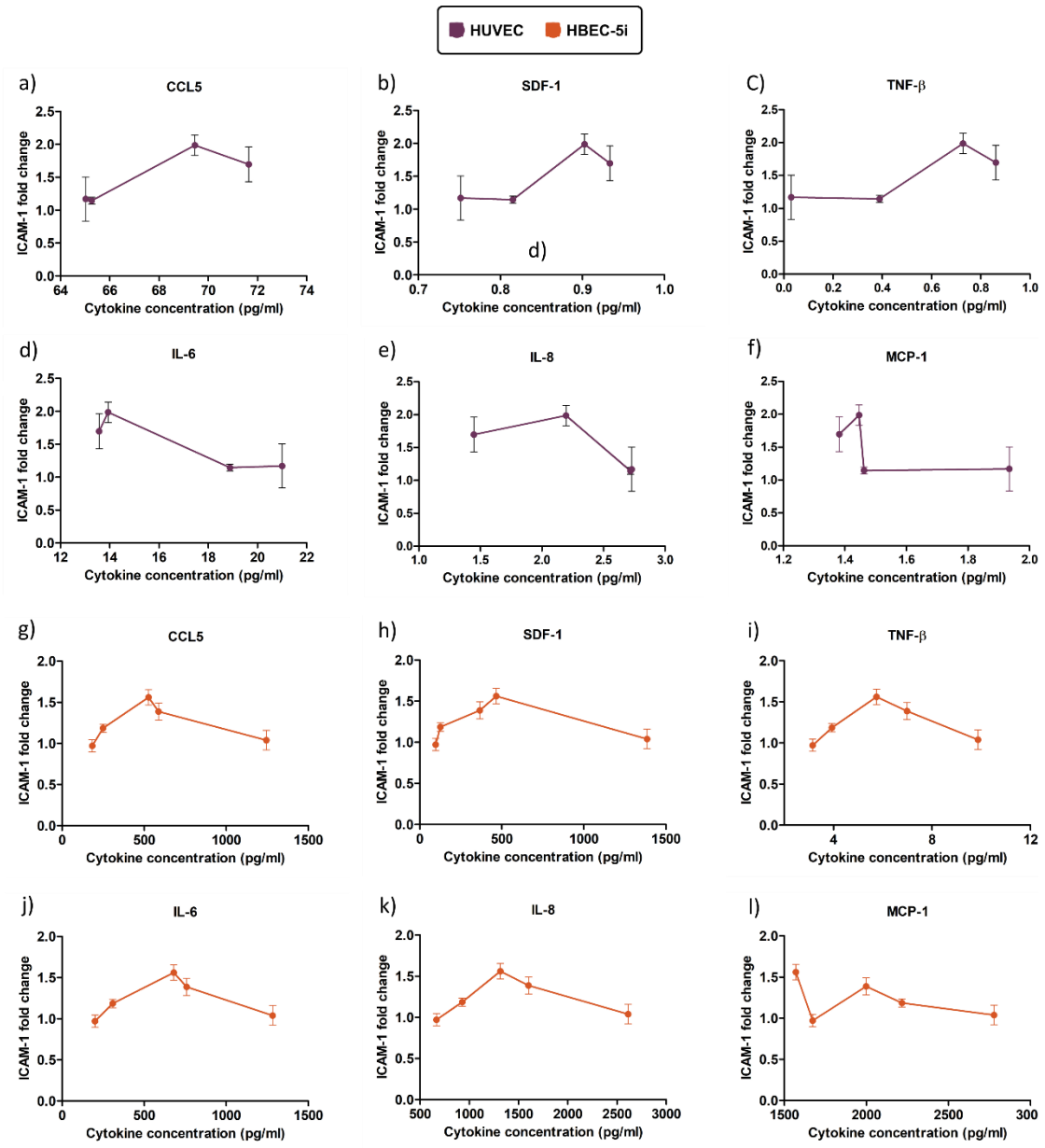

Figure 5.5: ICAM-1 surface expression on endothelial cells is correlated with shear flow-mediated cytokine secretion. These plots illustrate the correlation between individual cytokine concentration with ICAM-1 fold change in either a-f) HUVEC or g-l) HBEC-5i, subjected to 9 dyn/cm^2 laminar shear flow over time. The selected cytokines here are known to be involved in inflammation (CCL5, SDF-1, TNF-β) and chemotaxis (IL-6, IL-8, MCP-1). As plots show, ICAM-1 surface expression in either HUVEC or HBEC-5i has a non-linear correlation with inflammatory cytokines and chemokines concentration. This observation indicates that ICAM-1 expression fold change transiently increases up to a certain concentration of each cytokine, followed by a decrease or reaching a plateau in the higher concentration.

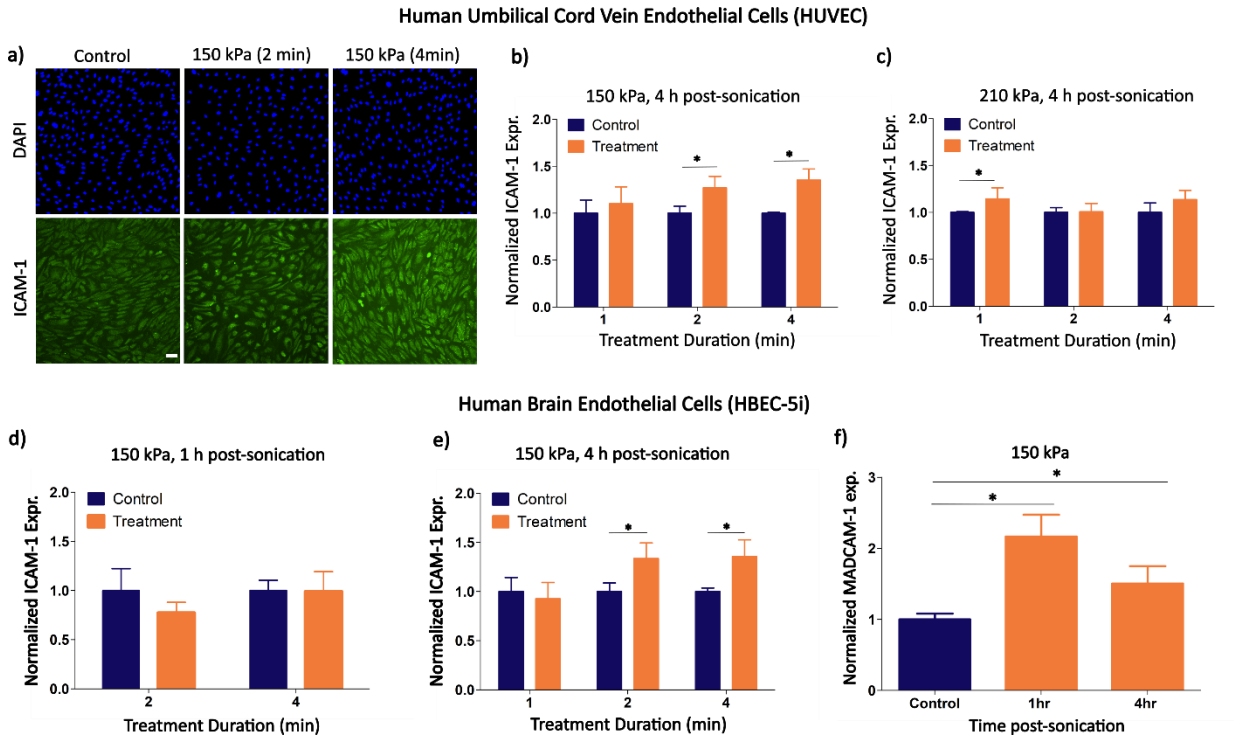

Figure 5.6: Ultrasound-stimulated microbubbles increase CAM surface expression in both endothelial cell types. Endothelial cell-seeded chamber slides were constantly perfused with microbubbles at a flow rate of 2.8 mL/min and sonicated with ultrasound at different acoustic pressures and sonication durations. a) Representative fluorescence microscopy examples of ICAM-1 expression on HUVEC treated under different acoustic pressures and sonication durations. The surface expression of ICAM-1 was assessed at 4 hours post-sonication. b,c) Quantitative analysis of ICAM-1 expression from HUVEC demonstrated its upregulation under three ultrasound conditions: sonication at acoustic pressure of 150 kPa for 2 or 4 min, and 210 kPa for 1 min. d) For the brain endothelial cells (HBEC-5i), quantification of ICAM-1 surface expression at 1-hour post-sonication demonstrated no change in the expression as compared to the untreated cells. e) In contrast, ultrasound treatment under similar conditions significantly upregulated the surface expression of ICAM-1 at 4 hours post-sonication, highlighting the importance of post-sonication time in the modulation of ICAM-1 expression for this endothelial cell type. f) Ultrasound treatment significantly increased the expression of MadCAM-1 on HBEC-5i as compared to untreated cells, with a peak expression observed at 1-hour post-sonication. The influence of ultrasound treatment was assessed on the expression of MadCAM-1 on both HUVEC and HBEC-5i, however only HBEC-5i experienced an upregulation of MadCAM-1 in response to treatment. Therefore, the data for HUVEC is not shown here. No statistical difference between the treatment and sham control was observed unless marked on the plot.

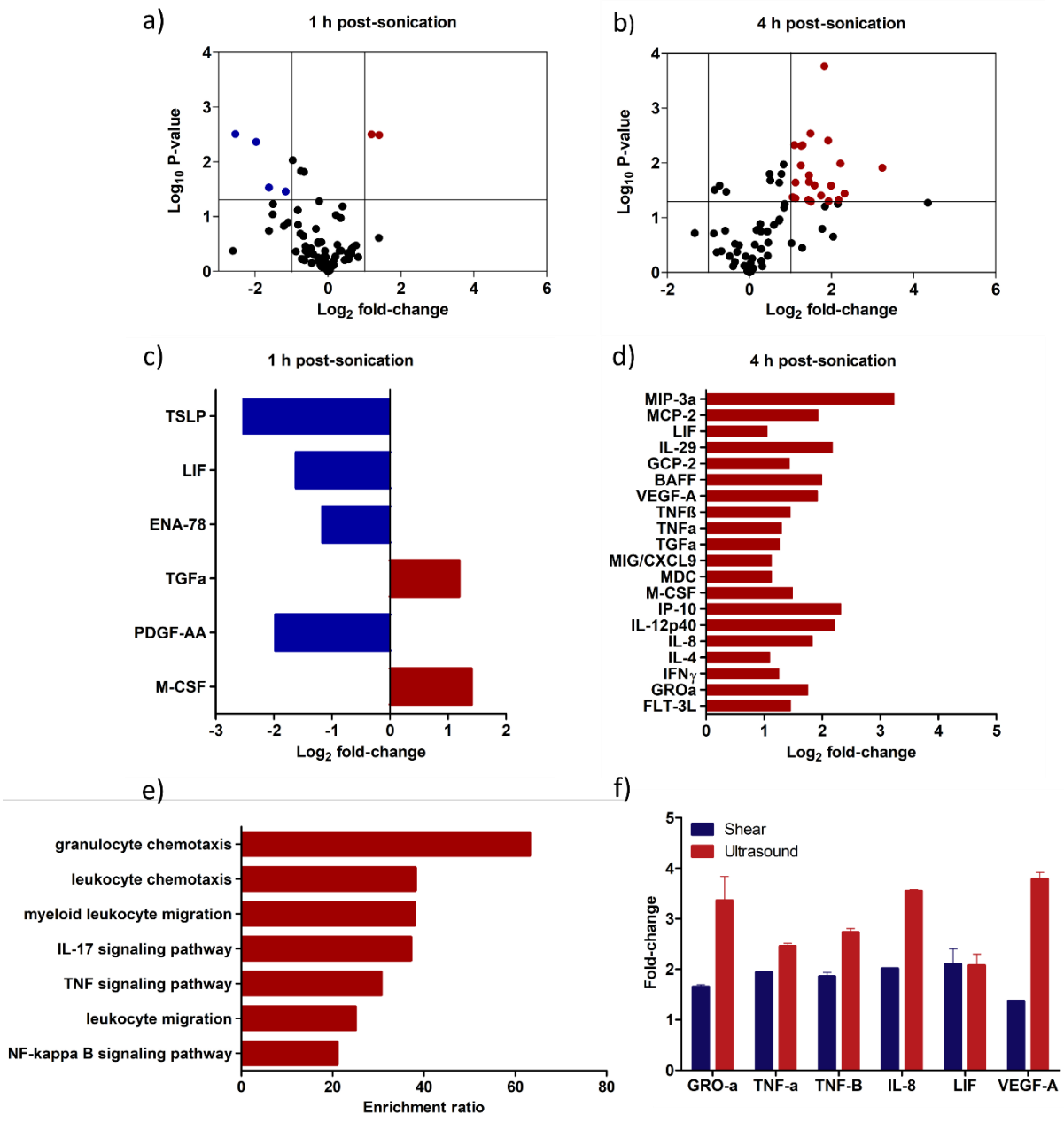

Figure 5.7: Microbubble-mediated treatment modulates HBEC-5i secretome profile. a,b) Volcano plots illustrating the differential secretion of various analytes at either 1 or 4 hours after ultrasound treatment compared to the non-sonicated cells. Each dot represents an analyte, where black dots show analytes with minimal or no change, red dots indicate analytes upregulated by at least 2-fold, and the blue dots represent analytes downregulated by at least 2-fold. c, d) Identification of cytokines with a minimum of 2-fold change and statistically significant at either 1 or 4 hours after ultrasound treatment. Ultrasound treatment led to the

differential secretion of a limited number of factors 1-hour post-sonication, whereas 4 hours after treatment, 20 analytes experienced a significant upregulation, most of which are known for their immune-activating function. e) Gene over-representation analysis (ORA) of this 4-hour dataset reveals that changes in the secretome are linked to known biological processes, including immune cell chemotaxis and migration, along with TNF and NF-κB signaling. f) Comparison of the fold-change secretion of seven cytokines 4 hours after exposure to either shear flow (blue) or ultrasound-stimulated microbubbles (red) in HBEC-5i. The plot indicates that these cytokines exhibit a stronger response to ultrasound treatment than to laminar shear flow, likely due to higher shear stress exerted by microbubbles on endothelial cells.

6. Investigating the effects of US on CAR NK-92 cell recruitment and infiltration *in vitro*.

Chapter 6 presents unpublished results investigating the influence of ultrasound-mediated modulation of endothelial secretome and enhanced CAM expression on improving CAR NK-92 cell recruitment and trafficking *in vitro.*

6.1. Introduction and Motivation

The limited success of conventional therapies for brain malignancies, a combination of surgery, radiotherapy and chemotherapy, emphasizes the importance for alternative treatment strategies. In this regard, molecular and cellular immunotherapies have emerged as promising treatments, particularly for hematological malignancies. One of the most extensively investigated immunotherapies, in both pre-clinical and clinical studies, is the adoptive transfer of T cells. This approach involves the extraction of tumor specific T cells from a patient, expanding them *ex vivo*, and reinfusing them into the patient to trigger a stronger adaptive immune response. Despite its therapeutic potential, adoptive T cell therapy encounters significant challenges due to the tumor's ability to prevent T cell recognition. Tumors use multiple mechanisms to evade immune surveillance including lack of immunogenic antigens, loss of MHC class 1 molecules, and absence of co-stimulatory signals. Therefore, tumor cells resemble self-cells, impairing the function of cytotoxic T cells, which ultimately results in tumor escape. To address these challenges, an alternative strategy was introduced involving genetic modification of patient-derived T cells to express chimeric antigen receptor (CAR), to target tumor-specific neoantigens. Unlike regular T cells, CAR-engineered T cells can recognize a broad range of targets without relying on the antigen presentation through MHC complexes. Despite the promising results of CD19-CAR T cells for relapsed B-Cell acute lymphoblastic leukemia and diffuse large B-cell lymphoma, their clinical application is restricted due to multiple challenges including the risk of neurotoxicity, cytokine release syndrome (CRS), and the need for autologous preparation due to HLA dependence [14]. Due to these challenges, the focus of cellular immunotherapy has shifted toward CAR-NK cells, given that these immune cells offer several key advantages over CAR T cells. Beyond the recognition of specific tumor antigens by CAR molecules, NK cells intrinsically recognize stress-induced ligands, further preventing tumor immune escape. Moreover, NK cells naturally secrete significantly lower levels of proinflammatory cytokines as compared to T cells, which prevents the risk of CRS. The HLA-independent function of NK cells also enables the allogenic preparation

of CAR-NK cells, without the risk of graft versus host disease (GVHD)[432]. Despite the potential of CAR-NK cells in cancer immunotherapy, their efficacy for brain tumors is hindered due to the presence of a suppressive TME and limited permeability of BBB. Additionally, the downregulation of critical CAMs on tumor vascular endothelial cells further impedes CAR-NK cells infiltration into the tumor site. Addressing these challenges in clinical settings requires novel strategies to locally promote immune cell trafficking, extravasation and intra-tumoral effector function. In the context of brain cancer immunotherapy, ultrasound-stimulated microbubbles present a promising solution to revolutionize CAR cell therapies. Microbubble cavitation near the tumor vascular endothelium can transiently open the BBB, which facilitates the infiltration of immune cells to the tumor. Beyond BBB disruption, microbubble-induced shear stress can activate signaling pathways that are involved in promoting an anti-tumor immune response, thus improving immune cells recruitment and trafficking. Our results in chapters 4 and 5 demonstrate that US treatment can modulate the endothelial cytokine profile and upregulate CAMs such as PECAM-1, ICAM-1 and MAdCAM-1. Building on this, our objective here is to examine the efficacy of CAR NK-92 cell homing and rolling on US-treated endothelial cells.

6.2. Experimental Methods

6.2.1. General Cell Culture

Human cerebral microvascular endothelial cells (HBEC-5i, CRL-3245TM; ATCC, Manassas, VA, USA) were cultivated in DMEM: F12 cell culture medium (Wisent, Canada), supplemented with 10% fetal bovine serum (FBS, Wisent) and 40 µg/mL of endothelial growth supplement (ECGS, ATCC). Before cell cultivation, culture dishes were pre-coated with 0.1% gelatin (ATCC) with a concentration of 1 ml per 10 cm^2 for 45 minutes at 37 °C. Additionally, $HER2^+$ CAR NK-92 cells (provided by our collaborator) were cultivated in X-VIVO 10 culture medium supplemented with 10% human serum from male AB plasma (Sigma-H3667) and 100 unit/ml human recombinant IL-2 (Miltenyi, premium grade). They were fluorescently labeled by incubating them with Hoechst (1:500 dilution) for 20 minutes at 37 °C. Excess fluorescent dye was removed by centrifuging the cells and resuspending in fresh medium.

6.2.2. CAR NK-92 Cell Rolling and Adhesion Assay

A confluent monolayer of HBEC-5i with a density of 120,000 cells/cm^2 was cultivated in 0.2 mm ibidi chamber slides under laminar shear stress of 9 dyn/cm^2 for two days to bring the cells to a

more physiological-like state. A subset of the slides was treated with 100 ng/ml of TNF-α 24 hours prior to the experiments to upregulate endothelial cell surface expression of CAM. For the ultrasound-treated group, each cell-seeded chamber slide was continuously perfused with Definity microbubbles using the ibidi fluidic system. Next, 4 non-overlapping locations on each slide were sonicated using optimized ultrasound parameters mentioned in chapter 5 (1MHz frequency, 150 kPa peak negative pressure, 20 cycles, 1 ms PRI and 2 min sonication duration). To allow the secretion of pro-inflammatory cytokines and maximize upregulation of ICAM-1, ultrasound treated slides were incubated at 37 °C for 4 hours. For the rolling and adhesion assay, three groups of untreated (negative control), TNF-α treated (positive control) and US treated HBEC-5i were examined. First, fluorescently labeled CAR-NK-92 cells (1×10^6 cells/ml) were perfused over the endothelial monolayer with a flow rate of 2.8 ml/min, corresponding to 1 dyn/cm^2 shear stress, for 3 minutes to ensure a uniform distribution of immune cells within the chamber slides. The flow then was halted for 12 minutes to allow NK cells to interact with endothelial cells. Subsequently, CAR NK-92 cells were perfused again over the endothelial monolayer for 20 minutes under the same flow condition, and the real-time fluorescence microscopy videos were recorded. At the end, the slides were disconnected from the fluidic system and washed with fresh media multiple times to remove any unattached CAR NK-92 cells to the endothelial monolayer. To quantify the average number of adhered CAR cells, a minimum of 10 random fluorescent images were captured per slide.

6.2.3. Transwell Migration Assay

The migration behavior of CAR NK-92 cells under different conditions was evaluated using 96 Transwell plates. Each well in the upper compartment of the plate contained a semi-permeable polycarbonate membrane with 3.0 μm pores (Corning). To assess the influence of US-stimulated microbubbles on CAR NK-92 cells transmigration, HBEC-5i cells were treated with the same ultrasound conditions as the rolling and adhesion assay. Cell supernatant was collected 4 hours post-treatment and diluted 8× before adding to the lower channels of the plate. Fluorescently labeled CAR NK-92 cells (1×10^6 cells/ml) were added to the upper channels and their migration to the lower wells was assessed over varied durations. Positive control was optimized by testing the influence of either TNF-α, CCL3, CCL5 or 10% human serum on CAR NK-92 cells migration and basal culture medium served as the negative control. To quantify the number of migrated cells, the fluorescence intensity was measured in the lower wells using a microplate reader. To determine

the percentage of migration for each group, a reference fluorescence intensity was established by directly adding an equal number of CAR NK-92 cells to a subset of lower wells and defined this as 100% migration.

6.2.4. Statistical Analysis

All data were analyzed using GraphPad prism and are presented as mean ± SD. The fluorescence microscopy videos and images were analyzed using ImageJ to quantify the number of fluorescent CAR NK-92 cells that were attached to the endothelial monolayer. For rolling and adhesion analysis, a minimum of 10 random fields of view were imaged for each sample. The transmigration datasets were repeated on at least three independent samples for each condition. Two-tailed, unpaired two-sample Student's T-tests were performed to determine the significance in comparison between treatment groups. For all datasets, a p-value of <0.05 was assumed to be statistically significant.

6.3. Results and Discussion

Our primary results have shown that US-stimulated microbubbles can trigger the secretion of immune activating cytokines and chemokines, along with upregulation of key CAMs, particularly ICAM-1. Building on these findings, here we investigate how ultrasound treatment influences the recruitment and extravasation of CAR NK-92 cells *in vitro.*

6.3.1. Ultrasound-mediated CAR NK-92 Cells homing

Fig. 1a depicts representative fluorescence microscopy images of CAR NK-92 cells (blue) adhered to the endothelial monolayer at the end of the rolling and adhesion experiment. Experimental conditions including endothelial cell density, CAR NK-92 cell concentration, shear flow and incubation time were kept consistent across all samples. As shown in microscopy images, US-stimulated microbubbles significantly enhanced the firm adhesion of CAR NK-92 cells to the endothelial monolayer as compared to the negative control. Quantification of adhered CAR NK-92 cells demonstrated 3.87-fold ($p < 0.001$) on TNF-α-treated and 2.94-fold ($p < 0.001$) on US-treated endothelial monolayers, relative to the negative control (no treatment). The strong adhesion to TNF-α-treated endothelial monolayer was as expected, given the critical role of TNF-α in activating pro-inflammatory signaling pathways and upregulating CAMs involved in immune cell homing. The influence of ultrasound treatment on immune cells trafficking is consistent with our previous work, showing a significant increase in the secretion of 20 cytokines and chemokines

including TNF-α, IL-6, IL-8, 4 hours post-sonication. Additionally, ICAM-1 surface expression peaked at 4 hours, which is a key contributor to immune cells trafficking. Lymphocyte recruitment follows a multi-step process in response to signals including elevated secretion of pro-inflammatory cytokines and chemokines, endothelial CAM modulation, and conformational changes in lymphocyte adhesion molecules. Therefore, the observed increase in firm adhesion of CAR NK-92 cells to the US-treated endothelial cells is consistent with essential signals needed for immune cell homing. To our knowledge, there is no direct study on the effect of US-stimulated microbubbles on CAR-NK cells. However, a study by Abe et al. in 2022 demonstrated that mechanical high intensity ultrasound (M-HIFU) drastically increased the infiltration of both $CD8^+$ T cells and NK cells into breast tumors in mouse model. To better understand the mechanisms of M-HIFU in improving lymphocytes trafficking and infiltration, they performed GO enrichment analysis of the differentially expressed genes GO analysis demonstrated that M-HIFU predominantly upregulated genes involved in inflammatory responses, leukocyte activation and cell chemotaxis. Moreover, a comparison of M-HIFU with thermal HIFU (T-HIFU) revealed the superiority of M-HIFU in eliciting an anti-tumor immune response. While our study differs in several aspects, these findings highlight the potential of US-mediated mechanical effects in improving lymphocytes homing which is aligned with our results[433].

6.3.2. The Effect of US on CAR NK-92 Cells Transmigration

To optimize positive control for the migration of CAR NK-92 cells, multiple stimuli including TNF-α, CCL3 and CCL5 were examined at different concentrations and incubation. However, none of these factors significantly enhanced CAR cell migration (data not shown). In contrast, 10% human serum led to approximately 3-fold increase in the CAR NK-92 cells migration as compared to negative control under similar conditions. This drastic response is likely due to its high cytokine and chemokine content, thus serving as a strong chemoattractant. Additionally, the transmigration assay revealed that ultrasound-mediated HBEC-5i secretome, collected 4 hours post-sonication, enhanced the migration of CAR NK-92 cells by 2.26-fold ($p<0.05$) in comparison to negative control (Fig. 2). Since migration assays showed no significant difference at 1-, 3- and 24-hours, transmigration assays were performed over 3 hours. These findings further confirm the ability of ultrasound-stimulated microbubbles in improving the chemotactic behavior of immune cells. In this context, Kovacs and colleagues demonstrated that US-assisted BBB disruption can trigger sterile inflammation, thus facilitating the infiltration of macrophages to the targeted

location. Genomics and proteomics results demonstrated that pulsed ultrasound modulates secretion of various cytokines and chemokines in a time-dependent manner including INF-γ, TNF-α, IL-2, IL-6, CCL5, CCL-20, G-CSF and M-CSF. Consequently, ultrasound-assisted secretion of chemotactic factors facilitated the migration of systemic macrophages to the sonicated regions. While this study focused on migration behavior of macrophages, the observed ultrasound-mediated secretome changes suggest a broader impact on effector immune cells homing and extravasation. Overall, these results highlight the potential of ultrasound-stimulated microbubbles to overcome tumor microenvironment and improve cellular immunotherapy.

Figures

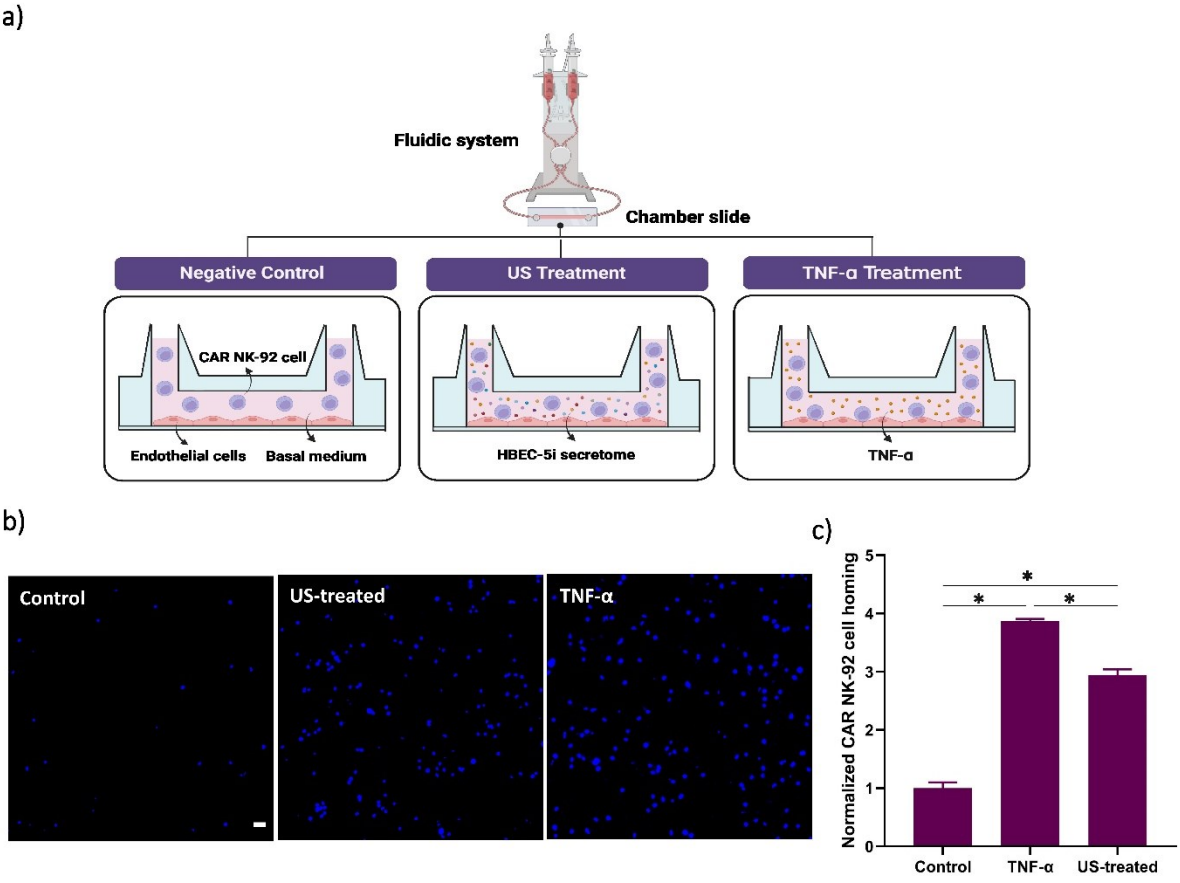

Figure 6.1. Schematic diagram of the rolling and adhesion assay and the effect of ultrasound on CAR NK-92 cells homing. a) A confluent monolayer of HBEC-5i was cultivated under 9 dyne/cm^2 shear flow for two days to provide a more physiological condition. Endothelial cells were categorized into three groups of non-treated (negative control), TNF-α-treated (positive control) and ultrasound-treated. CAR NK-92 cells were perfused over HBEC-5i monolayer for 3 minutes, stopped the flow for 12 minutes to allow their interaction, followed by resuming the flow for 20 minutes, while real-time fluorescent microscopy videos were recorded. At the end of the experiment, chamber slides were washed with fresh medium multiple times to remove non-adhered CAR cells, and fluorescence images were captured to quantify the number of adhered cells. b) Representative fluorescence microscopy images illustrate adhered CAR NK-92 cells, stained blue with Hoechst, under different treatment conditions. Scale bar is 50 µm. c) Quantifying the number of adhered CAR cells showed that treating HBEC-5i with TNF-α for 24 hours resulted in 3.87-fold ($p < 0.001$) increase in firm adhesion of CAR NK-92 cells. Notably, ultrasound-activated microbubbles, 4 hours post-sonication, led to a 2.94-fold ($p < 0.001$) increase in CAR NK-92 cells adhesion. Asterisks denote statistical significance.

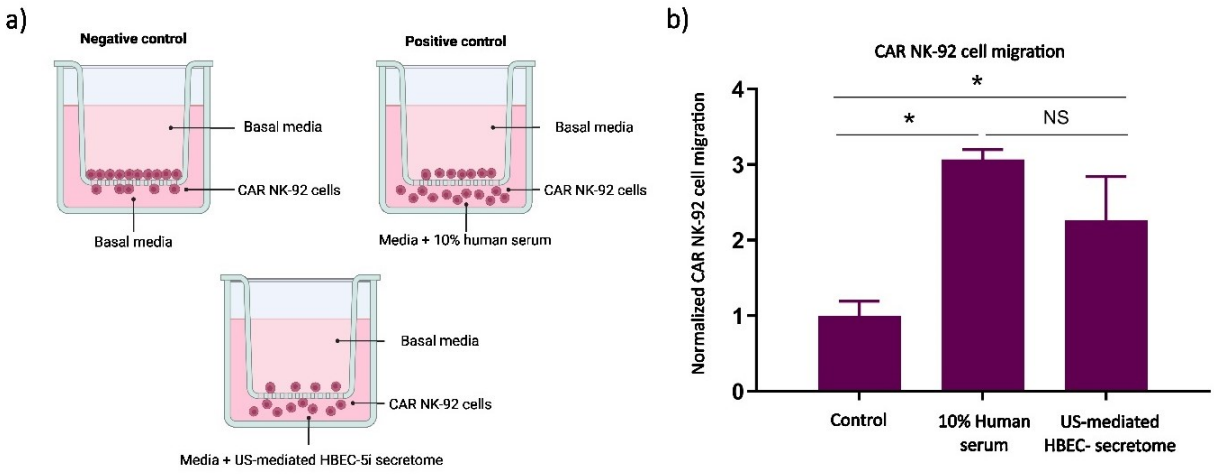

Figure 6.2. Schematic representation of transmigration assay and the effect of ultrasound-mediated HBEC-5i secretome on CAR NK-92 cell extravasation. a) The transmigration assay was conducted in 96-well Transwell plates to evaluate the effect of three groups including basal media (negative control), media supplemented with 10 % human serum (positive control), and US-mediated HBEC-5i secretome, collected 4 hours post-sonication, on CAR NK-92 cells migration over 3 hours. b) The plot shows the fold change in CAR NK-92 cells migration, with fluorescence intensity in lower wells normalized to the negative control. Results indicate that 10% human serum and US-mediated HBEC-5i secretome increased the CAR NK-92 cells migration by 3.06-fold ($p<0.05$) and 2.26-fold ($p<0.05$), respectively. Asterisks denote statistical significance.

7. Conclusion and Future Directions

In this Chapter, I will first present a summary of the major findings of my thesis and follow up with ideas for future directions. Notably, the work presented here can be synergized with many related US-assisted approaches, including MRI-guided BBB opening, cytokine-based immunotherapy, and immune checkpoint-inhibitor therapy.

7.1. Summary of Findings

Despite the promising potential of cellular immunotherapy for hematological malignancies, its success in treating brain cancers remains challenging due to multiple barriers, including the limited permeability of BBB and the suppressive nature of TME. Therefore, this thesis investigates the potential of ultrasound-stimulated microbubbles to modulate endothelial cell immunobiology and improve the recruitment and trafficking of CAR NK-92 cells *in vitro.* Given that fluid dynamics varies across different anatomical sites and pathological conditions, the effect of various fluid patterns was explored on ultrasound treatment outcomes.

Chapter 2 comprehensively reviews immunotherapy challenges for glioblastoma and metastatic brain cancers and explores the mechanisms by which focused ultrasound overcomes these obstacles. This review covers a broad range of literature on ultrasound-assisted molecular and cellular immunotherapy in both pre-clinical and clinical studies.

Chapter 3 investigates local fluid dynamics experienced with circulating microbubbles on ultrasound-assisted permeabilization of endothelial cells, either HUVECs or HBECs. To investigate the influence of flow rate on cell permeabilization, endothelial cells were sonicated (1 MHz frequency, 305 kPa PNP, 20 cycles, 1 ms PRI, and 2 second duration) and real-time microscopy videos were recorded to quantify cell permeabilization as a function of flow rate. Our findings revealed that microbubbles flowing at 30 ml/min under identical acoustic conditions resulted in a statistically significant increase in cell membrane permeability relative to the flow rate of 5 ml/min for both HUVECs and HBECs. Furthermore, our results revealed that fluid flow rate influences ultrasound-mediated intracellular calcium influx, showing a larger number of calcium-positive cells under faster flow. Interestingly, a slower flow rate led to an increased remote effect on the non-perforated cells. Additionally, the effect of inter-pulse delays Δt on endothelial permeability was investigated under a constant flow rate of 30 ml/min. The treatment paradigm consisting of a single pulse (N=20, PRI=1ms, duration 100 or 200 ms) versus a sequence with a

1s delay (N=20, PRI=1ms, duration 25 ms; repeated either 4 or 8 times at $\Delta t \approx 1s$) was compared. Our results revealed that multiple short pulses were more effective than a single pulse in increasing endothelial cell perforation, likely due to the reperfusion of new microbubbles in the acoustic field during the rest times between pulses.

Chapter 4 explores the effect of shear flow preconditioning and microbubble flow patterns on ultrasound-assisted endothelial permeabilization. Shear flow preconditioning influenced HUVEC physiology by overexpression of PECAM-1, downregulation of pro-inflammatory cytokines, and upregulation of angiogenic factors. Notably, shear flow preconditioning significantly increased ultrasound-assisted permeabilization (1.2-2.0x depending on treatment regimen), which was directly correlated with native levels of angiogenic cytokines. In another subset of experiments, ultrasound therapy under pulsatile flow (3.5-7 dyne/cm2, 1 Hz) enhanced the endothelial permeabilization up to 2-fold compared to shear-matched laminar flow. In contrast, ultrasound treatment under oscillatory flow resulted in a more variable result, showing 1.76-fold increase at 4 dyne/cm2 under 0.5 Hz oscillation frequency, no significant change at 4 dyne/cm2 under 1 Hz, or an absence of cell permeabilization at 2 dyne/cm2 with 0.5-1 Hz frequency, compared to laminar flow. This study provides insight into the role of vascular endothelial biology, into the design of a localized US-assisted drug delivery system.

Chapter 5 examines the potential of ultrasound-stimulated microbubbles to modulate the endothelial cell secretome and surface expression of CAMs involved in immune cell homing and trafficking. To investigate flow-dependent bioeffects, either HUVEC or HBEC-5i were subjected to 9 dyne/cm^2 laminar shear flow, which led to differential secretion of a variety of pro- and anti-inflammatory cytokines. Laminar shear stress significantly increased the secretion of inflammatory cytokines from HBEC-5i, including IL-6, TNF-α, TNF-β, GRO-α, and SDF-1. Interestingly, HUVEC responded differently to shear flow, downregulating most inflammatory cytokines. Moreover, shear flow under similar conditions significantly upregulated ICAM-1 on both HUVEC and HBEC-5i in a time-dependent and reversible manner, with a peak increase at 4 (1.98 ± 0.15) and 24 h (1.56-fold, $p<0.001$), respectively. In the second subset of experiments, ultrasound treatment enhanced the surface expression of ICAM-1 in both endothelial cell types at 4 hours post-sonication under the same acoustic stimulus. Conversely, MAdCAM-1

overexpression peaked at 1-hour post-sonication. In addition, ultrasound stimulated the secretion of 22 cytokines at 4 hours post-sonication, most of which had immune-activating properties.

Building on findings from chapter 5, showing ultrasound-modulated endothelial immunobiology, chapter 6 explores its influence on improving CAR NK-92 cells homing and infiltration. For the rolling and adhesion assay, three subsets of HBEC-5i monolayer, either non-treated, TNF-α-treated or ultrasound-treated were perfused with CAR NK-92 cells under 1 dyne/cm^2 shear stress. Fluorescence microscopy analysis demonstrated that ultrasound-stimulated microbubbles enhanced CAR NK-92 cell recruitment by approximately 2.94-fold as compared to the negative control. Furthermore, the ultrasound-mediated HBEC-5i secretome, collected 4 hours post-sonication, increased CAR NK-92 cell extravasation in a Transwell assay by 2.35-fold, which further highlights the potential of ultrasound in promoting cellular immunotherapy.

7.2. Future Directions

7.2.1. Immune Cell Homing and Migration in a 3D Gel Matrix

While the separate homing and transmigration assays performed in the work of Chapter 6 provide valuable insights into the effects of ultrasound treatment on CAR NK-92 cell behavior, they do not recreate the complexity of multi-step homing and trafficking. Additionally, the migration assay was performed in a static environment, which neglects dynamic immune cells infiltration seen *in vivo*. To provide a more physiologically relevant *in vitro* model, a 3D chamber slide like the µ-slide ibipore can be used. This 3D flow chamber allows the cultivation of endothelial monolayer on a semi-permeable membrane and mimics key aspects of vascular environment. The unique design of these slides enables the cultivation of endothelial cells in the lower channel and a 3D gel matrix, with or without embedded cells, in the upper channel. The lower channel can be perfused with immune cells with varying shear flow conditions, enabling observation of their rolling on endothelial monolayer, adhesion, followed by transmigration to the upper channel over time. Despite the potential of this device for examining ultrasound-mediated cell secretome and its influence on immune cell homing and trafficking, their acoustic properties restrict their application for direct ultrasound sonication. The unique geometry of these slides could significantly affect ultrasound propagation and microbubble cavitation behavior. Therefore, designing a custom-made 3D flow chamber that closely replicates vascular physiology, while maintaining optimized acoustic properties is of great significance. Furthermore, the flow chamber needs to be optically transparent

to allow real-time imaging of immune cell homing and infiltration. Notably, a comprehensive acoustic characterization of 3D chamber needs to be conducted to ensure minimum transmission loss, attenuation and risk of standing waves. Developing an ultrasound compatible 3D perfusion chamber bridges the gap between over-simplified 2D *in vitro* models and *in vivo* studies, making it a powerful tool for real-time investigation of ultrasound-assisted immunotherapy.

7.2.2. Ultrasound-assisted CAR NK-92 Cell Activation

While Chapter 6 explored modulating endothelial immunobiology to improve immune cell recruitment, another potential approach is to examine whether ultrasound can enhance the intrinsic homing ability of CAR NK cells. Multiple studies have investigated ultrasound-mediated infiltration of NK cells into tumors via BBB opening, however the direct effects of ultrasound on either NK or CAR NK cell activation remain unexplored. In general, a key component in NK cell rolling and adhesion is integrin expression, a molecule that is present in different affinity states depending on NK cells activation status. Similar to mechanosensitive CAMs on endothelial cells, integrin expression is shear-dependent, with their activation influenced by flow-induced shear stress. A critical integrin expressed on NK cells is LFA-1, which plays a dual role, involved in immune cell homing and contributing to NK cell cytotoxicity. Given that ultrasound-stimulated microbubbles generate large-magnitude shear stress, investigating their effects on integrin conformational change to a high affinity state will provide valuable insights into either NK or CAR NK cell recruitment and function

Beyond integrin activation, NK cell function is also influenced by proinflammatory cytokines, in particular IFN-γ and TNF-α, which promote NK cell activation and cytotoxicity. These cytokines upregulate ICAM-1 surface expression on the target cells through the NF-κB pathway, which enhances their susceptibility to NK cell adhesion and killing. Given that LFA-1 activation can further promote the secretion of these cytokines, examining the effect of ultrasound-stimulated microbubbles on IFN-γ and TNF-α level could provide valuable insights. Moreover, exploring the effect of ultrasound treatment on CAR NK-92 cell tumoricidal activity by co-culturing sonicated immune cells with their target tumor cells and quantifying their cytotoxicity would further reveal the therapeutic potential of this strategy.

7.2.3. Investigating the effects of ultrasound-stimulated microbubbles on CAR NK cells homing and trafficking *in vivo*.

In vitro studies provide a controlled environment that enables the precise investigation of various factors and allows the optimization of ultrasound parameters. However, they cannot fully replicate the complexity of the in vivo conditions, where the treatment outcome is influenced by various factors. As previously mentioned, using an MRI-guided focused ultrasound for BBB opening facilitates immune cell recruitment and infiltration by transiently increasing the permeability of BBB and triggering an immune response. While ultrasound-mediated BBB disruption offers outstanding potential for brain cancer therapy, it is unclear whether BBB opening is a necessary condition to increase immune cell trafficking, or whether microbubble-induced shear stress alone is sufficient. A key approach for exploring the extent of ultrasound-assisted BBB opening is delivering dextran molecules with varying molecular weights as drug surrogates. This helps to identify ultrasound parameters that enable efficient delivery of therapeutic agents across BBB with minimum tissue damage and hemorrhage. Next, immunohistochemistry could be used to evaluate the extent of BBB opening based on the extravasation of dextran with varying molecular weights, distinguished by fluorescent markers, into the brain. To assess ultrasound-mediated proinflammatory response, immunohistochemistry must be performed to examine CAM expression, while blood plasma should be evaluated for cytokine profile changes. Ultimately, the influence of ultrasound treatment on CAR NK-92 cell homing and trafficking into the targeted brain tissue can be examined through CD45 expression analysis. Investigating the effect of ultrasound-assisted BBB disruption on trafficking and intra-tumoral activity of other effector immune cells could provide further information on the broader immune response to ultrasound treatment.

7.2.4. Exploring the potential of ultrasound-assisted BBB opening for neuroinflammation

Microglia is a key primary resident immune cell in the brain, which is involved in the maintenance of brain function, plasticity and immune defense. In GBM however, microglia contribute to suppressive TME, by polarizing anti-tumor M1 macrophages to pro-tumor M2 phenotype, resulting in tumor progression. In this context, therapeutic ultrasound could be a potential approach for shifting microglia function toward an anti-tumor state. Multiple studies have investigated the role of ultrasound alone or in combination with microbubbles on the activation of microglia.

However, the ultrasound mechanism which leads to microglia modulation remains unclear. Given that microglia express several mechanosensitive ion channels, it has been suggested that ultrasound-induced radiation forces may modulate their activation. Additionally, BBB opening using ultrasound-stimulated microbubbles leads to extravasation of blood-borne substances to the brain parenchyma, further influencing microglia response. Therefore, ultrasound-mediated microglia treatment induces the secretion of pro-inflammatory cytokines, which may trigger either anti-tumor or pro-tumor response, which highlights the importance of optimizing ultrasound parameters. Ultrasound frequencies below 1 MHz are typically used for BBB opening and neuromodulation. However, at lower frequencies, the increased rarefactional period enhances the risk of bubble collapse, which can result in uncontrolled BBB disruption and tissue damage. A growing body of research has investigated the influence of ultrasound-mediated BBB opening on inducing neuroinflammation or sterile inflammation [319]. To explore ultrasound-induced changes in microglia function, brains of a subset of animals need to be harvested, followed by microglia extraction. Evaluating microglia genomics and proteomics and correlating it to the long-term survival would provide useful information. Additionally, microglia phagocytosis ability can be examined by coculturing extracted microglia and Alexa-488 labelled GBM cells for 2 h. Microglia then needs to be stained with anti-Iba1 antibody, and quantify the fluorescence overlap via flow cytometry. Examining the effect of ultrasound treatment on apoptotic activity of microglia via ANXA5/annexin V-FITC and PI, could further clarify the treatment potential. Lastly, it would be interesting to examine the morphological changes of microglia using electron microscopy in response to ultrasound treatment, as these structural modifications may influence their surveillance activity [319].

7.2.5. Ultrasound-assisted cellular and cytokine-based immunotherapy

As previously discussed, the challenges of CAR NK cells as a standalone treatment can be solved using therapeutic ultrasound. However, it would be beneficial to find strategies to further improve the durability and function of administered CAR NK cells to promote their therapeutic effects for malignant brain tumors. To this purpose, systemic cytokine delivery has been explored, which has largely failed due to high systemic cytotoxicity and the risk of cytokine release syndrome. Therefore, there is growing interest in local delivery of cytokine genes into tumor cells to minimize the risk of systemic toxicity and autoimmunity. In this context, ultrasound-stimulated microbubbles can be exploited for efficient delivery of cytokine genes into the tumor cells,

enabling sustained cytokine secretion within the TME prior to CAR NK cells delivery. More specifically, the intra-tumoral delivery of IL-2 and IL-15 can reshape the TME, along with enhancing CAR NK cells survival, proliferation and prime their activation. Additionally, IL-12 and IL-18 can promote CAR NK cells cytotoxicity by inducing the secretion of cytotoxic proteins and INF-γ, thus promoting their cytolytic function. The enhanced level of these cytokines in TME can also upregulate the expression of activating receptors on CAR NK cells and decrease the threshold of activating receptor signaling[12]. To implement this strategy, cytokine plasmid DNA can be co-injected with microbubbles, and their cellular uptake can be triggered by ultrasound exposure. Before combining this approach with CAR NK cell delivery, it is essential to evaluate the effects of local cytokine delivery on immune cells infiltration and tumor growth. Once the direct effects of cytokine delivery are identified, combination therapy with CAR NK cells can be performed. To optimize the treatment outcomes, ultrasound-assisted CAR NK cell delivery needs to be conducted 24-48 hours after cytokine plasmid delivery to allow sufficient cytokine secretion. Subsequent assessments should evaluate key therapeutic effects such as CAR NK cell infiltration, cytotoxicity, tumor growth and long-term survival.

7.2.6. Combination of CAR NK cells with immune checkpoint inhibitors

One of the escaping mechanisms of cancer from the immune system is suppressing the effector immune cell activation via immune checkpoints. Immune checkpoints, suppressive molecules on immune cells, keep the immune response in check and prevent autoimmunity. However, tumor cells take advantage of immune checkpoints by overexpressing their ligands, which results in immune exhaustion. Given the significance of immune checkpoints in immune evasion, numerous pre-clinical and clinical studies have investigated the therapeutic effects of checkpoint inhibitors across different cancer types. Most studies have focused on immune checkpoint inhibitors in combination with T cell-based immunotherapies, including adoptive T cells and CAR T cells, whereas relatively few have explored their efficacy on NK cell-based strategies. Similar to CAR T cells, CAR NK cells also experience immune exhaustion, which is mediated by immune checkpoints[320]. Key checkpoint receptors on CAR-NK cells that negatively regulate their function include T cell immunoreceptors with Ig and ITIM domains (TIGIT), NKG2A, lymphocyte activation gene-3 (LAG-3) and T cell immunoglobulin and mucin domain-containing protein 3 (TIM-3). Among these, TIGIT is specifically significant, as it is expressed in all human NK cell types and overexpressed on exhausted NK cells, which makes it a potential target for

immune checkpoint therapies. TIGIT exhibits a high binding affinity to CD155, an adhesion molecule that has been shown to often overexpress in malignant tumors. CD155 also interact with CD226, a costimulatory molecule on T and NK cells. However, due to TIGIT's superior affinity for CD155, CD226 fails to bind to CD155, reducing CAR NK cells cytotoxicity. Therefore, blocking TIGIT via checkpoint inhibitors can counteract this suppression, preventing CAR NK cell depletion and promoting their cytotoxicity [320]. While a limited number of pre-clinical studies have explored the potential of checkpoint inhibitors to improve CAR NK cell function, no study has examined the combination of CAR NK cells with checkpoint inhibitors for brain malignancies, likely due to the complexity of the brain environment. In this context, using ultrasound-stimulated microbubbles for co-delivery of CAR-NK cells and TIGIT inhibitors, simultaneously or with an interval, holds significant potential to revolutionize brain cancer immunotherapy by promoting CAR NK cell function.

7.3. Conclusion

Ultrasound-assisted cellular immunotherapy has long been explored for the treatment of a wide variety of cancers, with a growing interest in its application for brain malignancies. In this context, this thesis focused on designing physiologically relevant in vitro studies to examine key aspects of ultrasound-stimulated microbubbles in improving cellular immunotherapy. To this aim, first the influence of fluid flow dynamics was established on endothelial cell physiology and their susceptibility to ultrasound-mediated cell permeabilization. To better replicate in vivo conditions, the role of different microbubble flow patterns was investigated on the efficiency of ultrasound-assisted cell perforation. Following this, the influence of microbubble-induced shear stress was explored on endothelial cells immunobiology, and ultimately CAR NK-92 cells recruitment and trafficking. Overall, the findings of this study lay the foundation for a targeted and efficient ultrasound-based strategy for brain cancer cellular immunotherapy.

References

[1] P. A. Jablonska, J. Bosch-Barrera, D. Serrano, M. Valiente, A. Calvo, and J. Aristu, “Challenges and Novel Opportunities of Radiation Therapy for Brain Metastases in Non-Small Cell Lung Cancer,” *Cancers*, vol. 13, no. 9, p. 2141, Apr. 2021, doi: 10.3390/cancers13092141.

[2] J. H. Sampson, M. D. Gunn, P. E. Fecci, and D. M. Ashley, “Brain immunology and immunotherapy in brain tumours,” *Nat. Rev. Cancer*, vol. 20, no. 1, pp. 12–25, Jan. 2020, doi: 10.1038/s41568-019-0224-7.

[3] G. Kooij, J. Van Horssen, V. V. R. Bandaru, N. J. Haughey, and H. E. De Vries, “The Role of ATP-Binding Cassette Transporters in Neuro-Inflammation: Relevance for Bioactive Lipids,” *Front. Pharmacol.*, vol. 3, 2012, doi: 10.3389/fphar.2012.00074.

[4] L. Han and C. Jiang, “Evolution of blood–brain barrier in brain diseases and related systemic nanoscale brain-targeting drug delivery strategies,” *Acta Pharm. Sin. B*, vol. 11, no. 8, pp. 2306–2325, Aug. 2021, doi: 10.1016/j.apsb.2020.11.023.

[5] W. M. Pardridge, “The blood-brain barrier: Bottleneck in brain drug development,” *NeuroRX*, vol. 2, no. 1, pp. 3–14, Jan. 2005, doi: 10.1602/neurorx.2.1.3.

[6] Y. Meng *et al.*, “Safety and efficacy of focused ultrasound induced blood-brain barrier opening, an integrative review of animal and human studies,” *J. Controlled Release*, vol. 309, pp. 25–36, Sep. 2019, doi: 10.1016/j.jconrel.2019.07.023.

[7] M. W. Yu and D. F. Quail, “Immunotherapy for Glioblastoma: Current Progress and Challenges,” *Front. Immunol.*, vol. 12, p. 676301, May 2021, doi: 10.3389/fimmu.2021.676301.

[8] B. Cacho-Díaz, D. R. García-Botello, T. Wegman-Ostrosky, G. Reyes-Soto, E. Ortiz-Sánchez, and L. A. Herrera-Montalvo, “Tumor microenvironment differences between primary tumor and brain metastases,” *J. Transl. Med.*, vol. 18, no. 1, p. 1, Dec. 2020, doi: 10.1186/s12967-019-02189-8.

[9] W. Tomaszewski, L. Sanchez-Perez, T. F. Gajewski, and J. H. Sampson, “Brain Tumor Microenvironment and Host State: Implications for Immunotherapy,” *Clin. Cancer Res.*, vol. 25, no. 14, pp. 4202–4210, Jul. 2019, doi: 10.1158/1078-0432.CCR-18-1627.

[10] D. Kirschenbaum and I. Amit, “Brain metastases: Not all tumors are created equal,” *Neuron*, vol. 110, no. 7, pp. 1097–1099, Apr. 2022, doi: 10.1016/j.neuron.2022.03.027.

[11] W. H. Bae, S. Maraka, and A. Daher, “Challenges and advances in glioblastoma targeted therapy: the promise of drug repurposing and biomarker exploration,” *Front. Oncol.*, vol. 14, p. 1441460, Oct. 2024, doi: 10.3389/fonc.2024.1441460.

[12] J. H. W. Pahl, A. Cerwenka, and J. Ni, “Memory-Like NK Cells: Remembering a Previous Activation by Cytokines and NK Cell Receptors,” *Front. Immunol.*, vol. 9, p. 2796, Nov. 2018, doi: 10.3389/fimmu.2018.02796.

[13] G. Xie, H. Dong, Y. Liang, J. D. Ham, R. Rizwan, and J. Chen, “CAR-NK cells: A promising cellular immunotherapy for cancer,” *eBioMedicine*, vol. 59, p. 102975, Sep. 2020, doi: 10.1016/j.ebiom.2020.102975.

[14] K. Murphy, *Janeway’s Immunobiology*. 2011.

[15] M. Sadelain, R. Brentjens, and I. Rivière, “The Basic Principles of Chimeric Antigen Receptor Design,” *Cancer Discov.*, vol. 3, no. 4, pp. 388–398, Apr. 2013, doi: 10.1158/2159-8290.CD-12-0548.

[16] H. S. Budi *et al.*, “Human epidermal growth factor receptor 2 (HER2)-specific chimeric antigen receptor (CAR) for tumor immunotherapy; recent progress,” *Stem Cell Res. Ther.*, vol. 13, no. 1, p. 40, Jan. 2022, doi: 10.1186/s13287-022-02719-0.

[17] K. A. Gerhold and M. A. Schwartz, “Ion Channels in Endothelial Responses to Fluid Shear Stress,” *Physiology*, vol. 31, no. 5, pp. 359–369, Sep. 2016, doi: 10.1152/physiol.00007.2016.
[18] C. Rabut *et al.*, “Ultrasound Technologies for Imaging and Modulating Neural Activity,” *Neuron*, vol. 108, no. 1, pp. 93–110, Oct. 2020, doi: 10.1016/j.neuron.2020.09.003.
[19] T. L. Szabo, *Diagnostic ultrasound imaging: inside out*, Second edition. ELSEVIER, 2014.
[20] M. Versluis, E. Stride, G. Lajoinie, B. Dollet, and T. Segers, “Ultrasound Contrast Agent Modeling: A Review,” *Ultrasound Med. Biol.*, vol. 46, no. 9, pp. 2117–2144, 2020, doi: 10.1016/j.ultrasmedbio.2020.04.014.
[21] D. Omata, J. Unga, R. Suzuki, and K. Maruyama, “Lipid-based microbubbles and ultrasound for therapeutic application,” *Adv. Drug Deliv. Rev.*, vol. 154–155, pp. 236–244, 2020, doi: 10.1016/j.addr.2020.07.005.
[22] M. Azmin, C. Harfield, Z. Ahmad, M. Edirisinghe, and E. Stride, “How Do Microbubbles and Ultrasound Interact? Basic Physical, Dynamic and Engineering Principles,” *Curr. Pharm. Des.*, vol. 18, no. 15, pp. 2118–2134, Mar. 2012, doi: 10.2174/138161212800099955.
[23] J. Deprez, G. Lajoinie, Y. Engelen, S. C. De Smedt, and I. Lentacker, “Opening doors with ultrasound and microbubbles: Beating biological barriers to promote drug delivery,” *Adv. Drug Deliv. Rev.*, vol. 172, pp. 9–36, May 2021, doi: 10.1016/j.addr.2021.02.015.
[24] S. Qin, C. F. Caskey, and K. W. Ferrara, “Ultrasound contrast microbubbles in imaging and therapy: physical principles and engineering,” *Phys. Med. Biol.*, vol. 54, no. 6, pp. R27–R57, Mar. 2009, doi: 10.1088/0031-9155/54/6/R01.
[25] M. De Saint Victor, C. Crake, C.-C. Coussios, and E. Stride, “Properties, characteristics and applications of microbubbles for sonothrombolysis,” *Expert Opin. Drug Deliv.*, vol. 11, no. 2, pp. 187–209, Feb. 2014, doi: 10.1517/17425247.2014.868434.
[26] K. H. Martin and P. a Dayton, “Current status and prospects for microbubbles in ultrasound theranostics.,” *Wiley Interdiscip. Rev. Nanomed. Nanobiotechnol.*, vol. 5, no. 4, pp. 329–45, 2013, doi: 10.1002/wnan.1219.
[27] X. Jiang *et al.*, “A Review of Low-Intensity Pulsed Ultrasound for Therapeutic Applications,” *IEEE Trans. Biomed. Eng.*, vol. 66, no. 10, pp. 2704–2718, Oct. 2019, doi: 10.1109/TBME.2018.2889669.
[28] Y.-X. Zhong, J.-C. Liao, X. Liu, H. Tian, L.-R. Deng, and L. Long, “Low intensity focused ultrasound: a new prospect for the treatment of Parkinson’s disease,” *Ann. Med.*, vol. 55, no. 2, p. 2251145, Dec. 2023, doi: 10.1080/07853890.2023.2251145.
[29] E. J. Lee, A. Fomenko, and A. M. Lozano, “Magnetic Resonance-Guided Focused Ultrasound : Current Status and Future Perspectives in Thermal Ablation and Blood-Brain Barrier Opening,” *J. Korean Neurosurg. Soc.*, vol. 62, no. 1, pp. 10–26, Jan. 2019, doi: 10.3340/jkns.2018.0180.
[30] G. T. Clement and K. Hynynen, “A non-invasive method for focusing ultrasound through the human skull,” *Phys. Med. Biol.*, vol. 47, no. 8, pp. 1219–1236, Apr. 2002, doi: 10.1088/0031-9155/47/8/301.
[31] Y. Meng, K. Hynynen, and N. Lipsman, “Applications of focused ultrasound in the brain: from thermoablation to drug delivery,” *Nat. Rev. Neurol.*, vol. 17, no. 1, pp. 7–22, Jan. 2021, doi: 10.1038/s41582-020-00418-z.
[32] A. Burgess and K. Hynynen, “Microbubble-Assisted Ultrasound for Drug Delivery in the Brain and Central Nervous System,” in *Therapeutic Ultrasound*, vol. 880, J.-M. Escoffre and A. Bouakaz, Eds., in Advances in Experimental Medicine and Biology, vol. 880. , Cham: Springer International Publishing, 2016, pp. 293–308. doi: 10.1007/978-3-319-22536-4_16.
[33] A. K. W. Wood and C. M. Sehgal, “A Review of Low-Intensity Ultrasound for Cancer Therapy,” *Ultrasound Med. Biol.*, vol. 41, no. 4, pp. 905–928, Apr. 2015, doi: 10.1016/j.ultrasmedbio.2014.11.019.

[34] Y.-J. Ho, J.-P. Li, C.-H. Fan, H.-L. Liu, and C.-K. Yeh, “Ultrasound in tumor immunotherapy: Current status and future developments,” *J. Controlled Release*, vol. 323, pp. 12–23, Jul. 2020, doi: 10.1016/j.jconrel.2020.04.023.
[35] Canadian Cancer Statistics Advisory Committee, “Canadian Cancer Statistics: A 2022 special report on cancer prevalence,” *Can. Cancer Stat.*, pp. 1–35, 2022.
[36] R. Stupp *et al.*, “Radiotherapy plus concomitant and adjuvant temozolomide for glioblastoma,” *N. Engl. J. Med.*, vol. 352, no. 10, pp. 987–996, 2005, doi: 10.1007/s11060-008-9538-0.
[37] K. D. Miller *et al.*, “Brain and other central nervous system tumor statistics, 2021,” *CA. Cancer J. Clin.*, vol. 71, no. 5, pp. 381–406, 2021, doi: 10.3322/caac.21693.
[38] A. G. Osborn, D. N. Louis, T. Y. Poussaint, L. L. Linscott, and K. L. Salzman, “The 2021 World Health Organization Classification of Tumors of the Central Nervous System: What Neuroradiologists Need to Know,” *Am. J. Neuroradiol.*, vol. 43, no. 7, pp. 928–937, 2022, doi: 10.3174/ajnr.A7462.
[39] Q. T. Ostrom *et al.*, “CBTRUS statistical Report: primary brain and central nervous system tumors diagnosed in the United States in 2008-2012,” *Neuro-Oncol.*, vol. 17, pp. iv1–iv62, 2015, doi: 10.1093/neuonc/nov189.
[40] P. D. Delgado-López and E. M. Corrales-García, “Survival in glioblastoma: a review on the impact of treatment modalities,” *Clin. Transl. Oncol.*, vol. 18, no. 11, pp. 1062–1071, 2016, doi: 10.1007/s12094-016-1497-x.
[41] A. S. Achrol *et al.*, “Brain metastases,” *Nat. Rev. Dis. Primer*, vol. 5, no. 5, 2019.
[42] L. J. Schouten, J. Rutten, H. A. M. Huveneers, and A. Twijnstra, “Incidence of brain metastases in a cohort of patients with carcinoma of the breast, colon, kidney, and lung and melanoma,” *Cancer*, vol. 94, no. 10, pp. 2698–2705, 2002, doi: 10.1002/cncr.10541.
[43] R. L. Siegel, K. D. Miller, H. E. Fuchs, and A. Jemal, “Plain language summary of 2022 cancer statistics: focus on lung cancer,” *Future Oncol.*, vol. 72, no. 1, pp. 7–33, 2022, doi: 10.3322/caac.21708.
[44] P. W. Sperduto *et al.*, “Estimating Survival in Patients With Lung Cancer and Brain Metastases: An Update of the Graded Prognostic Assessment for Lung Cancer Using Molecular Markers (Lung-molGPA),” *JAMA Oncol.*, vol. 3, no. 6, pp. 827–831, 2017.
[45] A. G. Waks and E. P. Winer, “Breast Cancer Treatment: A Review,” *JAMA - J. Am. Med. Assoc.*, vol. 321, no. 3, pp. 288–300, 2019, doi: 10.1001/jama.2018.19323.
[46] N. Shah *et al.*, “Investigational chemotherapy and novel pharmacokinetic mechanisms for the treatment of breast cancer brain metastases,” *Pharmacol. Res.*, vol. 132, no. March, pp. 47–68, 2018, doi: 10.1016/j.phrs.2018.03.021.
[47] K. E. Wallner, J. H. Galicich, G. Krol, E. Arbit, and M. G. Malkin, “Patterns of failure following treatment for glioblastoma multiforme and anaplastic astrocytoma,” *Int. J. Radiat. Oncol. Biol. Phys.*, vol. 16, no. 6, pp. 1405–1409, 1989.
[48] N. Laperriere, L. Zuraw, and G. Cairncross, “Radiotherapy for newly diagnosed malignant glioma in adults: A systematic review,” *Radiother. Oncol.*, vol. 64, no. 3, pp. 259–273, 2002, doi: 10.1016/S0167-8140(02)00078-6.
[49] R. Stupp *et al.*, “Effects of radiotherapy with concomitant and adjuvant temozolomide versus radiotherapy alone on survival in glioblastoma in a randomised phase III study: 5-year analysis of the EORTC-NCIC trial,” *Lancet Oncol.*, vol. 10, no. 5, pp. 459–466, 2009, doi: 10.1016/S1470-2045(09)70025-7.
[50] N. Gaynor, J. Crown, and D. M. Collins, “Immune checkpoint inhibitors: Key trials and an emerging role in breast cancer,” *Semin. Cancer Biol.*, vol. 79, no. January 2020, pp. 44–57, 2022, doi: 10.1016/j.semcancer.2020.06.016.

[51] P. Jain, C. Jain, and V. Velcheti, “Role of immune-checkpoint inhibitors in lung cancer,” *Ther. Adv. Respir. Dis.*, vol. 12, pp. 1–13, 2018, doi: 10.1177/1753465817750075.
[52] M. S. Carlino, J. Larkin, and G. V. Long, “Immune checkpoint inhibitors in melanoma,” *The Lancet*, vol. 398, no. 10304, pp. 1002–1014, 2021, doi: 10.1016/S0140-6736(21)01206-X.
[53] H. Yusefi and B. Helfield, “Ultrasound Contrast Imaging : Fundamentals and Emerging Technology,” *Front. Phys.*, vol. 10, no. 791145, pp. 1–16, 2022, doi: 10.3389/fphy.2022.791145.
[54] B. Helfield, X. Chen, S. C. Watkins, and F. S. Villanueva, “Transendothelial Perforations and the Sphere of Influence of Single-Site Sonoporation,” *Ultrasound Med. Biol.*, vol. 46, no. 7, pp. 1686–1697, 2020, doi: 10.1016/j.ultrasmedbio.2020.02.017.
[55] Z. I. Kovacs, S. R. Burks, and J. A. Frank, “Focused ultrasound with microbubbles induces sterile inflammatory response proportional to the blood brain barrier opening: Attention to experimental conditions,” *Theranostics*, vol. 8, no. 8, pp. 2245–2248, 2018, doi: 10.7150/thno.24181.
[56] D. McMahon, A. Lassus, E. Gaud, V. Jeannot, and K. Hynynen, “Microbubble formulation influences inflammatory response to focused ultrasound exposure in the brain,” *Sci. Rep.*, vol. 10, no. 1, pp. 1–15, 2020, doi: 10.1038/s41598-020-78657-9.
[57] D. Mcmahon, R. Bendayan, and K. Hynynen, “Acute effects of focused ultrasound-induced increases in blood-brain barrier permeability on rat microvascular transcriptome,” *Sci. Rep.*, vol. 7, no. November 2016, pp. 1–15, 2017, doi: 10.1038/srep45657.
[58] Y. Meng *et al.*, “Safety and efficacy of focused ultrasound induced blood-brain barrier opening, an integrative review of animal and human studies,” *J. Controlled Release*, vol. 309, no. May, pp. 25–36, 2019, doi: 10.1016/j.jconrel.2019.07.023.
[59] Y. Meng, K. Hynynen, and N. Lipsman, “Applications of focused ultrasound in the brain: from thermoablation to drug delivery,” *Nat. Rev. Neurol.*, vol. 17, no. 1, pp. 7–22, 2021, doi: 10.1038/s41582-020-00418-z.
[60] K. Hynynen, N. McDannold, N. Vykhodtseva, and F. A. Jolesz, “Noninvasive MR imaging-guided focal opening of the blood-brain barrier in rabbits,” *Radiology*, vol. 220, no. 3, pp. 640–646, 2001.
[61] A. Burgess, K. Shah, O. Hough, and K. Hynynen, “Focused ultrasound-mediated drug delivery through the blood-brain barrier,” *Expert Rev. Neurother.*, vol. 15, no. 5, pp. 477–491, 2015, doi: 10.1586/14737175.2015.1028369.
[62] L. C. Tsao, J. Force, and Z. C. Hartman, “Mechanisms of therapeutic antitumor monoclonal antibodies,” *Cancer Res.*, vol. 81, no. 18, pp. 4641–4651, 2021, doi: 10.1158/0008-5472.CAN-21-1109.
[63] D. R. Leach, M. F. Krummel, and J. P. Allison, “Enhancement of Antitumor Immunity by CTLA-4 Blockade Published by : American Association for the Advancement of Science Stable URL : http://www.jstor.org/stable/2890840,” *Science*, vol. 271, no. 5256, pp. 1734–1736, 1996.
[64] P. Sharma and J. P. Allison, “The future of immune checkpoint therapy,” *Science*, vol. 348, no. 6230, pp. 56–61, 2015, doi: 10.1126/science.aaa8172.
[65] S. A. Rosenberg *et al.*, “Use of Tumor-Infiltrating Lymphocytes and Interleukin-2 in the Immunotherapy of Patients with Metastatic Melanoma,” *N. Engl. J. Med.*, vol. 319, pp. 1676–1680, 1988.
[66] C. H. June, R. S. O’Connor, O. U. Kawalekar, S. Ghassemi, and M. C. Milone, “CAR T cell immunotherapy for human cancer,” *Science*, vol. 359, no. 6382, pp. 1361–1365, 2018, doi: 10.1126/science.aar6711.
[67] K. L. Chohan, E. L. Siegler, and S. S. Kenderian, “CAR-T Cell Therapy: the Efficacy and Toxicity Balance,” *Curr. Hematol. Malig. Rep.*, vol. 18, no. 2, pp. 9–18, 2023, doi: 10.1007/s11899-023-00687-7.

[68] N. H. Fowler *et al.*, "Tisagenlecleucel in adult relapsed or refractory follicular lymphoma: the phase 2 ELARA trial," *Nat. Med.*, vol. 28, no. 2, pp. 325–332, 2022, doi: 10.1038/s41591-021-01622-0.
[69] S. J. Schuster *et al.*, "Tisagenlecleucel in Adult Relapsed or Refractory Diffuse Large B-Cell Lymphoma," *N. Engl. J. Med.*, vol. 380, no. 1, pp. 45–56, 2019, doi: 10.1056/nejmoa1804980.
[70] M. Wang *et al.*, "KTE-X19 CAR T-Cell Therapy in Relapsed or Refractory Mantle-Cell Lymphoma," *N. Engl. J. Med.*, vol. 382, no. 14, pp. 1331–1342, 2020, doi: 10.1056/nejmoa1914347.
[71] C. A. Jacobson *et al.*, "Axicabtagene ciloleucel in relapsed or refractory indolent non-Hodgkin lymphoma (ZUMA-5): a single-arm, multicentre, phase 2 trial," *Lancet Oncol.*, vol. 23, no. 1, pp. 91–103, 2022, doi: 10.1016/S1470-2045(21)00591-X.
[72] J. G. Berdeja *et al.*, "Ciltacabtagene autoleucel, a B-cell maturation antigen-directed chimeric antigen receptor T-cell therapy in patients with relapsed or refractory multiple myeloma (CARTITUDE-1): a phase 1b/2 open-label study," *The Lancet*, vol. 398, no. 10297, pp. 314–324, 2021, doi: 10.1016/S0140-6736(21)00933-8.
[73] U. Patel, J. Abernathy, B. N. Savani, O. Oluwole, S. Sengsayadeth, and B. Dholaria, "CAR T cell therapy in solid tumors: A review of current clinical trials," *eJHaem*, vol. 3, no. S1, pp. 24–31, 2022, doi: 10.1002/jha2.356.
[74] C. Robert *et al.*, "Pembrolizumab versus Ipilimumab in Advanced Melanoma," *N. Engl. J. Med.*, vol. 372, no. 26, pp. 2521–2532, 2015, doi: 10.1056/nejmoa1503093.
[75] R. K. Vaddepally, P. Kharel, R. Pandey, R. Garje, and A. B. Chandra, "Review of indications of FDA-approved immune checkpoint inhibitors per NCCN guidelines with the level of evidence," *Cancers*, vol. 12, no. 3, pp. 1–19, 2020, doi: 10.3390/cancers12030738.
[76] P. Sharma *et al.*, "The next decade of immune checkpoint therapy," *Cancer Discov.*, vol. 11, no. 4, pp. 838–857, 2021, doi: 10.1158/2159-8290.CD-20-1680.
[77] J. S. Weber *et al.*, "Nivolumab versus chemotherapy in patients with advanced melanoma who progressed after anti-CTLA-4 treatment (CheckMate 037): A randomised, controlled, open-label, phase 3 trial," *Lancet Oncol.*, vol. 16, no. 4, pp. 375–384, 2015, doi: 10.1016/S1470-2045(15)70076-8.
[78] S. J. Antonia *et al.*, "Durvalumab after Chemoradiotherapy in Stage III Non–Small-Cell Lung Cancer," *N. Engl. J. Med.*, vol. 377, no. 20, pp. 1919–1929, 2017, doi: 10.1056/nejmoa1709937.
[79] M. D. Hellmann *et al.*, "Nivolumab plus Ipilimumab in Advanced Non–Small-Cell Lung Cancer," *N. Engl. J. Med.*, vol. 381, no. 21, pp. 2020–2031, 2019, doi: 10.1056/nejmoa1910231.
[80] L. Horn *et al.*, "First-Line Atezolizumab plus Chemotherapy in Extensive-Stage Small-Cell Lung Cancer," *N. Engl. J. Med.*, vol. 379, no. 23, pp. 2220–2229, 2018, doi: 10.1056/nejmoa1809064.
[81] L. Paz-Ares *et al.*, "Durvalumab plus platinum–etoposide versus platinum–etoposide in first-line treatment of extensive-stage small-cell lung cancer (CASPIAN): a randomised, controlled, open-label, phase 3 trial," *The Lancet*, vol. 394, no. 10212, pp. 1929–1939, 2019, doi: 10.1016/S0140-6736(19)32222-6.
[82] T. Powles *et al.*, "Avelumab Maintenance Therapy for Advanced or Metastatic Urothelial Carcinoma," *N. Engl. J. Med.*, vol. 383, no. 13, pp. 1218–1230, 2020, doi: 10.1056/nejmoa2002788.
[83] R. J. Motzer *et al.*, "Nivolumab plus Ipilimumab versus Sunitinib in Advanced Renal-Cell Carcinoma," *N. Engl. J. Med.*, vol. 378, no. 14, pp. 1277–1290, 2018, doi: 10.1056/nejmoa1712126.
[84] T. Yau *et al.*, "Efficacy and Safety of Nivolumab plus Ipilimumab in Patients with Advanced Hepatocellular Carcinoma Previously Treated with Sorafenib: The CheckMate 040 Randomized Clinical Trial," *JAMA Oncol.*, vol. 6, no. 11, pp. 1–8, 2020, doi: 10.1001/jamaoncol.2020.4564.

[85] A. Scherpereel *et al.*, “Nivolumab or nivolumab plus ipilimumab in patients with relapsed malignant pleural mesothelioma (IFCT-1501 MAPS2): a multicentre, open-label, randomised, non-comparative, phase 2 trial,” *Lancet Oncol.*, vol. 20, no. 2, pp. 239–253, 2019, doi: 10.1016/S1470-2045(18)30765-4.
[86] M. J. Overman *et al.*, “Durable clinical benefit with nivolumab plus ipilimumab in DNA mismatch repair-deficient/microsatellite instability-high metastatic colorectal cancer,” *J. Clin. Oncol.*, vol. 36, no. 8, pp. 773–779, 2018, doi: 10.1200/JCO.2017.76.9901.
[87] V. A. Arrieta *et al.*, “Immune checkpoint blockade in glioblastoma: from tumor heterogeneity to personalized treatment,” *J. Clin. Invest.*, vol. 133, no. 2, 2023, doi: 10.1172/JCI163447.
[88] P. E. Fecci *et al.*, “Systemic CTLA-4 blockade ameliorates glioma-induced changes to the CD4 + T cell compartment without affecting regulatory T-cell function,” *Clin. Cancer Res.*, vol. 13, no. 7, pp. 2158–2167, 2007, doi: 10.1158/1078-0432.CCR-06-2070.
[89] J. P. Antonios *et al.*, “PD-1 blockade enhances the vaccination-induced immune response in glioma,” *JCI Insight*, vol. 1, no. 10, pp. 1–13, 2019, doi: 10.1172/jci.insight.87059.
[90] A. C. Filley, M. Henriquez, and M. Dey, “Recurrent glioma clinical trial, CheckMate-143: the game is not over yet,” *Oncotarget*, vol. 8, no. 53, pp. 91779–91794, 2017.
[91] A. Omuro *et al.*, “Radiotherapy combined with nivolumab or temozolomide for newly diagnosed glioblastoma with unmethylated MGMT promoter: An international randomized phase III trial,” *Neuro-Oncol.*, vol. 25, no. 1, pp. 123–134, 2023, doi: 10.1093/neuonc/noac099.
[92] M. E. Hegi *et al.*, “MGMT Gene Silencing and Benefit from Temozolomide in Glioblastoma,” *N. Engl. J. Med.*, vol. 352, no. 10, pp. 997–1003, 2005, doi: 10.1056/nejmoa043331.
[93] M. Lim *et al.*, “Phase III trial of chemoradiotherapy with temozolomide plus nivolumab or placebo for newly diagnosed glioblastoma with methylated MGMT promoter,” *Neuro-Oncol.*, vol. 24, no. 11, pp. 1935–1949, 2022, doi: 10.1093/neuonc/noac116.
[94] T. F. Cloughesy *et al.*, “Neoadjuvant anti-PD-1 immunotherapy promotes a survival benefit with intratumoral and systemic immune responses in recurrent glioblastoma,” *Nat. Med.*, vol. 25, no. 3, pp. 477–486, 2019, doi: 10.1038/s41591-018-0337-7.
[95] J. Zhao *et al.*, “Immune and genomic correlates of response to anti-PD-1 immunotherapy in glioblastoma,” *Nat. Med.*, vol. 25, no. 3, pp. 462–469, 2019, doi: 10.1038/s41591-019-0349-y.
[96] K. A. Schalper *et al.*, “Neoadjuvant nivolumab modifies the tumor immune microenvironment in resectable glioblastoma,” *Nat. Med.*, vol. 25, no. 3, pp. 470–476, 2019, doi: 10.1038/s41591-018-0339-5.
[97] J. De Groot *et al.*, “Window-of-opportunity clinical trial of pembrolizumab in patients with recurrent glioblastoma reveals predominance of immune-suppressive macrophages,” *Neuro-Oncol.*, vol. 22, no. 4, pp. 539–549, 2020, doi: 10.1093/neuonc/noz185.
[98] C. E. Brown *et al.*, “Regression of Glioblastoma after Chimeric Antigen Receptor T-Cell Therapy,” *N. Engl. J. Med.*, vol. 375, no. 26, pp. 2561–2569, 2016, doi: 10.1056/nejmoa1610497.
[99] D. M. O. Rourke *et al.*, “A single dose of peripherally infused EGFRvIII-directed CAR T cells mediates antigen loss and induces adaptive resistance in patients with recurrent glioblastoma,” *Sci. Transl. Med.*, vol. 9, no. 399, 2017, doi: 10.1126/scitranslmed.aaa0984.A.
[100] N. Ahmed *et al.*, “HER2-specific chimeric antigen receptor–modified virus-specific T cells for progressive glioblastoma: A phase 1 dose-escalation trial,” *JAMA Oncol.*, vol. 3, no. 8, pp. 1094–1101, 2017, doi: 10.1001/jamaoncol.2017.0184.
[101] M. C. Burger *et al.*, “Intracranial injection of natural killer cells engineered with a HER2-targeted chimeric antigen receptor in patients with recurrent glioblastoma,” *Neuro-Oncol.*, vol. 25, no. 11, pp. 2058–2071, 2023, doi: 10.1093/neuonc/noad087.

[102] K. B. Long *et al.*, “CAR T Cell Therapy of Non-hematopoietic Malignancies: Detours on the Road to Clinical Success,” *Front. Immunol.*, vol. 9, no. December, 2018, doi: 10.3389/fimmu.2018.02740.
[103] C. D. Arvanitis, G. B. Ferraro, and R. K. Jain, “The blood–brain barrier and blood–tumour barrier in brain tumours and metastases,” *Nat. Rev. Cancer*, vol. 20, no. 1, pp. 26–41, 2020, doi: 10.1038/s41568-019-0205-x.
[104] D. C. Hinshaw and L. A. Shevde, “The tumor microenvironment innately modulates cancer progression,” *Cancer Res.*, vol. 79, no. 18, pp. 4557–4567, 2019, doi: 10.1158/0008-5472.CAN-18-3962.
[105] A. Burgess and K. Hynynen, “Drug delivery across the blood-brain barrier using focused ultrasound,” *Expert Opin. Drug Deliv.*, vol. 11, no. 5, pp. 711–721, May 2014, doi: 10.1517/17425247.2014.897693.
[106] W. M. Pardridge, “Drug transport across the blood-brain barrier,” *J. Cereb. Blood Flow Metab.*, vol. 32, no. 11, pp. 1959–1972, 2012, doi: 10.1038/jcbfm.2012.126.
[107] M. M. Patel and B. M. Patel, “Crossing the Blood–Brain Barrier: Recent Advances in Drug Delivery to the Brain,” *CNS Drugs*, vol. 31, no. 2, pp. 109–133, 2017, doi: 10.1007/s40263-016-0405-9.
[108] Y. Chen and L. Liu, “Modern methods for delivery of drugs across the blood-brain barrier,” *Adv. Drug Deliv. Rev.*, vol. 64, no. 7, pp. 640–665, 2012, doi: 10.1016/j.addr.2011.11.010.
[109] H. Wolburg, S. Noell, P. Fallier-Becker, A. F. MacK, and K. Wolburg-Buchholz, “The disturbed blood-brain barrier in human glioblastoma,” *Mol. Aspects Med.*, vol. 33, no. 5–6, pp. 579–589, 2012, doi: 10.1016/j.mam.2012.02.003.
[110] B. K. Ahir, H. H. Engelhard, and S. S. Lakka, “Tumor Development and Angiogenesis in Adult Brain Tumor: Glioblastoma,” *Mol. Neurobiol.*, vol. 57, no. 5, pp. 2461–2478, 2020, doi: 10.1007/s12035-020-01892-8.
[111] W. Wang, W. L. Dentler, and R. T. Borchardt, “VEGF increases BMEC monolayer permeability by affecting occludin expression and tight junction assembly,” *Am. J. Physiol. - Heart Circ. Physiol.*, vol. 280, no. 1 49-1, pp. 434–440, 2001, doi: 10.1152/ajpheart.2001.280.1.h434.
[112] K. Wang *et al.*, “Regulation of pathological blood-brain barrier for intracranial enhanced drug delivery and anti-glioblastoma therapeutics,” *Oncol. Res.*, vol. 29, no. 5, pp. 351–363, 2021, doi: 10.32604/or.2022.025696.
[113] W. A. Banks and E. M. Rhea, “The blood–brain barrier, oxidative stress, and insulin resistance,” *Antioxidants*, vol. 10, no. 11, 2021, doi: 10.3390/antiox10111695.
[114] Y. Wang *et al.*, “Mitochondrial oxidative stress in brain microvascular endothelial cells: Triggering blood-brain barrier disruption,” *Mitochondrion*, vol. 69, no. October 2022, pp. 71–82, 2023, doi: 10.1016/j.mito.2023.01.007.
[115] C. Zhao, H. Wang, C. Xiong, and Y. Liu, “Hypoxic glioblastoma release exosomal VEGF-A induce the permeability of blood-brain barrier,” *Biochem. Biophys. Res. Commun.*, vol. 502, no. 3, pp. 324–331, 2018, doi: 10.1016/j.bbrc.2018.05.140.
[116] A. Ou, W. K. Alfred Yung, and N. Majd, “Molecular mechanisms of treatment resistance in glioblastoma,” *Int. J. Mol. Sci.*, vol. 22, no. 1, pp. 1–24, 2021, doi: 10.3390/ijms22010351.
[117] D. Wang, C. Wang, L. Wang, and Y. Chen, “A comprehensive review in improving delivery of small-molecule chemotherapeutic agents overcoming the blood-brain/brain tumor barriers for glioblastoma treatment,” *Drug Deliv.*, vol. 26, no. 1, pp. 551–565, 2019, doi: 10.1080/10717544.2019.1616235.
[118] Sheila K. Singh *et al.*, “Identification of human brain tumour initiating cells,” *Nature*, vol. 432, no. 7015, pp. 396–401, 2004, doi: 10.1038/nature03031.1.

[119] J. D. Lathia, S. C. Mack, E. E. Mulkearns-Hubert, C. L. L. Valentim, and J. N. Rich, “Cancer stem cells in glioblastoma,” *Genes Dev.*, pp. 539–552, 2023, doi: 10.1016/B978-0-323-99873-4.00001-3.
[120] S. Bao *et al.*, “Glioma stem cells promote radioresistance by preferential activation of the DNA damage response,” *Nature*, vol. 444, no. 7120, pp. 756–760, 2006, doi: 10.1038/nature05236.
[121] J. Chen *et al.*, “A restricted cell population propagates glioblastoma growth after chemotherapy,” *Nature*, vol. 488, no. 7412, pp. 522–526, 2012, doi: 10.1038/nature11287.
[122] D. Hambardzumyan, D. H. Gutmann, and H. Kettenmann, “The role of microglia and macrophages in glioma maintenance and progression,” *Nat. Neurosci.*, vol. 19, pp. 20–27, 2016, doi: 10.1038/nn.4185.The.
[123] S. J. Coniglio *et al.*, “Microglial stimulation of glioblastoma invasion involves epidermal growth factor receptor (EGFR) and colony stimulating factor 1 receptor (CSF-1R) signaling.,” *Mol. Med.*, vol. 18, no. 1, pp. 519–527, 2012, doi: 10.2119/molmed.2011.00217.
[124] P. Sharma, A. Aaroe, L. Jiyong, and V. K. Puduvalli, “Tumor microenvironment in glioblastoma: Current and emerging concepts,” *Neuro-Oncol. Adv.*, vol. 5, no. February, pp. 1–16, 2023.
[125] T. L. Whiteside, “The tumor microenvironment and its role in promoting tumor growth,” *Oncogene*, vol. 27, no. 45, pp. 5904–5912, 2008, doi: 10.1038/onc.2008.271.The.
[126] C. Hao, I. F. Parney, W. H. Roa, J. Turner, K. C. Petruk, and D. A. Ramsay, “Cytokine and cytokine receptor mRNA expression in human glioblastomas: Evidence of Th1, Th2 and Th3 cytokine dysregulation,” *Acta Neuropathol. (Berl.)*, vol. 103, no. 2, pp. 171–178, 2002, doi: 10.1007/s004010100448.
[127] F. Klemm *et al.*, “Interrogation of the Microenvironmental Landscape in Brain Tumors Reveals Disease-Specific Alterations of Immune Cells,” *Cell*, vol. 181, no. 7, pp. 1643-1660.e17, 2020, doi: 10.1016/j.cell.2020.05.007.
[128] K. I. Woroniecka, K. E. Rhodin, P. Chongsathidkiet, K. A. Keith, and P. E. Fecci, “T-Cell dysfunction in glioblastoma: Applying a new framework,” *Clin. Cancer Res.*, vol. 24, no. 16, pp. 3792–3802, 2018, doi: 10.1158/1078-0432.CCR-18-0047.
[129] Y. Soda *et al.*, “Transdifferentiation of glioblastoma cells into vascular endothelial cells,” *Proc. Natl. Acad. Sci.*, vol. 108, no. 11, pp. 4274–4280, 2011.
[130] S. El Hallani *et al.*, “A new alternative mechanism in glioblastoma vascularization: Tubular vasculogenic mimicry,” *Brain*, vol. 133, no. 4, pp. 973–982, 2010, doi: 10.1093/brain/awq044.
[131] W. J. Peng *et al.*, “Matrix metalloproteinases: A review of their structure and role in systemic sclerosis,” *J. Clin. Immunol.*, vol. 32, no. 6, pp. 1409–1414, 2012, doi: 10.1007/s10875-012-9735-7.
[132] C. Hagemann, “A complete compilation of matrix metalloproteinase expression in human malignant gliomas,” *World J. Clin. Oncol.*, vol. 3, no. 5, p. 67, 2012, doi: 10.5306/wjco.v3.i5.67.
[133] M. Wiranowska *et al.*, “Modulation of hyaluronan production by CD44 positive glioma cells,” *Int. J. Cancer*, vol. 127, no. 3, pp. 532–542, 2010, doi: 10.1002/ijc.25085.
[134] B. Annabi, M. Bouzeghrane, R. Moumdjian, A. Moghrabi, and R. Béliveau, “Probing the infiltrating character of brain tumors: Inhibition of RhoA/ROK-mediated CD44 cell surface shedding from glioma cells by the green tea catechin EGCg,” *J. Neurochem.*, vol. 94, no. 4, pp. 906–916, 2005, doi: 10.1111/j.1471-4159.2005.03256.x.
[135] L. A. Kankeu Fonkoua, O. Sirpilla, R. Sakemura, E. L. Siegler, and S. S. Kenderian, “CAR T cell therapy and the tumor microenvironment: Current challenges and opportunities,” *Mol. Ther. - Oncolytics*, vol. 25, no. June, pp. 69–77, 2022, doi: 10.1016/j.omto.2022.03.009.
[136] R. S. C. Cobbold, *Foundations of Biomedical Ultrasound*. Oxford Press, 2006.

[137] W. Qiu, A. Bouakaz, E. E. Konofagou, and H. Zheng, “Ultrasound for the Brain: A Review of Physical and Engineering Principles, and Clinical Applications,” *IEEE Trans. Ultrason. Ferroelectr. Freq. Control*, vol. 68, no. 1, pp. 6–20, 2021, doi: 10.1109/TUFFC.2020.3019932.
[138] J. Pomeraniec, W. J. Elias, and S. Moosa, “High-Frequency Ultrasound Ablation in Neurosurgery,” *Neurosurg. Clin. N. Am.*, vol. 34, no. 2, pp. 301–310, 2023.
[139] H. H. Jung *et al.*, “Bilateral thermal capsulotomy with MR-guided focused ultrasound for patients with treatment-refractory obsessive-compulsive disorder: A proof-of-concept study,” *Mol. Psychiatry*, vol. 20, no. 10, pp. 1205–1211, 2015, doi: 10.1038/mp.2014.154.
[140] B. Davidson *et al.*, “Magnetic resonance-guided focused ultrasound capsulotomy for refractory obsessive compulsive disorder and major depressive disorder: clinical and imaging results from two phase I trials,” *Mol. Psychiatry*, vol. 25, no. 9, pp. 1946–1957, 2020, doi: 10.1038/s41380-020-0737-1.
[141] E. Martin, D. Jeanmonod, A. Morel, E. Zadicario, and B. Werner, “High-intensity focused ultrasound for noninvasive functional neurosurgery,” *Ann. Neurol.*, vol. 66, no. 6, pp. 858–861, 2009, doi: 10.1002/ana.21801.
[142] N. D. Sheybani and R. J. Price, “Perspectives on recent progress in focused ultrasound immunotherapy,” *Theranostics*, vol. 9, no. 25, pp. 7749–7758, 2019, doi: 10.7150/thno.37131.
[143] K. Hynynen, N. McDannold, N. A. Sheikov, F. A. Jolesz, and N. Vykhodtseva, “Local and reversible blood-brain barrier disruption by noninvasive focused ultrasound at frequencies suitable for trans-skull sonications.,” *NeuroImage*, vol. 24, no. 1, pp. 12–20, Jan. 2005, doi: 10.1016/j.neuroimage.2004.06.046.
[144] B. Helfield, “A review of phospholipid encapsulated ultrasound contrast agent microbubble physics,” *Ultrasound Med. Biol.*, vol. 45, no. 2, pp. 282–300, 2019, doi: 10.1016/j.ultrasmedbio.2018.09.020.
[145] H. G. Flynn, “Cavitation dynamics: II. Free pulsations and models for cavitation bubbles,” *J. Acoust. Soc. Am.*, vol. 58, no. 6, pp. 1160–1170, 1975, doi: 10.1121/1.380799.
[146] N. de Jong *et al.*, “‘Compression-only’ behavior of phospholipid-coated contrast bubbles.,” *Ultrasound Med. Biol.*, vol. 33, no. 4, pp. 653–656, Apr. 2007, doi: 10.1016/j.ultrasmedbio.2006.09.016.
[147] M. Postema, A. van Wamel, C. T. Lancée, and N. de Jong, “Ultrasound-induced encapsulated microbubble phenomena.,” *Ultrasound Med. Biol.*, vol. 30, no. 6, pp. 827–40, Jun. 2004, doi: 10.1016/j.ultrasmedbio.2004.02.010.
[148] A. van Wamel, A. Bouakaz, M. Versluis, and N. de Jong, “Micromanipulation of endothelial cells: ultrasound-microbubble-cell interaction.,” *Ultrasound Med. Biol.*, vol. 30, no. 9, pp. 1255–1258, Sep. 2004, doi: 10.1016/j.ultrasmedbio.2004.07.015.
[149] E. Memari, F. Hui, H. Yusefi, and B. Helfield, “Fluid flow influences ultrasound-assisted endothelial membrane permeabilization and calcium flux,” *J. Controlled Release*, vol. 358, no. April, pp. 333–344, 2023, doi: 10.1016/j.jconrel.2023.05.004.
[150] Y. Hu, J. M. F. Wan, and A. C. H. Yu, “Membrane perforation and recovery dynamics in microbubble-mediated sonoporation,” *Ultrasound Med. Biol.*, vol. 39, no. 12, pp. 2393–2405, Dec. 2013, doi: 10.1016/j.ultrasmedbio.2013.08.003.
[151] N. Sheikov, N. McDannold, N. Vykhodtseva, F. Jolesz, and K. Hynynen, “Cellular mechanisms of the blood-brain barrier opening induced by ultrasound in presence of microbubbles,” *Ultrasound Med. Biol.*, vol. 30, no. 7, pp. 979–989, 2004, doi: 10.1016/j.ultrasmedbio.2004.04.010.
[152] B. Helfield, X. Chen, S. C. Watkins, and F. S. Villanueva, “Biophysical insight into mechanisms of sonoporation,” *Proc. Natl. Acad. Sci.*, vol. 113, no. 36, pp. 9983–9988, 2016, doi: 10.1073/pnas.1606915113.

[153] K. Kooiman, M. Foppen-Harteveld, A. F. W. van der Steen, and N. de Jong, “Sonoporation of endothelial cells by vibrating targeted microbubbles,” *J. Control. Release Off. J. Control. Release Soc.*, vol. 154, no. 1, pp. 35–41, Aug. 2011, doi: 10.1016/j.jconrel.2011.04.008.
[154] I. De Cock *et al.*, “Ultrasound and microbubble mediated drug delivery: Acoustic pressure as determinant for uptake via membrane pores or endocytosis,” *J. Controlled Release*, vol. 197, pp. 20–28, 2015, doi: 10.1016/j.jconrel.2014.10.031.
[155] H. J. Vos, B. Dollet, M. Versluis, and N. de Jong, “Nonspherical shape oscillations of coated microbubbles in contact with a wall.,” *Ultrasound Med. Biol.*, vol. 37, no. 6, pp. 935–948, Jun. 2011, doi: 10.1016/j.ultrasmedbio.2011.02.013.
[156] H. Chen, A. a Brayman, W. Kreider, M. R. Bailey, and T. J. Matula, “Observations of translation and jetting of ultrasound-activated microbubbles in mesenteric microvessels.,” *Ultrasound Med. Biol.*, vol. 37, no. 12, pp. 2139–2148, Dec. 2011, doi: 10.1016/j.ultrasmedbio.2011.09.013.
[157] J. M. Escoffre, P. Campomanes, M. Tarek, and A. Bouakaz, “New insights on the role of ROS in the mechanisms of sonoporation-mediated gene delivery,” *Ultrason. Sonochem.*, vol. 64, no. February, 2020, doi: 10.1016/j.ultsonch.2020.104998.
[158] I. Beekers *et al.*, “High-Resolution Imaging of Intracellular Calcium Fluctuations Caused by Oscillating Microbubbles,” *Ultrasound Med. Biol.*, vol. 46, no. 8, pp. 2017–2029, 2020, doi: 10.1016/j.ultrasmedbio.2020.03.029.
[159] Z. Fan, H. Liu, M. Mayer, and C. X. Deng, “Spatiotemporally controlled single cell sonoporation.,” *Proc. Natl. Acad. Sci.*, vol. 109, no. 41, pp. 16486–91, Oct. 2012, doi: 10.1073/pnas.1208198109.
[160] J. Park, Z. Fan, R. E. Kumon, M. E. H. El-Sayed, and C. X. Deng, “Modulation of intracellular Ca2+ concentration in brain microvascular endothelial cells in vitro by acoustic cavitation,” *Ultrasound Med. Biol.*, vol. 36, no. 7, pp. 1176–1187, 2010, doi: 10.1016/j.ultrasmedbio.2010.04.006.
[161] F. Moccetti *et al.*, “Flow Augmentation in the Myocardium by Ultrasound Cavitation of Microbubbles: Role of Shear-Mediated Purinergic Signaling,” *J. Am. Soc. Echocardiogr.*, vol. 33, no. 8, pp. 1023-1031.e2, 2020, doi: 10.1016/j.echo.2020.03.016.
[162] J. T. Belcik *et al.*, “Augmentation of Muscle Blood Flow by Ultrasound Cavitation is Mediated by ATP and Purinergic Signaling,” *Circulation*, vol. 135, no. 13, pp. 1240–1252, 2017.
[163] T. Mainprize *et al.*, “Blood-Brain Barrier Opening in Primary Brain Tumors with Non-invasive MR-Guided Focused Ultrasound: A Clinical Safety and Feasibility Study,” *Sci. Rep.*, vol. 9, no. 1, pp. 1–7, 2019, doi: 10.1038/s41598-018-36340-0.
[164] N. Lipsman *et al.*, “Blood–brain barrier opening in Alzheimer’s disease using MR-guided focused ultrasound,” *Nat. Commun.*, vol. 9, no. 1, p. 2336, 2018, doi: 10.1038/s41467-018-04529-6.
[165] A. Abrahao *et al.*, “First-in-human trial of blood–brain barrier opening in amyotrophic lateral sclerosis using MR-guided focused ultrasound,” *Nat. Commun.*, vol. 10, no. 1, pp. 1–9, 2019, doi: 10.1038/s41467-019-12426-9.
[166] H. Chen and E. E. Konofagou, “The size of blood-brain barrier opening induced by focused ultrasound is dictated by the acoustic pressure,” *J. Cereb. Blood Flow Metab.*, vol. 34, no. 7, pp. 1197–1204, 2014, doi: 10.1038/jcbfm.2014.71.
[167] M. A. O’Reilly, A. C. Waspe, M. Ganguly, and K. Hynynen, “Focused-ultrasound disruption of the blood-brain barrier using closely-timed short pulses: influence of sonication parameters and injection rate,” *Ultrasound Med. Biol.*, vol. 37, no. 4, pp. 587–594, Apr. 2011, doi: 10.1016/j.ultrasmedbio.2011.01.008.

[168] C. Bing *et al.*, “Characterization of different bubble formulations for blood-brain barrier opening using a focused ultrasound system with acoustic feedback control,” *Sci. Rep.*, vol. 8, no. 1, pp. 1–12, 2018, doi: 10.1038/s41598-018-26330-7.
[169] R. M. Jones and K. R. Hynynen, “Advances in acoustic monitoring and control of focused ultrasound-mediated increases in blood-brain barrier permeability,” *Br. J. Radiol.*, vol. 92, no. 1096, pp. 1–13, 2019, doi: 10.1259/bjr.20180601.
[170] A. Hughes, D. S. Khan, and R. Alkins, “Current and Emerging Systems for Focused Ultrasound-Mediated Blood–Brain Barrier Opening,” *Ultrasound Med. Biol.*, vol. 49, no. 7, pp. 1479–1490, 2023, doi: 10.1016/j.ultrasmedbio.2023.02.017.
[171] M. Kinoshita, N. McDannold, F. A. Jolesz, and K. Hynynen, “Targeted delivery of antibodies through the blood-brain barrier by MRI-guided focused ultrasound,” *Biochem. Biophys. Res. Commun.*, vol. 340, no. 4, pp. 1085–1090, 2006, doi: 10.1016/j.bbrc.2005.12.112.
[172] M. Kinoshita, N. McDannold, F. A. Jolesz, and K. Hynynen, “Noninvasive localized delivery of Herceptin to the mouse brain by MRI-guided focused ultrasound-induced blood-brain barrier disruption,” *Proc. Natl. Acad. Sci.*, vol. 103, no. 31, pp. 11719–11723, 2006, doi: 10.1073/pnas.0604318103.
[173] A. Sabbagh *et al.*, “Opening of the blood–brain barrier using low-intensity pulsed ultrasound enhances responses to immunotherapy in preclinical glioma models,” *Clin. Cancer Res.*, vol. 27, no. 15, pp. 4325–4337, 2021, doi: 10.1158/1078-0432.CCR-20-3760.
[174] C. D. Arvanitis *et al.*, “Mechanisms of enhanced drug delivery in brain metastases with focused ultrasound-induced blood–tumor barrier disruption,” *Proc. Natl. Acad. Sci.*, vol. 115, no. 37, pp. E8717–E8726, 2018, doi: 10.1073/pnas.1807105115.
[175] L. J. Liu and M. Schlesinger, “Interstitial hydraulic conductivity and interstitial fluid pressure for avascular or poorly vascularized tumors,” *J. Theor. Biol.*, vol. 380, pp. 1–8, 2015, doi: 10.1016/j.jtbi.2015.05.012.
[176] T. Kobus, I. K. Zervantonakis, Y. Zhang, and N. J. McDannold, “Growth inhibition in a brain metastasis model by antibody delivery using focused ultrasound-mediated blood-brain barrier disruption,” *J. Controlled Release*, vol. 238, pp. 281–288, 2016, doi: 10.1016/j.jconrel.2016.08.001.
[177] Y. C. Ooi *et al.*, “The role of regulatory T-cells in glioma immunology,” *Clin. Neurol. Neurosurg.*, vol. 119, pp. 125–132, 2014, doi: 10.1016/j.clineuro.2013.12.004.
[178] J. Ben-Shoshan, S. Maysel-Auslender, A. Mor, G. Keren, and J. George, “Hypoxia controls CD4+ CD25+ regulatory T-cell homeostasis via hypoxia-inducible factor-1α,” *Eur. J. Immunol.*, vol. 38, no. 9, pp. 2412–2418, 2008, doi: 10.1002/eji.200838318.
[179] R. Alkins *et al.*, “Focused ultrasound delivers targeted immune cells to metastatic brain tumors,” *Cancer Res.*, vol. 73, no. 6, pp. 1892–1899, 2013, doi: 10.1158/0008-5472.CAN-12-2609.
[180] W. Xu, X. Zhang, X. Hu, C. Zhiyi, and P. Huang, “Translational Prospects of ultrasound-mediated tumor immunotherapy: Preclinical advances and safety considerations,” *Cancer Lett.*, vol. 460, no. February, pp. 86–95, 2019, doi: 10.1016/j.canlet.2019.06.017.
[181] P. Y. Chen, H. Y. Hsieh, C. Y. Huang, C. Y. Lin, K. C. Wei, and H. L. Liu, “Focused ultrasound-induced blood-brain barrier opening to enhance interleukin-12 delivery for brain tumor immunotherapy: A preclinical feasibility study,” *J. Transl. Med.*, vol. 13, no. 1, pp. 1–12, 2015, doi: 10.1186/s12967-015-0451-y.
[182] B. L. Helfield and D. E. Goertz, “Nonlinear resonance behavior and linear shell estimates for Definity™ and MicroMarker™ assessed with acoustic microbubble spectroscopy.,” *J. Acoust. Soc. Am.*, vol. 133, no. 2, pp. 1158–1568, Feb. 2013, doi: 10.1121/1.4774379.

[183] J. M. Hyvelin *et al.*, "Characteristics and Echogenicity of Clinical Ultrasound Contrast Agents: An in Vitro and in Vivo Comparison Study," *J. Ultrasound Med.*, vol. 36, no. 5, pp. 941–953, 2017, doi: 10.7863/ultra.16.04059.
[184] B. L. Helfield, X. Huo, R. Williams, and D. E. Goertz, "The effect of preactivation vial temperature on the acoustic properties of Definity™.," *Ultrasound Med. Biol.*, vol. 38, no. 7, pp. 1298–305, Jul. 2012, doi: 10.1016/j.ultrasmedbio.2012.03.005.
[185] D. E. Goertz, N. de Jong, and A. F. W. van der Steen, "Attenuation and Size Distribution Measurements of Definity™ and Manipulated Definity™ Populations," *Ultrasound Med. Biol.*, vol. 33, no. 9, pp. 1376–1388, Sep. 2007, doi: 10.1016/j.ultrasmedbio.2007.03.009.
[186] J. J. Choi *et al.*, "Microbubble-Size Dependence of Focused Ultrasound-Induced Blood-Brain-Barrier Opening in Mice In Vivo," *IEE Trans. Biomed. Eng.*, vol. 57, no. 1, pp. 145–154, 2010.
[187] S. Wang, G. Samiotaki, O. Olumolade, J. A. Feshitan, and E. E. Konofagou, "Microbubble type and distribution dependence of focused ultrasound-induced blood-brain barrier opening," *Ultrasound Med. Biol.*, vol. 40, no. 1, pp. 130–137, 2014, doi: 10.1016/j.ultrasmedbio.2013.09.015.
[188] F. Vlachos, Y. S. Tung, and E. Konofagou, "Permeability dependence study of the focused ultrasound-induced blood-brain barrier opening at distinct pressures and microbubble diameters using DCE-MRI," *Magn. Reson. Med.*, vol. 66, no. 3, pp. 821–830, 2011, doi: 10.1002/mrm.22848.
[189] K. H. Song, A. C. Fan, J. J. Hinkle, J. Newman, M. A. Borden, and B. K. Harvey, "Microbubble gas volume: A unifying dose parameter in blood-brain barrier opening by focused ultrasound," *Theranostics*, vol. 7, no. 1, pp. 144–152, 2017, doi: 10.7150/thno.15987.
[190] J. W. Roberts, L. Powlovich, N. Sheybani, and S. LeBlang, "Focused ultrasound for the treatment of glioblastoma," *J. Neurooncol.*, vol. 157, no. 2, pp. 237–247, 2022, doi: 10.1007/s11060-022-03974-0.
[191] R. E. Apfel and C. K. Holland, "Gauging the likelihood of cavitation from short-pulse, low-duty cycle diagnostic ultrasound," *Ultrasound Med. Biol.*, vol. 17, no. 2, pp. 179–185, 1991, doi: 10.1016/0301-5629(91)90125-G.
[192] N. McDannold, N. Vykhodtseva, and K. Hynynen, "Blood-Brain Barrier Disruption Induced by Focused Ultrasound and Circulating Preformed Microbubbles Appears to Be Characterized by the Mechanical Index," *Ultrasound Med. Biol.*, vol. 34, no. 5, pp. 834–840, 2008, doi: 10.1016/j.ultrasmedbio.2007.10.016.
[193] J. J. Choi, S. Wang, Y. S. Tung, B. Morrison, and E. E. Konofagou, "Molecules of Various Pharmacologically-Relevant Sizes Can Cross the Ultrasound-Induced Blood-Brain Barrier Opening in vivo," *Ultrasound Med. Biol.*, vol. 36, no. 1, pp. 58–67, 2010, doi: 10.1016/j.ultrasmedbio.2009.08.006.
[194] H. Chen and E. E. Konofagou, "The size of blood-brain barrier opening induced by focused ultrasound is dictated by the acoustic pressure," *J. Cereb. Blood Flow Metab.*, vol. 34, no. 7, pp. 1197–1204, 2014, doi: 10.1038/jcbfm.2014.71.
[195] C. D. Hue *et al.*, "Time Course and Size of Blood-Brain Barrier Opening in a Mouse Model of Blast-Induced Traumatic Brain Injury," *J. Neurotrauma*, vol. 33, no. 13, pp. 1202–1211, 2016, doi: 10.1089/neu.2015.4067.
[196] P. W. Janowicz, G. Leinenga, J. Götz, and R. M. Nisbet, "Ultrasound-mediated blood-brain barrier opening enhances delivery of therapeutically relevant formats of a tau-specific antibody," *Sci. Rep.*, vol. 9, no. 1, pp. 1–9, 2019, doi: 10.1038/s41598-019-45577-2.
[197] S. Ohta, E. Kikuchi, A. Ishijima, T. Azuma, I. Sakuma, and T. Ito, "Investigating the optimum size of nanoparticles for their delivery into the brain assisted by focused ultrasound-induced

blood–brain barrier opening," *Sci. Rep.*, vol. 10, no. 1, pp. 1–13, 2020, doi: 10.1038/s41598-020-75253-9.
[198] N. D. Sheybani, A. R. Witter, W. J. Garrison, G. W. Miller, R. J. Price, and T. N. J. Bullock, "Profiling of the immune landscape in murine glioblastoma following blood brain/tumor barrier disruption with MR image-guided focused ultrasound," *J. Neurooncol.*, vol. 156, no. 1, pp. 109–122, 2022, doi: 10.1007/s11060-021-03887-4.
[199] C. Poon, C. Pellow, and K. Hynynen, "Neutrophil recruitment and leukocyte response following focused ultrasound and microbubble mediated blood-brain barrier treatments," *Theranostics*, vol. 11, no. 4, pp. 1655–1671, 2021, doi: 10.7150/thno.52710.
[200] R. Ji, M. E. Karakatsani, M. Burgess, M. Smith, M. F. Murillo, and E. E. Konofagou, "Cavitation-modulated inflammatory response following focused ultrasound blood-brain barrier opening," *J. Controlled Release*, vol. 337, no. July, pp. 458–471, 2021, doi: 10.1016/j.jconrel.2021.07.042.
[201] A. Kline-Schoder *et al.*, "Characterization of the responses of brain macrophages to focused ultrasound-mediated blood–brain barrier opening," *Nat. Biomed. Eng.*, 2023, doi: https://doi.org/10.1038/s41551-023-01107-0.
[202] V. Gulani, F. Calamante, F. G. Shellock, E. Kanal, and S. B. Reeder, "Gadolinium deposition in the brain: summary of evidence and recommendations," *Lancet Neurol.*, vol. 16, no. 7, pp. 564–570, 2017, doi: 10.1016/S1474-4422(17)30158-8.
[203] S. Y. Wu, C. S. Sanchez, G. Samiotaki, A. Buch, V. P. Ferrera, and E. E. Konofagou, "Characterizing Focused-Ultrasound Mediated Drug Delivery to the Heterogeneous Primate Brain in Vivo with Acoustic Monitoring," *Sci. Rep.*, vol. 6, no. November, pp. 1–13, 2016, doi: 10.1038/srep37094.
[204] T. Sun, G. Samiotaki, S. Wang, C. Acosta, C. C. Chen, and E. E. Konofagou, "Acoustic cavitation-based monitoring of the reversibility and permeability of ultrasound-induced blood-brain barrier opening," *Phys. Med. Biol.*, vol. 60, no. 23, pp. 9079–9094, 2015, doi: 10.1088/0031-9155/60/23/9079.
[205] M. Aryal, K. Fischer, C. Gentile, S. Gitto, Y. Z. Zhang, and N. McDannold, "Effects on P-glycoprotein expression after blood-brain barrier disruption using focused ultrasound and microbubbles," *PLoS ONE*, vol. 12, no. 1, pp. 1–15, 2017, doi: 10.1371/journal.pone.0166061.
[206] C. D. Arvanitis, M. S. Livingstone, N. Vykhodtseva, and N. McDannold, "Controlled Ultrasound-Induced Blood-Brain Barrier Disruption Using Passive Acoustic Emissions Monitoring," *PLoS ONE*, vol. 7, no. 9, 2012, doi: 10.1371/journal.pone.0045783.
[207] M. A. O'Reilly and K. Hynynen, "Real-time feedback-controlled focused ultrasound disruption by using an acoustic emissions – based controller," *Radiology*, vol. 263, no. 1, pp. 96–106, 2012.
[208] T. Sun *et al.*, "Closed-loop control of targeted ultrasound drug delivery across the blood–brain/tumor barriers in a rat glioma model," *Proc. Natl. Acad. Sci.*, vol. 114, no. 48, pp. E10281–E10290, 2017, doi: 10.1073/pnas.1713328114.
[209] Y. Huang *et al.*, "Cavitation Feedback Control of Focused Ultrasound Blood-Brain Barrier Opening for Drug Delivery in Patients with Parkinson's Disease," *Pharmaceutics*, vol. 14, no. 12, pp. 1–14, 2022, doi: 10.3390/pharmaceutics14122607.
[210] P. Anastasiadis *et al.*, "Localized blood-brain barrier opening in infiltrating gliomas with MRI-guided acoustic emissions-controlled focused ultrasound," *Proc. Natl. Acad. Sci. U. S. A.*, vol. 118, no. 37, 2021, doi: 10.1073/pnas.2103280118.
[211] H. Lee, Y. Guo, J. L. Ross, S. Schoen, F. L. Degertekin, and C. Arvanitis, "Spatially targeted brain cancer immunotherapy with closed-loop controlled focused ultrasound and immune checkpoint blockade," *Sci. Adv.*, vol. 8, no. 46, 2022, doi: 10.1126/sciadv.add2288.

[212] C. D. Arvanitis, G. T. Clement, and N. McDannold, “Transcranial assessment and visualization of acoustic cavitation: Modeling and experimental validation,” *IEEE Trans. Med. Imaging*, vol. 34, no. 6, pp. 1270–1281, 2015, doi: 10.1109/TMI.2014.2383835.
[213] R. M. Jones, L. Deng, K. Leung, D. McMahon, M. A. O’Reilly, and K. Hynynen, “Three-dimensional transcranial microbubble imaging for guiding volumetric ultrasound-mediated blood-brain barrier opening,” *Theranostics*, vol. 8, no. 11, pp. 2909–2926, 2018, doi: 10.7150/thno.24911.
[214] R. M. Jones, D. McMahon, and K. Hynynen, “Ultrafast three-dimensional microbubble imaging in vivo predicts tissue damage volume distributions during nonthermal brain ablation,” *Theranostics*, vol. 10, no. 16, pp. 7211–7230, 2020, doi: 10.7150/thno.47281.
[215] T. N. Kreisl *et al.*, “Phase II trial of single-agent bevacizumab followed by bevacizumab plus irinotecan at tumor progression in recurrent glioblastoma,” *J. Clin. Oncol.*, vol. 27, no. 5, pp. 740–745, 2009, doi: 10.1200/JCO.2008.16.3055.
[216] W. Taal *et al.*, “Single-agent bevacizumab or lomustine versus a combination of bevacizumab plus lomustine in patients with recurrent glioblastoma (BELOB trial): A randomised controlled phase 2 trial,” *Lancet Oncol.*, vol. 15, no. 9, pp. 943–953, 2014, doi: 10.1016/S1470-2045(14)70314-6.
[217] T. T. Batchelor *et al.*, “Phase III randomized trial comparing the efficacy of cediranib as monotherapy, and in combination with lomustine, versus lomustine alone in patients with recurrent glioblastoma,” *J. Clin. Oncol.*, vol. 31, no. 26, pp. 3212–3218, 2013, doi: 10.1200/JCO.2012.47.2464.
[218] N. Wang, R. K. Jain, and T. T. Batchelor, “New Directions in Anti-Angiogenic Therapy for Glioblastoma,” *Neurotherapeutics*, vol. 14, no. 2, pp. 321–332, 2017, doi: 10.1007/s13311-016-0510-y.
[219] I. Fischer, J. P. Gagner, M. Law, E. W. Newcomb, and D. Zagzag, “Angiogenesis in gliomas: Biology and molecular pathophysiology,” *Brain Pathol.*, vol. 15, no. 4, pp. 297–310, 2005, doi: 10.1111/j.1750-3639.2005.tb00115.x.
[220] V. Montana and H. Sontheimer, “Bradykinin promotes the Chemotactic invasion of primary brain tumors,” *J. Neurosci.*, vol. 31, no. 13, pp. 4858–4867, 2011, doi: 10.1523/JNEUROSCI.3825-10.2011.
[221] M. G. McCoy *et al.*, “Endothelial cells promote 3D invasion of GBM by IL-8-dependent induction of cancer stem cell properties,” *Sci. Rep.*, vol. 9, no. 1, pp. 1–14, 2019, doi: 10.1038/s41598-019-45535-y.
[222] M. DeLay *et al.*, “Microarray analysis verifies two distinct phenotypes of glioblastomas resistant to anti-angiogenic therapy,” *Clin. Cancer Res.*, vol. 23, no. 1, pp. 1–7, 2008, doi: 10.1158/1078-0432.CCR-11-2390.Microarray.
[223] D. Cosgrove, “Angiogenesis imaging - Ultrasound,” *Br. J. Radiol.*, vol. 76, no. SPEC. ISS. 1, pp. 43–49, 2003, doi: 10.1259/bjr/86364648.
[224] H. Leong-Poi *et al.*, “Therapeutic arteriogenesis by ultrasound-mediated VEGF165 plasmid gene delivery to chronically ischemic skeletal muscle,” *Circ. Res.*, vol. 101, no. 3, pp. 295–303, 2007, doi: 10.1161/CIRCRESAHA.107.148676.
[225] A. Presset *et al.*, “Endothelial Cells, First Target of Drug Delivery Using Microbubble-Assisted Ultrasound,” *Ultrasound Med. Biol.*, vol. 46, no. 7, pp. 1565–1583, 2020, doi: 10.1016/j.ultrasmedbio.2020.03.013.
[226] J. Cummings *et al.*, “Alzheimer’s disease drug development pipeline: 2022,” *Alzheimers Dement. Transl. Res. Clin. Interv.*, vol. 8, no. 1, 2022, doi: 10.1002/trc2.12295.
[227] M. Shi, F. Chu, F. Zhu, and J. Zhu, “Impact of Anti-amyloid-β Monoclonal Antibodies on the Pathology and Clinical Profile of Alzheimer’s Disease: A Focus on Aducanumab and

Lecanemab," *Front. Aging Neurosci.*, vol. 14, no. April, pp. 1–11, 2022, doi: 10.3389/fnagi.2022.870517.
[228] J. F. Jordao *et al.*, "Amyloid-β plaque reduction, endogenous antibody delivery and glial activation by brain-targeted, transcranial focused ultrasound," *Exp. Neurol.*, vol. 248, pp. 16–29, 2013, doi: 10.1016/j.expneurol.2013.05.008.Amyloid-.
[229] G. Leinenga and J. Götz, "Scanning ultrasound removes amyloid-b and restores memory in an Alzheimer's disease mouse model," *Sci. Transl. Med.*, vol. 7, no. 278, 2015, doi: 10.1126/scitranslmed.aaa2512.
[230] K. Xhima *et al.*, "Focused ultrasound delivery of a selective TrkA agonist rescues cholinergic function in a mouse model of Alzheimer's disease," *Sci. Adv.*, vol. 6, no. 4, 2020, doi: 10.1126/sciadv.aax6646.
[231] J. F. Jordão *et al.*, "Antibodies targeted to the brain with image-guided focused ultrasound reduces amyloid-β plaque load in the TgCRND8 mouse model of Alzheimer's disease," *PLoS ONE*, vol. 5, no. 5, pp. 4–11, 2010, doi: 10.1371/journal.pone.0010549.
[232] C. Kong *et al.*, "Enhanced delivery of a low dose of aducanumab via FUS in 5×FAD mice, an AD model," *Transl. Neurodegener.*, vol. 11, no. 1, pp. 1–15, 2022, doi: 10.1186/s40035-022-00333-x.
[233] L. Chen, E. Cruz, L. E. Oikari, P. Padmanabhan, J. Song, and J. Götz, "Opportunities and challenges in delivering biologics for Alzheimer's disease by low-intensity ultrasound," *Adv. Drug Deliv. Rev.*, vol. 189, p. 114517, 2022, doi: 10.1016/j.addr.2022.114517.
[234] C. R. Gurbatri, N. Arpaia, and T. Danino, "Engineering bacteria as interactive cancer therapies," *Science*, vol. 378, no. 6622, pp. 858–864, 2022, doi: 10.1126/science.add9667.
[235] S. Zhou, C. Gravekamp, D. Bermudes, and K. Liu, "Tumor-targeting bacteria engineered to fight cancer," *Nat. Rev. Cancer*, vol. 18, no. 12, pp. 139–148, 2018, doi: 10.1053/j.gastro.2016.08.014.CagY.
[236] D. I. Piraner, M. H. Abedi, B. A. Moser, A. Lee-Gosselin, and M. G. Shapiro, "Tunable thermal bioswitches for in vivo control of microbial therapeutics," *Food Pharm. Bioeng. Div. 2017 - Core Program. Area 2017 AIChE Annu. Meet.*, vol. 2, no. November 2016, pp. 695–702, 2017, doi: 10.1038/nchembio.2233.
[237] M. H. Abedi *et al.*, "Ultrasound-controllable engineered bacteria for cancer immunotherapy," *Nat. Commun.*, vol. 13, no. 1, 2022, doi: 10.1038/s41467-022-29065-2.
[238] Y. Chen, M. Du, Z. Yuan, Z. Chen, and F. Yan, "Spatiotemporal control of engineered bacteria to express interferon-γ by focused ultrasound for tumor immunotherapy," *Nat. Commun.*, vol. 13, no. 1, pp. 1–15, 2022, doi: 10.1038/s41467-022-31932-x.
[239] L. H. Treat, N. McDannold, Y. Zhang, N. Vykhodtseva, and K. Hynynen, "Targeted Anti-Tumor Effect of Liposomal Doxorubicin After Targeted Blood-Brain-Barrier Disruption by MRI-Guided Focused Ultrasound in Rat Glioma," *Ultrasound Med. Biol.*, vol. 38, no. 10, pp. 1716–1725, 2012, doi: 10.1016/j.ultrasmedbio.2012.04.015.
[240] M. Aryal, N. Vykhodtseva, Y. Z. Zhang, J. Park, and N. McDannold, "Multiple treatments with liposomal doxorubicin and ultrasound-induced disruption of blood-tumor and blood-brain barriers improve outcomes in a rat glioma model," *J. Controlled Release*, vol. 169, no. 1–2, pp. 103–111, 2013, doi: 10.1016/j.jconrel.2013.04.007.
[241] D. Coluccia *et al.*, "Enhancing glioblastoma treatment using cisplatin-gold-nanoparticle conjugates and targeted delivery with magnetic resonance-guided focused ultrasound," *Nanomedicine Nanotechnol. Biol. Med.*, vol. 14, no. 4, pp. 1137–1148, 2018, doi: 10.1016/j.nano.2018.01.021.

[242] C. H. Fan *et al.*, “Folate-conjugated gene-carrying microbubbles with focused ultrasound for concurrent blood-brain barrier opening and local gene delivery,” *Biomaterials*, vol. 106, pp. 46–57, 2016, doi: 10.1016/j.biomaterials.2016.08.017.
[243] E. Thévenot *et al.*, “Targeted delivery of self-complementary adeno-associated virus serotype 9 to the brain, using magnetic resonance imaging-guided focused ultrasound,” *Hum. Gene Ther.*, vol. 23, no. 11, pp. 1144–1155, 2012, doi: 10.1089/hum.2012.013.
[244] A. Burgess, C. A. Ayala-Grosso, M. Ganguly, J. F. Jordão, I. Aubert, and K. Hynynen, “Targeted delivery of neural stem cells to the brain using MRI-guided focused ultrasound to disrupt the blood-brain barrier,” *PLoS ONE*, vol. 6, no. 11, 2011, doi: 10.1371/journal.pone.0027877.
[245] M. Kinoshita, N. McDannold, F. A. Jolesz, and K. Hynynen, “Noninvasive localized delivery of Herceptin to the mouse brain by MRI-guided focused ultrasound-induced blood-brain barrier disruption,” *Proc. Natl. Acad. Sci. U. S. A.*, vol. 103, no. 31, pp. 11719–11723, 2006, doi: 10.1073/pnas.0604318103.
[246] E. J. Park, Y. Z. Zhang, N. Vykhodtseva, and N. McDannold, “Ultrasound-mediated blood-brain/blood-tumor barrier disruption improves outcomes with trastuzumab in a breast cancer brain metastasis model,” *J. Controlled Release*, vol. 163, no. 3, pp. 277–284, 2012, doi: 10.1016/j.jconrel.2012.09.007.
[247] H. L. Liu *et al.*, “Focused ultrasound enhances central nervous system delivery of bevacizumab for malignant glioma treatment,” *Radiology*, vol. 281, no. 1, 2016.
[248] C. Brighi *et al.*, “MR-guided focused ultrasound increases antibody delivery to nonenhancing high-grade glioma,” *Neuro-Oncol. Adv.*, vol. 2, no. 1, pp. 1–12, 2020, doi: 10.1093/noajnl/vdaa030.
[249] D. Ye, J. Yuan, Y. Yue, J. B. Rubin, and H. Chen, “Focused ultrasound-enhanced delivery of intranasally administered anti-programmed cell death-ligand 1 antibody to an intracranial murine glioma model,” *Pharmaceutics*, vol. 13, no. 2, pp. 1–12, 2021, doi: 10.3390/pharmaceutics13020190.
[250] N. D. Sheybani *et al.*, “ImmunoPET-informed sequence for focused ultrasound-targeted mCD47 blockade controls glioma,” *J. Controlled Release*, vol. 331, no. January, pp. 19–29, 2021, doi: 10.1016/j.jconrel.2021.01.023.
[251] Y. Meng *et al.*, “MR-guided focused ultrasound enhances delivery of trastuzumab to Her2-positive brain metastases,” *Sci. Transl. Med.*, vol. 13, no. 615, 2021.
[252] M. H. Ahmed *et al.*, “Low-Intensity Pulsed Ultrasound-Mediated Blood-Brain Barrier Opening Increases Anti-Programmed Death-Ligand 1 Delivery and Efficacy in Gl261 Mouse Model,” *Pharmaceutics*, vol. 15, no. 2, 2023, doi: 10.3390/pharmaceutics15020455.
[253] S. Fadera *et al.*, “Focused Ultrasound-Mediated Delivery of Anti-Programmed Cell Death-Ligand 1 Antibody to the Brain of a Porcine Model,” pp. 1–10, 2023.
[254] E. Porret *et al.*, “Refining the delivery and therapeutic efficacy of cetuximab using focused ultrasound in a mouse model of glioblastoma: An 89Zr-cetuximab immunoPET study,” *Eur. J. Pharm. Biopharm.*, vol. 182, no. August 2022, pp. 141–151, 2023, doi: 10.1016/j.ejpb.2022.12.006.
[255] R. Alkins, A. Burgess, R. Kerbel, W. S. Wels, and K. Hynynen, “Early treatment of HER2-amplified brain tumors with targeted NK-92 cells and focused ultrasound improves survival,” *Neuro-Oncol.*, vol. 18, no. 7, pp. 974–981, 2016, doi: 10.1093/neuonc/nov318.
[256] J. Lee *et al.*, “Non-invasively enhanced intracranial transplantation of mesenchymal stem cells using focused ultrasound mediated by overexpression of cell-adhesion molecules,” *Stem Cell Res.*, vol. 43, no. January, p. 101726, 2020, doi: 10.1016/j.scr.2020.101726.

[257] P. Frinking, T. Segers, Y. Luan, and F. Tranquart, “Three Decades of Ultrasound Contrast Agents: A Review of the Past, Present and Future Improvements,” *Ultrasound Med. Biol.*, vol. 46, no. 4, pp. 892–908, 2020, doi: 10.1016/j.ultrasmedbio.2019.12.008.
[258] H. Medwin, “Counting bubbles acoustically : a review,” *Ultrasonics*, no. January, pp. 7–13, 1977.
[259] J. M. Gorce, M. Arditi, and M. Schneider, “Influence of bubble size distribution on the echogenicity of ultrasound contrast agents - A study of SonoVue (TM),” *Invest. Radiol.*, vol. 35, no. 11, pp. 661–671, 2000, doi: 10.1097/00004424-200011000-00003.
[260] B. L. Helfield, E. Cherin, F. S. Foster, and D. E. Goertz, “Investigating the subharmonic response of individual phospholipid encapsulated microbubbles at high frequencies: a comparative study of five agents.,” *Ultrasound Med. Biol.*, vol. 38, no. 5, pp. 846–863, May 2012, doi: 10.1016/j.ultrasmedbio.2012.01.011.
[261] V. Garbin *et al.*, “Changes in microbubble dynamics near a boundary revealed by combined optical micromanipulation and high-speed imaging,” *Appl. Phys. Lett.*, vol. 90, no. 11, p. 114103, 2007, doi: 10.1063/1.2713164.
[262] B. L. Helfield, B. Y. C. Leung, and D. E. Goertz, “The influence of compliant boundary proximity on the fundamental and subharmonic emissions from individual microbubbles,” *J. Acoust. Soc. Am.*, vol. 136, no. 1, pp. EL40–EL46, 2014, doi: 10.1121/1.4885544.
[263] E. E. Cho, J. Drazic, M. Ganguly, B. Stefanovic, and K. Hynynen, “Two-photon fluorescence microscopy study of cerebrovascular dynamics in ultrasound-induced blood – brain barrier opening,” *J. Cereb. Blood Flow Metab.*, vol. 31, no. 9, pp. 1852–1862, 2011, doi: 10.1038/jcbfm.2011.59.
[264] A. R. Klotz, L. Lindvere, B. Stefanovic, and K. Hynynen, “Temperature change near microbubbles within a capillary network during focused ultrasound,” *Phys. Med. Biol.*, vol. 55, no. 6, pp. 1549–1561, 2010, doi: 10.1088/0031-9155/55/6/001.
[265] J. J. Pacella, J. Brands, F. G. Schnatz, J. J. Black, X. Chen, and F. S. Villanueva, “Treatment of microvascular micro-embolization using microbubbles and long-tone-burst ultrasound: an in vivo study,” *Ultrasound Med. Biol.*, vol. 41, no. 2, pp. 456–464, 2015, doi: 10.1016/j.ultrasmedbio.2014.09.033.
[266] J. Shi, T. Han, A. C. H. Yu, and P. Qin, “Faster calcium recovery and membrane resealing in repeated sonoporation for delivery improvement,” *J. Controlled Release*, vol. 352, no. 800, pp. 385–398, 2022, doi: 10.1016/j.jconrel.2022.10.027.
[267] Z. Fan, R. E. Kumon, J. Park, and C. X. Deng, “Intracellular delivery and calcium transients generated in sonoporation facilitated by microbubbles,” *J. Controlled Release*, vol. 142, no. 1, pp. 31–39, 2010, doi: 10.1016/j.jconrel.2009.09.031.
[268] J. Blackmore, S. Shrivastava, J. Sallet, C. R. Butler, and R. O. Cleveland, “Ultrasound Neuromodulation: A Review of Results, Mechanisms and Safety,” *Ultrasound Med. Biol.*, vol. 45, no. 7, pp. 1509–1536, 2019, doi: 10.1016/j.ultrasmedbio.2018.12.015.
[269] J. R. Lindner, “Microbubbles in medical imaging: current applications and future directions,” *Nat. Rev. Drug Discov.*, vol. 3, no. 6, pp. 527–532, 2004, doi: 10.1038/nrd1417.
[270] K. Kooiman, H. J. Vos, M. Versluis, and N. de Jong, “Acoustic behavior of microbubbles and implications for drug delivery.,” *Adv. Drug Deliv. Rev.*, pp. 1–21, Mar. 2014, doi: 10.1016/j.addr.2014.03.003.
[271] P. Marmottant and S. Hilgenfeldt, “Controlled vesicle deformation and lysis by single oscillating bubbles,” *Nature*, vol. 423, pp. 153–156, 2003, doi: 10.1038/nature01592.
[272] N. Hosseinkhah, H. Chen, T. J. Matula, P. N. Burns, and K. Hynynen, “Mechanisms of microbubble–vessel interactions and induced stresses: A numerical study,” *J. Acoust. Soc. Am.*, vol. 134, no. 3, pp. 1875–1885, 2013, doi: 10.1121/1.4817843.

[273] K. Kooiman *et al.*, “Ultrasound-Responsive Cavitation Nuclei for Therapy and Drug Delivery,” *Ultrasound Med. Biol.*, vol. 46, no. 6, pp. 1296–1325, 2020, doi: 10.1016/j.ultrasmedbio.2020.01.002.
[274] K. Hynynen, N. Mcdannold, N. Vykhodtseva, and F. A. Jolesz, “Noninvasive MR imaging–guided focal opening of the blood-brain barrier in rabbits,” *Radiology*, vol. 220, no. 3, pp. 640–646, 2001.
[275] C. Y. Ting *et al.*, “Concurrent blood-brain barrier opening and local drug delivery using drug-carrying microbubbles and focused ultrasound for brain glioma treatment,” *Biomaterials*, vol. 33, no. 2, pp. 704–712, 2012, doi: 10.1016/j.biomaterials.2011.09.096.
[276] D. Weber-Adrian *et al.*, “Gene delivery to the spinal cord using MRI-guided focused ultrasound,” *Gene Ther.*, vol. 22, no. 7, pp. 568–577, 2015, doi: 10.1038/gt.2015.25.
[277] F. Yan *et al.*, “Paclitaxel-liposome-microbubble complexes as ultrasound-triggered therapeutic drug delivery carriers,” *J. Controlled Release*, vol. 166, no. 3, pp. 246–255, 2013, doi: 10.1016/j.jconrel.2012.12.025.
[278] C. McEwan *et al.*, “Combined sonodynamic and antimetabolite therapy for the improved treatment of pancreatic cancer using oxygen loaded microbubbles as a delivery vehicle,” *Biomaterials*, vol. 80, pp. 20–32, 2016, doi: 10.1016/j.biomaterials.2015.11.033.
[279] A. R. Carson *et al.*, “Ultrasound-targeted microbubble destruction to deliver siRNA cancer therapy,” *Cancer Res.*, vol. 72, no. 23, pp. 6191–6199, Dec. 2012, doi: 10.1158/0008-5472.CAN-11-4079.
[280] K. Hynynen, “Ultrasound for drug and gene delivery to the brain,” *Adv. Drug Deliv. Rev.*, vol. 60, no. 10, pp. 1209–1217, 2008.
[281] M. R. Schwartz, A. C. Debski, and R. J. Price, “Ultrasound-targeted nucleic acid delivery for solid tumor therapy,” *J. Controlled Release*, vol. 339, no. October, pp. 531–546, 2021, doi: 10.1016/j.jconrel.2021.10.010.
[282] H. H. Chen, P. N. Matkar, K. Afrasiabi, M. A. Kuliszewski, and H. Leong-Poi, “Prospect of ultrasound-mediated gene delivery in cardiovascular applications,” *Expert Opin. Biol. Ther.*, vol. 16, no. 6, pp. 815–826, 2017, doi: 10.1517/14712598.2016.1169268.
[283] J. A. Kopechek *et al.*, “Ultrasound and microbubble-targeted delivery of a microRNA inhibitor to the heart suppresses cardiac hypertrophy and preserves cardiac function,” *Theranostics*, vol. 9, no. 23, pp. 7088–7098, 2019, doi: 10.7150/thno.34895.
[284] A. Ghanem *et al.*, “Focused ultrasound-induced stimulation of microbubbles augments site-targeted engraftment of mesenchymal stem cells after acute myocardial infarction,” *J. Mol. Cell. Cardiol.*, vol. 47, no. 3, pp. 411–418, 2009, doi: 10.1016/j.yjmcc.2009.06.008.
[285] S. Bulner, A. Prodeus, J. Gariepy, K. Hynynen, and D. E. Goertz, “Enhancing Checkpoint Inhibitor Therapy with Ultrasound Stimulated Microbubbles,” *Ultrasound Med. Biol.*, vol. 45, no. 2, pp. 500–512, 2019, doi: 10.1016/j.ultrasmedbio.2018.10.002.
[286] Y. J. Ho, J. P. Li, C. H. Fan, H. L. Liu, and C. K. Yeh, “Ultrasound in tumor immunotherapy: Current status and future developments,” *J. Controlled Release*, vol. 323, no. April, pp. 12–23, 2020, doi: 10.1016/j.jconrel.2020.04.023.
[287] Z. Fan, H. Liu, M. Mayer, and C. X. Deng, “Spatiotemporally controlled single cell sonoporation,” *Proc. Natl. Acad. Sci.*, vol. 109, no. 41, pp. 16486–16491, 2012, doi: 10.1073/pnas.1208198109/-/DCSupplemental.www.pnas.org/cgi/doi/10.1073/pnas.1208198109.
[288] R. Karshafian, P. D. Bevan, R. Williams, S. Samac, and P. N. Burns, “Sonoporation by ultrasound-activated microbubble contrast agents: effect of acoustic exposure parameters on cell membrane permeability and cell viability,” *Ultrasound Med. Biol.*, vol. 35, no. 5, pp. 847–860, May 2009, doi: 10.1016/j.ultrasmedbio.2008.10.013.

[289] N. Kudo, K. Okada, and K. Yamamoto, “Sonoporation by single-shot pulsed ultrasound with microbubbles adjacent to cells.,” *Biophys. J.*, vol. 96, no. 12, pp. 4866–4876, Jun. 2009, doi: 10.1016/j.bpj.2009.02.072.
[290] T. van Rooij *et al.*, “Viability of endothelial cells after ultrasound-mediated sonoporation: Influence of targeting, oscillation, and displacement of microbubbles,” *J. Controlled Release*, vol. 238, pp. 197–211, 2016, doi: 10.1016/j.jconrel.2016.07.037.
[291] Y. Zhou, K. Yang, J. Cui, J. Y. Ye, and C. X. Deng, “Controlled permeation of cell membrane by single bubble acoustic cavitation,” *J. Control. Release Off. J. Control. Release Soc.*, vol. 157, no. 1, pp. 103–111, Jan. 2012, doi: 10.1016/j.jconrel.2011.09.068.
[292] F. Yuan, M. Leunig, S. K. Huang, D. A. Berk, D. Papahadjopoulos, and R. K. Jain, “Microvascular Permeability and Interstitial Penetration of Sterically Stabilized (Stealth) Liposomes in a Human Tumor Xenograft,” *Cancer Res.*, vol. 54, no. 13, pp. 3352–3356, 1994.
[293] R. K. Jain, “Determinants of Tumor Blood Flow: A Review,” *Cancer Res.*, vol. 48, no. 10, pp. 2641–2658, 1988.
[294] A. Shuaib, K. Butcher, A. A. Mohammad, M. Saqqur, and D. S. Liebeskind, “Collateral blood vessels in acute ischaemic stroke: A potential therapeutic target,” *Lancet Neurol.*, vol. 10, no. 10, pp. 909–921, 2011, doi: 10.1016/S1474-4422(11)70195-8.
[295] J. C. Baron, “Perfusion thresholds in human cerebral ischemia: Historical perspective and therapeutic implications,” *Cerebrovasc. Dis.*, vol. 11, no. SUPPL. 1, pp. 2–8, 2001, doi: 10.1159/000049119.
[296] S. He, D. Singh, and B. Helfield, “An Overview of Cell Membrane Perforation and Resealing Mechanisms for Localized Drug Delivery,” *Pharmaceutics*, vol. 14, no. 4, pp. 886–906, 2022.
[297] M. Dewenter, A. Von Der Lieth, H. A. Katus, and J. Backs, “Calcium signaling and transcriptional regulation in cardiomyocytes,” *Circ. Res.*, vol. 121, no. 8, pp. 1000–1020, 2017, doi: 10.1161/CIRCRESAHA.117.310355.
[298] R. C. Brown and T. P. Davis, “Calcium modulation of adherens and tight junction function: A potential mechanism for blood-brain barrier disruption after stroke,” *Stroke*, vol. 33, no. 6, pp. 1706–1711, 2002, doi: 10.1161/01.STR.0000016405.06729.83.
[299] A. M. Malek and S. Izumo, “Mechanism of endothelial cell shape change and cytoskeletal remodeling in response to fluid shear stress,” *J. Cell Sci.*, vol. 109, no. 4, pp. 713–726, 1996, doi: 10.1242/jcs.109.4.713.
[300] S. Feske, “Calcium signalling in lymphocyte activation and disease,” *Nat. Rev. Immunol.*, vol. 7, no. 9, pp. 690–702, 2007, doi: 10.1038/nri2152.
[301] B. L. Helfield, B. Y. C. Leung, X. Huo, and D. E. Goertz, “Scaling of the viscoelastic shell properties of phospholipid encapsulated microbubbles with ultrasound frequency.,” *Ultrasonics*, vol. 54, no. 6, pp. 1419–1424, Apr. 2014, doi: 10.1016/j.ultras.2014.03.014.
[302] R. S. C. Cobbold, “CHAPTER 3 Field Profile Analysis,” pp. 1–80.
[303] J. S. H. Lee *et al.*, “Ballistic intracellular nanorheology reveals ROCK-hard cytoplasmic stiffening response to fluid flow,” *J. Cell Sci.*, vol. 119, no. 9, pp. 1760–1768, 2006, doi: 10.1242/jcs.02899.
[304] J. Park, Z. Fan, and C. X. Deng, “Effects of shear stress cultivation on cell membrane disruption and intracellular calcium concentration in sonoporation of endothelial cells,” *J. Biomech.*, vol. 44, no. 1, pp. 164–169, 2011, doi: 10.1016/j.jbiomech.2010.09.003.
[305] W. L. Nyborg, “Heat generation by ultrasound in a relaxing medium,” *J. Acoust. Soc. Am.*, vol. 70, pp. 310–312, 1981.
[306] W. D. O’Brien, “Ultrasound-biophysics mechanisms.,” *Prog. Biophys. Mol. Biol.*, vol. 93, no. 1–3, pp. 212–55, 2007, doi: 10.1016/j.pbiomolbio.2006.07.010.

[307] J. Lechleiter, S. Girard, E. Peralta, and D. Clapham, “Spiral calcium wave propagation and annihilation in Xenopus laevis oocytes,” *Science*, vol. 252, no. 5002, pp. 123–126, 1991, doi: 10.1126/science.2011747.
[308] R. S. Leow, J. M. F. Wan, and A. C. H. Yu, “Membrane blebbing as a recovery manoeuvre in site-specific sonoporation mediated by targeted microbubbles,” *J. R. Soc. Interface*, vol. 12, no. 105, pp. 1–10, 2015.
[309] B. L. Helfield and D. E. Goertz, “Nonlinear resonance behavior and linear shell estimates for Definity™ and MicroMarker™ assessed with acoustic microbubble spectroscopy.,” *J. Acoust. Soc. Am.*, vol. 133, no. 2, pp. 1158–1168, Feb. 2013, doi: 10.1121/1.4774379.
[310] W. Lauterborn, “Numerical investigation of nonlinear oscillations of gas bubbles in liquids,” pp. 283–293, 1974.
[311] M. Overvelde *et al.*, “Nonlinear shell behavior of phospholipid-coated microbubbles.,” *Ultrasound Med. Biol.*, vol. 36, no. 12, pp. 2080–2092, Dec. 2010, doi: 10.1016/j.ultrasmedbio.2010.08.015.
[312] C. A. Dessalles, C. Leclech, A. Castagnino, and A. I. Barakat, “Integration of substrate- and flow-derived stresses in endothelial cell mechanobiology,” *Commun. Biol.*, vol. 4, no. 1, 2021, doi: 10.1038/s42003-021-02285-w.
[313] P. F. Davies, “Hemodynamic shear stress and the endothelium in cardiovascular pathophysiology,” *Nat. Clin. Pract. Cardiovasc. Med.*, vol. 6, no. 1, pp. 16–26, 2009, doi: 10.1038/ncpcardio1397.
[314] P. F. Davies, “Flow-Mediated Mechanotransduction,” *Physiol. Rev.*, vol. 75, no. 3, pp. 519–560, 1995.
[315] Y. S. J. Li, J. H. Haga, and S. Chien, “Molecular basis of the effects of shear stress on vascular endothelial cells,” *J. Biomech.*, vol. 38, no. 10, pp. 1949–1971, 2005, doi: 10.1016/j.jbiomech.2004.09.030.
[316] G. K. Hansson and P. Libby, “The immune response in atherosclerosis: a double-edged sword.,” *Nat. Rev. Immunol.*, vol. 6, no. 7, pp. 508–19, Jul. 2006, doi: 10.1038/nri1882.
[317] W. Herrington, B. Lacey, P. Sherliker, J. Armitage, and S. Lewington, “Epidemiology of Atherosclerosis and the Potential to Reduce the Global Burden of Atherothrombotic Disease,” *Circ. Res.*, vol. 118, no. 4, pp. 535–546, Feb. 2016, doi: 10.1161/CIRCRESAHA.115.307611.
[318] V. Raygor and A. Khera, “New Recommendations and Revised Concepts in Recent Guidelines on the Management of Dyslipidemias to Prevent Cardiovascular Disease: the 2018 ACC/AHA and 2019 ESC/EAS Guidelines,” *Curr. Cardiol. Rep.*, vol. 22, no. 9, Sep. 2020, doi: 10.1007/s11886-020-01331-z.
[319] M. Bäck and G. K. Hansson, “Anti-inflammatory therapies for atherosclerosis,” *Nat. Rev. Cardiol.*, vol. 12, no. 4, pp. 199–211, Apr. 2015, doi: 10.1038/nrcardio.2015.5.
[320] P. M. Ridker *et al.*, “Low-Dose Methotrexate for the Prevention of Atherosclerotic Events,” *N. Engl. J. Med.*, vol. 380, no. 8, pp. 752–762, Feb. 2019, doi: 10.1056/nejmoa1809798.
[321] J.-C. Tardif *et al.*, “Efficacy and Safety of Low-Dose Colchicine after Myocardial Infarction,” *N. Engl. J. Med.*, vol. 381, no. 26, pp. 2497–2505, Dec. 2019, doi: 10.1056/nejmoa1912388.
[322] P. M. Ridker *et al.*, “Antiinflammatory Therapy with Canakinumab for Atherosclerotic Disease,” *N. Engl. J. Med.*, vol. 377, no. 12, pp. 1119–1131, Sep. 2017, doi: 10.1056/nejmoa1707914.
[323] A. W. Tan and F. Q. Nuttall, “Characteristics of the dephosphorylated form of phosphorylase purified from rat liver and measurement of its activity in crude liver preparations,” *Biochim. Biophys. Acta*, vol. 410, no. 1, pp. 45–60, Nov. 1975, doi: 10.1016/0005-2744(75)90206-5.

[324] J.-J. Chiu and S. Chien, “Effects of Disturbed Flow on Vascular Endothelium: Pathophysiological Basis and Clinical Perspectives,” *Physiol. Rev.*, vol. 91, no. 1, pp. 327–387, 2011, doi: 10.1152/physrev.00047.2009.-Vascular.
[325] I. A. Tamargo, K. I. Baek, Y. Kim, C. Park, and H. Jo, “Flow-induced reprogramming of endothelial cells in atherosclerosis,” *Nat. Rev. Cardiol.*, vol. 20, no. 11, pp. 738–753, Nov. 2023, doi: 10.1038/s41569-023-00883-1.
[326] B. Helfield, “A Review of Phospholipid Encapsulated Ultrasound Contrast Agent Microbubble Physics,” *Ultrasound Med. Biol.*, vol. 45, no. 2, pp. 282–300, Feb. 2019, doi: 10.1016/j.ultrasmedbio.2018.09.020.
[327] D. E. Goertz, “An overview of the influence of therapeutic ultrasound exposures on the vasculature: High intensity ultrasound and microbubble-mediated bioeffects,” *Int. J. Hyperthermia*, vol. 31, no. 2, pp. 134–144, 2015, doi: 10.3109/02656736.2015.1009179.
[328] P. R. Zellner, I. Taubert, and K. Wegener, “[Transplantation and preservation of tissue-typized skin in burns],” *Chir. Z. Alle Geb. Oper. Medizen*, vol. 46, no. 7, pp. 319–322, Jul. 1975.
[329] E. Memari, D. Khan, R. Alkins, and B. Helfield, “Focused ultrasound-assisted delivery of immunomodulating agents in brain cancer,” *J. Controlled Release*, vol. 367, pp. 283–299, Mar. 2024, doi: 10.1016/j.jconrel.2024.01.034.
[330] B. Helfield, X. Chen, S. C. Watkins, and F. S. Villanueva, “Transendothelial Perforations and the Sphere of Influence of Single-Site Sonoporation,” *Ultrasound Med. Biol.*, vol. 46, no. 7, pp. 1686–1697, Jul. 2020, doi: 10.1016/j.ultrasmedbio.2020.02.017.
[331] Z. Fan, R. E. Kumon, J. Park, and C. X. Deng, “Intracellular delivery and calcium transients generated in sonoporation facilitated by microbubbles,” *J. Controlled Release*, vol. 142, no. 1, pp. 31–39, Feb. 2010, doi: 10.1016/j.jconrel.2009.09.031.
[332] G. J. Griffin, T. S. Hora, and R. Baker, “Soil fungistasis: elevation of the exogenous carbon and nitrogen requirements for spore germination by fungistatic volatiles in soils,” *Can. J. Microbiol.*, vol. 21, no. 10, pp. 1468–1475, Oct. 1975, doi: 10.1139/m75-218.
[333] A. van Wamel *et al.*, “Vibrating microbubbles poking individual cells: drug transfer into cells via sonoporation,” *J. Control. Release Off. J. Control. Release Soc.*, vol. 112, no. 2, pp. 149–155, May 2006, doi: 10.1016/j.jconrel.2006.02.007.
[334] H. Y. Stevens, B. Melchior, K. S. Bell, Y. Sujin, J. C. Yeh, and J. A. Frangos, “PECAM-1 is a critical mediator of atherosclerosis,” *DMM Dis. Models Mech.*, vol. 1, no. 2–3, pp. 175–181, 2008, doi: 10.1242/dmm.000547.
[335] Z. Chen and E. Tzima, “PECAM-1 is necessary for flow-induced vascular remodeling,” *Arterioscler. Thromb. Vasc. Biol.*, vol. 29, no. 7, pp. 1067–1073, Jul. 2009, doi: 10.1161/ATVBAHA.109.186692.
[336] A. M. Malek, S. L. Alper, and S. Izumo, “Hemodynamic Shear Stress and Its Role in Atherosclerosis,” *J. Am. Med. Assoc.*, vol. 282, no. 21, pp. 2035–2042, 1999.
[337] D. N. Ku, D. P. Giddens, C. K. Zarins, and S. Glagov, “Pulsatile flow and atherosclerosis in the human carotid bifurcation. Positive correlation between plaque location and low oscillating shear stress.,” *Arterioscler. Off. J. Am. Heart Assoc. Inc*, vol. 5, no. 3, pp. 293–302, May 1985, doi: 10.1161/01.ATV.5.3.293.
[338] R. Goel *et al.*, “Site-specific effects of PECAM-1 on atherosclerosis in LDL receptor-deficient mice,” *Arterioscler. Thromb. Vasc. Biol.*, vol. 28, no. 11, pp. 1996–2002, Nov. 2008, doi: 10.1161/ATVBAHA.108.172270.
[339] J. R. Privratsky, D. K. Newman, and P. J. Newman, “PECAM-1: Conflicts of interest in inflammation,” *Life Sci.*, vol. 87, no. 3–4, pp. 69–82, Jul. 2010, doi: 10.1016/j.lfs.2010.06.001.

[340] C. Collins *et al.*, “Haemodynamic and extracellular matrix cues regulate the mechanical phenotype and stiffness of aortic endothelial cells,” *Nat. Commun.*, vol. 5, Jun. 2014, doi: 10.1038/ncomms4984.
[341] P. J. Butler, G. Norwich, S. Weinbaum, and S. Chien, “Shear stress induces a time- and position-dependent increase in endothelial cell membrane fluidity,” *Am. J. Physiol.-Cell Physiol.*, vol. 280, no. 4, pp. C962–C969, Apr. 2001, doi: 10.1152/ajpcell.2001.280.4.C962.
[342] M. A. Haidekker, N. L’heureux, and J. A. Frangos, “Fluid shear stress increases membrane fluidity in endothelial cells: a study with DCVJ fluorescence,” *Am. J. Physiol. Heart Circ. Physiol.*, vol. 278, no. 4, pp. H1401–H1406, 2000.
[343] T. Shimanouchi, H. Ishii, N. Yoshimoto, H. Umakoshi, and R. Kuboi, “Calcein permeation across phosphatidylcholine bilayer membrane: Effects of membrane fluidity, liposome size, and immobilization,” *Colloids Surf. B Biointerfaces*, vol. 73, no. 1, pp. 156–160, Oct. 2009, doi: 10.1016/j.colsurfb.2009.05.014.
[344] W. A. Hendrickson and K. B. Ward, “Atomic models for the polypeptide backbones of myohemerythrin and hemerythrin,” *Biochem. Biophys. Res. Commun.*, vol. 66, no. 4, pp. 1349–1356, Oct. 1975, doi: 10.1016/0006-291x(75)90508-2.
[345] Y. Gao and Z. S. Galis, “Exploring the Role of Endothelial Cell Resilience in Cardiovascular Health and Disease,” *Arterioscler. Thromb. Vasc. Biol.*, vol. 41, no. 1, pp. 179–185, Jan. 2021, doi: 10.1161/ATVBAHA.120.314346.
[346] P. Kong, Z. Y. Cui, X. F. Huang, D. D. Zhang, R. J. Guo, and M. Han, “Inflammation and atherosclerosis: signaling pathways and therapeutic intervention,” *Signal Transduct. Target. Ther.*, vol. 7, no. 1, Dec. 2022, doi: 10.1038/s41392-022-00955-7.
[347] S. Lee *et al.*, “Autocrine VEGF Signaling Is Required for Vascular Homeostasis,” *Cell*, vol. 130, no. 4, pp. 691–703, Aug. 2007, doi: 10.1016/j.cell.2007.06.054.
[348] S. M. Weis and D. A. Cheresh, “Pathophysiological consequences of VEGF-induced vascular permeability,” *Nature*, vol. 437, no. 7058, pp. 497–504, Sep. 2005, doi: 10.1038/nature03987.
[349] S. Esser, K. Wolburg, H. Wolburg, G. Breier, T. Kurzchalia, and W. Risau, “Vascular Endothelial Growth Factor Induces Endothelial Fenestrations In Vitro,” 1998. [Online]. Available: http://www.jcb.org
[350] J. Lachmajer, “Symposium on malaria research,” *Bull. Inst. Marit. Trop. Med. Gdynia*, vol. 26, no. 1, pp. 53–58, 1975.
[351] X. Bao, C. Lu, and J. A. Frangos, “Temporal Gradient in Shear But Not Steady Shear Stress Induces PDGF-A and MCP-1 Expression in Endothelial Cells: Role of NO, NFκB, and *egr*- 1,” *Arterioscler. Thromb. Vasc. Biol.*, vol. 19, no. 4, pp. 996–1003, Apr. 1999, doi: 10.1161/01.ATV.19.4.996.
[352] M. Papadaki, S. G. Eskin, J. Ruef, M. S. Runge, and L. V. McIntire, “Fluid shear stress as a regulator of gene expression in vascular cells: possible correlations with diabetic abnormalities,” *Diabetes Res. Clin. Pract.*, vol. 45, no. 2–3, pp. 89–99, Sep. 1999, doi: 10.1016/S0168-8227(99)00036-4.
[353] A. R. Brooks, P. I. Lelkes, and G. M. Rubanyi, “Gene expression profiling of human aortic endothelial cells exposed to disturbed flow and steady laminar flow,” 2002, doi: 10.1152/physiolgenomics.00075.2001.-Subtrac.
[354] Y. C. Tsai *et al.*, “Laminar flow attenuates interferon-induced inflammatory responses in endothelial cells,” *Cardiovasc. Res.*, vol. 74, no. 3, pp. 497–505, Jun. 2007, doi: 10.1016/j.cardiores.2007.02.030.
[355] “V.I. Gavrilov,” *Acta Virol.*, vol. 19, no. 6, p. 510, Nov. 1975.

[356] S. M. Mccormick *et al.*, “DNA microarray reveals changes in gene expression of shear stressed human umbilical vein endothelial cells.” [Online]. Available: www.pnas.orgcgidoi10.1073pnas.171259298
[357] X. Yu *et al.*, “CXCL16 induces angiogenesis in autocrine signaling pathway involving hypoxia-inducible factor 1α in human umbilical vein endothelial cells,” *Oncol. Rep.*, vol. 35, no. 3, pp. 1557–1565, Mar. 2016, doi: 10.3892/or.2015.4520.
[358] M. Werle, U. Schmal, K. Hanna, and J. Kreuzer¨innere, “M CP-1 induces activation of MAP-kinases ERK, JNK and p38 MAPK in human endothelial cells,” 2002. [Online]. Available: www.elsevier.com/locate/cardiores
[359] K. Yamamoto, Y. Nogimori, H. Imamura, and J. Ando, “Shear stress activates mitochondrial oxidative phosphorylation by reducing plasma membrane cholesterol in vascular endothelial cells,” *Proc. Natl. Acad. Sci.*, vol. 117, no. 52, pp. 33660–33667, 2020, doi: 10.1073/pnas.2014029117/-/DCSupplemental.
[360] W. Chen, D. B. Jump, W. J. Esselman, and J. V. Busik, “Inhibition of cytokine signaling in human retinal endothelial cells through modification of caveolae/lipid rafts by docosahexaenoic acid,” *Invest. Ophthalmol. Vis. Sci.*, vol. 48, no. 1, pp. 18–26, Jan. 2007, doi: 10.1167/iovs.06-0619.
[361] P. Varshney, V. Yadav, and N. Saini, “Lipid rafts in immune signalling: current progress and future perspective,” *Immunology*, vol. 149, no. 1, pp. 13–24, Sep. 2016, doi: 10.1111/imm.12617.
[362] H. Yusefi and B. Helfield, “The influence of inter-bubble spacing on the resonance response of ultrasound contrast agent microbubbles,” *Ultrason. Sonochem.*, vol. 90, Nov. 2022, doi: 10.1016/j.ultsonch.2022.106191.
[363] V. Wang, M. Gauthier, V. Decot, L. Reppel, and D. Bensoussan, “Systematic Review on CAR-T Cell Clinical Trials Up to 2022: Academic Center Input,” *Cancers*, vol. 15, no. 4, Feb. 2023, doi: 10.3390/cancers15041003.
[364] J. Hartmann, M. Schüßler-Lenz, A. Bondanza, and C. J. Buchholz, “Clinical development of CAR T cells—challenges and opportunities in translating innovative treatment concepts,” *EMBO Mol. Med.*, vol. 9, no. 9, pp. 1183–1197, Sep. 2017, doi: 10.15252/emmm.201607485.
[365] S. L. Maude *et al.*, “Tisagenlecleucel in Children and Young Adults with B-Cell Lymphoblastic Leukemia,” *N. Engl. J. Med.*, vol. 378, no. 5, pp. 439–448, Feb. 2018, doi: 10.1056/nejmoa1709866.
[366] T. W. Laetsch *et al.*, “Three-Year Update of Tisagenlecleucel in Pediatric and Young Adult Patients With Relapsed/Refractory Acute Lymphoblastic Leukemia in the ELIANA Trial,” *J Clin Oncol*, vol. 41, pp. 1664–1669, 2022, doi: 10.1200/JCO.22.
[367] S. J. Bagley and D. M. O’Rourke, “Clinical investigation of CAR T cells for solid tumors: Lessons learned and future directions,” *Pharmacol. Ther.*, vol. 205, Jan. 2020, doi: 10.1016/j.pharmthera.2019.107419.
[368] L. Piali, A. Fichtel, H. J. Terpe, B. A. Imhof, and R. H. Gisler, “Endothelial vascular cell adhesion molecule 1 expression is suppressed by melanoma and carcinoma.,” *J. Exp. Med.*, vol. 181, no. 2, pp. 811–816, Feb. 1995, doi: 10.1084/jem.181.2.811.
[369] C. Weishaupt, K. N. Munoz, E. Buzney, T. S. Kupper, and R. C. Fuhlbrigge, “T-cell distribution and adhesion receptor expression in metastatic melanoma,” *Clin. Cancer Res.*, vol. 13, no. 9, pp. 2549–2556, May 2007, doi: 10.1158/1078-0432.CCR-06-2450.
[370] H. T. Nia *et al.*, “Solid stress and elastic energy as measures of tumour mechanopathology,” *Nat. Biomed. Eng.*, vol. 1, no. 1, Jan. 2017, doi: 10.1038/s41551-016-0004.

[371] F. Mpekris, M. Panagi, A. Charalambous, C. Voutouri, and T. Stylianopoulos, “Modulating cancer mechanopathology to restore vascular function and enhance immunotherapy,” *Cell Rep. Med.*, vol. 5, no. 7, Jul. 2024, doi: 10.1016/j.xcrm.2024.101626.
[372] P. F. Davies, “Flow-mediated endothelial mechanotransduction,” *Physiol. Rev.*, vol. 75, no. 3, pp. 519–560, Jul. 1995, doi: 10.1152/physrev.1995.75.3.519.
[373] N. D. Sheybani, A. J. Batts, A. S. Mathew, E. Andrew Thim, and R. J. Price, “Focused ultrasound hyperthermia augments release of glioma-derived extracellular vesicles with differential immunomodulatory capacity,” *Theranostics*, vol. 10, no. 16, pp. 7436–7447, 2020, doi: 10.7150/thno.46534.
[374] D. Singh, E. Memari, S. He, H. Yusefi, and B. Helfield, “Cardiac gene delivery using ultrasound: State of the field,” *Mol. Ther. Methods Clin. Dev.*, vol. 32, no. 3, Sep. 2024, doi: 10.1016/j.omtm.2024.101277.
[375] K. Xhima, F. Nabbouh, K. Hynynen, I. Aubert, and A. Tandon, “Noninvasive delivery of an α-synuclein gene silencing vector with magnetic resonance–guided focused ultrasound,” *Mov. Disord.*, vol. 33, no. 10, pp. 1567–1579, Oct. 2018, doi: 10.1002/mds.101.
[376] A. Carpentier *et al.*, “Repeated blood–brain barrier opening with a nine-emitter implantable ultrasound device in combination with carboplatin in recurrent glioblastoma: a phase I/II clinical trial,” *Nat. Commun.*, vol. 15, no. 1, Dec. 2024, doi: 10.1038/s41467-024-45818-7.
[377] D. McMahon and K. Hynynen, “Acute inflammatory response following increased blood-brain barrier permeability induced by focused ultrasound is dependent on microbubble dose,” *Theranostics*, vol. 7, no. 16, pp. 3989–4000, 2017, doi: 10.7150/thno.21630.
[378] N. Sheikov, N. McDannold, S. Sharma, and K. Hynynen, “Effect of focused ultrasound applied with an ultrasound contrast agent on the tight junctional integrity of the brain microvascular endothelium,” *Ultrasound Med. Biol.*, vol. 34, no. 7, pp. 1093–1104, 2008, doi: 10.1016/j.ultrasmedbio.2007.12.015.
[379] H. Tsuboi, J. Ando, R. Korenaga, Y. Takada, and A. Kamiya, “Flow Stimulates ICAM-1 Expression Time and Shear Stress Dependently in Cultured Human Endothelial Cells,” *Biochem. Biophys. Res. Commun.*, vol. 206, no. 3, pp. 988–996, Jan. 1995, doi: 10.1006/bbrc.1995.1140.
[380] M. Morigi *et al.*, “Fluid Shear Stress Modulates Surface Expression of Adhesion Molecules by Endothelial Cells,” *Blood*, vol. 85, no. 7, pp. 1696–1703, 1995.
[381] B. J. Steffen, G. Breier, E. C. Butcher, M. Schulz, and B. Engelhardt, “ICAM-1, VCAM-1, and MAdCAM-1 are expressed on choroid plexus epithelium but not endothelium and mediate binding of lymphocytes in vitro,” *Am. J. Pathol.*, vol. 148, no. 6, pp. 1819–1838, Jun. 1996.
[382] J. Ando and K. Yamamoto, “Effects of Shear Stress and Stretch on Endothelial Function,” *Antioxid. Redox Signal.*, vol. 15, no. 5, pp. 1389–1403, 2011.
[383] L. Cucullo, M. Hossain, V. Puvenna, N. Marchi, and D. Janigro, “The role of shear stress in Blood-Brain Barrier endothelial physiology,” *BMC Neurosci.*, vol. 12, May 2011, doi: 10.1186/1471-2202-12-40.
[384] K. D. Rochfort and P. M. Cummins, “Thrombomodulin regulation in human brain microvascular endothelial cells in vitro: Role of cytokines and shear stress,” *Microvasc. Res.*, vol. 97, pp. 1–5, Jan. 2015, doi: 10.1016/j.mvr.2014.09.003.
[385] M. F. Stins, F. Gilles, and K. S. Kim, “Selective expression of adhesion molecules on human brain microvascular endothelial cells,” 1997.
[386] E. A. Lidington, D. L. Moyes, A. M. Mccormack, and M. L. Rose, “A comparison of primary endothelial cells and endothelial cell lines for studies of immune interactions,” 1999.

[387] G. Invernici *et al.*, “Human microvascular endothelial cells from different fetal organs demonstrate organ-specific CAM expression,” *Exp. Cell Res.*, vol. 308, no. 2, pp. 273–282, Aug. 2005, doi: 10.1016/j.yexcr.2005.04.033.
[388] H. Qazi, Z. D. Shi, and J. M. Tarbell, “Fluid shear stress regulates the invasive potential of glioma cells via modulation of migratory activity and matrix metalloproteinase expression,” *PLoS ONE*, vol. 6, no. 5, 2011, doi: 10.1371/journal.pone.0020348.
[389] A. Grossen *et al.*, “Physical Forces in Glioblastoma Migration: A Systematic Review,” *Int. J. Mol. Sci.*, vol. 23, no. 7, Apr. 2022, doi: 10.3390/ijms23074055.
[390] E. Memari and B. Helfield, “Shear stress preconditioning and microbubble flow pattern modulate ultrasound-assisted plasma membrane permeabilization,” *Mater. Today Bio*, vol. 27, Aug. 2024, doi: 10.1016/j.mtbio.2024.101128.
[391] N. T. Luu, M. Rahman, P. C. Stone, G. E. Rainger, and G. B. Nash, “Responses of endothelial cells from different vessels to inflammatory cytokines and shear Stress: Evidence for the pliability of endothelial phenotype,” *J. Vasc. Res.*, vol. 47, no. 5, pp. 451–461, Aug. 2010, doi: 10.1159/000302613.
[392] K. Ran, Z. Yang, Y. Zhao, and X. Wang, “Corrigendum to ‘Transmural pressure drives proliferation of human arterial smooth muscle cells via mechanism associated with NADPH oxidase and Survivin’ [Microvasc. Res. 126 (2019) 103905],” *Microvasc. Res.*, vol. 128, p. 103960, Mar. 2020, doi: 10.1016/j.mvr.2019.103960.
[393] K. Rennier and J. Y. Ji, “The role of death-associated protein kinase (DAPK) in endothelial apoptosis under fluid shear stress,” *Life Sci.*, vol. 93, no. 5–6, pp. 194–200, Aug. 2013, doi: 10.1016/j.lfs.2013.06.011.
[394] R. Alon and S. Feigelson, “From rolling to arrest on blood vessels: leukocyte tap dancing on endothelial integrin ligands and chemokines at sub-second contacts,” *Semin. Immunol.*, vol. 14, no. 2, pp. 93–104, Apr. 2002, doi: 10.1006/smim.2001.0346.
[395] S. J. O’Carroll *et al.*, “Pro-inflammatory TNFα and IL-1β differentially regulate the inflammatory phenotype of brain microvascular endothelial cells,” *J. Neuroinflammation*, vol. 12, no. 1, p. 131, Dec. 2015, doi: 10.1186/s12974-015-0346-0.
[396] V. Singh, R. Kaur, P. Kumari, C. Pasricha, and R. Singh, “ICAM-1 and VCAM-1: Gatekeepers in various inflammatory and cardiovascular disorders,” *Clin. Chim. Acta*, vol. 548, Aug. 2023, doi: 10.1016/j.cca.2023.117487.
[397] J. A. DiVietro, M. J. Smith, B. R. E. Smith, L. Petruzzelli, R. S. Larson, and M. B. Lawrence, “Immobilized IL-8 Triggers Progressive Activation of Neutrophils Rolling In Vitro on P-Selectin and Intercellular Adhesion Molecule-1,” *J. Immunol.*, vol. 167, no. 7, pp. 4017–4025, Oct. 2001, doi: 10.4049/jimmunol.167.7.4017.
[398] P. Theofilis *et al.*, “Inflammatory Mechanisms Contributing to Endothelial Dysfunction,” *Biomedicines*, vol. 9, no. 7, p. 781, Jul. 2021, doi: 10.3390/biomedicines9070781.
[399] E. Bergman *et al.*, “Cell stiffness predicts cancer cell sensitivity to ultrasound as a selective superficial cancer therapy,” *Bioeng. Transl. Med.*, vol. 6, no. 3, Sep. 2021, doi: 10.1002/btm2.10226.
[400] C. T. Curley *et al.*, “Immunomodulation of intracranial melanoma in response to blood-tumor barrier opening with focused ultrasound,” *Theranostics*, vol. 10, no. 19, pp. 8821–8833, 2020, doi: 10.7150/thno.47983.
[401] A. S. Mathew, C. M. Gorick, and R. J. Price, “Multiple regression analysis of a comprehensive transcriptomic data assembly elucidates mechanically- And biochemically-driven responses to focused ultrasound blood-brain barrier disruption,” *Theranostics*, vol. 11, no. 20, pp. 9847–9858, 2021, doi: 10.7150/thno.65064.

[402] M. Liu, S. Guo, and J. K. Stiles, “The emerging role of CXCL10 in cancer (Review),” *Oncol. Lett.*, vol. 2, no. 4, pp. 583–589, Jul. 2011, doi: 10.3892/ol.2011.300.
[403] X. bing Jiang, X. ling Lu, P. Hu, and R. en Liu, “Improved therapeutic efficacy using vaccination with glioma lysate-pulsed dendritic cells combined with IP-10 in murine glioma,” *Vaccine*, vol. 27, no. 44, pp. 6210–6216, Oct. 2009, doi: 10.1016/j.vaccine.2009.08.002.
[404] M. Fujita *et al.*, “Effective Immunotherapy against Murine Gliomas Using Type 1 Polarizing Dendritic Cells—Significant Roles of CXCL10,” *Cancer Res.*, vol. 69, no. 4, pp. 1587–1595, Feb. 2009, doi: 10.1158/0008-5472.CAN-08-2915.
[405] X. Xu *et al.*, “Recruiting T-Cells toward the Brain for Enhanced Glioblastoma Immunotherapeutic Efficacy by Co-Delivery of Cytokines and Immune Checkpoint Antibodies with Macrophage-Membrane-Camouflaged Nanovesicles,” *Adv. Mater.*, vol. 35, no. 25, p. 2209785, Jun. 2023, doi: 10.1002/adma.202209785.
[406] I. G. House *et al.*, “Macrophage-derived CXCL9 and CXCL10 are required for antitumor immune responses following immune checkpoint blockade,” *Clin. Cancer Res.*, vol. 26, no. 2, pp. 487–504, Jan. 2020, doi: 10.1158/1078-0432.CCR-19-1868.
[407] D. Hanahan and R. A. Weinberg, “Hallmarks of Cancer: The Next Generation,” *Cell*, vol. 144, no. 5, pp. 646–674, Mar. 2011, doi: 10.1016/j.cell.2011.02.013.
[408] A. Obermair *et al.*, “Correlation of Vascular Endothelial Growth Factor Expression and Microvessel Density in Cervical Intraepithelial Neoplasia,” *JNCI J. Natl. Cancer Inst.*, vol. 89, no. 16, pp. 1212–1217, Aug. 1997, doi: 10.1093/jnci/89.16.1212.
[409] I. H. Chaudhry, D. G. O’Donovan, P. E. C. Brenchley, H. Reid, and I. S. D. Roberts, “Vascular endothelial growth factor expression correlates with tumour grade and vascularity in gliomas,” *Histopathology*, vol. 39, no. 4, pp. 409–415, 2001, doi: 10.1046/j.1365-2559.2001.01230.x.
[410] J. M. L. Ebos and R. S. Kerbel, “Antiangiogenic therapy: Impact on invasion, disease progression, and metastasis,” *Nat. Rev. Clin. Oncol.*, vol. 8, no. 4, pp. 210–221, Apr. 2011, doi: 10.1038/nrclinonc.2011.21.
[411] O. Keunen *et al.*, “Anti-VEGF treatment reduces blood supply and increases tumor cell invasion in glioblastoma,” *Proc. Natl. Acad. Sci. U. S. A.*, vol. 108, no. 9, pp. 3749–3754, Mar. 2011, doi: 10.1073/pnas.1014480108.
[412] E. A. Kuczynski, P. B. Vermeulen, F. Pezzella, R. S. Kerbel, and A. R. Reynolds, “Vessel co-option in cancer,” *Nat. Rev. Clin. Oncol.*, vol. 16, no. 8, pp. 469–493, Aug. 2019, doi: 10.1038/s41571-019-0181-9.
[413] A. W. Griffioen, C. A. Damen, G. H. Blijham, and G. Groenewegen, “Tumor Angiogenesis Is Accompanied by a Decreased Inflammatory Response of Tumor-Associated Endothelium,” 1996.
[414] A. E. M. Dirkx *et al.*, “Tumor angiogenesis modulates leukocyte-vessel wall interactions in Vivo by reducing endothelial adhesion molecule expression,” *Cancer Res.*, vol. 63, pp. 2322–2329, 2003.
[415] C. Morrison, “Immuno-oncologists eye up macrophage targets,” *Nat. Rev. Drug Discov.*, vol. 15, no. 6, pp. 373–374, Jun. 2016, doi: 10.1038/nrd.2016.111.
[416] S. Wang *et al.*, “Targeting M2-like tumor-associated macrophages is a potential therapeutic approach to overcome antitumor drug resistance,” *Npj Precis. Oncol.*, vol. 8, no. 1, Dec. 2024, doi: 10.1038/s41698-024-00522-z.
[417] X. Valencia, G. Stephens, R. Goldbach-Mansky, M. Wilson, E. M. Shevach, and P. E. Lipsky, “TNF downmodulates the function of human CD4+CD25hi T-regulatory cells,” *Blood*, vol. 108, no. 1, pp. 253–261, Jul. 2006, doi: 10.1182/blood-2005-11-4567.

[418] F. J. Lejeune, D. Liénard, M. Matter, and C. Rüegg, “Efficiency of recombinant human TNF in human cancer therapy,” *Cancer Immun.*, vol. 6, no. 22, p. 6, 2006, doi: 10.1158/1424-9634.DCL-6.6.1/2368016/6.pdf.
[419] G. Landskron, M. De La Fuente, P. Thuwajit, C. Thuwajit, and M. A. Hermoso, “Chronic inflammation and cytokines in the tumor microenvironment,” *J. Immunol. Res.*, vol. 2014, 2014, doi: 10.1155/2014/149185.
[420] A. Mantovani, M. A. Cassatella, C. Costantini, and S. Jaillon, “Neutrophils in the activation and regulation of innate and adaptive immunity,” *Nat. Rev. Immunol.*, vol. 11, no. 8, pp. 519–531, Aug. 2011, doi: 10.1038/nri3024.
[421] S. B. Coffelt, M. D. Wellenstein, and K. E. de Visser, “Neutrophils in cancer: neutral no more,” *Nat. Rev. Cancer*, vol. 16, no. 7, pp. 431–446, Jul. 2016, doi: 10.1038/nrc.2016.52.
[422] G. He *et al.*, “Peritumoural neutrophils negatively regulate adaptive immunity via the PD-L1/PD-1 signalling pathway in hepatocellular carcinoma,” *J. Exp. Clin. Cancer Res.*, vol. 34, no. 1, Nov. 2015, doi: 10.1186/s13046-015-0256-0.
[423] Z. G. Fridlender and S. M. Albelda, “Tumor-associated neutrophils: Friend or foe?,” *Carcinogenesis*, vol. 33, no. 5, pp. 949–955, May 2012, doi: 10.1093/carcin/bgs123.
[424] Z. G. Fridlender *et al.*, “Transcriptomic analysis comparing tumor-associated neutrophils with granulocytic myeloid-derived suppressor cells and normal neutrophils,” *PLoS ONE*, vol. 7, no. 2, Feb. 2012, doi: 10.1371/journal.pone.0031524.
[425] B. L. Helfield, X. Huo, R. Williams, and D. E. Goertz, “The Effect of Preactivation Vial Temperature on the Acoustic Properties of DefinityTM,” *Ultrasound Med. Biol.*, vol. 38, no. 7, pp. 1298–1305, Jul. 2012, doi: 10.1016/j.ultrasmedbio.2012.03.005.
[426] X. Wang *et al.*, “Advances on fluid shear stress regulating blood-brain barrier,” *Microvasc. Res.*, vol. 128, Mar. 2020, doi: 10.1016/j.mvr.2019.103930.
[427] A. W. Griffioen, C. A. Damen, S. Martinotti, G. H. Blijham, and G. Groenewegen, “Endothelial intercellular adhesion molecule-1 expression is suppressed in human malignancies: The role of angiogenic factors,” *Cancer Res.*, vol. 56, no. 5, pp. 1111–1117, 1996.
[428] E. O. Long, “ICAM-1: Getting a Grip on Leukocyte Adhesion,” *J. Immunol.*, vol. 186, no. 9, pp. 5021–5023, May 2011, doi: 10.4049/jimmunol.1100646.
[429] T. M. Bui, H. L. Wiesolek, and R. Sumagin, “ICAM-1: A master regulator of cellular responses in inflammation, injury resolution, and tumorigenesis,” *J. Leukoc. Biol.*, vol. 108, no. 3, pp. 787–799, Sep. 2020, doi: 10.1002/JLB.2MR0220-549R.
[430] T. O. Kleine and L. Benes, “Immune surveillance of the human central nervous system (CNS): Different migration pathways of immune cells through theblood–brain barrier and blood–cerebrospinal fluid barrier in healthy persons,” *Cytometry A*, vol. 69A, no. 3, pp. 147–151, Mar. 2006, doi: 10.1002/cyto.a.20225.
[431] C. Y. Fears, H. W. Sontheimer, D. C. Bullard, and C. L. Gladson, “Could labeled neuronal progenitor cells be used to target glioma tumor endothelium?,” *Cancer Biol. Ther.*, vol. 3, no. 9, pp. 845–846, 2004, doi: 10.4161/cbt.3.9.1123.
[432] C. Zhang, Y. Hu, and C. Shi, “Targeting Natural Killer Cells for Tumor Immunotherapy,” *Front. Immunol.*, vol. 11, Feb. 2020, doi: 10.3389/fimmu.2020.00060.
[433] S. Abe *et al.*, “Combination of ultrasound-based mechanical disruption of tumor with immune checkpoint blockade modifies tumor microenvironment and augments systemic antitumor immunity,” *J. Immunother. Cancer*, vol. 10, no. 1, p. e003717, Jan. 2022, doi: 10.1136/jitc-2021-003717.